mαcrϕ@ufmg

Universidade Federal de Minas Gerais
Programa de Pós-Graduação em Engenharia Elétrica
Research group MACRO - Mechatronics, Control and Robotics

PATH TRACKING CONTROL OF A SUSPENDED LOAD USING A TILT-ROTOR UAV

Brenner Santana Rego

Belo Horizonte, Brazil
2016

Brenner Santana Rego

PATH TRACKING CONTROL OF A SUSPENDED LOAD USING A TILT-ROTOR UAV

Thesis submitted to the Graduate Program in Electrical Engineering of Escola de Engenharia at the Universidade Federal de Minas Gerais, in partial fulfillment of the requirements for the degree of Master in Electrical Engineering.

Advisor: Guilherme Vianna Raffo

Belo Horizonte, Brazil
2016

Rego, Brenner Santana.
R343p Path Tracking Control of a Suspended Load Using a Tilt-rotor UAV [recurso eletrônico] / Brenner Santana Rego. - 2016.
1 recurso online (xxxii,150 f. : il., color.) : pdf.

Orientador: Guilherme Vianna Raffo.

Dissertação (mestrado) - Universidade Federal de Minas Gerais, Escola de Engenharia.

Apêndices: f.129-150.
Bibliografia: f.121-128.

Exigências do sistema: Adobe Acrobat Reader.

1. Engenharia Elétrica - Teses. 2. Aeronave não tripulada – Teses. 3. Transporte de carga – Teses. I. Raffo, Guilherme Vianna. II. Universidade Federal de Minas Gerais. Escola de Engenharia. III. Título.

CDU: 621.3(043)

Ficha catalográfica elaborada pela Bibliotecária Letícia Alves Vieira - CRB-6/2337
Biblioteca Prof. Mário Werneck - Escola de Engenharia da UFMG

UNIVERSIDADE FEDERAL DE MINAS GERAIS
ESCOLA DE ENGENHARIA
Programa de Pós-Graduação em Engenharia Elétrica

ATA DA 947ª DEFESA DE DISSERTAÇÃO DE MESTRADO
DO PROGRAMA DE PÓS-GRADUAÇÃO EM ENGENHARIA ELÉTRICA

ATA DE DEFESA DE DISSERTAÇÃO DE MESTRADO do aluno **Brenner Santana Rego** - registro de matrícula de número 2014722972. Às 14:00 horas do dia 08 do mês de novembro de 2016, reuniu-se na Escola de Engenharia da UFMG a Comissão Examinadora da DISSERTAÇÃO DE MESTRADO para julgar, em exame final, o trabalho intitulado **"Path Tracking Control of a Suspended Load Using a Tilt-rotor UAV"** da Área de Concentração em Sinais e Sistemas, Linha de Pesquisa Controle, Automação e Robótica. O Prof. Guilherme Vianna Raffo, orientador do aluno, abriu a sessão apresentando os membros da Comissão e, dando continuidade aos trabalhos, informou aos presentes que, de acordo com o Regulamento do Programa no seu Art. 8.16, será considerado APROVADO na defesa da Dissertação de Mestrado o candidato que obtiver a aprovação unânime dos membros da Comissão Examinadora. Em seguida deu início à apresentação do trabalho pelo Candidato. Ao final da apresentação seguiu-se a arguição do candidato pelos examinadores. Logo após o término da arguição a Comissão Examinadora se reuniu, sem a presença do Candidato e do público, e elegeu o Prof GUILHERME VIANNA RAFFO para presidir a fase de avaliação do trabalho, constituída de deliberação individual de APROVAÇÃO ou de REPROVAÇÃO e expedição do resultado final. As deliberações individuais de cada membro da Comissão Examinadora foram as seguintes:

Membro da Comissão Examinadora	Instituição de Origem	Deliberação	Assinatura
Prof. Dr. Guilherme Vianna Raffo - Orientador	DELT (UFMG)	aprovação	
Prof. Dr. Bruno Otávio Soares Teixeira	DELT (UFMG)	aprovação	
Prof. Dr. Leonardo Antônio Borges Tôrres	DELT (UFMG)	Aprovação	Leonardo A.B. Tôrres

Tendo como base as deliberações dos membros da Comissão Examinadora a Dissertação de Mestrado foi APROVADA O resultado final de APROVAÇÃO foi comunicado publicamente ao Candidato pelo Presidente da Comissão, ressaltando que a obtenção do Grau de Mestre em ENGENHARIA ELÉTRICA fica condicionada à entrega do TEXTO FINAL da Dissertação de Mestrado.O Candidato terá um prazo máximo de 30 (trinta) dias, a partir desta data, para fazer as CORREÇÕES DE FORMA e entregar o texto final da Dissertação de Mestrado na secretaria do PPGEE/UFMG. As correções de forma exigidas pelos membros da Comissão Examinadora deverão ser registradas em um exemplar do texto da Dissertação de Mestrado, cuja verificação ficará sob a responsabilidade do Presidente da Banca Examinadora. Nada mais havendo a tratar o Presidente encerrou a reunião e lavrou a presente ATA, que será assinada pelo Presidente da Comissão Examinadora. Belo Horizonte, 08 de novembro de 2016.

ASSINATURA DO PRESIDENTE DA COMISSÃO EXAMINADORA

To Maria José Rego
and Osvaldo Santana Ferreira

Acknowledgements

Firstly, I would like to thank our Lord, for giving me enough strength and wisdom, and supporting me emotionally and spiritually throughout this journey. Without His help, even the first steps would not have been possible.

To my parents, Maria José Rego and Osvaldo Santana Ferreira, and also to my brother, Felipe Santana Rego, for supporting me and cheering me up along the path.

To my advisor, Prof. Guilherme Vianna Raffo, to whom I would like to express my sincere gratitude for accepting me as his student, guiding me and also supporting me at every hard time.

To my colleagues and ex-colleagues from MACRO, ProVANT, MACSIN, CORO and other laboratories, for their friendship and also for supporting me when going through hard times: Alex, Ana Christine, Antônio, Arthur Lara, Brayan, Daniel, Diana, Diego, Ernesto Lana, Fernanda, Frederico, Fredy, Fulvia, Gabriela, Heitor, Iuro, Jaime Arturo, Juan Camilo, Juan José (Juancho), Laysa Mello, Leandro, Lucas Coelho, Marcelo, Marcus, Maria Victoria, Mariana, Paulo Eduardo, Pedro André, Petrus, Rafael Palma, Raphael Padrão, Stella, Wendy. I would like to thank also Marcelino Almeida, who, through his master thesis, taught me several things in the beginning of this journey, without knowing it.

To Prof. Mara Figueiredo, Prof. Rodrigo Lemos and Prof. Reinaldo Palhares, who together made the bridge that I crossed from the UFG to the UFMG, arriving at the PPGEE, where I get to know Prof. Guilherme Vianna Raffo. A special thanks to Prof. Mara Figueiredo and Prof. Antônio Baleeiro from UFG, who cheered me up throughout the master's selection process.

To Prof. Bruno Teixeira and Prof. Leonardo Torres, for accepting to review my thesis, and for contributing with ideas and suggestions that improved the work.

To the funding agencies CAPES, CNPq and FAPEMIG, for the financial support, which was essential for the accomplishment of this work.

Finally, I would like to thank the Graduate Program in Electrical Engineering, for providing the infrastructure required for the accomplishment of this work.

Resumo

Este trabalho trata o problema de transporte de carga usando um veículo aéreo não tripulado (VANT) do tipo *tilt-rotor*. Um VANT *tilt-rotor* é uma aeronave híbrida capaz de realizar voos com velocidade de cruzeiro elevada, como VANTs de asa fixa, e decolagem e pouso vertical, como VANTs de asa rotativa. Aborda-se o problema de rastreio de trajetória da carga suspensa, no qual a carga deve seguir uma trajetória desejada enquanto o VANT *tilt-rotor* é mantido estável. A cinemática do sistema é formulada do ponto de vista da carga, a partir da qual um modelo dinâmico rigoroso é obtido através da formulação de Euler-Lagrange. Obtém-se uma representação em espaço de estados não linear altamente acoplada e afim nas entradas, na qual a posição e a orientação da carga são diretamente representadas por variáveis de estado. Este fato permite que estratégias de controle por realimentação de estados possam conduzir a carga através de uma trajetória de referência com relação a um sistema de coordenadas inercial. Assumindo que todos os estados do sistema são medidos, duas estratégias de controle linear em tempo discreto são propostas para solucionar o problema de rastreio de trajetória da carga com rejeição a perturbações constantes: um regulador linear quadrático de tempo discreto e um controlador $\mathcal{H}_2/\mathcal{H}_\infty$ misto de tempo discreto com restrições na alocação de polos. O primeiro controlador é projetado através da solução de uma equação algébrica de Riccati de tempo discreto, enquanto o segundo controlador é projetado através de uma abordagem de desigualdades matriciais lineares. As equações de estado são linearizadas em torno da trajetória de referência, aumentadas com ações integrais e discretizadas para que os controladores sejam projetados. Por outro lado, considerando que nem todos os estados estão disponíveis para realimentação, medições estão corrompidas com ruído e sensores possuem diferentes períodos de amostragem, propõe-se estratégias de estimação de estados com o intuito de fornecer todo o vetor de estados para os controladores. Um filtro de Kalman linearizado é proposto para um cenário no qual apenas a metade do vetor de estados é medida (variáveis de posição), e corrompida com ruído Gaussiano com média nula. Para a segunda estratégia de estimação propõe-se um estimador de estados zonotópico, considerando um cenário no qual as medições são fornecidas por sensores que possuem diferentes períodos de amostragem, corrompidas com ruído desconhecido porém limitado. Ambos os estimadores são projetados baseados em equações dinâmicas linearizadas e discretizadas, aumentadas

com perturbações externas que afetam o sistema. Para corroborar o bom desempenho das estratégias propostas, resultados de simulação numérica são apresentados.

Palavras-chave: Transporte de carga, Veículos aéreos não tripulados, Rastreio de trajetória, Estimação de estados.

Abstract

This work deals with the problem of load transportation using a tilt-rotor unmanned aerial vehicle (UAV). A tilt-rotor UAV is a hybrid aircraft capable of performing flights with improved forward speed, as fixed-wing UAVs, and vertical take-off and landing and hover, as rotary-wing UAVs. We address the problem of path tracking control of the suspended load in hover flight, in which the load must follow a desired trajectory while the tilt-rotor UAV is stabilized. The kinematics of the system are formulated from the load's perspective, from which a rigorous dynamic model is derived using the Euler-Lagrange approach. We obtain a highly coupled, nonlinear state-space representation of the system, affine in the inputs, with the load's position and orientation directly represented by state variables. This fact allows designed state-feedback control strategies to steer the trajectory of the load with respect to an inertial frame. Assuming that all the system states can be measured, we propose two linear discrete-time state-feedback control strategies to solve the problem of path tracking of the load, with constant disturbances rejection: a discrete-time linear quadratic regulator (DLQR) and a discrete-time mixed $\mathcal{H}_2/\mathcal{H}_\infty$ controller with pole-placement constraints. The first one is designed through the solution of a discrete-time algebraic Riccati equation, whilst the second one is designed through Linear Matrix Inequality (LMI) approach. The nonlinear state-space equations are linearized around the reference trajectory, augmented with integral actions and further discretized in order to design the controllers. On the other hand, considering that not all the system states are available for feedback, measurements are corrupted with noise and sensors have different sampling times, we propose state estimation strategies in order to provide the entire state vector to the controllers. A linearized Kalman filter is proposed for a scenario in which only a half of the state vector is measured (position variables), corrupted with zero-mean Gaussian noise. In the second estimation strategy, a zonotopic state estimator is proposed for a scenario in which measurements are provided by sensors with different sampling times, corrupted with unknown but bounded noise. Both estimators are designed based on discretized linearized dynamic equations, augmented with external disturbances affecting the system. Numerical simulation results are presented to corroborate the good performance of the proposed strategies.

Keywords: Load transportation, Unmanned aerial vehicles, Path tracking, State esti-

mation.

List of Figures

List of Tables

Acronyms

CAD	Computer Aided Design
DLQR	Discrete-time Linear Quadratic Regulator
DOF	Degrees of Freedom
EKF	Extended Kalman Filter
FSI	Full State Information
GPS	Global Positioning System
IAVU	Integrated Absolute Variation of the Control signal
iLQG	Iterative Linear Quadratic Gaussian
IMU	Inertial Measurement Unit
ISE	Integral Square Error
LKF	Linearized Kalman Filter
LMI	Linear Matrix Inequality
LQR	Linear Quadratic Regulator
MIQP	Mixed Integer Quadratic Programming
MPC	Model Predictive Control
PID	Proportional-Integral-Derivative
RPT	Robust and Perfect Tracking
SLAM	Simultaneous Localization and Mapping
UAV	Unmanned Aerial Vehicle
UKF	Unscented Kalman Filter

VTOL	Vertical Take-off and Landing
ZOH	Zero-order-holder
ZSE	Zonotopic State Estimator

Notation

General notation

a	Italic lower case letters denote scalars
$\boldsymbol{a}$	Boldface italic lower case letters denote vectors
$\boldsymbol{A}$	Boldface italic upper case letters denote matrices
$\mathbb{A}$	Blackboard bold letters denote sets

General symbols and operators

$\mathbb{R}$	Set of real numbers
$\mathbf{0}_{n\times m}$	Matrix of zeros with n lines and m columns
$\mathbf{1}_{n\times m}$	Matrix of ones with n lines and m columns
$\mathbb{I}_{n\times n}$	Identity matrix with dimension n
$\dot{\boldsymbol{A}}$	Time derivative of $\boldsymbol{A}$
$\boldsymbol{A}^T$	Transpose of $\boldsymbol{A}$
$\boldsymbol{A}^{-1}$	Inverse of $\boldsymbol{A}$
$\boldsymbol{A}^+$	Pseudo-inverse of $\boldsymbol{A}$
$\det(\boldsymbol{A})$	Determinant of $\boldsymbol{A}$
$\mathrm{tr}\,\{\boldsymbol{A}\}$	Trace of $\boldsymbol{A}$
$\mathrm{rs}(\boldsymbol{A})$	Row sum of $\boldsymbol{A}$

Modeling (Chapter 2)

$\boldsymbol{d}_{\mathcal{B}}^{\mathcal{A}}$	Displacement vector from $\mathcal{A}$ to $\mathcal{B}$, expressed in $\mathcal{A}$
$\boldsymbol{R}_{\mathcal{B}}^{\mathcal{A}}$	Rotation matrix from $\mathcal{A}$ to $\mathcal{B}$

$\boldsymbol{R}_{n,\alpha}$	Rotation of angle α about axis n
$\boldsymbol{\omega}_{\mathcal{BC}}^{\mathcal{A}}$	Angular velocity of frame $\mathcal{C}$ with respect to $\mathcal{B}$, expressed in $\mathcal{A}$
$S(\cdot)$	Skew-symmetric matrix operator
$\text{vex}(\cdot)$	Vex operator, the inverse of $S(\cdot)$
$\mathfrak{L}$	Lagrangian of the mechanical system
$\mathcal{K}$	Kinetic energy
$\mathcal{U}$	Potential energy
$\mathcal{I}$	Inertial reference frame
$\mathcal{L}$	Reference frame rigidly attached to the suspended load's center of mass
$\mathcal{B}$	Reference frame rigidly attached to the aircraft's geometric center
$\mathcal{C}_1$	Reference frame rigidly attached to the main body's center of mass
$\mathcal{C}_2$	Reference frame rigidly attached to the right thruster group's center of mass
$\mathcal{C}_3$	Reference frame rigidly attached to the left thruster group's center of mass
$\boldsymbol{\xi} = [x\ y\ z]^T$	Load's position with respect to $\mathcal{I}$
$\boldsymbol{\eta} = [\phi\ \theta\ \psi]$	Euler angles parametrizing the load's orientation with respect to $\mathcal{I}$
$\boldsymbol{\gamma} = [\gamma_1\ \gamma_2]$	Angles parametrizing the aircraft's orientation with respect to the load
α_{R}	Tilting angle of the right thruster group
α_{L}	Tilting angle of the left thruster group
β	Fixed inclination angle of the thrusters towards the aircraft's geometric center
f_{R}	Magnitude of the thrust generated by the right propeller
f_{L}	Magnitude of the thrust generated by the left propeller
$\tau_{\alpha_{\text{R}}}$	Magnitude of the torque generated by the right servomotor
$\tau_{\alpha_{\text{L}}}$	Magnitude of the torque generated by the left servomotor
$\boldsymbol{q}$	Vector of generalized coordinates

$\boldsymbol{M}(\boldsymbol{q})$	Inertia matrix
$\boldsymbol{C}(\boldsymbol{q}, \dot{\boldsymbol{q}})$	Coriolis and centripetal forces matrix
$\boldsymbol{g}(\boldsymbol{q})$	Gravitational forces vector
$\boldsymbol{\vartheta}$	Vector of generalized forces
$\boldsymbol{f}$	Force vector
$\boldsymbol{\tau}$	Torque vector
$\boldsymbol{I}$	Inertia tensor
$\boldsymbol{J}$	Inertia tensor resulting from applying the Steiner's theorem to $\boldsymbol{I}$
$\boldsymbol{D}$	Inertia tensor resulting from applying the Steiner's theorem to $\boldsymbol{J}$
$\hat{\boldsymbol{g}}$	Gravitational acceleration vector
$\boldsymbol{x}$	State vector
$\boldsymbol{u}$	Input vector
$\boldsymbol{d}$	Disturbance vector

Control (Chapter 3)

$(\cdot)^{\mathrm{tr}}$	Trajectory values
$(\cdot)^{\mathrm{eq}}$	Equilibrium values
$\delta(\cdot)$	$(\cdot) - (\cdot)^{\mathrm{tr}}$
$\boldsymbol{\chi}$	State vector $\delta\boldsymbol{x}$ augmented with integral actions
T_c	Controller sampling time
$(\cdot)_{k\pm p}$	$(\cdot)\ (kt \pm pT_c)$
$\boldsymbol{K}$	State-feedback gain matrix
$\boldsymbol{\Omega}_{\boldsymbol{\chi}}, \boldsymbol{\Omega}_{\boldsymbol{u}}$	Weighting matrices of the DLQR
$\mathcal{Z}$	Z transform
$\boldsymbol{\Psi}_{\boldsymbol{dz}}(\varsigma)$	Discrete-time transfer matrix from $\boldsymbol{d}$ to $\boldsymbol{z}$
$\lVert\boldsymbol{\Psi}_{\boldsymbol{dz}}(\varsigma)\rVert_2$	$\mathcal{H}_2$ norm of the transfer matrix $\boldsymbol{\Psi}_{\boldsymbol{dz}}(\varsigma)$

$\|\boldsymbol{\Psi}_{\boldsymbol{dz}}(\varsigma)\|_\infty$	$\mathcal{H}_\infty$ norm of the transfer matrix $\boldsymbol{\Psi}_{\boldsymbol{dz}}(\varsigma)$
$\sigma_{\max}\{\cdot\}$	Highest singular value
γ	Upper-bound for the $\mathcal{H}_\infty$ norm
$\tilde{\gamma}$	Square of the upper-bound for the $\mathcal{H}_\infty$ norm
$\boldsymbol{H_z}, \boldsymbol{D_{zu}}, \boldsymbol{D_{zd}}$	Weighting matrices of the mixed $\mathcal{H}_2/\mathcal{H}_\infty$ controller
ε	Adjustment parameter of the first LMI region
ϖ	Adjustment parameter of the second LMI region

Estimation (Chapter 4)

$\mathbb{IR}$	Set of real compact intervals
$\llcorner a \urcorner$	Italic lower case letters with corners denote interval scalars
$\llcorner \boldsymbol{a} \urcorner$	Boldface italic lower case letters with corners denote interval vectors
$\llcorner \boldsymbol{A} \urcorner$	Boldface italic upper case letters with corners denote interval matrices
$\underline{a}$, $\overline{a}$	Endpoints of $\llcorner a \urcorner$
$\text{mid}(\llcorner a \urcorner)$	Midpoint of $\llcorner a \urcorner$
$\text{diam}(\llcorner a \urcorner)$	Diameter of $\llcorner a \urcorner$
$\square \{f(x)\}\|_{x=\llcorner a \urcorner}$	Interval extension of $f(x)$ at $x \in \llcorner a \urcorner$
$\square_{\text{N}} \{f(x)\}\|_{x=\llcorner a \urcorner}$	Natural interval extension of $f(x)$ at $x \in \llcorner a \urcorner$
$\square_{\text{MV}} \{f(x)\}\|_{x=\llcorner a \urcorner}$	Mean value extension of $f(x)$ at $x \in \llcorner a \urcorner$
$\oplus$	Minkowski sum
$\mathbb{B}$	Unitary interval
$\mathbb{B}^r$	r-dimensional unitary box
$\boldsymbol{c}$	Zonotope center
$\boldsymbol{g}_i$	Zonotope i-th generator
$\boldsymbol{G}$	Zonotope generator matrix
r	Zonotope order

$\mathbb{Z}_{\llcorner}^{\urcorner}$	Family of zonotopes
$\diamond\{\cdot\}$	Zonotope inclusion
$\boldsymbol{\rho}, \gamma, \sigma$	Strip parameters
$\Delta(\cdot)$	$(\cdot) - (\cdot)^{\text{eq}}$
$\boldsymbol{\nu}$	State vector $\Delta\boldsymbol{x}$ augmented with external disturbances
$\boldsymbol{y}$	Measurement vector
$\boldsymbol{w}$	Unmodeled dynamics regarded as process noise
$\boldsymbol{v}$	Measurement noise
$(\cdot)_{m\|n}$	Information at time instant m given measurements up to instant n
$\boldsymbol{\xi}_{\mathcal{B}} = [x_{\mathcal{B}}\ y_{\mathcal{B}}\ z_{\mathcal{B}}]^T$	Tilt-rotor UAV's position with respect to $\mathcal{I}$
$\boldsymbol{\eta}_{\mathcal{B}} = [\phi_{\mathcal{B}}\ \theta_{\mathcal{B}}\ \psi_{\mathcal{B}}]^T$	Euler angles parametrizing the UAV's orientation with respect to $\mathcal{I}$
$\boldsymbol{d}_{\mathcal{B}\mathcal{L}}^{\mathcal{B}}$	Load's position with respect to the tilt-rotor UAV, expressed in $\mathcal{B}$
$\boldsymbol{A}(i)$	i-th line of $\boldsymbol{A}$
$\boldsymbol{A}(i,j)$	Element from the i-th line and j-column of $\boldsymbol{A}$
$\mathbb{I}_k$	Set of available measurements at time instant k

Formation control of tilt-rotor UAVs (Appendix B)

$\mathbb{H}$	Set of quaternions
$\mathcal{H}$	Set of dual quaternions
$\hat{\imath}$, $\hat{\jmath}$, $\hat{k}$	Quaternionic units
ε	Dual unit
$\underline{x}$	A dual quaternion
$\underline{x}_{\mathcal{T}}^{\mathcal{S}}$	Unit dual quaternion associated with the rigid transformation from $\mathcal{S}$ to $\mathcal{T}$
$\overset{+}{\mathbf{H}}_4$, $\overset{-}{\mathbf{H}}_4$	Hamilton operators for quaternions
$\overset{+}{\mathbf{H}}_8$, $\overset{-}{\mathbf{H}}_8$	Hamilton operators for dual quaternions
$\boldsymbol{J}$	Analytical Jacobian

$\boldsymbol{\xi} = [x\ y\ z]^T$	Tilt-rotor UAV's position with respect to $\mathcal{I}$
$\boldsymbol{\eta} = [\phi\ \theta\ \psi]$	Euler angles parametrizing the UAV's orientation with respect to $\mathcal{I}$
$\boldsymbol{\Psi_{dz}}(s)$	Continuous-time transfer matrix from $\boldsymbol{d}$ to $\boldsymbol{z}$

Contents

1 Introduction

1.1 Motivation

Unmanned aerial vehicles (UAVs) have woken up great interest of engineers and researchers in the last decades. Firstly used only for military purposes, recent advances in technology, mainly on small scale embedded electronics, allowed scale reduction and cost lowering, making possible their commercial production. Nowadays, unmanned aerial vehicles have a wide range of military and civilian applications, such as search-and-rescue missions, precision agriculture, field recognition, surveillance, cargo transportation, archeology, cinematographic filming, inspection of power lines and crowd monitoring. They are also used for performing tasks in dangerous and inaccessible environments.

The most popular unmanned aerial vehicles are in fixed-wing, helicopter and quadrotor configurations. Fixed-wing UAVs (Fig. 1.1a) are commonly used in tasks that require improved forward flight, whilst helicopters and quadrotor UAVs (Fig. 1.1b) are used in tasks that require vertical take-off and landing (VTOL) and hovering capabilities.

The ability of performing VTOL, hover and improved forward flights has granted substantial attention to hybrid aircrafts. One configuration of hybrid aircrafts is the tilt-rotor, which is provided with fixed-wings and rotary-wings, and switches between helicopter and airplane flight-modes by tilting its thrusters. The first tilt-rotor aircraft built which was able to perform both VTOL and forward flights was the Bell XV-15 (Fig. 1.2a), in the 70's. Following its success, the military Bell Boeing V-22 Osprey (Fig. 1.2b) is produced in full-scale nowadays and is quite popular due to its multi-mission capability.

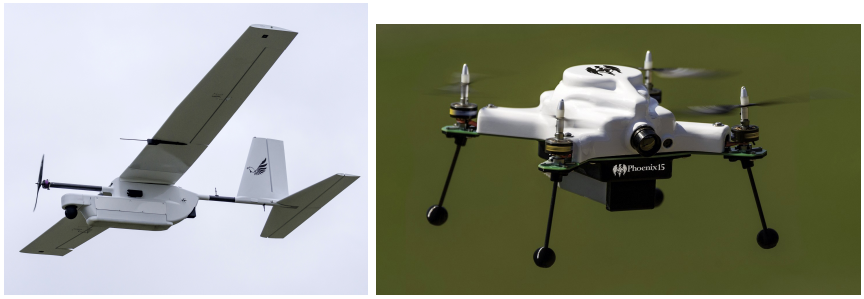

(a) Talon 240 (b) Phoenix 15

Figure 1.1: Examples of unmanned aerial vehicles: (a) Talon 240 fixed-wing UAV (Courtesy of UnmannedSystemsTechnology) and (b) Phoenix 15 quadrotor UAV (Courtesy of UnmannedSystemsTechnology).

Another example is the Agusta Westland AW609 (Fig. 1.2c), which is also used for civilian purposes, such as passenger transport. A third, yet under development, tilt-rotor aircraft is the military Bell V-280 Valor (Fig. 1.2d), which is designed for a record cruising speed of 280 knots (520 km/h).

Inspired by the advantages of those aircrafts, recent researches are looking into the design of small-scale tilt-rotor UAVs. An example is the military Bell Eagle Eye TR918 (Fig. 1.3). Their hybrid characteristics offer advantages over fixed-wing and quadrotor UAVs, which also comes with design and control challenges. They are complex, underactuated mechanical systems with highly coupled dynamics. Universities around the world are engaging into this challenging subject, including the brazilian ones Federal University of Santa Catarina and Federal University of Minas Gerais, which together founded the ProVANT project.

The first tilt-rotor UAV developed by the ProVANT project is shown in Figure 1.4. Its first flight was performed in 2013, at Federal University of Santa Catarina, and several master theses were developed based on it (Gonçalves, 2014; Bodanese, 2014; Almeida, 2014; Donadel, 2015; Santos, 2015; Alfaro, 2016). The ProVANT UAV 2.0, shown in Figure 1.5, is currently under flight tests at Federal University of Minas Gerais. Designed using Computer Aided Design (CAD) software, and with ABS structure built using a 3D printer, its main purposes include the development and validation of robust control strategies for load transportation tasks in helicopter flight mode.

Currently under development, the ProVANT UAV 3.0, shown in Figure 1.6, has improved aerodynamic fuselage and tail controlled surfaces. Some studies on adaptive control strategies to perform flights with improved forward speed have been made recently (Cardoso et al., 2016a,b). Furthermore, the more recent ProVANT UAV 4.0, shown in Figure 1.7, is currently being designed for full flight envelope, being capable of operating in helicopter and airplane flight modes.

A recent subject of interest is load transportation using UAVs. Taking advantage of their versatility and autonomous operation, UAVs can be used for aerial load transportation,

(a) Bell XV-15 Tilt-rotor

(b) Bell Boeing V-22 Osprey Tilt-rotor

(c) Agusta Westland AW609 Tilt-rotor

(d) Bell V-280 Valor Tilt-rotor

Figure 1.2: Tilt-rotor aircrafts: (a) Bell XV-15 Tilt-rotor (Courtesy of HistoryNet), (b) Bell Boeing V-22 Osprey Tilt-rotor (Courtesy of Bell Helicopter), (c) Agusta Westland AW609 Tilt-rotor (Courtesy of New Atlas) and (d) Bell V-280 Valor Tilt-rotor (Courtesy of Bell Helicopter) .

Figure 1.3: Bell Eagle Eye TR918 (Courtesy of MilitaryFactory).

with applications including rapid deployment of supplies in search-and-rescue missions (Bernard et al., 2011), vertical replenishment of seaborne vessels (Wang et al., 2014), and safe landmine detection (Bisgaard, 2008).

The load transportation task is a challenging subject in terms of modeling and control.

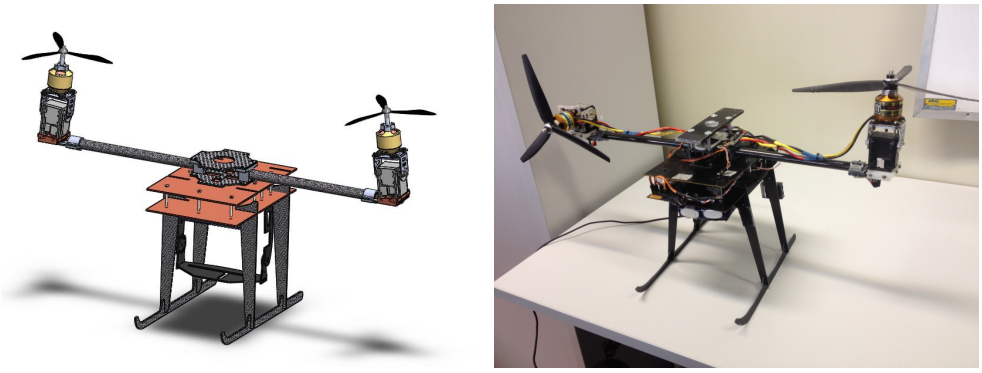

Figure 1.4: ProVANT UAV 1.0 (Donadel, 2015).

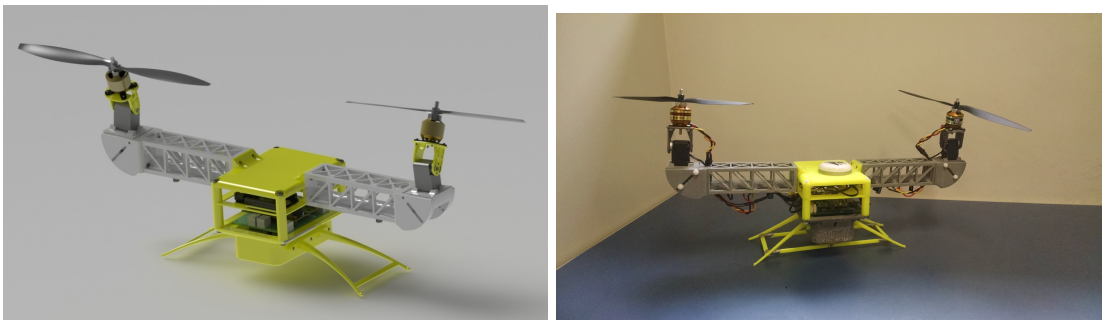

Figure 1.5: ProVANT UAV 2.0.

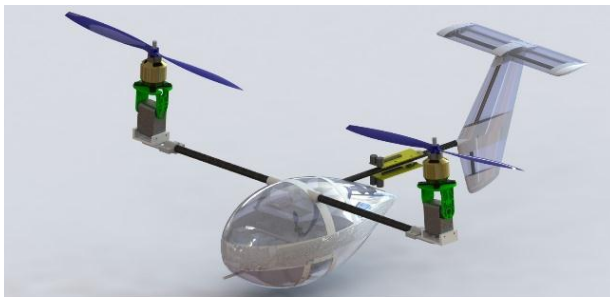

Figure 1.6: ProVANT UAV 3.0.

The payload is usually connected to the UAV by means of a rope (Fig. 1.8), changing its dynamic behavior considerably and adding underactuated degrees of freedom to the system. Moreover, the rope is a non-rigid body and is not always taut, which increases the challenge.

Another issue in load transportation is that the knowledge on the load position is usually necessary to accomplish the task. Then, the problem of estimating the load position arises, being commonly addressed through visual systems and state estimators.

Due to its hybrid capabilities, a tilt-rotor UAV is a promising platform for aerial load transportation. Improved forward speed is a desired feature for missions such as rapid deployment, which cannot be achieved by rotary-wing UAVs. Moreover, missions that require precise positioning of the load and obstacle avoidance cannot be addressed by

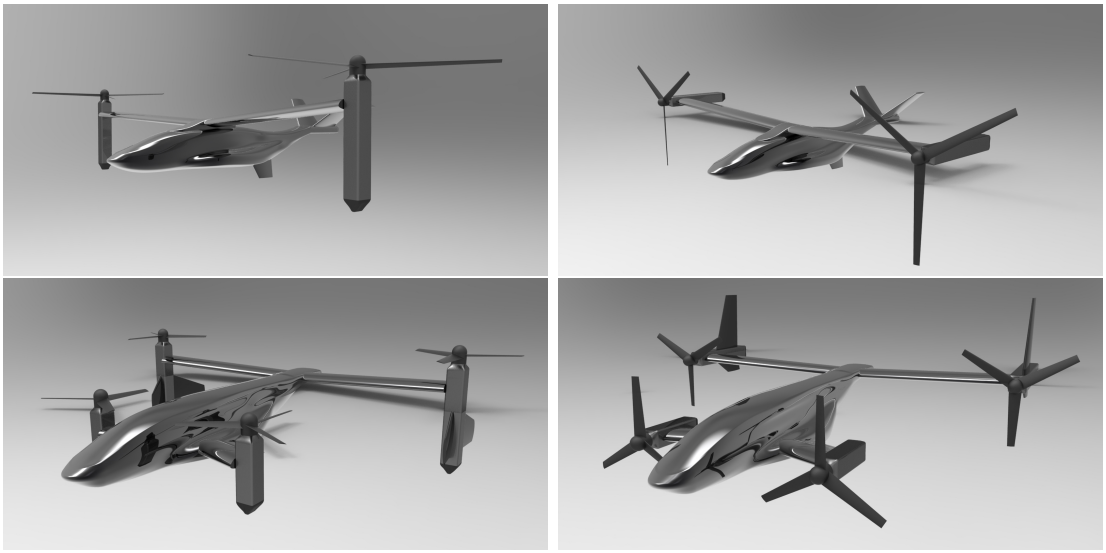

Figure 1.7: ProVANT UAV 4.0.

fixed-wing UAVs, since they cannot perform hover flights. On the other hand, the tilt-rotor UAV can be used in both scenarios.

Figure 1.8: Load transportation using unmanned helicopters (Bernard et al., 2011).

1.2 State of the Art

This section presents a literature review concerning load transportation using UAVs, and on state estimation techniques employed for the accomplishment of such tasks.

1.2.1 Load transportation using UAVs

Load transportation using UAVs is a subject addressed by many recent works, using different kinds of aircrafts and with different objectives to be achieved, ranging from path tracking of the aircraft with reduced load swing, obstacle avoidance, transportation by multiple aircrafts and path tracking of the suspended load. This subsection is organized according to the type of aircraft used.

Unmanned helicopters

In la Cour-Harbo & Bisgaard (2009), a strategy combining state-feedback Linear Quadratic Regulator (LQR) with optimal trajectory generation is proposed, to solve the path following problem of an unmanned helicopter with reduced load swing. The control design is based on the redundant model[1] proposed by Bisgaard et al. (2009a), which takes into account effects from slackening and tightening of the rope, as well as aerodynamic coupling between the helicopter and load. The objective is achieved through the process of trajectory generation, which is performed by solving an optimal control problem with specified waypoints in trim condition as constraints, yielding feedforward control signals and reference signals for the LQR. Obstacle avoidance is also achieved by means of state constraints in the optimization problem. Besides achieving the proposed objectives, the authors refer to the process of control design based on the redundant model as a challenging task, and depict the considerable computational effort necessary to solve the optimal trajectory generation problem. Moreover, the strategy relies on trajectory generation, thus it is an open-loop approach and is not robust to external disturbances and unmodelled dynamics.

Another control strategy for reduced load swing motion of a unmanned helicopter is proposed in Bisgaard et al. (2009b). Assuming that a controller for stabilization and/or tracking of the helicopter is already available, a proportional feedback controller with time delay is introduced in an outer-loop for load swing reduction. The time delay is introduced in order to compensate vibrations in the rope. The controller parameters are adjusted for maximum damping ratio of the load's position with respect to the helicopter, and a feedforward term based on input shaping is also employed. Simulation results show that the load swing is substantially reduced, however the proposed strategy does not take into account the dynamic coupling between helicopter and load.

A similar control structure is proposed in Omar (2009), for swing-free motion of a helicopter with suspended load. However, the inner-loop controller is an LQR designed based on the linearized dynamic equations considering entire system dynamics, and the outer-loop delayed controller is designed based on fuzzy rules. Simulation results show that the control strategy reduces the load swing over time, however requires large motion

[1] By redundant model we mean that the dynamics of the system is not described by a minimum number of independent coordinates.

of the helicopter and a substantial amount of time in order to eliminate the oscillations (around one minute or even more).

Load transportation using multiple unmanned helicopters is explored in Bernard & Kondak (2009). A redundant model is proposed based on the Kane's method (Kane & Levinson, 1985), in which an arbitrary number of helicopters is allowed. A cascade control strategy is proposed for path tracking of either the helicopters or the suspended load, composed of an outer-loop controller for translational motion of the entire system, and inner-loop controllers for orientation of each helicopter individually. Despite the generality of the proposed model, a simplified model is considered for design of the outer-loop controller, in which each helicopter is a point of mass that can apply arbitrary forces to the system. The design is further particularized for one and three helicopters: the first case is addressed by linear state-feedback strategies, and the second one by inverse dynamics. The inner-loop controllers are designed through individual inverse rotational dynamics, in which the the system coupling is taken into account by means of force sensors in the ropes. Despite being capable of performing path tracking of the helicopters or the load, this feature is not well explained by the authors. Moreover, the strategy relies on the use of force sensors in the ropes to take into account the dynamic coupling of the system. The authors further discuss the developed platform and new experiments in Maza et al. (2009) and Bernard et al. (2011).

Wang et al. (2014) study the problem of load transportation by unmanned helicopters inspired in the problem of vertical replenishment of seaborn vessels. The authors propose a cascade control strategy of a helicopter for load transportation, composed of a linear $\mathcal{H}_\infty$ controller for the helicopter attitude dynamics in inner-loop and a linear strategy called Robust and Perfect Tracking (RPT) control method for the helicopter position in outer-loop. However, the authors do not take into account the dynamics of the load neither in the modeling nor in the control design. Also inspired in vertical replenishment, Wu et al. (2015) propose a cascade control strategy for a unmanned helicopter with suspended load, applied in autonomous transportation of barrels. The strategy is composed of gain-scheduled PID controllers for attitude control and position control of the helicopter, adjusted empirically, and does not take into account the suspended load dynamics.

Quadrotor UAVs

The problem of load transportation using a quadrotor UAV is addressed in Palunko et al. (2012), where an approach for reduced load swing motion based on optimal trajectory generation is proposed. The quadrotor's dynamic equations are obtained through the Euler-Lagrange formulation, in which the load's dynamics are considered as applied external forces and torques. The suspended load is regarded as a pendulum coupled to the quadrotor, and its equations of motion are obtained separately through equilibrium of forces and torques at the suspension point. Despite the derived model, the authors propose

an adaptive control strategy based on inverse dynamics for path tracking of the quadrotor, making use of the adaptation law to take into account changes in the system's center of mass due to the inclusion of the suspended load. The optimal trajectory generation is performed through dynamic programming, derived from the approach presented in Starr et al. (2005). Simulation and experimental results show that the load swing is substantially reduced by tracking the optimal trajectory, however it is an open-loop approach.

Faust et al. (2013) propose another strategy based on trajectory generation for reduced load swing using a quadrotor UAV. The trajectory generation process is based entirely on machine learning, without assumptions on the system's dynamics. The authors point it out as an advantage with respect to the dynamic programming approach, which requires knowledge on the system model. The approach is based on reinforcement learning and is separated in two phases: (i) the value approximation function is learned for a particular load through simulations; (ii) the value function is used for generating the trajectory leading the aircraft to its final position, with minimized swing motion. Palunko et al. (2013) also propose a model-free approach based on trajectory generation by reinforcement learning for solving the problem of path tracking of the suspended load instead of reduced load swing. These strategies are also open-loop approaches, and despite advantageous with respect to being model-free, the entire process of reinforcement learning must be repeated if there are any changes in the system.

A nonlinear cascade control strategy based on system decoupling is proposed in Sreenath et al. (2013b) for path tracking of a suspended load using a quadrotor UAV for the planar case. The authors derive rigorous dynamical models for the cases in which the cable is taut and when it is loose, yielding a nonlinear hybrid system, and prove that it is differentially-flat. This property is explored for trajectory generation for the suspended load with minimum snap motion of the quadrotor UAV. The control strategy is validated through simulations and real experiments. Sreenath et al. (2013a) extend the technique for the three-dimensional case, keeping the decoupling-dependent cascade structure, and validate it through simulations. In both works, the authors prove exponential stability for the proposed controllers. However, the strategies are not robust to external disturbances and unmodeled dynamics.

Load transportation using multiple quadrotor UAVs is studied by Lee et al. (2013b). A nonlinear cascade control strategy is proposed for transportation of a point mass by an arbitrary number of quadrotor UAVs. The strategy is composed of an attitude controller based on Sreenath et al. (2013b) for each aircraft and a formation controller, allowing either path tracking of the suspended load or formation maintaining of the UAVs with respect to the load or the inertial frame. The authors validate the strategy through simulations involving path tracking of the suspended load and a special case of path tracking of an inverted pendulum over a quadrotor UAV. Lee (2014) extends the study for a rigid body suspended load, in which its orientation is also taken into account in the control strategy.

Since these strategies use the controller proposed in Sreenath et al. (2013b) as base, they inherit its advantages and disadvantages.

The use of a flexible cable is studied in Goodarzi et al. (2014) for load transportation using a quadrotor UAV. A rigorous model is obtained for the system, in which the cable is considered as a non-actuated multi-link rigid body. The authors propose linear and nonlinear control strategies for stabilization of the whole system, validated through simulations and compared through experiments against control strategies that consider only the dynamics of quadrotor UAV. However, the authors consider a one-link cable for control design in the real experiments, being inconsistent with the flexible cable motivation. Dai et al. (2014) extend this study for the case where the mass of the suspended load is unknown. The authors propose an adaptive cascade control strategy for path tracking of the quadrotor UAV. Despite the flexible cable motivation, the control strategies require information about the position of each link instead of only the load position.

de Crousaz et al. (2014) designs a control strategy based on iterative Linear Quadratic Gaussian (iLQG) method for a quadrotor UAV with suspended load. The authors derive a hybrid model for the system, from either the quadrotor's perspective or the load's perspective. The proposed algorithm generates locally optimal linear feedback controllers for chosen nonlinear cost functions. The authors validate the strategy through simulations, showing that it is able to perform path tracking of the UAV with reduced load swing, and aggressive maneuvers, e.g. pass the whole system through a narrow window, which requires large load swing.

A trajectory planning algorithm is proposed in Tang & Kumar (2015) for the problem of path tracking of a suspended load with obstacle avoidance using a quadrotor UAV. The proposed method is based on optimal trajectory planning through mixed integer quadratic programming (MIQP). The system model and control strategy are the same from Sreenath et al. (2013a), for which the cable is taut, and the control strategy is the same as in Lee et al. (2011), for which the cable is loose. Taking advantage of both configurations of the system, this strategy is capable of performing aggressive maneuvers, including moving through a narrow window, and also perform tasks such as load pick-up and release[2].

Linear Model Predictive Control (MPC) strategies are studied in Jain (2015) for set-point tracking of a quadrotor UAV with suspended load. The author derives the whole-body system dynamics through the Euler-Lagrange formulation, which is linearized around hover conditions and discretized for a given sampling time in order to design the control strategies. Then, a linear time-invariant MPC is proposed with integral action over the tracking error, and an MPC with integral actions over the system inputs (incremental formulation), and compare the strategies against an LQR with integral actions over the tracking error through simulation and experimental results.

Raffo & Almeida (2016) propose a robust nonlinear control strategy for swing-free path

[2]A video with real experiments is available at *https://www.youtube.com/watch?v=qO4MsiuLCoc*.

tracking of a quadrotor UAV with suspended load, based on nonlinear $\mathcal{H}_\infty$ control theory and Lyapunov redesign. The authors derive a whole-body nonlinear dynamic model for the system using the Euler-Lagrange formulation. In order to design the controller, the authors partition the dynamic equations according to the actuated and unactuated degrees of freedom (DOF), and further partition the equations associated with the actuated DOF according to the variables to be regulated and variables to be only stabilized. The authors then define an augmented state vector according to the control objectives, derive the associated state-space equations based on which the nonlinear $\mathcal{H}_\infty$ controller is designed. Then, through Lyapunov redesign, the authors introduce in the control law a term based on the load's velocity with respect to the UAV in order to achieve swing-free motion.

A nonlinear solution to the problem of path tracking of a suspended load using a quadrotor UAV is proposed in Pereira et al. (2016). The authors assume the quadrotor as a system actuated by total thrust and orientation, derive a whole-body dynamical model for the system and define the positions and velocities of the load and quadrotor as states. Through a nonlinear change of coordinates, the control problem is casted into the framework presented in Pereira & Dimarogonas (2016), which solves the problem of path tracking of underactuated systems driven by directed thrust and angular velocity with a double-integrator structure. The strategy ensures that the cable is always taut, and provides rejection to constant disturbances in the system inputs, however is limited to systems driven by directed thrust and angular velocity.

Tilt-rotor UAVs

For the knowledge of the author, up to the elaboration of this thesis only the ProVANT project has studied the problem of load transportation using tilt-rotor UAVs.

Almeida et al. (2014) study the problem of load transportation using a tilt-rotor UAV in helicopter flight-mode. The authors derive a whole-body dynamical model through the Euler-Lagrange formulation, and design linear controllers based on $\mathcal{D}$-stability and $\mathcal{H}_\infty$ theory for path tracking of the tilt-rotor UAV with stabilization of the suspended load. The control strategies are validated through simulations in which the system is subjected to external disturbances and parametric uncertainties.

A nonlinear cascade control strategy of a tilt-rotor UAV for load transportation is proposed in Almeida & Raffo (2015b), composed of three levels of feedback linearization controllers. The authors propose two different control designs: (i) the goal is to perform path tracking of the UAV with stabilization of the suspended load; (ii) based on the work of Lee et al. (2013a), terms involving the load's velocity with respect to the UAV are introduced in the control laws in order to achieve reduced load swing motion, which is verified through simulations. The strategy is modified in Almeida & Raffo (2015a) for stabilization of an inverted pendulum over a tilt-rotor UAV, while it performs path tracking.

Santos & Raffo (2016a) propose a linear adaptive control strategy for trajectory tracking of a tilt-rotor UAV with suspended load. The authors derive a time-varying linearized model of the system, which is a function of the desired accelerations. For the control design, these accelerations are considered as uncertain parameters, yielding a polytopic representation of the system. State-feedback gains are then computed for each vertex through Linear Matrix Inequality (LMI) approach, whose convex combination of these gains, obtained by means of an adaptive law, is used for the closed-loop system. Through simulations, the adaptive control strategy is compared against a LQR designed based on the nominal model, in which is shown that for higher acceleration trajectories the proposed strategy is successful in performing the path tracking, while the LQR destabilizes the system.

Model Predictive Control (MPC) strategies are studied in Andrade et al. (2016) and Santos & Raffo (2016b) for path tracking of a tilt-rotor UAV for load transportation. In Andrade et al. (2016), the authors propose the control strategy based on discrete-time linearized, time-varying error dynamics of the system, augmented with integral actions over the error of the regulated states in order to achieve null-steady state error. On the other hand, in Santos & Raffo (2016a), besides the integral actions over the tracking error, the control strategy includes an incremental formulation, adding integral actions also to the control inputs. Both strategies are validated through simulations, and in (Andrade et al., 2016) the results are compared with an LQR controller, showing that the proposed MPC strategy yields smoother control signals for the closed-loop system.

1.2.2 State estimation for load transportation

In load transportation tasks, in order to achieve specified goals such as obstacle avoidance and path tracking of the suspended load, it is important to have knowledge of the load's position, and sometimes its orientation and velocity, which usually are not directly measured. Although several works study the load transportation problem, only a few propose state estimation techniques to provide this information, mainly those that present experimental results.

In order to estimate the load's position and velocity for a helicopter with suspended load system, Bisgaard et al. (2007b) design a fusion algorithm based on the Unscented Kalman Filter (UKF). The authors propose the use of dynamic equations of a 3D pendulum as process model for the filter, which receives measurements from an Inertia Measurement Unit (IMU) and a vision system, both located at the helicopter. In the vision system, a camera recognizes a marker located at the suspended load, yielding images that are converted to the angles of the wire with respect to the helicopter, and later to the load's position with respect to the UAV by means of trigonometric relationships. The authors also propose methods for estimating the wire's length. The algorithm is tested in real

experiments, considering aggressive maneuvers that induce large load swing, such that the load leaves the camera range. Bisgaard et al. (2010) combine this estimation algorithm with the delayed feedback control strategy proposed in Bisgaard et al. (2009b) for reduced load swing motion, taking advantage of the estimation of the wire's length as an adaptive feature, and validate the resulting control structure via experimental results.

Bisgaard et al. (2007a) propose two algorithms based on the UKF for estimation of the full state vector of an unmanned helicopter with suspended load. The first one is based on the kinematic model of the system, and requires measurements from a Global Positioning System (GPS) equipment, a magnetometer, a camera and two IMUs: one on the helicopter and the other on the load. The second algorithm is based on the redundant model proposed in Bisgaard et al. (2006), in which the use of an IMU on the load is optional. By means of state vector augmentation, both algorithms estimate measurement bias and take it into account for providing the system states, while the second one also estimate external disturbances. The authors also propose a practical solution to deal with the different sampling times of the available sensors, in which the columns of the Kalman gain matrix associated with the missing measurements are set to zero.

In Bernard & Kondak (2009), a linear observer is proposed for estimation of the load position, first considering a model of the rope composed of multiple mass points, and then considering a rigid massless rope model. The authors does not specify the estimation technique used, and despite mentioning the models, the associated dynamic equations are not provided.

A Linear Kalman Filter is proposed in Jain (2015) for state estimation of a quadrotor UAV with suspended load, based on discrete-time linearized dynamics of the whole system. Measurements are provided by external cameras and sensors embedded at the UAV, and the algorithm is adapted to take into account the higher sampling time of the sensors in comparison to the filter sampling time, by performing the correction step only when all the measurements are available.

Machado & Raffo (2015) develop an integrated platform on ROS (Robot Operating System) for load transportation by a AR.Drone quadrotor UAV using visual feedback. The proposed platform combines information from on-board sensors and computer vision algorithms of the UAV's frontal camera for navigation, and its lower camera for estimating the load's position and velocity. The algorithm for navigation is composed of a simultaneous localization and mapping (SLAM) system and an Extended Kalman Filter (EKF). The EKF is based on a simplified model of the quadrotor UAV, and estimates its position, velocity, orientation angles and yaw rate. The computer vision algorithm based on the UAV's lower camera tracks a marker placed on the suspended load and returns its position and velocity with respect to the aircraft. The information provided by the EKF and from this computer vision algorithm are used in PID controllers to perform path tracking of the UAV with stabilization of the suspended load with or without swing-free motion.

1.3 Justification

As presented in the previous section, some works deal with path tracking of suspended loads, using unmanned helicopters and quadrotor UAVs. Nevertheless, to the best knowledge of the author, the problem of path tracking of a suspended load using a tilt-rotor UAV has not been addressed in the literature yet.

A tilt-rotor UAV is as highly coupled dynamic system, thus the presented decoupling-based nonlinear cascade control approaches cannot be applied without making simplifications in the model. On the order hand, disturbance rejection will be of interest in this work, which makes trajectory generation strategies not suitable for this purpose, since they are open-loop approaches. Moreover, although it is a proper assumption for a quadrotor UAV, a tilt-rotor UAV cannot be regarded as a system actuated by total thrust and orientation, which is a condition required by the only nonlinear control strategy for path tracking of suspended load presented in the previous section featuring disturbance rejection.

Load transportation using tilt-rotor UAVs is a part of the research developed in the ProVANT project. The previous section presented the works already developed in this line, which focused on path tracking of a tilt-rotor UAV with stabilization of the suspended load, part of them considering swing-free motion. This thesis contributes to this research by addressing the problem of path tracking of the suspended load, proposing a modeling approach, robust control and state estimation strategies, for the accomplishment of the task even when the system is subjected to external disturbances, incomplete state information, noisy measurements and sensors with different sampling times.

1.4 Objectives

The main objective of this work is to deal with load transportation using a tilt-rotor UAV, addressing the problem of path tracking control of the suspended load. The aircraft under study is the ProVANT UAV 2.0, shown in Figure 1.5. It was designed specially for load transportation tasks, and can operate only in helicopter flight-mode.

Figure 1.9 shows a flow chart used in the development of this master thesis. Specific objectives are:

- Develop the equations of motion for the tilt-rotor UAV with suspended load from the load's perspective, using the Euler-Lagrange formulation, in order to obtain a nonlinear state-space representation of the system with the load's position and orientation among the system states;

- Design robust, discrete-time linear state-feedback control strategies, for path tracking of the suspended load with stabilization of the tilt-rotor UAV, featuring constant disturbances rejection;

- Propose state estimation strategies for scenarios in which not all the system states are available for feedback connection, measurements are corrupted with noise and sensors have different sampling times.

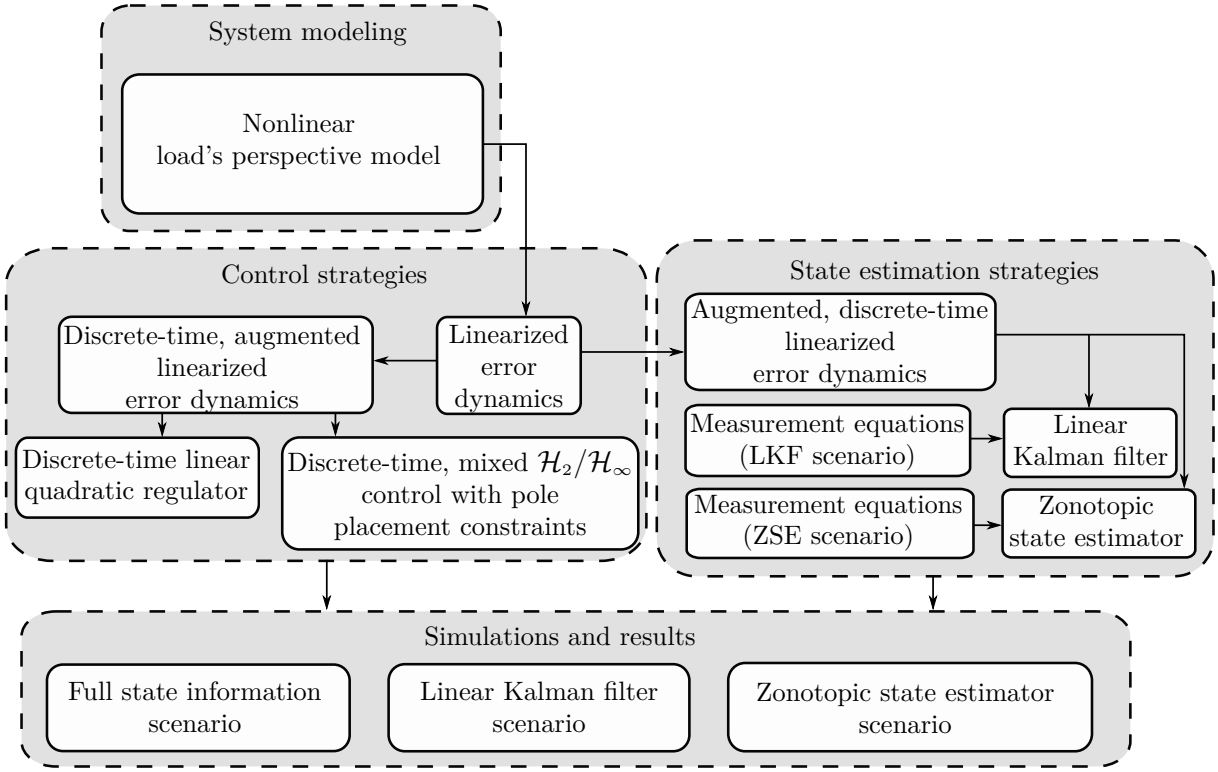

Figure 1.9: Thesis flow chart.

1.5 Structure of the text

This thesis is organized as follows:

- **Chapter 2** develops the equations of motion of the tilt-rotor UAV with suspended load, from the load's perspective, using the Euler-Lagrange formulation. A nonlinear state-space representation of the system is achieved, with the load's position and orientation among the system states.

- **Chapter 3** describes two discrete-time, linear state-feedback control strategies, proposed for path tracking of the suspended load: a discrete-time linear quadratic regulator and a mixed $\mathcal{H}_2/\mathcal{H}_\infty$ controller with pole placement constraints, both based on discrete-time linearized error dynamics.

- **Chapter 4** describes two state estimation strategies: a linearized Kalman filter, proposed for a scenario in which only a half of the state vector is measured, corrupted with zero-mean Gaussian noise; and a zonotopic state estimator, proposed for a

scenario in which measurements are provided by sensors with different sampling times, corrupted with unknown but bounded noise.

- **Chapter 5** presents simulations results, evaluating the proposed control and state estimation strategies for two specified trajectories and three scenarios concerning available measurements.

- **Chapter 6** summarizes the contributions and results of this work, and presents suggestions for future works in this line of research.

- **Appendix A** addresses the problem of path tracking control for a tilt-rotor UAV, in the presence of external disturbances, measurements corrupted with unknown but bounded noise, and sensors with different sampling times. A zonotopic state estimator and a discrete-time linear quadratic regulator are designed for the task.

- **Appendix B** deals with formation control of tilt-rotor UAVs. A formation backstepping control strategy is designed based on dual quaternion algebra and the cooperative dual task-space framework, and linear $\mathcal{D}$-stable $\mathcal{H}_\infty$ controllers are designed for individual trajectory tracking of each tilt-rotor UAV.

When necessary, preliminary sections are presented within the chapters in order to provide necessary background to the reader.

1.6 List of publications

The following articles were accepted for publication during the elaboration of this work:

Conference papers:

1. (Rego et al., 2016) Rego, B. S., Adorno, B. V., & Raffo, G. V. (2016). Formation backstepping control based on the cooperative dual task-space framework: a case study on unmanned aerial vehicles. In *Proc. of the 2016 XIII Latin American Robotics Symposium and IV Brazilian Robotics Symposium* (pp. 163–168).

2. (Rego & Raffo, 2016a) Rego, B. S. & Raffo, G. V. (2016a). Path tracking control based on guaranteed state estimation for a tilt-rotor uav. In *Proc. of the XXI Congresso Brasileiro de Automática.* (pp. 1–6).

3. (Rego & Raffo, 2016c) Rego, B. S. & Raffo, G. V. (2016c). Suspended load path tracking control based on zonotopic state estimation using a tilt-rotor uav. In *Proc. of the IEEE 19th International Conference on Intelligent Transportation Systems.* (pp. 1445–1451).

4. (Rego & Raffo, 2016b) Rego, B. S. & Raffo, G. V. (2016b). Suspended load path tracking by a tilt-rotor UAV. In *Proc. of the 1st IFAC Conference on Cyber-Physical & Human-Systems.* To be published.

2 System modeling

This chapter develops the equations of motion of a tilt-rotor UAV with suspended load. The aircraft under study is the ProVANT UAV 2.0, and a generic payload is considered to be coupled to it through a rod. The objective is to obtain dynamic equations describing explicitly the time evolution of the suspended load's position and orientation with respect to an inertial reference frame, while the system is subject to forces and torques from the aircraft's actuators, viscous friction, external disturbances, and gravity.

The dynamic equations are obtained through the Euler-Lagrange formulation, in which the dynamic coupling between the aircraft and the load is taken into account naturally. The suspended load's variables are chosen as degrees of freedom of the mechanical system, while addressing the aircraft's position and orientation only with respect to the load. This choice of perspective, henceforth called *the load's perspective approach*, leads to a state-space representation of the system with the load's position and orientation being represented by state variables. Therefore, state-feedback control strategies are capable of directly steering the trajectory of the load.

The chapter is organized as follows: Section 2.1 introduces the background material concerning kinematics and dynamics of multi-body mechanical systems; Section 2.2 formulates the kinematics of the tilt-rotor UAV with suspended load, from the load's perspective, and defines the generalized coordinates; Section 2.3 obtains the kinetic and potential energies of the system, from which the inertia matrix, Coriolis and centripetal forces matrix, and the vector of gravitational forces are computed; Section 2.4 obtains the contributions to the generalized forces of all non-conservative forces and torques that

are considered to be actuating over the system; and Section 2.5 achieves the state-space representation of the tilt-rotor UAV with suspended load.

2.1 Preliminaries

This section presents a brief introduction on rigid transformations in the three-dimensional Euclidean space, kinematics and dynamics for multi-body mechanical systems, and also the so-called Euler-Lagrange formulation.

2.1.1 Rigid transformations in $\mathbb{R}^3$

According to Murray et al. (1994), rigid transformations in $\mathbb{R}^3$ are composed of translations and rotations, and preserve the Euclidean metric and the cross product between vectors. Translations can be represented by vectors in $\mathbb{R}^3$, while rotations by matrices that belong to the special orthogonal group $SO(3) \subset \mathbb{R}^{3\times3}$. Those are henceforth called *displacement vectors* and *rotation matrices*, respectively.

Some properties of the special orthogonal group must be registered. Let $\boldsymbol{A}, \boldsymbol{B} \in SO(3)$. Then:

- $\boldsymbol{AB} \in SO(3)$;
- $\boldsymbol{A}^{-1} = \boldsymbol{A}^T$;
- $\det(\boldsymbol{A}) = 1$.

Rotations about the x, y and z axes of a given reference frame correspond to elementary rotation matrices (Spong et al., 2006). These are denoted by $\boldsymbol{R}_{x,\alpha}$, $\boldsymbol{R}_{y,\alpha}$ and $\boldsymbol{R}_{z,\alpha}$, respectively (in which α is the angle of rotation), and are given by

$$\boldsymbol{R}_{x,\alpha} = \begin{bmatrix} 1 & 0 & 0 \\ 0 & \mathrm{c}_\alpha & -\mathrm{s}_\alpha \\ 0 & \mathrm{s}_\alpha & \mathrm{c}_\alpha \end{bmatrix}, \quad \boldsymbol{R}_{y,\alpha} = \begin{bmatrix} \mathrm{c}_\alpha & 0 & \mathrm{s}_\alpha \\ 0 & 1 & 0 \\ -\mathrm{s}_\alpha & 0 & \mathrm{c}_\alpha \end{bmatrix}, \quad \boldsymbol{R}_{z,\alpha} = \begin{bmatrix} \mathrm{c}_\alpha & -\mathrm{s}_\alpha & 0 \\ \mathrm{s}_\alpha & \mathrm{c}_\alpha & 0 \\ 0 & 0 & 1 \end{bmatrix},$$

where $\mathrm{s}_{(\cdot)}$ and $\mathrm{c}_{(\cdot)}$ are shorthands for $\sin(\cdot)$ and $\cos(\cdot)$.

Some parametrizations of rotation matrices are found in the literature. The Euler angle parametrization (Spong et al., 2006) consists in defining a rotation matrix as a sequence of three basic rotations, resulting in a matrix that is a function of three independent parameters. For instance, the ZYZ convention about local axes is defined by $\boldsymbol{R}_{z,\psi}\boldsymbol{R}_{y,\theta}\boldsymbol{R}_{z,\phi}$, where ϕ, θ and ψ are those parameters. The local roll-pitch-yaw convention (Jazar, 2010) is equivalent to the ZYX convention about local axes. Another parametrization is the axis/angle one (Spong et al., 2006), in which the rotation matrix is defined by a rotation

about an arbitrary axis. The elementary rotation matrices can be seen as special cases of this parametrization.

Let $\mathcal{A}$ be a right-handed reference frame in $\mathbb{R}^3$, and denote as $\mathcal{B}$ the frame resulting from applying a rigid transformation to $\mathcal{A}$, composed of a translation followed by a rotation (see Figure 2.1). Furthermore, denote the associated displacement vector and rotation matrix as $\boldsymbol{d}_{\mathcal{B}}^{\mathcal{A}}$ and $\boldsymbol{R}_{\mathcal{B}}^{\mathcal{A}}$, respectively, and the position vector of a point expressed in $\mathcal{B}$ as $\boldsymbol{p}^{\mathcal{B}}$. Then, the position vector of this point is given in $\mathcal{A}$ by

$$\boldsymbol{p}^{\mathcal{A}} = \boldsymbol{d}_{\mathcal{B}}^{\mathcal{A}} + \boldsymbol{R}_{\mathcal{B}}^{\mathcal{A}} \boldsymbol{p}^{\mathcal{B}}. \tag{2.1}$$

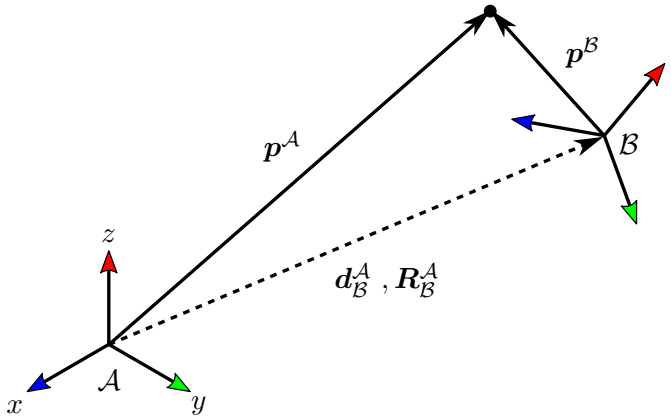

Figure 2.1: Position vectors of a point given in a right-handed reference frame $\mathcal{A}$, and in a frame $\mathcal{B}$ resulting from applying a rigid transformation to $\mathcal{A}$.

Translations and rotations can be combined into a single algebraic structure, the so-called *homogeneous transformation matrices*, which compose the special Euclidean group $SE(3)$ (Spong et al., 2006). However, these entities are not exploited in this work. Alternatively, translations and rotations can both be represented by *quaternions*, which can be further merged into another single algebraic structure, the *unit dual quaternions*, which compose the group $\text{Spin}(3) \ltimes \mathbb{R}^3$, with $\ltimes$ denoting the semi-direct product (Selig, 2005). The latter is exploited in the design of a formation control strategy in Appendix B.

2.1.2 Rigid body kinematics and dynamics

According to the Chasles' theorem (Goldstein et al., 2001), the general displacement of a rigid body can be represented by a translation followed by a rotation. Therefore, it can be equivalently represented by a rigid transformation applied to a reference frame, rigidly attached to the body.

Consider a mechanical system composed of r rigid bodies, depicted in Figure 2.2. Let $\mathcal{I}$ denote a inertial reference frame, and $\mathcal{C}_i$ denote a reference frame rigidly attached to the i-th rigid body, with $i \in \{1, 2, ..., r\}$. Furthermore, let $\boldsymbol{p}_i^{\mathcal{C}_i}$ denote the position vector of

an elementary particle that belongs to the i-th rigid body, given in $\mathcal{C}_i$. Then, the *forward kinematics* of this particle is obtained by recursive application of (2.1), yielding

$$\boldsymbol{p}_i^{\mathcal{I}} = \boldsymbol{d}_{\mathcal{C}_1}^{\mathcal{I}} + \boldsymbol{R}_{\mathcal{C}_1}^{\mathcal{I}}(\boldsymbol{d}_{\mathcal{C}_2}^{\mathcal{C}_1} + \boldsymbol{R}_{\mathcal{C}_2}^{\mathcal{C}_1}(\boldsymbol{d}_{\mathcal{C}_3}^{\mathcal{C}_2} + \boldsymbol{R}_{\mathcal{C}_3}^{\mathcal{C}_2}(\dots))), \tag{2.2}$$

which finishes at $\boldsymbol{d}_{\mathcal{C}_i}^{\mathcal{C}_{i-1}} + \boldsymbol{R}_{\mathcal{C}_i}^{\mathcal{C}_{i-1}}\boldsymbol{p}_i^{\mathcal{C}_i}$.

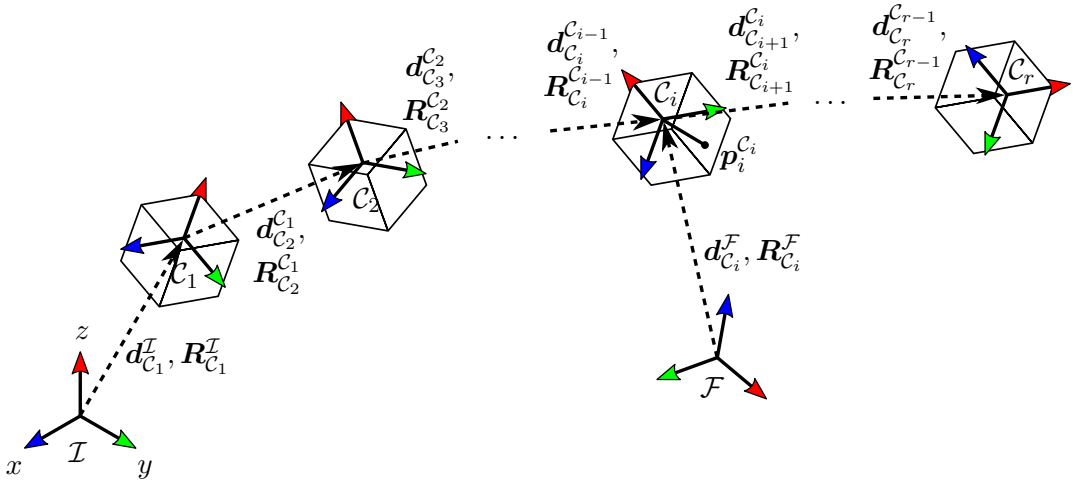

Figure 2.2: A mechanical system composed of r rigid bodies.

The velocity of the particle with respect to the inertial reference frame, expressed in $\mathcal{I}$, is given by the time derivative of (2.2). Moreover, let $\boldsymbol{R}_{\mathcal{C}_i}^{\mathcal{I}} \triangleq \boldsymbol{R}_{\mathcal{C}_1}^{\mathcal{I}}\boldsymbol{R}_{\mathcal{C}_2}^{\mathcal{C}_1}\boldsymbol{R}_{\mathcal{C}_3}^{\mathcal{C}_2}\dots\boldsymbol{R}_{\mathcal{C}_i}^{\mathcal{C}_{i-1}}$. Then, the time derivative of $\boldsymbol{R}_{\mathcal{C}_i}^{\mathcal{I}}$ satisfies (Spong et al., 2006)

$$\dot{\boldsymbol{R}}_{\mathcal{C}_i}^{\mathcal{I}} = \boldsymbol{R}_{\mathcal{C}_i}^{\mathcal{I}} S(\boldsymbol{\omega}_{\mathcal{I}\mathcal{C}_i}^{\mathcal{C}_i}), \tag{2.3}$$

where $S(\cdot)$ is an operator that maps a vector to a skew-symmetric matrix, and $\boldsymbol{\omega}_{\mathcal{I}\mathcal{C}_i}^{\mathcal{C}_i}$ denotes the angular velocity of $\mathcal{C}_i$ with respect to $\mathcal{I}$, expressed in $\mathcal{C}_i$. The latter can be obtained by

$$\boldsymbol{\omega}_{\mathcal{I}\mathcal{C}_i}^{\mathcal{C}_i} = \text{vex}((\boldsymbol{R}_{\mathcal{C}_i}^{\mathcal{I}})^T \dot{\boldsymbol{R}}_{\mathcal{C}_i}^{\mathcal{I}}), \tag{2.4}$$

where $\text{vex}(\cdot)$ corresponds to the inverse of $S(\cdot)$. Furthermore, it can also be obtained by addition of angular velocities (Spong et al., 2006) as follows,

$$\boldsymbol{\omega}_{\mathcal{I}\mathcal{C}_i}^{\mathcal{C}_i} = \boldsymbol{\omega}_{\mathcal{I}\mathcal{C}_1}^{\mathcal{C}_i} + \boldsymbol{\omega}_{\mathcal{C}_1\mathcal{C}_2}^{\mathcal{C}_i} + \dots + \boldsymbol{\omega}_{\mathcal{C}_{i-1}\mathcal{C}_i}^{\mathcal{C}_i}. \tag{2.5}$$

From now on, let the center of mass of the i-th rigid body coincide with the origin of $\mathcal{C}_i$, and let ρ_i and V_i denote the density and volume associated with the rigid body, respectively. Then, the mass of the i-th rigid body is given by

$$m_i = \int_{V_i} \rho_i \mathrm{d}V_i. \tag{2.6}$$

The inertia tensor of the i-th rigid body, expressed in $\mathcal{C}_i$, is defined by (Shabana, 2010)

$$\boldsymbol{I}_i \triangleq \int_{V_i} \rho_i S(\boldsymbol{p}_i^{\mathcal{C}_i})^T S(\boldsymbol{p}_i^{\mathcal{C}_i}) \mathrm{d}V_i. \tag{2.7}$$

According to the parallel axis theorem (also known as Steiner's theorem), the inertia tensor $\boldsymbol{I}_i$, expressed in a frame $\mathcal{F}$ displaced from $\mathcal{C}_i$ by $\boldsymbol{d}_{\mathcal{C}_i}^{\mathcal{F}}$ (see Figure 2.2), denoted as $\boldsymbol{J}_i$, is given by (Shabana, 2010, p. 384)

$$\boldsymbol{J}_i = m_i S(\boldsymbol{d}_{\mathcal{C}_i}^{\mathcal{F}})^T S(\boldsymbol{d}_{\mathcal{C}_i}^{\mathcal{F}}) + \boldsymbol{R}_{\mathcal{C}_i}^{\mathcal{F}} \boldsymbol{I}_i (\boldsymbol{R}_{\mathcal{C}_i}^{\mathcal{F}})^T. \tag{2.8}$$

Moreover, since $\mathcal{C}_i$ is attached to the center of mass of the i-th rigid body, the following property holds (Shabana, 2013, p. 144):

$$\int_{V_i} \rho_i S(\boldsymbol{p}_i^{\mathcal{C}_i}) \mathrm{d}V_i = 0. \tag{2.9}$$

The kinetic and potential energies of the i-th rigid body can be obtained through the volume integrals (Siciliano et al., 2009)

$$\mathcal{K}_i = \frac{1}{2} \int_{V_i} \rho_i (\dot{\boldsymbol{p}}_i^{\mathcal{I}})^T (\dot{\boldsymbol{p}}_i^{\mathcal{I}}) \mathrm{d}V_i, \tag{2.10}$$

$$\mathcal{U}_i = -\int_{V_i} \rho_i \hat{\boldsymbol{g}}^T \boldsymbol{p}_i^{\mathcal{I}} \mathrm{d}V_i = -m_i \hat{\boldsymbol{g}}^T \boldsymbol{o}_{\mathcal{C}_i}^{\mathcal{I}}, \tag{2.11}$$

respectively, where $\hat{\boldsymbol{g}} \triangleq [0\ 0\ -\hat{g}_z]^T$ is the gravitational acceleration vector expressed in $\mathcal{I}$, and $\boldsymbol{o}_{\mathcal{C}_i}^{\mathcal{I}}$ is the position vector obtained from the forward kinematics of the origin of $\mathcal{C}_i$. Then, the total kinetic and potential energies of the mechanical system are computed by $\mathcal{K} = \sum_{i=1}^{r} \mathcal{K}_i$ and $\mathcal{U} = \sum_{i=1}^{r} \mathcal{U}_i$, respectively.

2.1.3 The Euler-Lagrange formulation

The dynamic behavior of a multi-body mechanical system can be described by a set of differential equations, called the Euler-Lagrange equations of motion. These consist of a theoretical result from classical mechanics that can be derived using several approaches, such as the principle of virtual work along with the D'alembert's principle, or the Hamilton's principle of least action (Goldstein et al., 2001).

Let $\mathcal{K} \in \mathbb{R}$ and $\mathcal{U} \in \mathbb{R}$ denote the total kinetic and potential energies of a mechanical system with n degrees of freedom, respectively. Then, defining the Lagrangian as

$$\mathfrak{L} \triangleq \mathcal{K} - \mathcal{U}, \tag{2.12}$$

the equations of motion of the system that describe its time evolution are given by (Spong

et al., 2006)

$$\frac{d}{dt}\left(\frac{\partial \mathfrak{L}}{\partial \dot{\boldsymbol{q}}}\right) - \frac{\partial \mathfrak{L}}{\partial \boldsymbol{q}} = \boldsymbol{\vartheta}, \tag{2.13}$$

where $\boldsymbol{q} \in \mathbb{R}^n$ are the generalized coordinates, and $\boldsymbol{\vartheta} \in \mathbb{R}^n$ are the generalized forces, which correspond to projections of all non-conservative forces and torques that actuate on the mechanical system onto the generalized coordinates.

Substituting (2.12) in (2.13) leads to the canonical equation (Spong et al., 2006)

$$\boldsymbol{M}(\boldsymbol{q})\ddot{\boldsymbol{q}} + \boldsymbol{C}(\boldsymbol{q}, \dot{\boldsymbol{q}})\dot{\boldsymbol{q}} + \boldsymbol{g}(\boldsymbol{q}) = \boldsymbol{\vartheta}, \tag{2.14}$$

where $\boldsymbol{M}(\boldsymbol{q}) \in \mathbb{R}^{n\times n}$ is called the inertia matrix, obtained from rewriting the total kinetic energy in the quadratic form $\mathcal{K} = \frac{1}{2}\dot{\boldsymbol{q}}^T\boldsymbol{M}(\boldsymbol{q})\dot{\boldsymbol{q}}$, $\boldsymbol{C}(\boldsymbol{q}, \dot{\boldsymbol{q}}) \in \mathbb{R}^{n\times n}$ is called the Coriolis and centripetal forces matrix, and $\boldsymbol{g}(\boldsymbol{q}) \triangleq \partial \mathcal{U}/\partial \boldsymbol{q} \in \mathbb{R}^n$ is called the gravitational forces vector.

Let $\boldsymbol{f} \in \mathbb{R}^3$ and $\boldsymbol{\tau} \in \mathbb{R}^3$ denote a non-conservative force and a non-conservative torque, respectively, actuating on the mechanical system. Furthermore, let $\boldsymbol{p} \in \mathbb{R}^3$ denote the point of application of $\boldsymbol{f}$, and $\mathcal{F}$ be a reference frame rigidly attached to the body to which $\boldsymbol{\tau}$ is applied. The contributions of $\boldsymbol{f}$ and $\boldsymbol{\tau}$ to the generalized forces can be computed through the following mappings[1]:

$$\boldsymbol{\vartheta}_{\boldsymbol{f}} = (\mathcal{J}_{\boldsymbol{p}})^T \boldsymbol{f}^{\mathcal{I}} \in \mathbb{R}^n, \tag{2.15}$$

$$\boldsymbol{\vartheta}_{\boldsymbol{\tau}} = (\mathcal{W}_{\mathcal{F}})^T \boldsymbol{\tau}^{\mathcal{I}} \in \mathbb{R}^n, \tag{2.16}$$

where $\mathcal{J}_{\boldsymbol{p}} \triangleq \partial \dot{\boldsymbol{p}}^{\mathcal{I}}/\partial \dot{\boldsymbol{q}} \in \mathbb{R}^{3\times n}$ and $\mathcal{W}_{\mathcal{F}} \triangleq \partial \boldsymbol{\omega}^{\mathcal{I}}_{\mathcal{I}\mathcal{F}}/\partial \dot{\boldsymbol{q}} \in \mathbb{R}^{3\times n}$, $\mathcal{I}$ denotes the inertial reference frame and $\boldsymbol{\omega}_{\mathcal{I}\mathcal{F}}$ denotes the angular velocity of $\mathcal{F}$ with respect to $\mathcal{I}$. The total generalized forces, $\boldsymbol{\vartheta}$, is given by summing up the contributions of all the non-conservative forces and torques that actuate on the mechanical system.

2.2 Kinematics from the load's perspective

The tilt-rotor UAV with suspended load is illustrated in Fig. 2.3. It is regarded as a mechanical system composed of four rigid bodies: (i) the aircraft's main body, composed of ABS structure, landing gear, batteries and electronics; (ii) the right thruster group, which includes the right thruster and its tilting mechanism (a revolute joint); (iii) the left thruster group, which includes the left thruster and its tilting mechanism; and (iv) the suspended load group, composed of the load and the rod. The following assumptions are made:

- The rod is rigid and has negligible mass;
- The rod is connected to the aircraft's geometric center;

[1] This a particular case of the approach presented by Kane & Levinson (1985).

- The main body's center of mass does not coincide with the aircraft's geometric center;
- The thrusters groups' centers of mass are located at their respective tilting axes.

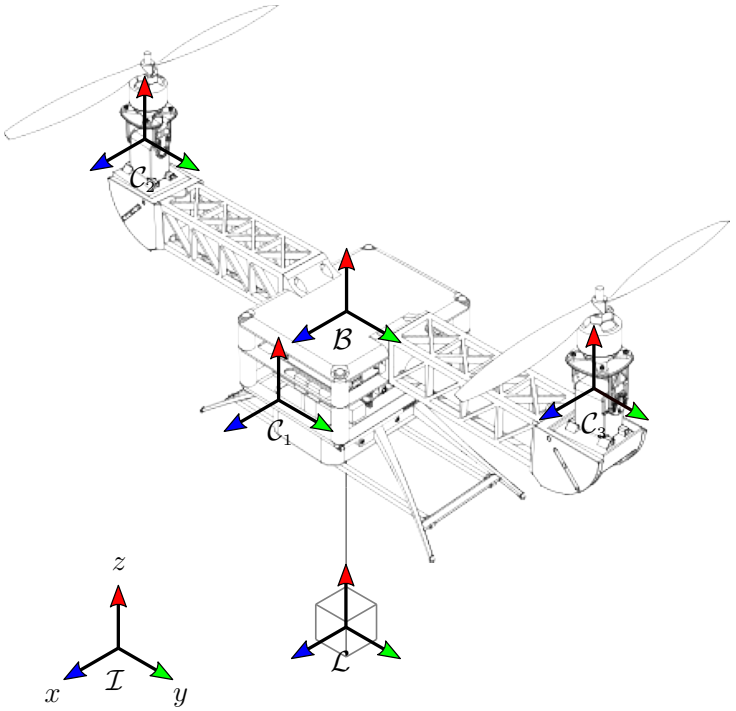

Figure 2.3: The tilt-rotor UAV with suspended load and reference frames.

The essence of the load's perspective approach consists in formulating the system's kinematics by starting from the suspended load. The latter is regarded as a rigid body with free position and orientation, and the aircraft as a multi-body mechanical system rigidly coupled to it. Six reference frames are then defined: (i) the inertial reference frame, $\mathcal{I}$; (ii) the aircraft's geometric center frame, $\mathcal{B}$; (iii) the main body center of mass frame, $\mathcal{C}_1$; (iv) the right thruster group center of mass frame, $\mathcal{C}_2$; (v) the left thruster group center of mass frame, $\mathcal{C}_3$; and (vi) the suspended load group center of mass frame, $\mathcal{L}$.

The load's position with respect to $\mathcal{I}$ is denoted by $\boldsymbol{\xi} \triangleq [x \ y \ z]^T$. The displacement vector from $\mathcal{L}$ to $\mathcal{B}$ corresponds to the rod, and is expressed in $\mathcal{L}$ by $\boldsymbol{d}_{\mathcal{B}}^{\mathcal{L}} \triangleq [0 \ 0 \ l]^T$, being l the rod's length. The displacement vectors from $\mathcal{B}$ to $\mathcal{C}_i$ are physical parameters of the tilt-rotor UAV, and expressed in $\mathcal{B}$ are denoted by $\boldsymbol{d}_{\mathcal{C}_i}^{\mathcal{B}}$, with $i \in \{1, 2, 3\}$.

The orientation of the load with respect to $\mathcal{I}$ is parametrized by Euler angles, $\boldsymbol{\eta} \triangleq [\phi \ \theta \ \psi]^T$, using the local roll-pitch-yaw convention. The associated rotation matrix is given by

$$\boldsymbol{R}_{\mathcal{L}}^{\mathcal{I}} \triangleq \boldsymbol{R}_{z,\psi}\boldsymbol{R}_{y,\theta}\boldsymbol{R}_{x,\phi} = \begin{bmatrix} \mathrm{c}_\psi \mathrm{c}_\theta & \mathrm{c}_\psi \mathrm{s}_\theta \mathrm{s}_\phi - \mathrm{s}_\psi \mathrm{c}_\phi & \mathrm{c}_\psi \mathrm{s}_\theta \mathrm{c}_\phi + \mathrm{s}_\psi \mathrm{s}_\phi \\ \mathrm{s}_\psi \mathrm{c}_\theta & \mathrm{s}_\psi \mathrm{s}_\theta \mathrm{s}_\phi + \mathrm{c}_\psi \mathrm{c}_\phi & \mathrm{s}_\psi \mathrm{s}_\theta \mathrm{c}_\phi - \mathrm{c}_\psi \mathrm{s}_\phi \\ -\mathrm{s}_\theta & \mathrm{c}_\theta \mathrm{s}_\phi & \mathrm{c}_\theta \mathrm{c}_\phi \end{bmatrix}.$$

The orientation of the aircraft's geometric center frame with respect to $\mathcal{L}$, corresponds to the inclination of the UAV with respect to the rod. It is described using two angles $\boldsymbol{\gamma} \triangleq [\gamma_1 \ \gamma_2]^T$, such that[2]

$$\boldsymbol{R}_{\mathcal{B}}^{\mathcal{L}} \triangleq \boldsymbol{R}_{x,-\gamma_1}\boldsymbol{R}_{y,-\gamma_2} = \begin{bmatrix} \mathrm{c}_{\gamma_2} & 0 & -\mathrm{s}_{\gamma_2} \\ \mathrm{s}_{\gamma_1}\mathrm{s}_{\gamma_2} & \mathrm{c}_{\gamma_1} & \mathrm{s}_{\gamma_1}\mathrm{c}_{\gamma_2} \\ \mathrm{c}_{\gamma_1}\mathrm{s}_{\gamma_2} & -\mathrm{s}_{\gamma_1} & \mathrm{c}_{\gamma_1}\mathrm{c}_{\gamma_2} \end{bmatrix}.$$

Frames $\mathcal{B}$ and $\mathcal{C}_1$ are parallel to each other and attached to the same rigid body, then the relative orientation is null, i.e., $\boldsymbol{R}_{\mathcal{C}_1}^{\mathcal{B}} = \mathbb{I}_{3\times 3}$. Furthermore, the orientations of the thrusters groups with respect to $\mathcal{B}$ are described by

$$\boldsymbol{R}_{\mathcal{C}_2}^{\mathcal{B}} \triangleq \boldsymbol{R}_{x,-\beta}\boldsymbol{R}_{y,\alpha_\mathrm{R}} = \begin{bmatrix} \mathrm{c}_{\alpha_\mathrm{R}} & 0 & \mathrm{s}_{\alpha_\mathrm{R}} \\ -\mathrm{s}_\beta\mathrm{s}_{\alpha_\mathrm{R}} & \mathrm{c}_\beta & \mathrm{s}_\beta\mathrm{c}_{\alpha_\mathrm{R}} \\ -\mathrm{c}_\beta\mathrm{s}_{\alpha_\mathrm{R}} & -\mathrm{s}_\beta & \mathrm{c}_\beta\mathrm{c}_{\alpha_\mathrm{R}} \end{bmatrix}, \quad \boldsymbol{R}_{\mathcal{C}_3}^{\mathcal{B}} \triangleq \boldsymbol{R}_{x,\beta}\boldsymbol{R}_{y,\alpha_\mathrm{L}} = \begin{bmatrix} \mathrm{c}_{\alpha_\mathrm{L}} & 0 & \mathrm{s}_{\alpha_\mathrm{L}} \\ \mathrm{s}_\beta\mathrm{s}_{\alpha_\mathrm{L}} & \mathrm{c}_\beta & -\mathrm{s}_\beta\mathrm{c}_{\alpha_\mathrm{L}} \\ -\mathrm{c}_\beta\mathrm{s}_{\alpha_\mathrm{L}} & \mathrm{s}_\beta & \mathrm{c}_\beta\mathrm{c}_{\alpha_\mathrm{L}} \end{bmatrix},$$

where α_R and α_L are the tilting angles of the right and left thrusters, respectively, and β is a fixed inclination angle of the thrusters towards the aircraft geometric center, designed with the purpose of improving the aircraft's controllability (Raffo et al., 2011).

The associated angular velocities are given by

$$\boldsymbol{\omega}_{\mathcal{I}\mathcal{L}}^{\mathcal{L}} = \mathrm{vex}((\boldsymbol{R}_{\mathcal{L}}^{\mathcal{I}})^T\dot{\boldsymbol{R}}_{\mathcal{L}}^{\mathcal{I}}) = \begin{bmatrix} 1 & 0 & -\mathrm{s}_\theta \\ 0 & \mathrm{c}_\phi & \mathrm{s}_\phi\mathrm{c}_\theta \\ 0 & -\mathrm{s}_\phi & \mathrm{c}_\phi\mathrm{c}_\theta \end{bmatrix}\begin{bmatrix} \dot{\phi} \\ \dot{\theta} \\ \dot{\psi} \end{bmatrix} \triangleq \boldsymbol{W}_{\boldsymbol{\eta}}\dot{\boldsymbol{\eta}}, \tag{2.17}$$

$$\boldsymbol{\omega}_{\mathcal{L}\mathcal{B}}^{\mathcal{B}} = \mathrm{vex}((\boldsymbol{R}_{\mathcal{B}}^{\mathcal{L}})^T\dot{\boldsymbol{R}}_{\mathcal{B}}^{\mathcal{L}}) = \begin{bmatrix} -\mathrm{c}_{\gamma_2} & 0 \\ 0 & -1 \\ \mathrm{s}_{\gamma_2} & 0 \end{bmatrix}\begin{bmatrix} \dot{\gamma}_1 \\ \dot{\gamma}_2 \end{bmatrix} \triangleq \boldsymbol{Q}\dot{\boldsymbol{\gamma}}, \tag{2.18}$$

$$\boldsymbol{\omega}_{\mathcal{B}\mathcal{C}_1}^{\mathcal{C}_1} = \mathrm{vex}((\boldsymbol{R}_{\mathcal{C}_1}^{\mathcal{B}})^T\dot{\boldsymbol{R}}_{\mathcal{C}_1}^{\mathcal{B}}) = \boldsymbol{0}_{3\times 1}, \tag{2.19}$$

$$\boldsymbol{\omega}_{\mathcal{B}\mathcal{C}_2}^{\mathcal{C}_2} = \mathrm{vex}((\boldsymbol{R}_{\mathcal{C}_2}^{\mathcal{B}})^T\dot{\boldsymbol{R}}_{\mathcal{C}_2}^{\mathcal{B}}) = \begin{bmatrix} 0 & 1 & 0 \end{bmatrix}^T\dot{\alpha}_\mathrm{R} = \boldsymbol{a}_y\dot{\alpha}_\mathrm{R}, \tag{2.20}$$

$$\boldsymbol{\omega}_{\mathcal{B}\mathcal{C}_3}^{\mathcal{C}_3} = \mathrm{vex}((\boldsymbol{R}_{\mathcal{C}_3}^{\mathcal{B}})^T\dot{\boldsymbol{R}}_{\mathcal{C}_3}^{\mathcal{B}}) = \begin{bmatrix} 0 & 1 & 0 \end{bmatrix}^T\dot{\alpha}_\mathrm{L} = \boldsymbol{a}_y\dot{\alpha}_\mathrm{L}, \tag{2.21}$$

in which $\boldsymbol{a}_y \triangleq [0 \ 1 \ 0]^T$. Unitary vectors such as the latter will be used when appropriate to provide more compact mathematical expressions throughout the chapter.

From the rigid transformations of the system, which are summarized in Figure 2.4, the

[2]The convention was chosen as the inverse of the one used by Almeida (2014), to describe the orientation of the suspended load with respect to a tilt-rotor UAV.

forward kinematics of elementary particles that belong to each rigid body are given by

$$\boldsymbol{p}_{\mathcal{L}}^{\mathcal{I}} = \boldsymbol{\xi} + \boldsymbol{R}_{\mathcal{L}}^{\mathcal{I}} \boldsymbol{p}_{\mathcal{L}}^{\mathcal{L}}, \tag{2.22}$$

$$\boldsymbol{p}_{i}^{\mathcal{I}} = \boldsymbol{\xi} + \boldsymbol{R}_{\mathcal{L}}^{\mathcal{I}} \boldsymbol{d}_{\mathcal{B}}^{\mathcal{L}} + \boldsymbol{R}_{\mathcal{L}}^{\mathcal{I}} \boldsymbol{R}_{\mathcal{B}}^{\mathcal{L}} \boldsymbol{d}_{\mathcal{C}_i}^{\mathcal{B}} + \boldsymbol{R}_{\mathcal{L}}^{\mathcal{I}} \boldsymbol{R}_{\mathcal{B}}^{\mathcal{L}} \boldsymbol{R}_{\mathcal{C}_i}^{\mathcal{B}} \boldsymbol{p}_{i}^{\mathcal{C}_i}, \tag{2.23}$$

where $\boldsymbol{p}_{\mathcal{L}}$ is the position of a point that belongs to the suspended load body, and $\boldsymbol{p}_i$ belongs to the rigid body with attached frame $\mathcal{C}_i$.

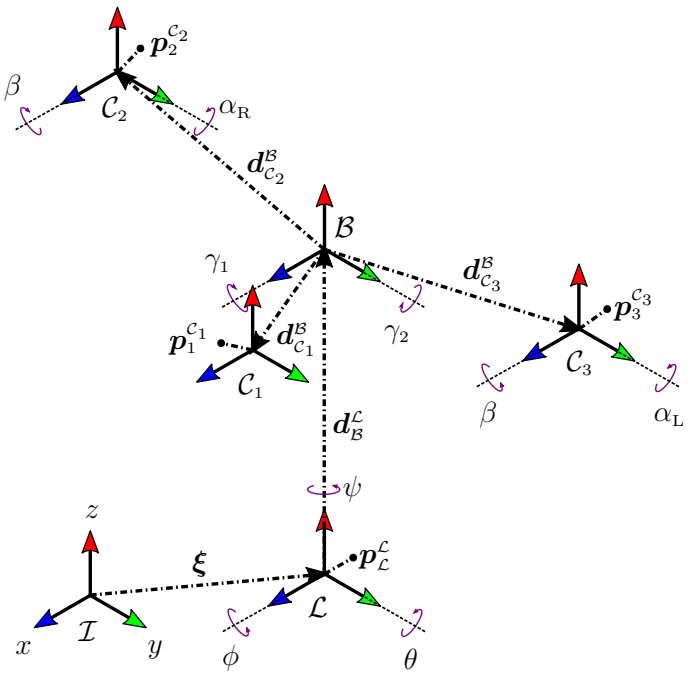

Figure 2.4: Rigid transformations of the system and positions of elementary particles that belong to each rigid body.

Taking the time derivatives of (2.22) and (2.23) yields

$$\dot{\boldsymbol{p}}_{\mathcal{L}}^{\mathcal{I}} = \dot{\boldsymbol{\xi}} + \boldsymbol{R}_{\mathcal{L}}^{\mathcal{I}} S(\boldsymbol{p}_{\mathcal{L}}^{\mathcal{L}})^T \boldsymbol{\omega}_{\mathcal{I}\mathcal{L}}^{\mathcal{L}}, \tag{2.24}$$

$$\begin{aligned} \dot{\boldsymbol{p}}_{i}^{\mathcal{I}} = \dot{\boldsymbol{\xi}} &+ \left[\boldsymbol{R}_{\mathcal{L}}^{\mathcal{I}} S(\boldsymbol{d}_{\mathcal{B}}^{\mathcal{L}})^T + \boldsymbol{R}_{\mathcal{L}}^{\mathcal{I}} \boldsymbol{R}_{\mathcal{B}}^{\mathcal{L}} S(\boldsymbol{d}_{\mathcal{C}_i}^{\mathcal{B}})^T (\boldsymbol{R}_{\mathcal{B}}^{\mathcal{L}})^T + \boldsymbol{R}_{\mathcal{L}}^{\mathcal{I}} \boldsymbol{R}_{\mathcal{B}}^{\mathcal{L}} \boldsymbol{R}_{\mathcal{C}_i}^{\mathcal{B}} S(\boldsymbol{p}_{i}^{\mathcal{C}_i})^T (\boldsymbol{R}_{\mathcal{B}}^{\mathcal{L}} \boldsymbol{R}_{\mathcal{C}_i}^{\mathcal{B}})^T \right] \boldsymbol{\omega}_{\mathcal{I}\mathcal{L}}^{\mathcal{L}} \\ &+ \left[\boldsymbol{R}_{\mathcal{L}}^{\mathcal{I}} \boldsymbol{R}_{\mathcal{B}}^{\mathcal{L}} S(\boldsymbol{d}_{\mathcal{C}_i}^{\mathcal{B}})^T + \boldsymbol{R}_{\mathcal{L}}^{\mathcal{I}} \boldsymbol{R}_{\mathcal{B}}^{\mathcal{L}} \boldsymbol{R}_{\mathcal{C}_i}^{\mathcal{B}} S(\boldsymbol{p}_{i}^{\mathcal{C}_i})^T (\boldsymbol{R}_{\mathcal{C}_i}^{\mathcal{B}})^T \right] \boldsymbol{\omega}_{\mathcal{L}\mathcal{B}}^{\mathcal{B}} + \boldsymbol{R}_{\mathcal{L}}^{\mathcal{I}} \boldsymbol{R}_{\mathcal{B}}^{\mathcal{L}} \boldsymbol{R}_{\mathcal{C}_i}^{\mathcal{B}} S(\boldsymbol{p}_{i}^{\mathcal{C}_i})^T \boldsymbol{\omega}_{\mathcal{B}\mathcal{C}_i}^{\mathcal{C}_i}. \end{aligned} \tag{2.25}$$

The generalized coordinates of the system are chosen according to its degrees of freedom. Therefore, based on the system's rigid transformations, they are chosen as

$$\boldsymbol{q} \triangleq \begin{bmatrix} \boldsymbol{\xi} \\ \boldsymbol{\eta} \\ \boldsymbol{\gamma} \\ \alpha_{\mathrm{R}} \\ \alpha_{\mathrm{L}} \end{bmatrix} \in \mathbb{R}^{10}, \tag{2.26}$$

where $\boldsymbol{\xi} = [x \ y \ z]^T$ is the position vector of the load with respect to the inertial frame, $\boldsymbol{\eta} = [\phi \ \theta \ \psi]^T$ is the vector of Euler angles describing the orientation of the load with respect to the inertial frame, $\boldsymbol{\gamma} = [\gamma_1 \ \gamma_2]^T$ is the vector of angles describing the orientation of the UAV with respect to the rod, α_{R} and α_{L} are the tilting angles of the thrusters.

2.3 Kinetic and potential energies

The kinetic energy of each rigid body can be calculated using (2.10), in which the quadratic terms $(\dot{\boldsymbol{p}}_{\mathcal{L}}^{\mathcal{I}})^T\dot{\boldsymbol{p}}_{\mathcal{L}}^{\mathcal{I}}$ and $(\dot{\boldsymbol{p}}_i^{\mathcal{I}})^T\dot{\boldsymbol{p}}_i^{\mathcal{I}}$, $i \in \{1,2,3\}$, are obtained using (2.24) and (2.25), respectively. Taking into account (2.6)-(2.9), we have that

$$\mathcal{K}_{\mathcal{L}} = \frac{1}{2}\int_{V_{\mathcal{L}}} \rho_{\mathcal{L}}(\dot{\boldsymbol{p}}_{\mathcal{L}}^{\mathcal{I}})^T(\dot{\boldsymbol{p}}_{\mathcal{L}}^{\mathcal{I}})\mathrm{d}V_{\mathcal{L}} = \frac{1}{2}m_{\mathcal{L}}\dot{\boldsymbol{\xi}}^T\dot{\boldsymbol{\xi}} + \frac{1}{2}(\boldsymbol{\omega}_{\mathcal{IL}}^{\mathcal{L}})^T\boldsymbol{I}_{\mathcal{L}}\boldsymbol{\omega}_{\mathcal{IL}}^{\mathcal{L}}, \tag{2.27}$$

$$\begin{aligned}\mathcal{K}_i = \frac{1}{2}\int_{V_i} \rho_i(\dot{\boldsymbol{p}}_i^{\mathcal{I}})^T(\dot{\boldsymbol{p}}_i^{\mathcal{I}})\mathrm{d}V_i &= \frac{1}{2}m_i\dot{\boldsymbol{\xi}}^T\dot{\boldsymbol{\xi}} + \dot{\boldsymbol{\xi}}^T\left[m_i\boldsymbol{R}_{\mathcal{L}}^{\mathcal{I}}S(\boldsymbol{d}_{\mathcal{B}}^{\mathcal{L}})^T + \boldsymbol{R}_{\mathcal{L}}^{\mathcal{I}}\boldsymbol{R}_{\mathcal{B}}^{\mathcal{L}}S(m_i\boldsymbol{d}_{\mathcal{C}_i}^{\mathcal{B}})^T(\boldsymbol{R}_{\mathcal{B}}^{\mathcal{L}})^T\right]\boldsymbol{\omega}_{\mathcal{IL}}^{\mathcal{L}} \\ &+ \dot{\boldsymbol{\xi}}^T\left[\boldsymbol{R}_{\mathcal{L}}^{\mathcal{I}}\boldsymbol{R}_{\mathcal{B}}^{\mathcal{L}}S(m_i\boldsymbol{d}_{\mathcal{C}_i}^{\mathcal{B}})^T\right]\boldsymbol{\omega}_{\mathcal{LB}}^{\mathcal{B}} + \frac{1}{2}(\boldsymbol{\omega}_{\mathcal{IL}}^{\mathcal{L}})^T\left[\boldsymbol{D}_i + S(\boldsymbol{d}_{\mathcal{B}}^{\mathcal{L}})\boldsymbol{R}_{\mathcal{B}}^{\mathcal{L}}S(m_i\boldsymbol{d}_{\mathcal{C}_i}^{\mathcal{B}})^T(\boldsymbol{R}_{\mathcal{B}}^{\mathcal{L}})^T\right. \\ &\left.+\boldsymbol{R}_{\mathcal{B}}^{\mathcal{L}}S(m_i\boldsymbol{d}_{\mathcal{C}_i}^{\mathcal{B}})(\boldsymbol{R}_{\mathcal{B}}^{\mathcal{L}})^TS(\boldsymbol{d}_{\mathcal{B}}^{\mathcal{L}})^T\right]\boldsymbol{\omega}_{\mathcal{IL}}^{\mathcal{L}} + (\boldsymbol{\omega}_{\mathcal{IL}}^{\mathcal{L}})^T\left[S(\boldsymbol{d}_{\mathcal{B}}^{\mathcal{L}})\boldsymbol{R}_{\mathcal{B}}^{\mathcal{L}}S(m_i\boldsymbol{d}_{\mathcal{C}_i}^{\mathcal{B}})^T + \boldsymbol{R}_{\mathcal{B}}^{\mathcal{L}}\boldsymbol{J}_i\right]\boldsymbol{\omega}_{\mathcal{LB}}^{\mathcal{B}} \\ &+ (\boldsymbol{\omega}_{\mathcal{IL}}^{\mathcal{L}})^T\boldsymbol{R}_{\mathcal{B}}^{\mathcal{L}}\boldsymbol{R}_{\mathcal{C}_i}^{\mathcal{B}}\boldsymbol{I}_i\boldsymbol{\omega}_{\mathcal{BC}_i}^{\mathcal{C}_i} + \frac{1}{2}(\boldsymbol{\omega}_{\mathcal{LB}}^{\mathcal{B}})^T\boldsymbol{J}_i\boldsymbol{\omega}_{\mathcal{LB}}^{\mathcal{B}} + (\boldsymbol{\omega}_{\mathcal{LB}}^{\mathcal{B}})^T\boldsymbol{R}_{\mathcal{C}_i}^{\mathcal{B}}\boldsymbol{I}_i\boldsymbol{\omega}_{\mathcal{BC}_i}^{\mathcal{C}_i} + \frac{1}{2}(\boldsymbol{\omega}_{\mathcal{BC}_i}^{\mathcal{C}_i})^T\boldsymbol{I}_i\boldsymbol{\omega}_{\mathcal{BC}_i}^{\mathcal{C}_i},\end{aligned} \tag{2.28}$$

where $\boldsymbol{D}_i \triangleq m_iS(\boldsymbol{d}_{\mathcal{B}}^{\mathcal{L}})S(\boldsymbol{d}_{\mathcal{B}}^{\mathcal{L}})^T + \boldsymbol{R}_{\mathcal{B}}^{\mathcal{L}}\boldsymbol{J}_i(\boldsymbol{R}_{\mathcal{B}}^{\mathcal{L}})^T$ corresponds to a second application of the parallel axis theorem (2.8).

The total kinetic energy is computed by $\mathcal{K} = \mathcal{K}_{\mathcal{L}} + \sum_{i=1}^{3}\mathcal{K}_i$, and with (2.17)-(2.21) it can be written in the quadratic form $\mathcal{K} = \frac{1}{2}\dot{\boldsymbol{q}}^T\boldsymbol{M}(\boldsymbol{q})\dot{\boldsymbol{q}}$, yielding the inertia matrix $\boldsymbol{M}(\boldsymbol{q}) \in \mathbb{R}^{10\times 10}$,

$$\boldsymbol{M}(\boldsymbol{q}) = \begin{bmatrix} (m_{\mathcal{L}}+m)\mathbb{I}_{3\times 3} & \boldsymbol{M}_{12} & -\boldsymbol{R}_{\mathcal{L}}^{\mathcal{I}}\boldsymbol{R}_{\mathcal{B}}^{\mathcal{L}}S(\boldsymbol{d}_m)\boldsymbol{Q} & \boldsymbol{0}_{3\times 1} & \boldsymbol{0}_{3\times 1} \\ * & \boldsymbol{M}_{22} & \boldsymbol{M}_{23} & \boldsymbol{W}_{\boldsymbol{\eta}}^T\boldsymbol{R}_{\mathcal{B}}^{\mathcal{L}}\boldsymbol{R}_{\mathcal{C}_2}^{\mathcal{B}}\boldsymbol{I}_2\boldsymbol{a}_y & \boldsymbol{W}_{\boldsymbol{\eta}}^T\boldsymbol{R}_{\mathcal{B}}^{\mathcal{L}}\boldsymbol{R}_{\mathcal{C}_3}^{\mathcal{B}}\boldsymbol{I}_3\boldsymbol{a}_y \\ * & * & \boldsymbol{Q}^T\boldsymbol{J}\boldsymbol{Q} & \boldsymbol{Q}^T\boldsymbol{R}_{\mathcal{C}_2}^{\mathcal{B}}\boldsymbol{I}_2\boldsymbol{a}_y & \boldsymbol{Q}^T\boldsymbol{R}_{\mathcal{C}_3}^{\mathcal{B}}\boldsymbol{I}_3\boldsymbol{a}_y \\ * & * & * & \boldsymbol{a}_y^T\boldsymbol{I}_2\boldsymbol{a}_y & 0 \\ * & * & * & * & \boldsymbol{a}_y^T\boldsymbol{I}_3\boldsymbol{a}_y \end{bmatrix}, \tag{2.29}$$

with $*$ denoting terms that are deduced by symmetry, and

$$\begin{aligned}\boldsymbol{M}_{12} &= -m\boldsymbol{R}_{\mathcal{L}}^{\mathcal{I}}S(\boldsymbol{d}_{\mathcal{B}}^{\mathcal{L}})\boldsymbol{W}_{\boldsymbol{\eta}} - \boldsymbol{R}_{\mathcal{L}}^{\mathcal{I}}\boldsymbol{R}_{\mathcal{B}}^{\mathcal{L}}S(\boldsymbol{d}_m)(\boldsymbol{R}_{\mathcal{B}}^{\mathcal{L}})^T\boldsymbol{W}_{\boldsymbol{\eta}}, \\ \boldsymbol{M}_{22} &= \boldsymbol{W}_{\boldsymbol{\eta}}^T\left[\boldsymbol{I}_{\mathcal{L}} + \boldsymbol{D} - S(\boldsymbol{d}_{\mathcal{B}}^{\mathcal{L}})\boldsymbol{R}_{\mathcal{B}}^{\mathcal{L}}S(\boldsymbol{d}_m)(\boldsymbol{R}_{\mathcal{B}}^{\mathcal{L}})^T - \boldsymbol{R}_{\mathcal{B}}^{\mathcal{L}}S(\boldsymbol{d}_m)(\boldsymbol{R}_{\mathcal{B}}^{\mathcal{L}})^TS(\boldsymbol{d}_{\mathcal{B}}^{\mathcal{L}})\right]\boldsymbol{W}_{\boldsymbol{\eta}}, \\ \boldsymbol{M}_{23} &= \boldsymbol{W}_{\boldsymbol{\eta}}^T\left[-S(\boldsymbol{d}_{\mathcal{B}}^{\mathcal{L}})\boldsymbol{R}_{\mathcal{B}}^{\mathcal{L}}S(\boldsymbol{d}_m) + \boldsymbol{R}_{\mathcal{B}}^{\mathcal{L}}\boldsymbol{J}\right]\boldsymbol{Q},\end{aligned}$$

where $m_{\mathcal{L}}$ is the load's mass, $m \triangleq \sum_{i=1}^{3}m_i$, $\boldsymbol{J} \triangleq \sum_{i=1}^{3}\boldsymbol{J}_i$, $\boldsymbol{D} \triangleq \sum_{i=1}^{3}\boldsymbol{D}_i$ and $\boldsymbol{d}_m \triangleq \sum_{i=1}^{3}m_i\boldsymbol{d}_{\mathcal{C}_i}^{\mathcal{B}}$.

Once the inertia matrix is obtained, the Coriolis and centripetal forces matrix, $\boldsymbol{C}(\boldsymbol{q},\dot{\boldsymbol{q}}) \in \mathbb{R}^{10\times 10}$, can be calculated via Christoffel symbols of the first kind (Spong et al., 2006).

Then, the element from its k-th row and j-th column is computed through

$$C_{kj} = \sum_{i=1}^{10} \frac{1}{2} \left(\frac{\partial M_{kj}}{\partial q_i} + \frac{\partial M_{ki}}{\partial q_j} - \frac{\partial M_{ij}}{\partial q_k} \right) \dot{q}_i, \tag{2.30}$$

where M is an element of the inertia matrix, and $k, j \in \{1, 2, \ldots, 10\}$.

The forward kinematics of each body's center of mass can be obtained using (2.22) and (2.23), by

$$\boldsymbol{o}_{\mathcal{L}}^{\mathcal{I}} = \boldsymbol{p}_{\mathcal{L}}^{\mathcal{I}}|_{\boldsymbol{p}_{\mathcal{L}}^{\mathcal{L}} = \boldsymbol{0}_{3\times 1}} = \boldsymbol{\xi}, \tag{2.31}$$

$$\boldsymbol{o}_{\mathcal{C}_i}^{\mathcal{I}} = \boldsymbol{p}_i^{\mathcal{I}}|_{\boldsymbol{p}_i^{\mathcal{C}_i} = \boldsymbol{0}_{3\times 1}} = \boldsymbol{\xi} + \boldsymbol{R}_{\mathcal{L}}^{\mathcal{I}} \boldsymbol{d}_{\mathcal{B}}^{\mathcal{L}} + \boldsymbol{R}_{\mathcal{L}}^{\mathcal{I}} \boldsymbol{R}_{\mathcal{B}}^{\mathcal{L}} \boldsymbol{d}_{\mathcal{C}_i}^{\mathcal{B}}. \tag{2.32}$$

Then, the potential energies of the load and of each body of the aircraft can be obtained using (2.11). Thereafter, the total potential energy of the system is computed by $\mathcal{U} = \mathcal{U}_{\mathcal{L}} + \sum_{i=1}^{3} \mathcal{U}_i$, yielding

$$\mathcal{U} = -\hat{\boldsymbol{g}}^T \left[(m_{\mathcal{L}} + m)\boldsymbol{\xi} + m\boldsymbol{R}_{\mathcal{L}}^{\mathcal{I}} \boldsymbol{d}_{\mathcal{B}}^{\mathcal{L}} + \boldsymbol{R}_{\mathcal{L}}^{\mathcal{I}} \boldsymbol{R}_{\mathcal{B}}^{\mathcal{L}} \boldsymbol{d}_m \right].$$

Then, the gravitational force vector is calculated as

$$\boldsymbol{g}(\boldsymbol{q}) = \frac{\partial \mathcal{U}}{\partial \boldsymbol{q}} \in \mathbb{R}^{10}. \tag{2.33}$$

2.4 Generalized forces

This section obtains the contributions to the generalized forces of all non-conservative forces and torques that actuate on the tilt-rotor UAV with suspended load.

2.4.1 Input forces and torques

The thrust forces generated by the aircraft's propellers, denoted by $\boldsymbol{f}_{\mathrm{R}}$ and $\boldsymbol{f}_{\mathrm{L}}$, and the torques generated by the servomotors composing the tilting mechanisms, denoted by $\boldsymbol{\tau}_{\alpha_{\mathrm{R}}}$ and $\boldsymbol{\tau}_{\alpha_{\mathrm{L}}}$, correspond to the input forces and torques of the system. Expressed in their respective thrusters' frames, they are given by (see Figure 2.5)

$$\begin{aligned}
\boldsymbol{f}_{\mathrm{R}}^{\mathcal{C}_2} &= \begin{bmatrix} 0 & 0 & 1 \end{bmatrix}^T f_{\mathrm{R}} \triangleq \boldsymbol{a}_z f_{\mathrm{R}}, \\
\boldsymbol{f}_{\mathrm{L}}^{\mathcal{C}_3} &= \begin{bmatrix} 0 & 0 & 1 \end{bmatrix}^T f_{\mathrm{L}} = \boldsymbol{a}_z f_{\mathrm{L}}, \\
\boldsymbol{\tau}_{\alpha_{\mathrm{R}}}^{\mathcal{C}_2} &= \begin{bmatrix} 0 & 1 & 0 \end{bmatrix}^T \tau_{\alpha_{\mathrm{R}}} = \boldsymbol{a}_y \tau_{\alpha_{\mathrm{R}}}, \\
\boldsymbol{\tau}_{\alpha_{\mathrm{L}}}^{\mathcal{C}_3} &= \begin{bmatrix} 0 & 1 & 0 \end{bmatrix}^T \tau_{\alpha_{\mathrm{L}}} = \boldsymbol{a}_y \tau_{\alpha_{\mathrm{L}}}.
\end{aligned}$$

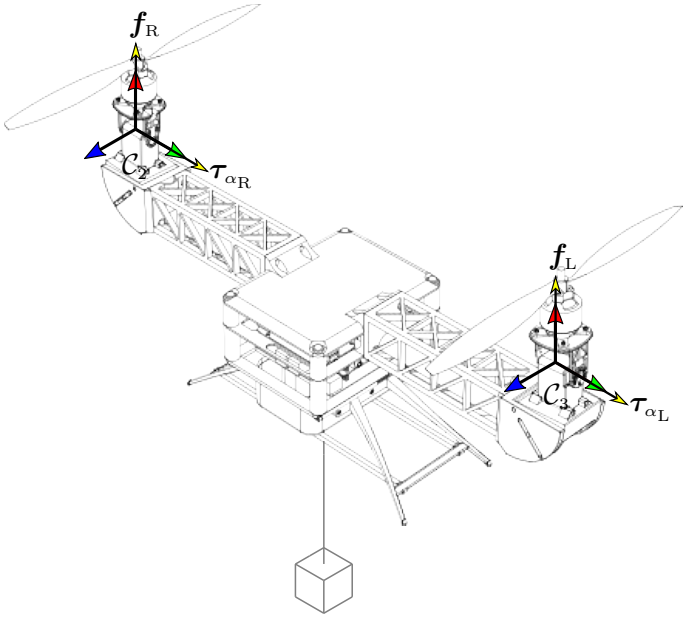

Figure 2.5: Input forces and torques.

In the inertial reference frame, these vectors are expressed as

$$\boldsymbol{f}_{\mathrm{R}}^{\mathcal{I}} = \boldsymbol{R}_{\mathcal{C}_2}^{\mathcal{I}} \boldsymbol{f}_{\mathrm{R}}^{\mathcal{C}_2} = \boldsymbol{R}_{\mathcal{L}}^{\mathcal{I}} \boldsymbol{R}_{\mathcal{B}}^{\mathcal{L}} \boldsymbol{R}_{\mathcal{C}_2}^{\mathcal{B}} \boldsymbol{a}_z f_{\mathrm{R}}, \tag{2.34}$$

$$\boldsymbol{f}_{\mathrm{L}}^{\mathcal{I}} = \boldsymbol{R}_{\mathcal{C}_3}^{\mathcal{I}} \boldsymbol{f}_{\mathrm{L}}^{\mathcal{C}_3} = \boldsymbol{R}_{\mathcal{L}}^{\mathcal{I}} \boldsymbol{R}_{\mathcal{B}}^{\mathcal{L}} \boldsymbol{R}_{\mathcal{C}_3}^{\mathcal{B}} \boldsymbol{a}_z f_{\mathrm{L}}. \tag{2.35}$$

$$\boldsymbol{\tau}_{\alpha_{\mathrm{R}}}^{\mathcal{I}} = \boldsymbol{R}_{\mathcal{C}_2}^{\mathcal{I}} \boldsymbol{\tau}_{\alpha_{\mathrm{R}}}^{\mathcal{C}_2} = \boldsymbol{R}_{\mathcal{L}}^{\mathcal{I}} \boldsymbol{R}_{\mathcal{B}}^{\mathcal{L}} \boldsymbol{R}_{\mathcal{C}_2}^{\mathcal{B}} \boldsymbol{a}_y \tau_{\alpha_{\mathrm{R}}}, \tag{2.36}$$

$$\boldsymbol{\tau}_{\alpha_{\mathrm{L}}}^{\mathcal{I}} = \boldsymbol{R}_{\mathcal{C}_3}^{\mathcal{I}} \boldsymbol{\tau}_{\alpha_{\mathrm{L}}}^{\mathcal{C}_3} = \boldsymbol{R}_{\mathcal{L}}^{\mathcal{I}} \boldsymbol{R}_{\mathcal{B}}^{\mathcal{L}} \boldsymbol{R}_{\mathcal{C}_3}^{\mathcal{B}} \boldsymbol{a}_y \tau_{\alpha_{\mathrm{L}}}. \tag{2.37}$$

It is assumed that the thrust forces are applied to the centers of mass of their respective thrusters groups, which correspond the origins of $\mathcal{C}_2$ and $\mathcal{C}_3$. Thus, in order to map them to generalized forces, it is necessary to compute $\mathcal{J}_{o_{\mathcal{C}_2}} = \partial \dot{\boldsymbol{o}}_{\mathcal{C}_2}^{\mathcal{I}} / \partial \dot{\boldsymbol{q}}$ and $\mathcal{J}_{o_{\mathcal{C}_3}} = \partial \dot{\boldsymbol{o}}_{\mathcal{C}_3}^{\mathcal{I}} / \partial \dot{\boldsymbol{q}}$. Making $\boldsymbol{p}_i^{\mathcal{C}_i} = \boldsymbol{o}_{\mathcal{C}_i}^{\mathcal{C}_i} = \boldsymbol{0}_{3\times 1}$ in (2.23) yields

$$\begin{aligned}
\dot{\boldsymbol{o}}_{\mathcal{C}_i}^{\mathcal{I}} &= \dot{\boldsymbol{\xi}} + \left(\boldsymbol{R}_{\mathcal{L}}^{\mathcal{I}} S(\boldsymbol{d}_{\mathcal{B}}^{\mathcal{L}})^T + \boldsymbol{R}_{\mathcal{L}}^{\mathcal{I}} \boldsymbol{R}_{\mathcal{B}}^{\mathcal{L}} S(\boldsymbol{d}_{\mathcal{C}_i}^{\mathcal{B}})^T (\boldsymbol{R}_{\mathcal{B}}^{\mathcal{L}})^T \right) \boldsymbol{\omega}_{\mathcal{IL}}^{\mathcal{L}} + \boldsymbol{R}_{\mathcal{L}}^{\mathcal{I}} \boldsymbol{R}_{\mathcal{B}}^{\mathcal{L}} S(\boldsymbol{d}_{\mathcal{C}_i}^{\mathcal{B}})^T \boldsymbol{\omega}_{\mathcal{LB}}^{\mathcal{B}} \\
&= \dot{\boldsymbol{\xi}} + \left(\boldsymbol{R}_{\mathcal{L}}^{\mathcal{I}} S(\boldsymbol{d}_{\mathcal{B}}^{\mathcal{L}})^T + \boldsymbol{R}_{\mathcal{L}}^{\mathcal{I}} \boldsymbol{R}_{\mathcal{B}}^{\mathcal{L}} S(\boldsymbol{d}_{\mathcal{C}_i}^{\mathcal{B}})^T (\boldsymbol{R}_{\mathcal{B}}^{\mathcal{L}})^T \right) \boldsymbol{W}_{\boldsymbol{\eta}}^T \dot{\boldsymbol{\eta}} + \boldsymbol{R}_{\mathcal{L}}^{\mathcal{I}} \boldsymbol{R}_{\mathcal{B}}^{\mathcal{L}} S(\boldsymbol{d}_{\mathcal{C}_i}^{\mathcal{B}})^T \boldsymbol{Q} \dot{\boldsymbol{\gamma}} \\
&= \begin{bmatrix} \mathbb{I}_{3\times 3} & \left(\boldsymbol{R}_{\mathcal{L}}^{\mathcal{I}} S(\boldsymbol{d}_{\mathcal{B}}^{\mathcal{L}})^T + \boldsymbol{R}_{\mathcal{L}}^{\mathcal{I}} \boldsymbol{R}_{\mathcal{B}}^{\mathcal{L}} S(\boldsymbol{d}_{\mathcal{C}_i}^{\mathcal{B}})^T (\boldsymbol{R}_{\mathcal{B}}^{\mathcal{L}})^T \right) \boldsymbol{W}_{\boldsymbol{\eta}} & \boldsymbol{R}_{\mathcal{L}}^{\mathcal{I}} \boldsymbol{R}_{\mathcal{B}}^{\mathcal{L}} S(\boldsymbol{d}_{\mathcal{C}_i}^{\mathcal{B}})^T \boldsymbol{Q} & \boldsymbol{0}_{3\times 1} & \boldsymbol{0}_{3\times 1} \end{bmatrix} \dot{\boldsymbol{q}},
\end{aligned}$$

from which

$$\begin{aligned}
\mathcal{J}_{o_{\mathcal{C}_i}} &= \partial \dot{\boldsymbol{o}}_{\mathcal{C}_i}^{\mathcal{I}} / \partial \dot{\boldsymbol{q}} \\
&= \begin{bmatrix} \mathbb{I}_{3\times 3} & \left(\boldsymbol{R}_{\mathcal{L}}^{\mathcal{I}} S(\boldsymbol{d}_{\mathcal{B}}^{\mathcal{L}})^T + \boldsymbol{R}_{\mathcal{L}}^{\mathcal{I}} \boldsymbol{R}_{\mathcal{B}}^{\mathcal{L}} S(\boldsymbol{d}_{\mathcal{C}_i}^{\mathcal{B}})^T (\boldsymbol{R}_{\mathcal{B}}^{\mathcal{L}})^T \right) \boldsymbol{W}_{\boldsymbol{\eta}} & \boldsymbol{R}_{\mathcal{L}}^{\mathcal{I}} \boldsymbol{R}_{\mathcal{B}}^{\mathcal{L}} S(\boldsymbol{d}_{\mathcal{C}_i}^{\mathcal{B}})^T \boldsymbol{Q} & \boldsymbol{0}_{3\times 1} & \boldsymbol{0}_{3\times 1} \end{bmatrix}.
\end{aligned} \tag{2.38}$$

Using (2.15), (2.34) and (2.38), we obtain

$$\boldsymbol{\vartheta}_{f_{\mathrm{R}}} = (\mathcal{J}_{o_2})^T \boldsymbol{f}_{\mathrm{R}}^{\mathcal{I}} = \begin{bmatrix} \boldsymbol{R}_{\mathcal{L}}^{\mathcal{I}} \boldsymbol{R}_{\mathcal{B}}^{\mathcal{L}} \boldsymbol{R}_{\mathcal{C}_2}^{\mathcal{B}} \boldsymbol{a}_z \\ \boldsymbol{W}_{\boldsymbol{\eta}}^T S(\boldsymbol{d}_{\mathcal{B}}^{\mathcal{L}}) \boldsymbol{R}_{\mathcal{B}}^{\mathcal{L}} \boldsymbol{R}_{\mathcal{C}_2}^{\mathcal{B}} \boldsymbol{a}_z + \boldsymbol{W}_{\boldsymbol{\eta}}^T \boldsymbol{R}_{\mathcal{B}}^{\mathcal{L}} S(\boldsymbol{d}_{\mathcal{C}_2}^{\mathcal{B}}) \boldsymbol{R}_{\mathcal{C}_2}^{\mathcal{B}} \boldsymbol{a}_z \\ \boldsymbol{Q}^T S(\boldsymbol{d}_{\mathcal{C}_2}^{\mathcal{B}}) \boldsymbol{R}_{\mathcal{C}_2}^{\mathcal{B}} \boldsymbol{a}_z \\ 0 \\ 0 \end{bmatrix} f_{\mathrm{R}}. \tag{2.39}$$

Analogously, through (2.15), (2.35) and (2.38),

$$\boldsymbol{\vartheta}_{f_{\mathrm{L}}} = (\mathcal{J}_{o_3})^T \boldsymbol{f}_{\mathrm{L}}^{\mathcal{I}} = \begin{bmatrix} \boldsymbol{R}_{\mathcal{L}}^{\mathcal{I}} \boldsymbol{R}_{\mathcal{B}}^{\mathcal{L}} \boldsymbol{R}_{\mathcal{C}_3}^{\mathcal{B}} \boldsymbol{a}_z \\ \boldsymbol{W}_{\boldsymbol{\eta}}^T S(\boldsymbol{d}_{\mathcal{B}}^{\mathcal{L}}) \boldsymbol{R}_{\mathcal{B}}^{\mathcal{L}} \boldsymbol{R}_{\mathcal{C}_3}^{\mathcal{B}} \boldsymbol{a}_z + \boldsymbol{W}_{\boldsymbol{\eta}}^T \boldsymbol{R}_{\mathcal{B}}^{\mathcal{L}} S(\boldsymbol{d}_{\mathcal{C}_3}^{\mathcal{B}}) \boldsymbol{R}_{\mathcal{C}_3}^{\mathcal{B}} \boldsymbol{a}_z \\ \boldsymbol{Q}^T S(\boldsymbol{d}_{\mathcal{C}_3}^{\mathcal{B}}) \boldsymbol{R}_{\mathcal{C}_3}^{\mathcal{B}} \boldsymbol{a}_z \\ 0 \\ 0 \end{bmatrix} f_{\mathrm{L}}. \tag{2.40}$$

The servomotors torques are applied to their respective thrusters' bodies, however opposite torques due to reaction are also applied to the aircraft's main body. These pairs of torques are mapped to generalized forces through (2.16), for which it is necessary to compute $\mathcal{W}_{\mathcal{C}_2} = \partial \boldsymbol{\omega}_{\mathcal{I}\mathcal{C}_2}^{\mathcal{I}} / \partial \dot{\boldsymbol{q}}$, $\mathcal{W}_{\mathcal{C}_3} = \partial \boldsymbol{\omega}_{\mathcal{I}\mathcal{C}_3}^{\mathcal{I}} / \partial \dot{\boldsymbol{q}}$ and $\mathcal{W}_{\mathcal{B}} = \partial \boldsymbol{\omega}_{\mathcal{I}\mathcal{B}}^{\mathcal{I}} / \partial \dot{\boldsymbol{q}}$.

From the addition of angular velocities,

$$\begin{aligned} \boldsymbol{\omega}_{\mathcal{I}\mathcal{B}}^{\mathcal{I}} = \boldsymbol{\omega}_{\mathcal{I}\mathcal{L}}^{\mathcal{I}} + \boldsymbol{\omega}_{\mathcal{L}\mathcal{B}}^{\mathcal{I}} &= \boldsymbol{R}_{\mathcal{L}}^{\mathcal{I}} \boldsymbol{\omega}_{\mathcal{I}\mathcal{L}}^{\mathcal{L}} + \boldsymbol{R}_{\mathcal{L}}^{\mathcal{I}} \boldsymbol{R}_{\mathcal{B}}^{\mathcal{L}} \boldsymbol{\omega}_{\mathcal{L}\mathcal{B}}^{\mathcal{B}} \\ &= \boldsymbol{R}_{\mathcal{L}}^{\mathcal{I}} \boldsymbol{W}_{\boldsymbol{\eta}} \dot{\boldsymbol{\eta}} + \boldsymbol{R}_{\mathcal{L}}^{\mathcal{I}} \boldsymbol{R}_{\mathcal{B}}^{\mathcal{L}} \boldsymbol{Q} \dot{\boldsymbol{\gamma}} \\ &= \begin{bmatrix} \boldsymbol{0}_{3\times 3} & \boldsymbol{R}_{\mathcal{L}}^{\mathcal{I}} \boldsymbol{W}_{\boldsymbol{\eta}} & \boldsymbol{R}_{\mathcal{L}}^{\mathcal{I}} \boldsymbol{R}_{\mathcal{B}}^{\mathcal{L}} \boldsymbol{Q} & \boldsymbol{0}_{3\times 1} & \boldsymbol{0}_{3\times 1} \end{bmatrix} \dot{\boldsymbol{q}}, \end{aligned}$$

from which

$$\mathcal{W}_{\mathcal{B}} = \partial \boldsymbol{\omega}_{\mathcal{I}\mathcal{B}}^{\mathcal{I}} / \partial \dot{\boldsymbol{q}} = \begin{bmatrix} \boldsymbol{0}_{3\times 3} & \boldsymbol{R}_{\mathcal{L}}^{\mathcal{I}} \boldsymbol{W}_{\boldsymbol{\eta}} & \boldsymbol{R}_{\mathcal{L}}^{\mathcal{I}} \boldsymbol{R}_{\mathcal{B}}^{\mathcal{L}} \boldsymbol{Q} & \boldsymbol{0}_{3\times 1} & \boldsymbol{0}_{3\times 1} \end{bmatrix}. \tag{2.41}$$

Furthermore,

$$\begin{aligned} \boldsymbol{\omega}_{\mathcal{I}\mathcal{C}_2}^{\mathcal{I}} = \boldsymbol{\omega}_{\mathcal{I}\mathcal{L}}^{\mathcal{I}} + \boldsymbol{\omega}_{\mathcal{L}\mathcal{B}}^{\mathcal{I}} + \boldsymbol{\omega}_{\mathcal{B}\mathcal{C}_2}^{\mathcal{I}} &= \boldsymbol{R}_{\mathcal{L}}^{\mathcal{I}} \boldsymbol{\omega}_{\mathcal{I}\mathcal{L}}^{\mathcal{L}} + \boldsymbol{R}_{\mathcal{L}}^{\mathcal{I}} \boldsymbol{R}_{\mathcal{B}}^{\mathcal{L}} \boldsymbol{\omega}_{\mathcal{L}\mathcal{B}}^{\mathcal{B}} + \boldsymbol{R}_{\mathcal{L}}^{\mathcal{I}} \boldsymbol{R}_{\mathcal{B}}^{\mathcal{L}} \boldsymbol{R}_{\mathcal{C}_2}^{\mathcal{B}} \boldsymbol{\omega}_{\mathcal{B}\mathcal{C}_2}^{\mathcal{C}_2} \\ &= \boldsymbol{R}_{\mathcal{L}}^{\mathcal{I}} \boldsymbol{W}_{\boldsymbol{\eta}} \dot{\boldsymbol{\eta}} + \boldsymbol{R}_{\mathcal{L}}^{\mathcal{I}} \boldsymbol{R}_{\mathcal{B}}^{\mathcal{L}} \boldsymbol{Q} \dot{\boldsymbol{\gamma}} + \boldsymbol{R}_{\mathcal{L}}^{\mathcal{I}} \boldsymbol{R}_{\mathcal{B}}^{\mathcal{L}} \boldsymbol{R}_{\mathcal{C}_2}^{\mathcal{B}} \boldsymbol{a}_y \dot{\alpha}_{\mathrm{R}} \\ &= \begin{bmatrix} \boldsymbol{0}_{3\times 3} & \boldsymbol{R}_{\mathcal{L}}^{\mathcal{I}} \boldsymbol{W}_{\boldsymbol{\eta}} & \boldsymbol{R}_{\mathcal{L}}^{\mathcal{I}} \boldsymbol{R}_{\mathcal{B}}^{\mathcal{L}} \boldsymbol{Q} & \boldsymbol{R}_{\mathcal{L}}^{\mathcal{I}} \boldsymbol{R}_{\mathcal{B}}^{\mathcal{L}} \boldsymbol{R}_{\mathcal{C}_2}^{\mathcal{B}} \boldsymbol{a}_y & \boldsymbol{0}_{3\times 1} \end{bmatrix} \dot{\boldsymbol{q}}, \end{aligned}$$

and

$$\begin{aligned} \boldsymbol{\omega}_{\mathcal{I}\mathcal{C}_3}^{\mathcal{I}} = \boldsymbol{\omega}_{\mathcal{I}\mathcal{L}}^{\mathcal{I}} + \boldsymbol{\omega}_{\mathcal{L}\mathcal{B}}^{\mathcal{I}} + \boldsymbol{\omega}_{\mathcal{B}\mathcal{C}_3}^{\mathcal{I}} &= \boldsymbol{R}_{\mathcal{L}}^{\mathcal{I}} \boldsymbol{\omega}_{\mathcal{I}\mathcal{L}}^{\mathcal{L}} + \boldsymbol{R}_{\mathcal{L}}^{\mathcal{I}} \boldsymbol{R}_{\mathcal{B}}^{\mathcal{L}} \boldsymbol{\omega}_{\mathcal{L}\mathcal{B}}^{\mathcal{B}} + \boldsymbol{R}_{\mathcal{L}}^{\mathcal{I}} \boldsymbol{R}_{\mathcal{B}}^{\mathcal{L}} \boldsymbol{R}_{\mathcal{C}_3}^{\mathcal{B}} \boldsymbol{\omega}_{\mathcal{B}\mathcal{C}_3}^{\mathcal{C}_3} \\ &= \boldsymbol{R}_{\mathcal{L}}^{\mathcal{I}} \boldsymbol{W}_{\boldsymbol{\eta}} \dot{\boldsymbol{\eta}} + \boldsymbol{R}_{\mathcal{L}}^{\mathcal{I}} \boldsymbol{R}_{\mathcal{B}}^{\mathcal{L}} \boldsymbol{Q} \dot{\boldsymbol{\gamma}} + \boldsymbol{R}_{\mathcal{L}}^{\mathcal{I}} \boldsymbol{R}_{\mathcal{B}}^{\mathcal{L}} \boldsymbol{R}_{\mathcal{C}_3}^{\mathcal{B}} \boldsymbol{a}_y \dot{\alpha}_{\mathrm{L}} \\ &= \begin{bmatrix} \boldsymbol{0}_{3\times 3} & \boldsymbol{R}_{\mathcal{L}}^{\mathcal{I}} \boldsymbol{W}_{\boldsymbol{\eta}} & \boldsymbol{R}_{\mathcal{L}}^{\mathcal{I}} \boldsymbol{R}_{\mathcal{B}}^{\mathcal{L}} \boldsymbol{Q} & \boldsymbol{0}_{3\times 1} & \boldsymbol{R}_{\mathcal{L}}^{\mathcal{I}} \boldsymbol{R}_{\mathcal{B}}^{\mathcal{L}} \boldsymbol{R}_{\mathcal{C}_3}^{\mathcal{B}} \boldsymbol{a}_y \end{bmatrix} \dot{\boldsymbol{q}}, \end{aligned}$$

from which

$$\mathcal{W}_{\mathcal{C}_2} = \partial \boldsymbol{\omega}^{\mathcal{I}}_{\mathcal{I}\mathcal{C}_2}/\partial \dot{\boldsymbol{q}} = \begin{bmatrix} \mathbf{0}_{3\times 3} & \boldsymbol{R}^{\mathcal{I}}_{\mathcal{L}}\boldsymbol{W}_{\boldsymbol{\eta}} & \boldsymbol{R}^{\mathcal{I}}_{\mathcal{L}}\boldsymbol{R}^{\mathcal{L}}_{\mathcal{B}}\boldsymbol{Q} & \boldsymbol{R}^{\mathcal{I}}_{\mathcal{L}}\boldsymbol{R}^{\mathcal{L}}_{\mathcal{B}}\boldsymbol{R}^{\mathcal{B}}_{\mathcal{C}_2}\boldsymbol{a}_y & \mathbf{0}_{3\times 1} \end{bmatrix}, \tag{2.42}$$

$$\mathcal{W}_{\mathcal{C}_3} = \partial \boldsymbol{\omega}^{\mathcal{I}}_{\mathcal{I}\mathcal{C}_3}/\partial \dot{\boldsymbol{q}} = \begin{bmatrix} \mathbf{0}_{3\times 3} & \boldsymbol{R}^{\mathcal{I}}_{\mathcal{L}}\boldsymbol{W}_{\boldsymbol{\eta}} & \boldsymbol{R}^{\mathcal{I}}_{\mathcal{L}}\boldsymbol{R}^{\mathcal{L}}_{\mathcal{B}}\boldsymbol{Q} & \mathbf{0}_{3\times 1} & \boldsymbol{R}^{\mathcal{I}}_{\mathcal{L}}\boldsymbol{R}^{\mathcal{L}}_{\mathcal{B}}\boldsymbol{R}^{\mathcal{B}}_{\mathcal{C}_3}\boldsymbol{a}_y \end{bmatrix}. \tag{2.43}$$

Using (2.16), (2.42), (2.36) and (2.41), we have

$$\begin{aligned} \boldsymbol{\vartheta}_{\boldsymbol{\tau}_{\alpha_{\mathrm{R}}}} &= (\mathcal{W}_{\mathcal{C}_2})^T \boldsymbol{\tau}^{\mathcal{I}}_{\alpha_{\mathrm{R}}} + (\mathcal{W}_{\mathcal{B}})^T (-\boldsymbol{\tau}^{\mathcal{I}}_{\alpha_{\mathrm{R}}}) \\ &= \left(\begin{bmatrix} \mathbf{0}_{3\times 3} \\ \boldsymbol{W}_{\boldsymbol{\eta}}^T (\boldsymbol{R}^{\mathcal{I}}_{\mathcal{L}})^T \\ \boldsymbol{Q}^T (\boldsymbol{R}^{\mathcal{I}}_{\mathcal{L}}\boldsymbol{R}^{\mathcal{L}}_{\mathcal{B}})^T \\ \boldsymbol{a}_y^T (\boldsymbol{R}^{\mathcal{I}}_{\mathcal{L}}\boldsymbol{R}^{\mathcal{L}}_{\mathcal{B}}\boldsymbol{R}^{\mathcal{B}}_{\mathcal{C}_2})^T \\ \mathbf{0}_{1\times 3} \end{bmatrix} - \begin{bmatrix} \mathbf{0}_{3\times 3} \\ \boldsymbol{W}_{\boldsymbol{\eta}}^T (\boldsymbol{R}^{\mathcal{I}}_{\mathcal{L}})^T \\ \boldsymbol{Q}^T (\boldsymbol{R}^{\mathcal{I}}_{\mathcal{L}}\boldsymbol{R}^{\mathcal{L}}_{\mathcal{B}})^T \\ \mathbf{0}_{1\times 3} \\ \mathbf{0}_{1\times 3} \end{bmatrix} \right) \boldsymbol{R}^{\mathcal{I}}_{\mathcal{L}}\boldsymbol{R}^{\mathcal{L}}_{\mathcal{B}}\boldsymbol{R}^{\mathcal{B}}_{\mathcal{C}_2}\boldsymbol{a}_y \tau_{\alpha_{\mathrm{R}}} = \begin{bmatrix} \mathbf{0}_{3\times 1} \\ \mathbf{0}_{3\times 1} \\ \mathbf{0}_{2\times 1} \\ 1 \\ 0 \end{bmatrix} \tau_{\alpha_{\mathrm{R}}}. \end{aligned} \tag{2.44}$$

Analogously, through (2.16), (2.43), (2.37) and (2.41),

$$\begin{aligned} \boldsymbol{\vartheta}_{\boldsymbol{\tau}_{\alpha_{\mathrm{L}}}} &= (\mathcal{W}_{\mathcal{C}_3})^T \boldsymbol{\tau}^{\mathcal{I}}_{\alpha_{\mathrm{L}}} + (\mathcal{W}_{\mathcal{B}})^T (-\boldsymbol{\tau}^{\mathcal{I}}_{\alpha_{\mathrm{L}}}) \\ &= \left(\begin{bmatrix} \mathbf{0}_{3\times 3} \\ \boldsymbol{W}_{\boldsymbol{\eta}}^T (\boldsymbol{R}^{\mathcal{I}}_{\mathcal{L}})^T \\ \boldsymbol{Q}^T (\boldsymbol{R}^{\mathcal{I}}_{\mathcal{L}}\boldsymbol{R}^{\mathcal{L}}_{\mathcal{B}})^T \\ \mathbf{0}_{1\times 3} \\ \boldsymbol{a}_y^T (\boldsymbol{R}^{\mathcal{I}}_{\mathcal{L}}\boldsymbol{R}^{\mathcal{L}}_{\mathcal{B}}\boldsymbol{R}^{\mathcal{B}}_{\mathcal{C}_3})^T \end{bmatrix} - \begin{bmatrix} \mathbf{0}_{3\times 3} \\ \boldsymbol{W}_{\boldsymbol{\eta}}^T (\boldsymbol{R}^{\mathcal{I}}_{\mathcal{L}})^T \\ \boldsymbol{Q}^T (\boldsymbol{R}^{\mathcal{I}}_{\mathcal{L}}\boldsymbol{R}^{\mathcal{L}}_{\mathcal{B}})^T \\ \mathbf{0}_{1\times 3} \\ \mathbf{0}_{1\times 3} \end{bmatrix} \right) \boldsymbol{R}^{\mathcal{I}}_{\mathcal{L}}\boldsymbol{R}^{\mathcal{L}}_{\mathcal{B}}\boldsymbol{R}^{\mathcal{B}}_{\mathcal{C}_3}\boldsymbol{a}_y \tau_{\alpha_{\mathrm{L}}} = \begin{bmatrix} \mathbf{0}_{3\times 1} \\ \mathbf{0}_{3\times 1} \\ \mathbf{0}_{2\times 1} \\ 0 \\ 1 \end{bmatrix} \tau_{\alpha_{\mathrm{L}}}. \end{aligned} \tag{2.45}$$

Drag torques generated by the propellers are also considered. They are reaction torques applied to the thrusters' bodies, due to the blades' acceleration and drag (Castillo et al., 2005). If steady-state is assumed for the angular velocity of the blades, these torques are given in the thrusters' frames as

$$\boldsymbol{\tau}^{\mathcal{C}_2}_{\mathrm{drag,R}} = \lambda_{\mathrm{R}} \frac{k_\tau}{b} \boldsymbol{f}^{\mathcal{C}_2}_{\mathrm{R}}, \quad \boldsymbol{\tau}^{\mathcal{C}_3}_{\mathrm{drag,L}} = \lambda_{\mathrm{L}} \frac{k_\tau}{b} \boldsymbol{f}^{\mathcal{C}_3}_{\mathrm{L}},$$

where k_τ and b are parameters that are obtained experimentally, and λ_{R} and λ_{L} depend on the direction that the corresponding propeller rotates: if counter-clockwise, 1; if clockwise, -1. In the inertial reference frame, we have

$$\boldsymbol{\tau}^{\mathcal{I}}_{\mathrm{drag,R}} = \boldsymbol{R}^{\mathcal{I}}_{\mathcal{C}_2}\boldsymbol{\tau}^{\mathcal{C}_2}_{\mathrm{drag,R}} = \lambda_{\mathrm{R}} \frac{k_\tau}{b} \boldsymbol{R}^{\mathcal{I}}_{\mathcal{C}_2}\boldsymbol{f}^{\mathcal{C}_2}_{\mathrm{R}} = \lambda_{\mathrm{R}} \frac{k_\tau}{b} \boldsymbol{R}^{\mathcal{I}}_{\mathcal{L}}\boldsymbol{R}^{\mathcal{L}}_{\mathcal{B}}\boldsymbol{R}^{\mathcal{B}}_{\mathcal{C}_2}\boldsymbol{a}_z f_{\mathrm{R}}, \tag{2.46}$$

$$\boldsymbol{\tau}^{\mathcal{I}}_{\mathrm{drag,L}} = \boldsymbol{R}^{\mathcal{I}}_{\mathcal{C}_3}\boldsymbol{\tau}^{\mathcal{C}_3}_{\mathrm{drag,L}} = \lambda_{\mathrm{L}} \frac{k_\tau}{b} \boldsymbol{R}^{\mathcal{I}}_{\mathcal{C}_3}\boldsymbol{f}^{\mathcal{C}_3}_{\mathrm{L}} = \lambda_{\mathrm{L}} \frac{k_\tau}{b} \boldsymbol{R}^{\mathcal{I}}_{\mathcal{L}}\boldsymbol{R}^{\mathcal{L}}_{\mathcal{B}}\boldsymbol{R}^{\mathcal{B}}_{\mathcal{C}_3}\boldsymbol{a}_z f_{\mathrm{L}}. \tag{2.47}$$

Since the drag torques are applied to the thrusters' bodies, it is necessary to compute $\mathcal{W}_{\mathcal{C}_2} = \partial \boldsymbol{\omega}^{\mathcal{I}}_{\mathcal{I}\mathcal{C}_2}/\partial \dot{\boldsymbol{q}}$ and $\mathcal{W}_{\mathcal{C}_3} = \partial \boldsymbol{\omega}^{\mathcal{I}}_{\mathcal{I}\mathcal{C}_3}/\partial \dot{\boldsymbol{q}}$ in order to map them to the generalized forces. Those have already been obtained in (2.42) and (2.43), respectively. Thus, using (2.16), (2.46)

and (2.42), we have

$$\boldsymbol{\vartheta}_{\boldsymbol{\tau}_{\text{drag,R}}} = (\mathcal{W}_{\mathcal{C}_2})^T \boldsymbol{\tau}^{\mathcal{I}}_{\text{drag,R}} = \lambda_{\text{R}} \frac{k_\tau}{b} \begin{bmatrix} \mathbf{0}_{3\times 1} \\ \boldsymbol{W}_{\boldsymbol{\eta}}^T \boldsymbol{R}^{\mathcal{L}}_{\mathcal{B}} \boldsymbol{R}^{\mathcal{B}}_{\mathcal{C}_2} \boldsymbol{a}_z \\ \boldsymbol{Q}^T \boldsymbol{R}^{\mathcal{B}}_{\mathcal{C}_2} \boldsymbol{a}_z \\ 0 \\ 0 \end{bmatrix} f_{\text{R}}. \tag{2.48}$$

Analogously, through (2.16), (2.47) and (2.43),

$$\boldsymbol{\vartheta}_{\boldsymbol{\tau}_{\text{drag,L}}} = (\mathcal{W}_{\mathcal{C}_3})^T \boldsymbol{\tau}^{\mathcal{I}}_{\text{drag,L}} = \lambda_{\text{L}} \frac{k_\tau}{b} \begin{bmatrix} \mathbf{0}_{3\times 1} \\ \boldsymbol{W}_{\boldsymbol{\eta}}^T \boldsymbol{R}^{\mathcal{L}}_{\mathcal{B}} \boldsymbol{R}^{\mathcal{B}}_{\mathcal{C}_3} \boldsymbol{a}_z \\ \boldsymbol{Q}^T \boldsymbol{R}^{\mathcal{B}}_{\mathcal{C}_3} \boldsymbol{a}_z \\ 0 \\ 0 \end{bmatrix} f_{\text{L}}. \tag{2.49}$$

Finally, the total mapping of the system inputs to generalized forces is obtained by summing up the contributions of the thrust forces, servomotor torques and drag torques. Then, from (2.39), (2.40), (2.44), (2.45), (2.48) and (2.49),

$$\begin{aligned} \boldsymbol{\vartheta}_{\text{in}} &= \boldsymbol{\vartheta}_{f_{\text{R}}} + \boldsymbol{\vartheta}_{f_{\text{L}}} + \boldsymbol{\vartheta}_{\tau_{\alpha_{\text{R}}}} + \boldsymbol{\vartheta}_{\tau_{\alpha_{\text{L}}}} + \boldsymbol{\vartheta}_{\boldsymbol{\tau}_{\text{drag,R}}} + \boldsymbol{\vartheta}_{\boldsymbol{\tau}_{\text{drag,L}}} \\ &= \begin{bmatrix} \boldsymbol{R}^{\mathcal{I}}_{\mathcal{L}} \boldsymbol{R}^{\mathcal{L}}_{\mathcal{B}} \boldsymbol{r}_{\text{R}} & \boldsymbol{R}^{\mathcal{I}}_{\mathcal{L}} \boldsymbol{R}^{\mathcal{L}}_{\mathcal{B}} \boldsymbol{r}_{\text{L}} & \mathbf{0}_{3\times 1} & \mathbf{0}_{3\times 1} \\ \boldsymbol{W}_{\boldsymbol{\eta}}^T \boldsymbol{\Lambda}_{\text{R}} \boldsymbol{r}_{\text{R}} & \boldsymbol{W}_{\boldsymbol{\eta}}^T \boldsymbol{\Lambda}_{\text{L}} \boldsymbol{r}_{\text{L}} & \mathbf{0}_{3\times 1} & \mathbf{0}_{3\times 1} \\ \boldsymbol{Q}^T \boldsymbol{\Gamma}_{\text{R}} \boldsymbol{r}_{\text{R}} & \boldsymbol{Q}^T \boldsymbol{\Gamma}_{\text{L}} \boldsymbol{r}_{\text{L}} & \mathbf{0}_{2\times 1} & \mathbf{0}_{2\times 1} \\ 0 & 0 & 1 & 0 \\ 0 & 0 & 0 & 1 \end{bmatrix} \begin{bmatrix} f_{\text{R}} \\ f_{\text{L}} \\ \tau_{\alpha_{\text{R}}} \\ \tau_{\alpha_{\text{L}}} \end{bmatrix} \triangleq \boldsymbol{L}_{\text{in}}(\boldsymbol{q}) \boldsymbol{u}, \end{aligned} \tag{2.50}$$

where

$$\begin{aligned} &\boldsymbol{r}_{\text{R}} \triangleq \boldsymbol{R}^{\mathcal{B}}_{\mathcal{C}_2} \boldsymbol{a}_z, && \boldsymbol{\Lambda}_{\text{R}} \triangleq S(\boldsymbol{d}^{\mathcal{L}}_{\mathcal{B}}) \boldsymbol{R}^{\mathcal{L}}_{\mathcal{B}} + \boldsymbol{R}^{\mathcal{L}}_{\mathcal{B}} S(\boldsymbol{d}^{\mathcal{B}}_{\mathcal{C}_2}) + \lambda_{\text{R}} \frac{k_\tau}{b} \boldsymbol{R}^{\mathcal{L}}_{\mathcal{B}}, && \boldsymbol{\Gamma}_{\text{R}} \triangleq S(\boldsymbol{d}^{\mathcal{B}}_{\mathcal{C}_2}) + \lambda_{\text{R}} \frac{k_\tau}{b} \mathbb{I}_{3\times 3}, \\ &\boldsymbol{r}_{\text{L}} \triangleq \boldsymbol{R}^{\mathcal{B}}_{\mathcal{C}_3} \boldsymbol{a}_z, && \boldsymbol{\Lambda}_{\text{L}} \triangleq S(\boldsymbol{d}^{\mathcal{L}}_{\mathcal{B}}) \boldsymbol{R}^{\mathcal{L}}_{\mathcal{B}} + \boldsymbol{R}^{\mathcal{L}}_{\mathcal{B}} S(\boldsymbol{d}^{\mathcal{B}}_{\mathcal{C}_3}) + \lambda_{\text{L}} \frac{k_\tau}{b} \boldsymbol{R}^{\mathcal{L}}_{\mathcal{B}}, && \boldsymbol{\Gamma}_{\text{L}} \triangleq S(\boldsymbol{d}^{\mathcal{B}}_{\mathcal{C}_3}) + \lambda_{\text{L}} \frac{k_\tau}{b} \mathbb{I}_{3\times 3}. \end{aligned}$$

2.4.2 Friction and external disturbances

The existence of viscous friction is considered at the point of connection between the rod and the tilt-rotor UAV. It is assumed that the friction torques are mapped to generalized forces by

$$\boldsymbol{\vartheta}_{\text{fr}} = -\boldsymbol{L}_{\text{fr}} \dot{\boldsymbol{q}}, \tag{2.51}$$

where $\boldsymbol{L}_{\text{fr}} \triangleq \text{diag}(0,0,0,0,0,0,\mu_\gamma,\mu_\gamma,0,0)$, with μ_γ a constant parameter.

Furthermore, the possibility of external disturbances affecting the suspended load is

also taken into account. Define these external disturbances in the inertial reference frame as a force vector $\boldsymbol{d} \triangleq \begin{bmatrix} d_x & d_y & d_z \end{bmatrix}^T \in \mathbb{R}^3$. Assuming that it is applied to the load's center of mass, it can be mapped to the generalized forces through (2.15), for which it is necessary to obtain $\mathcal{J}_{o_\mathcal{L}} = \partial \dot{\boldsymbol{o}}_\mathcal{L}^\mathcal{I} / \partial \dot{\boldsymbol{q}}$. Making $\boldsymbol{p}_\mathcal{L}^\mathcal{L} = \boldsymbol{0}_{3\times1}$ in (2.24) yields $\dot{\boldsymbol{o}}_\mathcal{L}^\mathcal{I} = \dot{\boldsymbol{\xi}}$, from which

$$\mathcal{J}_{o_\mathcal{L}} = \partial \dot{\boldsymbol{o}}_\mathcal{L}^\mathcal{I} / \partial \dot{\boldsymbol{q}} = \begin{bmatrix} \mathbb{I}_{3\times3} & \boldsymbol{0}_{3\times3} & \boldsymbol{0}_{3\times2} & \boldsymbol{0}_{3\times1} & \boldsymbol{0}_{3\times1} \end{bmatrix}. \tag{2.52}$$

Thus, using (2.15) and (2.52) results in

$$\boldsymbol{\vartheta}_{\text{db}} = (\mathcal{J}_{o_\mathcal{L}})^T \boldsymbol{d} = \begin{bmatrix} \mathbb{I}_{3\times3} & \boldsymbol{0}_{3\times3} & \boldsymbol{0}_{3\times2} & \boldsymbol{0}_{3\times1} & \boldsymbol{0}_{3\times1} \end{bmatrix}^T \boldsymbol{d} \triangleq \boldsymbol{L}_{\text{db}} \boldsymbol{d}. \tag{2.53}$$

It must be noted that other external disturbances can be included in the dynamic equations in a similar way. For instance, disturbance forces affecting the tilt-rotor UAV, applied to the origin of $\mathcal{B}$, can be mapped to the generalized forces by computing $\mathcal{J}_{o_\mathcal{B}}$, and using (2.15).

2.4.3 Total generalized forces

The total generalized forces are finally obtained by summing up the contributions from the input forces and torques, viscous friction torques and external disturbances. From (2.50), (2.51) and (2.53),

$$\boldsymbol{\vartheta} = \boldsymbol{\vartheta}_{\text{in}} + \boldsymbol{\vartheta}_{\text{fr}} + \boldsymbol{\vartheta}_{\text{db}} = \boldsymbol{L}_{\text{in}}(\boldsymbol{q})\boldsymbol{u} - \boldsymbol{L}_{\text{fr}}\dot{\boldsymbol{q}} + \boldsymbol{L}_{\text{db}}\boldsymbol{d}. \tag{2.54}$$

2.5 State-space representation

Substituting (2.54) in (2.14) yields the equations of motion

$$\boldsymbol{M}(\boldsymbol{q})\ddot{\boldsymbol{q}} + (\boldsymbol{C}(\boldsymbol{q}, \dot{\boldsymbol{q}}) + \boldsymbol{L}_{\text{fr}})\dot{\boldsymbol{q}} + \boldsymbol{g}(\boldsymbol{q}) = \boldsymbol{L}_{\text{in}}(\boldsymbol{q})\boldsymbol{u} + \boldsymbol{L}_{\text{db}}\boldsymbol{d}, \tag{2.55}$$

which describes the dynamic behavior of the tilt-rotor UAV with suspended load, from the load's perspective. Finally, by defining the state vector

$$\boldsymbol{x} \triangleq \begin{bmatrix} \boldsymbol{q} \\ \dot{\boldsymbol{q}} \end{bmatrix} \in \mathbb{R}^{20}, \tag{2.56}$$

and recalling the input vector defined in (2.50), the dynamic equations (2.55) can be written in the state-space representation

$$\dot{\boldsymbol{x}} = \boldsymbol{\varphi}(\boldsymbol{x}, \boldsymbol{u}, \boldsymbol{d}) = \frac{d}{dt}\begin{bmatrix} \boldsymbol{q} \\ \dot{\boldsymbol{q}} \end{bmatrix} = \begin{bmatrix} \dot{\boldsymbol{q}} \\ \boldsymbol{M}(\boldsymbol{q})^{-1}\left[-(\boldsymbol{C}(\boldsymbol{q}, \dot{\boldsymbol{q}}) + \boldsymbol{L}_{\text{fr}})\dot{\boldsymbol{q}} - \boldsymbol{g}(\boldsymbol{q}) + \boldsymbol{L}_{\text{in}}(\boldsymbol{q})\boldsymbol{u} + \boldsymbol{L}_{\text{db}}\boldsymbol{d}\right] \end{bmatrix}, \tag{2.57}$$

which is nonlinear and highly coupled, but affine in the inputs and disturbances. Note that, since the load's position and orientation are among the generalized coordinates (2.26), they are directly represented by the state variables (2.56). Then, the load's behavior is described explicitly by (2.57). On the other hand, the aircraft's position and orientation are described only with respect to the load, thus appearing in (2.57) only implicitly.

2.6 Final remarks

This chapter presented the dynamic modeling of the tilt-rotor UAV with suspended load, developed from the load's perspective using the Euler-Lagrange formulation.

The kinematics of the tilt-rotor UAV with suspended load were formulated from the load's perspective, in which the load was regarded as a rigid body with free position and orientation, and the aircraft as a multi-body mechanical system rigidly coupled to it. The degrees of freedom of the system were chosen as:

- x, y, z: The position of the load with respect to the inertial reference frame;
- ϕ, θ, ψ: Euler angles parametrizing the load orientation with respect to the inertial reference frame;
- γ_1, γ_2: Angles describing the orientation of the tilt-rotor UAV with respect to the rod;
- α_{R}, α_{L}: Tilting angles of the thrusters groups.

The whole-body dynamic equations were then obtained through the Euler-Lagrange formulation, yielding a highly coupled nonlinear state-space representation of the system, affine in the inputs, with the load's coordinates among the system states.

In the next chapters, the obtained state-space representation will be used to design controllers and state estimators, aiming path tracking control of the suspended load.

3
Control strategies

This chapter presents the design of state-feedback control strategies for path tracking of the suspended load, based on the state-space equations obtained in the previous chapter.

Since the load's position and orientation are represented by state variables, state-feedback strategies can directly steer the trajectory of the suspended load with respect to the inertial reference frame. Besides, the aircraft's behavior is implicit in the state-space equations, then stabilization of the system implies stabilization of the tilt-rotor UAV.

In real applications, controllers designed for UAVs are often implemented in embedded microprocessors. If continuous-time control strategies are employed, a discretization method must be applied to the controllers in order to allow their implementations. Therefore, this work focuses on the design of discrete-time control strategies, which can be directly implemented on digital systems.

Due to its simple design, as a proof of concept, a classical discrete-time linear quadratic regulator (DLQR) is proposed for path tracking of the suspended load with stabilization of the tilt-rotor UAV, based on discrete-time linearized error dynamics obtained from the derived model. In order to improve trajectory tracking and provide rejection to constant disturbances, the system dynamics are augmented with integral actions. The design of the DLQR is performed by solving a discrete-time algebraic Riccati equation.

Based on the same discrete-time, augmented linearized error dynamics, a discrete-time mixed $\mathcal{H}_2/\mathcal{H}_\infty$ controller with pole placement constraints is also proposed for path tracking of the suspended load with stabilization of the tilt-rotor UAV. The controller features constant disturbances rejection due to state augmentation, and achieves disturbance

attenuation by mininizing the $\mathcal{H}_2$ norm of the closed-loop system and guaranteeing a specified upper-bound for its $\mathcal{H}_\infty$ norm, respectively. Furthermore, time response requirements are satisfied by imposing constraints in the pole placement process. Its design is performed based on the linear matrix inequalities (LMI) approach.

The chapter is organized as follows: Section 3.1 introduces some background material on analysis of discrete-time linear systems; Section 3.2 presents the linearization and state augmentation of the state-space equations from the previous chapter; Section 3.3 describes the design of the discrete-time linear quadratic regulator; and Section 3.4 presents the design of the discrete-time mixed $\mathcal{H}_2/\mathcal{H}_\infty$ controller with pole placement constraints.

3.1 Preliminaries

3.1.1 Discrete-time linear systems

According to Chen (1999), a system is called a discrete-time system if its inputs and outputs are discrete-time signals. The control of physical systems with digital computers or micro-controllers is very common in practice, as well as the use of digital sensors for sampling their outputs. Then, the analysis of discrete-time systems becomes important.

The dynamics of a discrete-time, linear time-invariant system can be described by the set of first-order difference equations

$$\begin{aligned} \boldsymbol{x}_{k+1} &= \boldsymbol{A}\boldsymbol{x}_k + \boldsymbol{B}\boldsymbol{u}_k, \\ \boldsymbol{y}_k &= \boldsymbol{H}\boldsymbol{x}_k + \boldsymbol{D}\boldsymbol{u}_k, \end{aligned} \tag{3.1}$$

called state-space equations, where $\boldsymbol{x} \in \mathbb{R}^{n_x}$ are the system states, $\boldsymbol{u} \in \mathbb{R}^{n_u}$ are the system inputs, and $\boldsymbol{y} \in \mathbb{R}^{n_y}$ are the system outputs, $\boldsymbol{A} \in \mathbb{R}^{n_x \times n_x}$, $\boldsymbol{B} \in \mathbb{R}^{n_x \times n_u}$, $\boldsymbol{H} \in \mathbb{R}^{n_y \times n_x}$ and $\boldsymbol{D} \in \mathbb{R}^{n_y \times n_u}$. The subscript k denotes the instant time kT_s, where T_s is the system's sampling time.

3.1.2 Controllability and observability

Two important concepts on linear dynamic systems are *controllability* and *observability*. Controllability is often a sufficient condition for the existence of solutions in control design problems, whereas observability is often a sufficient condition for state estimation problems. These concepts are defined below for discrete-time linear systems (Chen, 1999).

Definition 3.1. (Controllability) The discrete-time system (3.1) or the pair $(\boldsymbol{A}, \boldsymbol{B})$ is said to be *controllable* if for any initial state $\boldsymbol{x}_0$ and any final state $\boldsymbol{x}_{\bar{k}}$, there exists an input sequence of finite length that transfers $\boldsymbol{x}_0$ to $\boldsymbol{x}_{\bar{k}}$.

Definition 3.2. (Observability) The discrete-time system (3.1) or the pair $(\boldsymbol{A}, \boldsymbol{H})$ is said to be *observable* if for any unknown initial state $\boldsymbol{x}_0$, there is a finite integer $\bar{k} > 0$ such that

the knowledge of the input sequence $\boldsymbol{u}_k$ and output sequence $\boldsymbol{y}_k$ from $k = 0$ to $\bar{k}$ suffices to determine uniquely the initial state $\boldsymbol{x}_0$.

In order to analyze if a discrete-time linear system is either controllable or observable, the following theorems can be applied (Chen, 1999).

Theorem 3.1. *The discrete-time linear system* (3.1) *or the pair* $(\boldsymbol{A}, \boldsymbol{B})$ *is controllable if, and only if,*

$$rank\left\{\begin{bmatrix}\boldsymbol{B} & \boldsymbol{AB} & \boldsymbol{A}^2\boldsymbol{B} & \cdots \boldsymbol{A}^{n_x-1}\boldsymbol{B}\end{bmatrix}\right\} = n_x.$$

Theorem 3.2. *The discrete-time linear system* (3.1) *or the pair* $(\boldsymbol{A}, \boldsymbol{H})$ *is observable if, and only if,*

$$rank\left\{\begin{bmatrix}\boldsymbol{H} \\ \boldsymbol{HA} \\ \boldsymbol{HA}^2 \\ \vdots \\ \boldsymbol{HA}^{n_x-1}\end{bmatrix}\right\} = n_x.$$

3.1.3 Lyapunov stability for discrete-time linear systems

Stability analysis of dynamic systems is also an important subject. The discrete-time linear system (3.1) is *asymptotically stable* (in the sense of Lyapunov) if there exists a scalar function $V(\boldsymbol{x}_k) : \mathbb{R}^{n_x} \mapsto \mathbb{R}$ such that

- $V(\boldsymbol{x}_k) > 0 \ \forall \boldsymbol{x}_k \neq \boldsymbol{0}$ and $V(\boldsymbol{0}) = 0$;
- $\Delta V(\boldsymbol{x}_k) \triangleq V(\boldsymbol{x}_{k+1}) - V(\boldsymbol{x}_k) < 0 \ \forall \boldsymbol{x}_k \neq \boldsymbol{0}$ and $\Delta V(\boldsymbol{0}) = 0$.

It is common to choose the quadratic function $V(\boldsymbol{x}_k) = \boldsymbol{x}_k^T \boldsymbol{P} \boldsymbol{x}_k$ for stability analysis of linear time invariant systems (Slotine, 1991, p. 80). For this function, assuming that $\boldsymbol{u}_k = \boldsymbol{0}$ (open-loop system), we have that

$$\Delta V(\boldsymbol{x}_k) = \boldsymbol{x}_{k+1}^T \boldsymbol{P} \boldsymbol{x}_{k+1} - \boldsymbol{x}_k^T \boldsymbol{P} \boldsymbol{x}_k = \boldsymbol{x}_k^T \boldsymbol{A}^T \boldsymbol{P} \boldsymbol{A} \boldsymbol{x}_k - \boldsymbol{x}_k^T \boldsymbol{P} \boldsymbol{x}_k = \boldsymbol{x}_k^T (\boldsymbol{A}^T \boldsymbol{P} \boldsymbol{A} - \boldsymbol{P}) \boldsymbol{x}_k.$$

Hence, considering the two mentioned conditions, the stability analysis for the discrete-time linear system (3.1) turns into verifying if there exists a symmetric matrix $\boldsymbol{P}$ that simultaneously satisfies[1]

$$\boldsymbol{P} > 0, \tag{3.2}$$

$$\boldsymbol{A}^T \boldsymbol{P} \boldsymbol{A} - \boldsymbol{P} < 0. \tag{3.3}$$

Equivalently, system (3.1) is asymptotically stable if, and only if, all the eigenvalues of $\boldsymbol{A}$ are inside the unitary circle in the complex plane (Chen, 1999).

[1] In this work, $\boldsymbol{P} > 0$ means that $\boldsymbol{P}$ is positive definite, $\boldsymbol{P} < 0$ means that $-\boldsymbol{P}$ is positive definite, and $\boldsymbol{P}_1 > \boldsymbol{P}_2$ means that $\boldsymbol{P}_1 - \boldsymbol{P}_2$ is positive definite.

3.1.4 Linear matrix inequalities

Several control design problems can be formulated in terms of optimization problems with linear matrix inequality (LMI) constraints. An LMI is an inequality that can be written in the form (Boyd et al., 1994)

$$\boldsymbol{F}(\boldsymbol{m}) \triangleq \boldsymbol{F}_0 + \sum_{i=1}^{p} m_i \boldsymbol{F}_i > 0,$$

where $\boldsymbol{m} \in \mathbb{R}^p$ are the decision variables, and $\boldsymbol{F}_i \in \mathbb{R}^{q \times q}$, $i \in \{1, 2, \ldots, p\}$ are given symmetric matrices. The Lyapunov stability conditions (3.2) and (3.3) are examples of LMIs, where the elements of $\boldsymbol{P}$ correspond to the decision variables.

Working with LMIs have some advantages. For instance, the associated optimization problems are convex, and thus can be solved efficiently. Furthermore, several constraints can be incorporated into a single problem, allowing multi-criteria control design to be handled easily (Boyd et al., 1994).

3.1.5 Schur complement and congruence transformations

Control design problems often leads to inequalities that are nonlinear in the decision variables. The Schur complement is a useful tool that can be used for transforming a nonlinear matrix inequality into an LMI one.

Let $\boldsymbol{N}_1(\boldsymbol{m}) = \boldsymbol{N}_1(\boldsymbol{m})^T$, $\boldsymbol{N}_2(\boldsymbol{m}) = \boldsymbol{N}_2(\boldsymbol{m})^T$ and $\boldsymbol{N}_3(\boldsymbol{m})$ be affine functions of decision variables $\boldsymbol{m}$. Then, the Schur complement lemma states that the following inequalities are equivalent (Boyd et al., 1994):

a) $\boldsymbol{N}_1(\boldsymbol{m}) - \boldsymbol{N}_3(\boldsymbol{m})^T \boldsymbol{N}_2(\boldsymbol{m})^{-1} \boldsymbol{N}_3(\boldsymbol{m}) > 0$, with $\boldsymbol{N}_2(\boldsymbol{m}) > 0$;

b) $\begin{bmatrix} \boldsymbol{N}_1(\boldsymbol{m}) & \boldsymbol{N}_3(\boldsymbol{m})^T \\ \boldsymbol{N}_3(\boldsymbol{m}) & \boldsymbol{N}_2(\boldsymbol{m}) \end{bmatrix} > 0.$

Congruence transformations consist in another useful tool for the same purposes. Let $\boldsymbol{N} > 0$, then, for any invertible $\boldsymbol{T}$, we have that $\boldsymbol{T}^T \boldsymbol{N} \boldsymbol{T} > 0$ (Trofino et al., 2015, p. 30).

3.2 Linearized error dynamics

The tilt-rotor UAV with suspended load is a mechanical system with more degrees of freedom than control inputs, therefore being characterized as an underactuated mechanical system. As it has four control inputs, only up to four degrees of freedom can be steered along a desired, arbitrary trajectory, while the remaining DOF can only be stabilized. Aiming path tracking control of the suspended load, the position $\boldsymbol{\xi} = [x\ y\ z]^T$ and yaw angle ψ of the load are chosen to be regulated.

To design linear control strategies for path tracking of the suspended load, the system's state-space equations are linearized around a time-varying trajectory. Then, before proceeding, some facts on (2.57) must be pointed out. It is possible to verify that[2] the inertia matrix (2.29) and the mapping matrix (2.50) are not functions of $\boldsymbol{\xi}$, and also that the Coriolis matrix obtained using (2.30) is neither a function of $\boldsymbol{\xi}$ nor of $\dot{\boldsymbol{\xi}}$. Moreover, assuming that the gravitational acceleration vector is constant, the gravitational forces vector (2.33) is also not a function of $\boldsymbol{\xi}$. Thus, by defining the auxiliary variable $\boldsymbol{\zeta} \triangleq [\boldsymbol{\eta}^T \ \boldsymbol{\gamma}^T \ \alpha_{\mathrm{R}} \ \alpha_{\mathrm{L}}]^T \in \mathbb{R}^7$, we have that

$$\boldsymbol{M} \triangleq \boldsymbol{M}(\boldsymbol{\zeta}), \quad \boldsymbol{C} \triangleq \boldsymbol{C}(\boldsymbol{\zeta}, \dot{\boldsymbol{\zeta}}), \quad \boldsymbol{g} \triangleq \boldsymbol{g}(\boldsymbol{\zeta}), \quad \boldsymbol{L}_{\mathrm{in}} \triangleq \boldsymbol{L}_{\mathrm{in}}(\boldsymbol{\zeta}).$$

Let $\boldsymbol{x}^{\mathrm{tr}}(t)$, $\boldsymbol{u}^{\mathrm{tr}}(t)$ and $\boldsymbol{d}^{\mathrm{tr}}(t)$ denote trajectory values for $\boldsymbol{x}$, $\boldsymbol{u}$ and $\boldsymbol{d}$, respectively. This work assumes that the desired trajectory is feasible, i.e.,

$$\dot{\boldsymbol{x}}^{\mathrm{tr}} = \boldsymbol{\varphi}(\boldsymbol{x}^{\mathrm{tr}}, \boldsymbol{u}^{\mathrm{tr}}, \boldsymbol{d}^{\mathrm{tr}}).$$

Then, linearizing the state-space equations (2.57) around these variables, through first-order expansion in Taylor series, yields

$$\delta\dot{\boldsymbol{x}} = \boldsymbol{A}_{\mathrm{c}}(t)\delta\boldsymbol{x} + \boldsymbol{B}_{\mathrm{c}}(t)\delta\boldsymbol{u} + \boldsymbol{F}_{\mathrm{c}}(t)\delta\boldsymbol{d}, \tag{3.4}$$

where the subscript 'c' denotes continuous-time, and $\delta\boldsymbol{x} \triangleq \boldsymbol{x} - \boldsymbol{x}^{\mathrm{tr}}$, $\delta\boldsymbol{u} \triangleq \boldsymbol{u} - \boldsymbol{u}^{\mathrm{tr}}$, $\delta\boldsymbol{d} \triangleq \boldsymbol{d} - \boldsymbol{d}^{\mathrm{tr}}$,

$$\begin{aligned}
\boldsymbol{A}_{\mathrm{c}}(t) &= \left.\frac{\partial\boldsymbol{\varphi}(\boldsymbol{x},\boldsymbol{u},\boldsymbol{d})}{\partial\boldsymbol{x}}\right|_{\substack{\boldsymbol{x}=\boldsymbol{x}^{\mathrm{tr}}(t)\\ \boldsymbol{u}=\boldsymbol{u}^{\mathrm{tr}}(t)\\ \boldsymbol{d}=\boldsymbol{d}^{\mathrm{tr}}(t)}} = \left[\begin{array}{c|c} \boldsymbol{0}_{10\times10} & \mathbb{I}_{10\times10} \\ \hline \bar{\boldsymbol{A}}_{\mathrm{c}}(\boldsymbol{\zeta}^{\mathrm{tr}}(t), \dot{\boldsymbol{\zeta}}^{\mathrm{tr}}(t), \boldsymbol{u}^{\mathrm{tr}}(t), \boldsymbol{d}^{\mathrm{tr}}(t)) \end{array}\right] \in \mathbb{R}^{20\times20}, \\
\boldsymbol{B}_{\mathrm{c}}(t) &= \left.\frac{\partial\boldsymbol{\varphi}(\boldsymbol{x},\boldsymbol{u},\boldsymbol{d})}{\partial\boldsymbol{u}}\right|_{\substack{\boldsymbol{x}=\boldsymbol{x}^{\mathrm{tr}}(t)\\ \boldsymbol{u}=\boldsymbol{u}^{\mathrm{tr}}(t)\\ \boldsymbol{d}=\boldsymbol{d}^{\mathrm{tr}}(t)}} = \begin{bmatrix} \boldsymbol{0}_{10\times4} \\ \boldsymbol{M}(\boldsymbol{\zeta}^{\mathrm{tr}}(t))^{-1}\boldsymbol{L}_{\mathrm{in}}(\boldsymbol{\zeta}^{\mathrm{tr}}(t)) \end{bmatrix} \in \mathbb{R}^{20\times4}, \\
\boldsymbol{F}_{\mathrm{c}}(t) &= \left.\frac{\partial\boldsymbol{\varphi}(\boldsymbol{x},\boldsymbol{u},\boldsymbol{d})}{\partial\boldsymbol{d}}\right|_{\substack{\boldsymbol{x}=\boldsymbol{x}^{\mathrm{tr}}(t)\\ \boldsymbol{u}=\boldsymbol{u}^{\mathrm{tr}}(t)\\ \boldsymbol{d}=\boldsymbol{d}^{\mathrm{tr}}(t)}} = \begin{bmatrix} \boldsymbol{0}_{10\times3} \\ \boldsymbol{M}(\boldsymbol{\zeta}^{\mathrm{tr}}(t))^{-1}\boldsymbol{L}_{\mathrm{db}} \end{bmatrix} \in \mathbb{R}^{20\times3}.
\end{aligned} \tag{3.5}$$

Now, define $\boldsymbol{\zeta}^{\mathrm{tr}}(t) \triangleq [\phi^{\mathrm{eq}} \ \ \theta^{\mathrm{eq}} \ \ \psi^{\mathrm{tr}}(t) \ \ (\boldsymbol{\gamma}^{\mathrm{eq}})^T \ \ \alpha_{\mathrm{R}}^{\mathrm{eq}} \ \ \alpha_{\mathrm{L}}^{\mathrm{eq}}]^T$. Assuming that for the desired trajectory ψ^{tr} is constant, we have that $\boldsymbol{\zeta}^{\mathrm{tr}}$ is also constant. Then, $\dot{\boldsymbol{\zeta}}^{\mathrm{tr}} = \boldsymbol{0}_{7\times1}$, and by defining $\boldsymbol{q}^{\mathrm{tr}} \triangleq [(\boldsymbol{\xi}^{\mathrm{tr}})^T \ \ (\boldsymbol{\zeta}^{\mathrm{tr}})^T]^T$, we also have that $\dot{\boldsymbol{q}}^{\mathrm{tr}} = [(\dot{\boldsymbol{\xi}}^{\mathrm{tr}})^T \ \ \boldsymbol{0}_{1\times7}]^T$ and $\ddot{\boldsymbol{q}}^{\mathrm{tr}} = [(\ddot{\boldsymbol{\xi}}^{\mathrm{tr}})^T \ \ \boldsymbol{0}_{1\times7}]^T$. Moreover, define $\boldsymbol{x}^{\mathrm{tr}} \triangleq [(\boldsymbol{q}^{\mathrm{tr}})^T \ \ (\dot{\boldsymbol{q}}^{\mathrm{tr}})^T]^T$ and $\boldsymbol{u}^{\mathrm{tr}} \triangleq [f_{\mathrm{R}}^{\mathrm{tr}} \ \ f_{\mathrm{L}}^{\mathrm{tr}} \ \ \tau_{\alpha_{\mathrm{R}}}^{\mathrm{tr}} \ \ \tau_{\alpha_{\mathrm{L}}}^{\mathrm{tr}}]^T$. Evaluating the linearized state-space equations (3.4) at $\boldsymbol{x}^{\mathrm{tr}}$ and $\boldsymbol{u}^{\mathrm{tr}}$, and considering a scenario without external

[2] Through a symbolic computation software, such as MATLAB's Symbolic Toolbox. In fact, since the gravitational acceleration vector is assumed to be constant, and effects due to aerodynamic forces and air friction are being neglected, it is expected that the system dynamics are independent of its position and velocity with respect to the inertial frame.

disturbances (i.e., $\boldsymbol{d}^{\text{tr}} = \mathbf{0}_{3\times1}$), leads to the error dynamics

$$\delta\dot{\boldsymbol{x}} = \boldsymbol{A}_{\text{c}}(t)\delta\boldsymbol{x} + \boldsymbol{B}_{\text{c}}\delta\boldsymbol{u} + \boldsymbol{F}_{\text{c}}\boldsymbol{d}, \tag{3.6}$$

in which, since $\boldsymbol{\zeta}^{\text{tr}}$ is constant, $\dot{\boldsymbol{\zeta}}^{\text{tr}} = \mathbf{0}_{7\times1}$ and $\boldsymbol{d}^{\text{tr}} = \mathbf{0}_{3\times1}$, $\boldsymbol{A}_{\text{c}}(t)$ is time-varying only due to $\boldsymbol{u}^{\text{tr}}(t)$ (see equation (3.5)), and $\boldsymbol{B}_{\text{c}}$ and $\boldsymbol{F}_{\text{c}}$ are constant matrices.

In order to improve the trajectory tracking and provide constant disturbance rejection by the controllers to be designed, the state vector $\delta\boldsymbol{x}$ is augmented with integral actions, computed by integrating the error of the regulated degrees of freedom, yielding

$$\boldsymbol{\chi} \triangleq \begin{bmatrix} \delta\boldsymbol{x} \\ \int(\boldsymbol{\xi} - \boldsymbol{\xi}^{\text{tr}}) \\ \int(\psi - \psi^{\text{tr}}) \end{bmatrix} \in \mathbb{R}^{24}, \tag{3.7}$$

whose dynamics are given by

$$\dot{\boldsymbol{\chi}} = \left[\begin{array}{cccccc|c|c} \multicolumn{6}{c|}{\boldsymbol{A}_{\text{c}}(t)} & & \mathbf{0}_{20\times4} \\ \hline 1 & 0 & 0 & 0 & 0 & 0 & & \\ 0 & 1 & 0 & 0 & 0 & 0 & \mathbf{0}_{4\times14} & \mathbf{0}_{4\times4} \\ 0 & 0 & 1 & 0 & 0 & 0 & & \\ 0 & 0 & 0 & 0 & 0 & 1 & & \end{array}\right] \boldsymbol{\chi} + \begin{bmatrix} \boldsymbol{B}_{\text{c}} \\ \mathbf{0}_{4\times4} \end{bmatrix} \delta\boldsymbol{u} + \begin{bmatrix} \boldsymbol{F}_{\text{c}} \\ \mathbf{0}_{4\times3} \end{bmatrix} \boldsymbol{d}. \tag{3.8}$$

3.3 Discrete-time linear quadratic regulator

In this section, to test the concept of the load's perspective model, a discrete-time linear quadratic regulator is proposed for path tracking of the suspended load with stabilization of the tilt-rotor UAV, with constant disturbances rejection.

In order to design a discrete-time linear quadratic regulator for path tracking of the suspended load, it is assumed that the desired trajectory requires low accelerations to be performed, i.e., $\ddot{\boldsymbol{q}}^{\text{tr}} \approx \mathbf{0}_{10\times1}$, being the associated control signals close to equilibrium values. Therefore, $\boldsymbol{A}_{\text{c}}(t) \approx \boldsymbol{A}_{\text{c}}(t)|_{\boldsymbol{u}^{\text{tr}}=\boldsymbol{u}^{\text{eq}}} \triangleq \boldsymbol{A}_{\text{c}}$, which is a constant matrix[3]. Resulting effects from this approximation will be considered as unmodeled dynamics, and the controller will be assumed to be robust enough to deal with the subsequent error.

By applying the zero-order-holder (ZOH) discretization method (Chen, 1999) over (3.8), for a sampling time T_c (henceforth called the *controller sampling time*), yields the discrete-time, augmented error dynamics

$$\boldsymbol{\chi}_{k+1} = \boldsymbol{A}_{\boldsymbol{\chi}}\boldsymbol{\chi}_k + \boldsymbol{B}_{\boldsymbol{\chi}}\delta\boldsymbol{u}_k + \boldsymbol{F}_{\boldsymbol{\chi}}\boldsymbol{d}_k, \tag{3.9}$$

[3]Due to limited computational resources, an analytical expression for $\boldsymbol{M}(\boldsymbol{q})^{-1}$ could not be obtained in (2.57), hence neither an expression for $\boldsymbol{\varphi}(\boldsymbol{x}, \boldsymbol{u}, \boldsymbol{d})$. Therefore, an analytical expression for the time-varying matrix $\boldsymbol{A}_{\text{c}}(t)$ could not be computed either.

in which $\cdot_k \triangleq \cdot(kt)$ and $\cdot_{k+1} \triangleq \cdot(kt + T_c)$, with $\boldsymbol{A}_{\boldsymbol{\chi}} \in \mathbb{R}^{24\times24}$, $\boldsymbol{B}_{\boldsymbol{\chi}} \in \mathbb{R}^{24\times4}$ and $\boldsymbol{F}_{\boldsymbol{\chi}} \in \mathbb{R}^{24\times3}$.

A state-feedback, discrete-time linear quadratic regulator for (3.9) is an optimal controller that minimizes the quadratic cost functional with infinite time horizon

$$J_{\text{DLQR}} = \sum_{k=0}^{\infty} \boldsymbol{\chi}_k^T \boldsymbol{\Omega}_{\boldsymbol{\chi}} \boldsymbol{\chi}_k + \delta\boldsymbol{u}_k^T \boldsymbol{\Omega}_{\boldsymbol{u}} \delta\boldsymbol{u}_k, \tag{3.10}$$

where $\boldsymbol{\Omega}_{\boldsymbol{\chi}} \in \mathbb{R}^{24\times24}$ is a symmetric, positive semi-definite matrix, and $\boldsymbol{\Omega}_{\boldsymbol{u}} \in \mathbb{R}^{4\times4}$ is a symmetric, positive definite matrix. This cost functional is a measure of the energy of the state vector $\boldsymbol{\chi}_k$ and the control signals $\delta\boldsymbol{u}_k$, weighted by the matrices $\boldsymbol{\Omega}_{\boldsymbol{\chi}}$ and $\boldsymbol{\Omega}_{\boldsymbol{u}}$.

This work derives the solution to this optimal control problem analogously to the procedure used in Donadel et al. (2014) and Donadel (2015) for a continuous-time linear quadratic regulator. A deeper treatment can be found in, e.g., Dorato & Levis (1971) and Phillips & Nagle (1995).

Consider the Lyapunov function candidate $V(\boldsymbol{\chi}_k) = \boldsymbol{\chi}_k^T \boldsymbol{P} \boldsymbol{\chi}_k$, with $\boldsymbol{P} > 0$. Then,

$$\Delta V(\boldsymbol{\chi}_k) \triangleq V(\boldsymbol{\chi}_{k+1}) - V(\boldsymbol{\chi}_k) = \boldsymbol{\chi}_{k+1}^T \boldsymbol{P} \boldsymbol{\chi}_{k+1} - \boldsymbol{\chi}_k^T \boldsymbol{P} \boldsymbol{\chi}_k. \tag{3.11}$$

Substituting (3.9) in (3.11), and assuming $\boldsymbol{d}_k = \boldsymbol{0}_{3\times1}$, yields

$$\begin{aligned}\Delta V(\boldsymbol{\chi}_k) &= (\boldsymbol{A}_{\boldsymbol{\chi}}\boldsymbol{\chi}_k + \boldsymbol{B}_{\boldsymbol{\chi}}\delta\boldsymbol{u}_k)^T \boldsymbol{P}(\boldsymbol{A}_{\boldsymbol{\chi}}\boldsymbol{\chi}_k + \boldsymbol{B}_{\boldsymbol{\chi}}\delta\boldsymbol{u}_k) - \boldsymbol{\chi}_k^T \boldsymbol{P} \boldsymbol{\chi}_k \\ &= \boldsymbol{\chi}_k^T (\boldsymbol{A}_{\boldsymbol{\chi}}^T \boldsymbol{P} \boldsymbol{A}_{\boldsymbol{\chi}} - \boldsymbol{P})\boldsymbol{\chi}_k + \boldsymbol{\chi}_k^T \boldsymbol{A}_{\boldsymbol{\chi}}^T \boldsymbol{P} \boldsymbol{B}_{\boldsymbol{\chi}} \delta\boldsymbol{u}_k + \delta\boldsymbol{u}_k^T \boldsymbol{B}_{\boldsymbol{\chi}}^T \boldsymbol{P} \boldsymbol{A}_{\boldsymbol{\chi}} \boldsymbol{\chi}_k + \delta\boldsymbol{u}_k^T \boldsymbol{B}_{\boldsymbol{\chi}}^T \boldsymbol{P} \boldsymbol{B}_{\boldsymbol{\chi}} \delta\boldsymbol{u}_k.\end{aligned}$$

Considering the state-feedback control law $\delta\boldsymbol{u}_k = -\boldsymbol{K}\boldsymbol{\chi}_k$, we have that

$$\Delta V(\boldsymbol{\chi}_k) = \boldsymbol{\chi}_k^T (\boldsymbol{A}_{\boldsymbol{\chi}}^T \boldsymbol{P} \boldsymbol{A}_{\boldsymbol{\chi}} - \boldsymbol{P} - \boldsymbol{A}_{\boldsymbol{\chi}}^T \boldsymbol{P} \boldsymbol{B}_{\boldsymbol{\chi}} \boldsymbol{K} - \boldsymbol{K}^T \boldsymbol{B}_{\boldsymbol{\chi}}^T \boldsymbol{P} \boldsymbol{A}_{\boldsymbol{\chi}} + \boldsymbol{K}^T \boldsymbol{B}_{\boldsymbol{\chi}}^T \boldsymbol{P} \boldsymbol{B}_{\boldsymbol{\chi}} \boldsymbol{K}) \boldsymbol{\chi}_k. \tag{3.12}$$

Assuming that $\delta\boldsymbol{u}_k = -\boldsymbol{K}\boldsymbol{\chi}_k$ stabilizes the system (3.9) asymptotically, we have that $\Delta V(\boldsymbol{\chi}_k) < 0$ for all $k > 0$. Then, $\lim_{k\to\infty} V(\boldsymbol{\chi}_k) = 0$ and

$$\sum_{k=0}^{\infty} \Delta V(\boldsymbol{\chi}_k) = \lim_{k\to\infty} V(\boldsymbol{\chi}_k) - V(\boldsymbol{\chi}_0) = 0 - \boldsymbol{\chi}_0^T \boldsymbol{P} \boldsymbol{\chi}_0 = -\boldsymbol{\chi}_0^T \boldsymbol{P} \boldsymbol{\chi}_0. \tag{3.13}$$

Substituting (3.12) in (3.13) yields

$$\begin{aligned}&\sum_{k=0}^{\infty} \boldsymbol{\chi}_k^T (\boldsymbol{A}_{\boldsymbol{\chi}}^T \boldsymbol{P} \boldsymbol{A}_{\boldsymbol{\chi}} - \boldsymbol{P} - \boldsymbol{A}_{\boldsymbol{\chi}}^T \boldsymbol{P} \boldsymbol{B}_{\boldsymbol{\chi}} \boldsymbol{K} - \boldsymbol{K}^T \boldsymbol{B}_{\boldsymbol{\chi}}^T \boldsymbol{P} \boldsymbol{A}_{\boldsymbol{\chi}} + \boldsymbol{K}^T \boldsymbol{B}_{\boldsymbol{\chi}}^T \boldsymbol{P} \boldsymbol{B}_{\boldsymbol{\chi}} \boldsymbol{K}) \boldsymbol{\chi}_k = -\boldsymbol{\chi}_0^T \boldsymbol{P} \boldsymbol{\chi}_0 \\ \implies &\sum_{k=0}^{\infty} \boldsymbol{\chi}_k^T (\boldsymbol{A}_{\boldsymbol{\chi}}^T \boldsymbol{P} \boldsymbol{A}_{\boldsymbol{\chi}} - \boldsymbol{P} - \boldsymbol{A}_{\boldsymbol{\chi}}^T \boldsymbol{P} \boldsymbol{B}_{\boldsymbol{\chi}} \boldsymbol{K} - \boldsymbol{K}^T \boldsymbol{B}_{\boldsymbol{\chi}}^T \boldsymbol{P} \boldsymbol{A}_{\boldsymbol{\chi}} + \boldsymbol{K}^T \boldsymbol{B}_{\boldsymbol{\chi}}^T \boldsymbol{P} \boldsymbol{B}_{\boldsymbol{\chi}} \boldsymbol{K}) \boldsymbol{\chi}_k + \boldsymbol{\chi}_0^T \boldsymbol{P} \boldsymbol{\chi}_0 = 0.\end{aligned} \tag{3.14}$$

Adding (3.14) to the cost functional (3.10) results in

$$J = \sum_{k=0}^{\infty} \boldsymbol{\chi}_k^T (\boldsymbol{A}_{\boldsymbol{\chi}}^T \boldsymbol{P} \boldsymbol{A}_{\boldsymbol{\chi}} - \boldsymbol{P} - \boldsymbol{A}_{\boldsymbol{\chi}}^T \boldsymbol{P} \boldsymbol{B}_{\boldsymbol{\chi}} \boldsymbol{K} - \boldsymbol{K}^T \boldsymbol{B}_{\boldsymbol{\chi}}^T \boldsymbol{P} \boldsymbol{A}_{\boldsymbol{\chi}} + \boldsymbol{K}^T \boldsymbol{B}_{\boldsymbol{\chi}}^T \boldsymbol{P} \boldsymbol{B}_{\boldsymbol{\chi}} \boldsymbol{K} + \boldsymbol{\Omega}_{\boldsymbol{\chi}} + \boldsymbol{K}^T \boldsymbol{\Omega}_{\boldsymbol{u}} \boldsymbol{K}^T) \boldsymbol{\chi}_k + \boldsymbol{\chi}_0^T \boldsymbol{P} \boldsymbol{\chi}_0,$$

whose minimum $\boldsymbol{\chi}_0^T \boldsymbol{P} \boldsymbol{\chi}_0$ is found by making

$$\boldsymbol{A}_{\boldsymbol{\chi}}^T \boldsymbol{P} \boldsymbol{A}_{\boldsymbol{\chi}} - \boldsymbol{P} - \boldsymbol{A}_{\boldsymbol{\chi}}^T \boldsymbol{P} \boldsymbol{B}_{\boldsymbol{\chi}} \boldsymbol{K} - \boldsymbol{K}^T \boldsymbol{B}_{\boldsymbol{\chi}}^T \boldsymbol{P} \boldsymbol{A}_{\boldsymbol{\chi}} + \boldsymbol{K}^T \boldsymbol{B}_{\boldsymbol{\chi}}^T \boldsymbol{P} \boldsymbol{B}_{\boldsymbol{\chi}} \boldsymbol{K} = -\boldsymbol{\Omega}_{\boldsymbol{\chi}} - \boldsymbol{K}^T \boldsymbol{\Omega}_{\boldsymbol{u}} \boldsymbol{K}. \tag{3.15}$$

Then, choosing the gain matrix as

$$\boldsymbol{K} = (\boldsymbol{B}_{\boldsymbol{\chi}}^T \boldsymbol{P} \boldsymbol{B}_{\boldsymbol{\chi}} + \boldsymbol{\Omega}_{\boldsymbol{u}})^{-1} \boldsymbol{B}_{\boldsymbol{\chi}}^T \boldsymbol{P} \boldsymbol{A}_{\boldsymbol{\chi}}, \tag{3.16}$$

equation (3.15) becomes the algebraic Riccati equation

$$\boldsymbol{P} = \boldsymbol{A}_{\boldsymbol{\chi}}^T \boldsymbol{P} \boldsymbol{A}_{\boldsymbol{\chi}} + \boldsymbol{\Omega}_{\boldsymbol{\chi}} - \boldsymbol{A}_{\boldsymbol{\chi}}^T \boldsymbol{P} \boldsymbol{B}_{\boldsymbol{\chi}} (\boldsymbol{B}_{\boldsymbol{\chi}}^T \boldsymbol{P} \boldsymbol{B}_{\boldsymbol{\chi}} + \boldsymbol{\Omega}_{\boldsymbol{u}})^{-1} \boldsymbol{B}_{\boldsymbol{\chi}}^T \boldsymbol{P} \boldsymbol{A}_{\boldsymbol{\chi}}. \tag{3.17}$$

Therefore, the discrete-time linear quadratic regulator for (3.9) consists in the state-feedback control law $\delta \boldsymbol{u}_k = -\boldsymbol{K} \boldsymbol{\chi}_k$, whose gain matrix $\boldsymbol{K} \in \mathbb{R}^{4 \times 24}$ is given by (3.16), in which $\boldsymbol{P} \in \mathbb{R}^{24 \times 24}$ is obtained by solving (3.17). It is important to mention that a sufficient condition for such solution to exist is that system (3.9) to be controllable (Dorato & Levis, 1971). Moreover, since $\boldsymbol{\Omega}_{\boldsymbol{\chi}}$, $\boldsymbol{\Omega}_{\boldsymbol{u}} > 0$, it is possible to show that, by substituting (3.15) in (3.12), $\Delta \boldsymbol{V}(\boldsymbol{\chi}_k) < 0 \ \forall \boldsymbol{\chi}_k \neq \boldsymbol{0}_{24 \times 1}$, hence the closed loop system is asymptotically stable. The design of the controller then lies in the appropriate choice of the weighting matrices $\boldsymbol{\Omega}_{\boldsymbol{\chi}}$ and $\boldsymbol{\Omega}_{\boldsymbol{u}}$, through some criteria, such as the Bryson's rule (Johnson & Grimble, 1987).

Furthermore, since the control signals provided by the DLQR are associated with the linearized dynamics (3.9), in order to apply the control signals to the tilt-rotor UAV with suspended load, the feed-forward term

$$\boldsymbol{u}_k^{\text{tr}} = \boldsymbol{L}_{\text{in}}(\boldsymbol{q}_k^{\text{tr}})^+ \left[\boldsymbol{M}(\boldsymbol{q}_k^{\text{tr}}) \ddot{\boldsymbol{q}}_k^{\text{tr}} + (\boldsymbol{C}(\boldsymbol{q}_k^{\text{tr}}, \dot{\boldsymbol{q}}_k^{\text{tr}}) + \boldsymbol{L}_{\text{fr}}) \dot{\boldsymbol{q}}_k^{\text{tr}} + \boldsymbol{g}(\boldsymbol{q}_k^{\text{tr}}) \right] \tag{3.18}$$

is introduced, where $\boldsymbol{L}_{\text{in}}(\boldsymbol{q}_k^{\text{tr}})^+$ denotes the left pseudo-inverse of $\boldsymbol{L}_{\text{in}}(\boldsymbol{q}_k^{\text{tr}})$, and $\boldsymbol{q}_k^{\text{tr}}$, $\dot{\boldsymbol{q}}_k^{\text{tr}}$ and $\ddot{\boldsymbol{q}}_k^{\text{tr}}$ are provided reference signals at instant k. The complete control law is then given by $\boldsymbol{u}_k = \boldsymbol{u}_k^{\text{tr}} + \delta \boldsymbol{u}_k = \boldsymbol{L}_{\text{in}}(\boldsymbol{q}_k^{\text{tr}})^+ \left[\boldsymbol{M}(\boldsymbol{q}_k^{\text{tr}}) \ddot{\boldsymbol{q}}_k^{\text{tr}} + (\boldsymbol{C}(\boldsymbol{q}_k^{\text{tr}}, \dot{\boldsymbol{q}}_k^{\text{tr}}) + \boldsymbol{L}_{\text{fr}}) \dot{\boldsymbol{q}}_k^{\text{tr}} + \boldsymbol{g}(\boldsymbol{q}_k^{\text{tr}}) \right] - \boldsymbol{K} \boldsymbol{\chi}_k$.

Notice that, since $\boldsymbol{u}_k^{\text{tr}}$ is computed using a left pseudo-inverse, it is an exact solution to the dynamic equations (2.55) only if the desired trajectory is feasible. Moreover, equation (3.18) assumes a scenario without disturbances, and the control signal $\boldsymbol{u}_k^{\text{tr}}$ will be sustained for T_c seconds. The subsequent errors are also considered as unmodeled dynamics, and the DLQR is assumed to be robust enough to deal with these effects.

3.4 Discrete-time mixed $\mathcal{H}_2/\mathcal{H}_\infty$ control

In this section, the discrete-time, augmented error dynamics (3.9), obtained for the design of the DLQR in the previous section, is also considered for control design purposes. A discrete-time, linear mixed $\mathcal{H}_2/\mathcal{H}_\infty$ controller with pole placement constraints is designed for path tracking of the suspended load with stabilization of the tilt-rotor UAV, featuring constant disturbances rejection. Instead of only minimizing the energy of the tracking error and control signals, the controller is designed for improved transient response and compensation of unmodelled dynamics and external disturbances, while guaranteeing settling time requirements for the closed-loop system.

The discrete-time, linear $\mathcal{H}_2$ and $\mathcal{H}_\infty$ control design problems are first presented separately, followed by the pole placement constraints technique. The design is performed following an LMI approach.

3.4.1 Discrete-time state-feedback $\mathcal{H}_2$ control

Consider the discrete-time linear system

$$\begin{aligned} \boldsymbol{\chi}_{k+1} &= \boldsymbol{A}_{\boldsymbol{\chi}}\boldsymbol{\chi}_k + \boldsymbol{B}_{\boldsymbol{\chi}}\delta\boldsymbol{u}_k + \boldsymbol{F}_{\boldsymbol{\chi}}\boldsymbol{d}_k, \\ \boldsymbol{z}_k &= \boldsymbol{H}_{\boldsymbol{z}}\boldsymbol{\chi}_k + \boldsymbol{D}_{\boldsymbol{z}}\delta\boldsymbol{u}_k, \end{aligned} \tag{3.19}$$

where $\boldsymbol{z} \in \mathbb{R}^{n_z}$ are cost variables, $\boldsymbol{H}_{\boldsymbol{z}} \in \mathbb{R}^{n_z \times 24}$ and $\boldsymbol{D}_{\boldsymbol{z}} \in \mathbb{R}^{n_z \times 4}$ are design weighting matrices.

Let $\boldsymbol{\Psi}_{\boldsymbol{dz}}(\varsigma)$ denote the discrete-time transfer matrix from $\boldsymbol{d}$ to $\boldsymbol{z}$, with $\varsigma \in \mathbb{C}$. Then, the $\mathcal{H}_2$ norm of the discrete-time linear system (3.19) is defined as

$$\|\boldsymbol{\Psi}_{\boldsymbol{dz}}(\varsigma)\|_2 \triangleq \sqrt{\sum_{k=0}^{\infty} \operatorname{tr}\left\{\boldsymbol{\Psi}_{\boldsymbol{dz},k}\boldsymbol{\Psi}_{\boldsymbol{dz},k}^T\right\}}, \tag{3.20}$$

where $\boldsymbol{\Psi}_{\boldsymbol{dz},k} \triangleq \mathcal{Z}^{-1}\{\boldsymbol{\Psi}_{\boldsymbol{dz}}(\varsigma)\}$ is the impulse response matrix associated with the channel $\boldsymbol{d} \to \boldsymbol{z}$, and $\operatorname{tr}\{\cdot\}$ denotes the trace operator. The $\mathcal{H}_2$ norm can be interpreted as a measure of the energy of the system (3.19) when it is excited by impulse sequences in $\boldsymbol{d}$.

Now, consider the state-feedback control law $\delta\boldsymbol{u}_k = -\boldsymbol{K}\boldsymbol{\chi}_k$. The $\mathcal{H}_2$ control design problem consists in computing the gain matrix $\boldsymbol{K}$ that minimizes the $\mathcal{H}_2$ norm of the closed-loop system[4]

$$\begin{aligned} \boldsymbol{\chi}_{k+1} &= (\boldsymbol{A}_{\boldsymbol{\chi}} - \boldsymbol{B}_{\boldsymbol{\chi}}\boldsymbol{K})\boldsymbol{\chi}_k + \boldsymbol{F}_{\boldsymbol{\chi}}\boldsymbol{d}_k, \\ \boldsymbol{z}_k &= (\boldsymbol{H}_{\boldsymbol{z}} - \boldsymbol{D}_{\boldsymbol{z}}\boldsymbol{K})\boldsymbol{\chi}_k. \end{aligned} \tag{3.21}$$

The solution of this optimal control problem is derived based on the procedure used in Trofino et al. (2015) for the continuous-time linear $\mathcal{H}_2$ control. Applying the $\mathcal{Z}$-transform

[4] The DLQR is a special case of the $\mathcal{H}_2$ control, by choosing $\boldsymbol{H}_{\boldsymbol{z}}$ and $\boldsymbol{D}_{\boldsymbol{z}}$ such that $\boldsymbol{H}_{\boldsymbol{z}}^T\boldsymbol{H}_{\boldsymbol{z}} = \boldsymbol{\Omega}_{\boldsymbol{\chi}}$, $\boldsymbol{D}_{\boldsymbol{z}}^T\boldsymbol{D}_{\boldsymbol{z}} = \boldsymbol{\Omega}_{\boldsymbol{u}}$ and $\boldsymbol{H}_{\boldsymbol{z}}^T\boldsymbol{D}_{\boldsymbol{z}} = \boldsymbol{0}_{24\times 4}$ (Peres & Geromel, 1993). For instance, $\boldsymbol{H}_{\boldsymbol{z}} = [\sqrt{\boldsymbol{\Omega}_{\boldsymbol{\chi}}}\ \ \boldsymbol{0}]^T$ and $\boldsymbol{D}_{\boldsymbol{z}} = [\boldsymbol{0}\ \ \sqrt{\boldsymbol{\Omega}_{\boldsymbol{u}}}]^T$.

to the closed-loop system (3.21) yields the discrete transfer matrix

$$\boldsymbol{\Psi}_{\boldsymbol{dz}}(\varsigma) = (\boldsymbol{H_z} - \boldsymbol{D_z K})(\varsigma \mathbb{I}_{24\times 24} - \boldsymbol{A_\chi} + \boldsymbol{B_\chi K})^{-1}\boldsymbol{F_\chi}.$$

Taking its inverse $\mathcal{Z}$-transform yields

$$\boldsymbol{\Psi}_{\boldsymbol{dz},k} = \mathcal{Z}^{-1}\{\boldsymbol{\Psi}_{\boldsymbol{dz}}(\varsigma)\} = \mathcal{Z}^{-1}\{(\boldsymbol{H_z} - \boldsymbol{D_z K})(\varsigma \mathbb{I}_{24\times 24} - \boldsymbol{A_\chi} + \boldsymbol{B_\chi K})^{-1}\boldsymbol{F_\chi}\} \tag{3.22}$$

$$= (\boldsymbol{H_z} - \boldsymbol{D_z K})(\boldsymbol{A_\chi} - \boldsymbol{B_\chi K})^{k-1}\boldsymbol{F_\chi}. \tag{3.23}$$

Taking the square of (3.20), and substituting (3.23) in the resulting equation yields

$$\begin{aligned}
\|\boldsymbol{\Psi}_{\boldsymbol{dz}}(\varsigma)\|_2^2 &= \sum_{k=0}^{\infty} \mathrm{tr}\left\{(\boldsymbol{H_z} - \boldsymbol{D_z K})(\boldsymbol{A_\chi} - \boldsymbol{B_\chi K})^{k-1}\boldsymbol{F_\chi}\boldsymbol{F_\chi}^T((\boldsymbol{A_\chi} - \boldsymbol{B_\chi K})^{k-1})^T(\boldsymbol{H_z} - \boldsymbol{D_z K})^T\right\} \\
&= \mathrm{tr}\left\{(\boldsymbol{H_z} - \boldsymbol{D_z K})\sum_{k=0}^{\infty}(\boldsymbol{A_\chi} - \boldsymbol{B_\chi K})^{k-1}\boldsymbol{F_\chi}\boldsymbol{F_\chi}^T((\boldsymbol{A_\chi} - \boldsymbol{B_\chi K})^{k-1})^T(\boldsymbol{H_z} - \boldsymbol{D_z K})^T\right\} \\
&= \mathrm{tr}\left\{(\boldsymbol{H_z} - \boldsymbol{D_z K})\boldsymbol{P}_{\mathrm{c}}(\boldsymbol{H_z} - \boldsymbol{D_z K})^T\right\},
\end{aligned}$$

where $\boldsymbol{P}_{\mathrm{c}} \triangleq \sum_{k=0}^{\infty}(\boldsymbol{A_\chi} - \boldsymbol{B_\chi K})^{k-1}\boldsymbol{F_\chi}\boldsymbol{F_\chi}^T((\boldsymbol{A_\chi} - \boldsymbol{B_\chi K})^{k-1})^T$ is the controllability Gramian of the closed loop system (3.21), and if the latter is asymptotically stable, this Gramian is the unique solution to the Lyapunov equation (Chen, 1999)

$$(\boldsymbol{A_\chi} - \boldsymbol{B_\chi K})\boldsymbol{P}_{\mathrm{c}}(\boldsymbol{A_\chi} - \boldsymbol{B_\chi K})^T - \boldsymbol{P}_{\mathrm{c}} + \boldsymbol{F_\chi}\boldsymbol{F_\chi}^T = 0.$$

In order to bring this control design problem to a LMI framework, a positive definite matrix $\boldsymbol{P}_2$ is defined, such that $\boldsymbol{P}_2 > \boldsymbol{P}_{\mathrm{c}}$[5]. Then, we have the inequalities

$$\begin{aligned}
\mathrm{tr}\left\{(\boldsymbol{H_z} - \boldsymbol{D_z K})\boldsymbol{P}_2(\boldsymbol{H_z} - \boldsymbol{D_z K})^T\right\} &> \mathrm{tr}\left\{(\boldsymbol{H_z} - \boldsymbol{D_z K})\boldsymbol{P}_{\mathrm{c}}(\boldsymbol{H_z} - \boldsymbol{D_z K})^T\right\}, \\
(\boldsymbol{A_\chi} - \boldsymbol{B_\chi K})\boldsymbol{P}_2(\boldsymbol{A_\chi} - \boldsymbol{B_\chi K})^T - \boldsymbol{P}_2 + \boldsymbol{F_\chi}\boldsymbol{F_\chi}^T &< 0.
\end{aligned} \tag{3.24}$$

Define also a symmetric matrix $\boldsymbol{N}$, such that $\boldsymbol{N} - (\boldsymbol{H_z} - \boldsymbol{D_z K})\boldsymbol{P}_2(\boldsymbol{H_z} - \boldsymbol{D_z K})^T > 0$. Hence,

$$\mathrm{tr}\{\boldsymbol{N}\} > \mathrm{tr}\left\{(\boldsymbol{H_z} - \boldsymbol{D_z K})\boldsymbol{P}_2(\boldsymbol{H_z} - \boldsymbol{D_z K})^T\right\} > \mathrm{tr}\left\{(\boldsymbol{H_z} - \boldsymbol{D_z K})\boldsymbol{P}_{\mathrm{c}}(\boldsymbol{H_z} - \boldsymbol{D_z K})^T\right\}.$$

As $\|\boldsymbol{\Psi}_{\boldsymbol{dz}}(\varsigma)\|_2^2 = \mathrm{tr}\left\{(\boldsymbol{H_z} - \boldsymbol{D_z K})\boldsymbol{P}_{\mathrm{c}}(\boldsymbol{H_z} - \boldsymbol{D_z K})^T\right\}$, we have that $\mathrm{tr}\{\boldsymbol{N}\} > \|\boldsymbol{\Psi}_{\boldsymbol{dz}}(\varsigma)\|_2^2$, thus $\sqrt{\mathrm{tr}\{\boldsymbol{N}\}}$ is an upper bound on the $\mathcal{H}_2$ norm of the closed-loop system. In addition, the definition of $\boldsymbol{N}$ is equivalent to

$$\boldsymbol{N} - (\boldsymbol{H_z} - \boldsymbol{D_z K})\boldsymbol{P}_2\boldsymbol{P}_2^{-1}\boldsymbol{P}_2(\boldsymbol{H_z} - \boldsymbol{D_z K})^T > 0,$$

[5]It is possible to show that $\boldsymbol{P}_2^{-1}$ satisfy the inequalities (3.2) and (3.3), associated with Lyapunov stability, for the closed-loop system (3.21). See Appendix C for a proof.

for which applying the Schur complement results in

$$\begin{bmatrix} \boldsymbol{N} & \boldsymbol{H}_z\boldsymbol{P}_2 - \boldsymbol{D}_z\boldsymbol{K}\boldsymbol{P}_2 \\ * & \boldsymbol{P}_2 \end{bmatrix} > 0. \tag{3.25}$$

Furthermore, the condition (3.24) is equivalent to $\boldsymbol{P}_2 - \boldsymbol{F}_\chi\boldsymbol{F}_\chi^T - (\boldsymbol{A}_\chi - \boldsymbol{B}_\chi\boldsymbol{K})\boldsymbol{P}_2\boldsymbol{P}_2^{-1}\boldsymbol{P}_2(\boldsymbol{A}_\chi - \boldsymbol{B}_\chi\boldsymbol{K})^T > 0$, for which applying the Schur complement yields

$$\begin{bmatrix} \boldsymbol{P}_2 - \boldsymbol{F}_\chi\boldsymbol{F}_\chi^T & (\boldsymbol{A}_\chi - \boldsymbol{B}_\chi\boldsymbol{K})\boldsymbol{P}_2 \\ * & \boldsymbol{P}_2 \end{bmatrix} > 0.$$

This result can be rewritten as

$$\begin{bmatrix} \boldsymbol{P}_2 & (\boldsymbol{A}_\chi - \boldsymbol{B}_\chi\boldsymbol{K})\boldsymbol{P}_2 \\ * & \boldsymbol{P}_2 \end{bmatrix} - \begin{bmatrix} \boldsymbol{F}_\chi \\ \boldsymbol{0} \end{bmatrix} \mathbb{I} \begin{bmatrix} \boldsymbol{F}_\chi^T & \boldsymbol{0} \end{bmatrix} > 0,$$

for which applying the Schur complement yields

$$\begin{bmatrix} \boldsymbol{P}_2 & (\boldsymbol{A}_\chi - \boldsymbol{B}_\chi\boldsymbol{K})\boldsymbol{P}_2 & \boldsymbol{F}_\chi \\ * & \boldsymbol{P}_2 & \boldsymbol{0} \\ * & \boldsymbol{0} & \mathbb{I} \end{bmatrix} > 0. \tag{3.26}$$

Finally, by introducing an instrumental variable $\boldsymbol{X}_2$ in order to reduce conservativeness (de Oliveira et al., 2002) and defining $\boldsymbol{Y} \triangleq -\boldsymbol{K}\boldsymbol{X}_2$, gathering the conditions (3.25) and (3.26), and recalling that $\|\boldsymbol{\Psi}_{\boldsymbol{dz}}(\varsigma)\|_2^2 < \operatorname{tr}\{\boldsymbol{N}\}$, the problem of computing the gain matrix $\boldsymbol{K}$ that minimizes the $\mathcal{H}_2$ norm of the closed-loop system (3.21) is casted into the optimization problem

$$\min_{\boldsymbol{P}_2, \boldsymbol{X}_2, \boldsymbol{Y}, \boldsymbol{N}} \operatorname{tr}\{\boldsymbol{N}\} \quad \text{subject to}$$

$$\begin{bmatrix} \boldsymbol{N} & \boldsymbol{H}_z\boldsymbol{X}_2 + \boldsymbol{D}_z\boldsymbol{Y} \\ * & \boldsymbol{X}_2 + \boldsymbol{X}_2^T - \boldsymbol{P}_2 \end{bmatrix} > 0, \tag{3.27}$$

$$\begin{bmatrix} \boldsymbol{P}_2 & \boldsymbol{A}_\chi\boldsymbol{X}_2 + \boldsymbol{B}_\chi\boldsymbol{Y} & \boldsymbol{F}_\chi \\ * & \boldsymbol{X}_2 + \boldsymbol{X}_2^T - \boldsymbol{P}_2 & \boldsymbol{0} \\ * & \boldsymbol{0} & \mathbb{I} \end{bmatrix} > 0, \tag{3.28}$$

with $\boldsymbol{N} = \boldsymbol{N}^T$ and $\boldsymbol{P}_2 = \boldsymbol{P}_2^T$, while no properties are required on $\boldsymbol{Y}$ and $\boldsymbol{X}_2$.

It is important to note that, by choosing $\boldsymbol{X}_2 = \boldsymbol{X}_2^T = \boldsymbol{P}_2$, the original conditions (3.25) and (3.26) are recovered. Asymptotic stability is guaranteed by feasibility of (3.28), and minimization of the $\mathcal{H}_2$ norm is guaranteed by feasibility of (3.27). The gain matrix $\boldsymbol{K}$ is then obtained from $\boldsymbol{K} = -\boldsymbol{Y}\boldsymbol{X}_2^{-1}$.

3.4.2 Discrete-time state-feedback $\mathcal{H}_\infty$ control

Consider the discrete-time linear system

$$\begin{aligned} \boldsymbol{\chi}_{k+1} &= \boldsymbol{A}_{\boldsymbol{\chi}}\boldsymbol{\chi}_k + \boldsymbol{B}_{\boldsymbol{\chi}}\delta\boldsymbol{u}_k + \boldsymbol{F}_{\boldsymbol{\chi}}\boldsymbol{d}_k, \\ \boldsymbol{z}_k &= \boldsymbol{H}_{\boldsymbol{z}}\boldsymbol{\chi}_k + \boldsymbol{D}_{\boldsymbol{zu}}\delta\boldsymbol{u}_k + \boldsymbol{D}_{\boldsymbol{zd}}\boldsymbol{d}_k, \end{aligned} \tag{3.29}$$

where $\boldsymbol{z} \in \mathbb{R}^{n_z}$ are cost variables, $\boldsymbol{H}_{\boldsymbol{z}} \in \mathbb{R}^{n_z \times 24}$, $\boldsymbol{D}_{\boldsymbol{zu}} \in \mathbb{R}^{n_z \times 4}$ and $\boldsymbol{D}_{\boldsymbol{zd}} \in \mathbb{R}^{n_z \times 3}$ are design weighting matrices.

Let $\boldsymbol{\Psi}_{\boldsymbol{dz}}(\varsigma)$ denote the discrete-time transfer matrix from $\boldsymbol{d}$ to $\boldsymbol{z}$. Then, the $\mathcal{H}_\infty$ norm of the discrete-time system (3.29) is defined as (de Souza & Xie, 1992)

$$\|\boldsymbol{\Psi}_{\boldsymbol{dz}}(\varsigma)\|_\infty \triangleq \sup_{0\leq\phi\leq 2\pi} \sigma_{\max}\{\boldsymbol{\Psi}_{\boldsymbol{dz}}(e^{j\phi})\},$$

where $\phi \triangleq \omega T_c$, and $\sigma_{\max}\{\cdot\}$ denotes the highest singular value. The $\mathcal{H}_\infty$ norm can be interpreted as the highest gain of the system's frequency response associated with the channel $\boldsymbol{d} \to \boldsymbol{z}$, and can also be formulated in terms of the energies of the signals $\boldsymbol{d}_k$ and $\boldsymbol{z}_k$. Through the Parseval's theorem we have (Lathi, 2005)

$$\begin{aligned} \|\boldsymbol{z}_k\|_2^2 &\triangleq \sum_{k=0}^{\infty} \boldsymbol{z}_k^T\boldsymbol{z}_k = \frac{1}{2\pi}\int_0^{2\pi} (\boldsymbol{z}(e^{j\phi}))^H \boldsymbol{z}(e^{j\phi})\mathrm{d}\phi, \\ \|\boldsymbol{d}_k\|_2^2 &\triangleq \sum_{k=0}^{\infty} \boldsymbol{d}_k^T\boldsymbol{d}_k = \frac{1}{2\pi}\int_0^{2\pi} (\boldsymbol{d}(e^{j\phi}))^H \boldsymbol{d}(e^{j\phi})\mathrm{d}\phi, \end{aligned}$$

where $(\cdot)^H$ denotes the Hermitian conjugate[6]. As $\boldsymbol{z}(e^{j\phi}) = \boldsymbol{\Psi}_{\boldsymbol{dz}}(e^{j\phi})\boldsymbol{d}(e^{j\phi})$,

$$\begin{aligned} \|\boldsymbol{z}_k\|_2^2 &= \frac{1}{2\pi}\int_0^{2\pi} (\boldsymbol{d}(e^{j\phi}))^H (\boldsymbol{\Psi}_{\boldsymbol{dz}}(e^{j\phi}))^H \boldsymbol{\Psi}_{\boldsymbol{dz}}(e^{j\phi})\boldsymbol{d}(e^{j\phi})\mathrm{d}\phi \\ &\leq \frac{1}{2\pi}\int_0^{2\pi} (\sigma_{\max}\{\boldsymbol{\Psi}_{\boldsymbol{dz}}(e^{j\phi})\})^2 (\boldsymbol{d}(e^{j\phi}))^H \boldsymbol{d}(e^{j\phi})\mathrm{d}\phi \\ &\leq \left(\sup_{0\leq\phi\leq 2\pi} \sigma_{\max}\{\boldsymbol{\Psi}_{\boldsymbol{dz}}(e^{j\phi})\}\right)^2 \frac{1}{2\pi}\int_0^{2\pi} (\boldsymbol{d}(e^{j\phi}))^H \boldsymbol{d}(e^{j\phi})\mathrm{d}\phi \\ \implies \|\boldsymbol{z}_k\|_2^2 &\leq \|\boldsymbol{\Psi}_{\boldsymbol{dz}}(\varsigma)\|_\infty^2 \|\boldsymbol{d}_k\|_2^2, \end{aligned}$$

which, analogously to the continuous-time case, yields (Trofino et al., 2015)

$$\|\boldsymbol{\Psi}_{\boldsymbol{dz}}(\varsigma)\|_\infty = \sup_{\|\boldsymbol{d}_k\|_2 \neq 0} \frac{\|\boldsymbol{z}_k\|_2}{\|\boldsymbol{d}_k\|_2}. \tag{3.30}$$

Now, consider the state-feedback control law $\delta\boldsymbol{u}_k = -\boldsymbol{K}\boldsymbol{\chi}_k$. The $\mathcal{H}_\infty$ control design problem consists in computing the gain matrix $\boldsymbol{K}$ that minimizes the $\mathcal{H}_\infty$ norm of the

[6] Conjugate transpose.

closed-loop system

$$\begin{aligned} \boldsymbol{\chi}_{k+1} &= (\boldsymbol{A}_{\boldsymbol{\chi}} - \boldsymbol{B}_{\boldsymbol{\chi}}\boldsymbol{K})\boldsymbol{\chi}_k + \boldsymbol{F}_{\boldsymbol{\chi}}\boldsymbol{d}_k, \\ \boldsymbol{z}_k &= (\boldsymbol{H}_{\boldsymbol{z}} - \boldsymbol{D}_{\boldsymbol{zu}}\boldsymbol{K})\boldsymbol{\chi}_k + \boldsymbol{D}_{\boldsymbol{zd}}\boldsymbol{d}_k. \end{aligned} \tag{3.31}$$

This optimal control problem is known to be hard to solve, then, instead of minimizing the $\mathcal{H}_\infty$ norm, it is common to seek a sub-optimal solution that minimizes an upper bound γ, such that $\|\boldsymbol{\Psi}_{\boldsymbol{dz}}(\varsigma)\|_\infty < \gamma$. Then, from (3.30) we have

$$\begin{aligned} \sup_{\|\boldsymbol{d}_k\|_2 \neq 0} \frac{\|\boldsymbol{z}_k\|_2}{\|\boldsymbol{d}_k\|_2} < \gamma \implies \sup_{\|\boldsymbol{d}_k\|_2 \neq 0} \frac{\|\boldsymbol{z}_k\|_2^2}{\|\boldsymbol{d}_k\|_2^2} < \gamma^2 \implies \frac{\|\boldsymbol{z}_k\|_2^2}{\|\boldsymbol{d}_k\|_2^2} < \gamma^2 \implies \sum_{k=0}^{\infty} \boldsymbol{z}_k^T \boldsymbol{z}_k < \gamma^2 \sum_{k=0}^{\infty} \boldsymbol{d}_k^T \boldsymbol{d}_k \\ \implies \sum_{k=0}^{\infty} (\boldsymbol{z}_k^T \boldsymbol{z}_k - \gamma^2 \boldsymbol{d}_k^T \boldsymbol{d}_k) < 0. \end{aligned} \tag{3.32}$$

A sufficient condition for (3.32) to be satisfied is

$$\boldsymbol{z}_k^T \boldsymbol{z}_k - \gamma^2 \boldsymbol{d}_k^T \boldsymbol{d}_k < 0. \tag{3.33}$$

In order to bring the control design problem to a LMI framework, consider the Lyapunov function candidate $V(\boldsymbol{\chi}_k) = \boldsymbol{\chi}_k^T \boldsymbol{P} \boldsymbol{\chi}_k$, with $\boldsymbol{P} > 0$. Then,

$$\begin{aligned} \Delta V(\boldsymbol{\chi}_k) \triangleq V(\boldsymbol{\chi}_{k+1}) - V(\boldsymbol{\chi}_k) &= \boldsymbol{\chi}_{k+1}^T \boldsymbol{P} \boldsymbol{\chi}_{k+1} - \boldsymbol{\chi}_k^T \boldsymbol{P} \boldsymbol{\chi}_k \\ &= ((\boldsymbol{A}_{\boldsymbol{\chi}} - \boldsymbol{B}_{\boldsymbol{\chi}}\boldsymbol{K})\boldsymbol{\chi}_k + \boldsymbol{F}_{\boldsymbol{\chi}}\boldsymbol{d}_k)^T \boldsymbol{P} ((\boldsymbol{A}_{\boldsymbol{\chi}} - \boldsymbol{B}_{\boldsymbol{\chi}}\boldsymbol{K})\boldsymbol{\chi}_k + \boldsymbol{F}_{\boldsymbol{\chi}}\boldsymbol{d}_k) - \boldsymbol{\chi}_k^T \boldsymbol{P} \boldsymbol{\chi}_k \\ &= \boldsymbol{\chi}_k^T ((\boldsymbol{A}_{\boldsymbol{\chi}} - \boldsymbol{B}_{\boldsymbol{\chi}}\boldsymbol{K})^T \boldsymbol{P} (\boldsymbol{A}_{\boldsymbol{\chi}} - \boldsymbol{B}_{\boldsymbol{\chi}}\boldsymbol{K}) - \boldsymbol{P}) \boldsymbol{\chi}_k + \boldsymbol{\chi}_k^T (\boldsymbol{A}_{\boldsymbol{\chi}} - \boldsymbol{B}_{\boldsymbol{\chi}}\boldsymbol{K})^T \boldsymbol{P} \boldsymbol{F}_{\boldsymbol{\chi}} \boldsymbol{d}_k \\ &\quad + \boldsymbol{d}_k^T \boldsymbol{F}_{\boldsymbol{\chi}}^T \boldsymbol{P} (\boldsymbol{A}_{\boldsymbol{\chi}} - \boldsymbol{B}_{\boldsymbol{\chi}}\boldsymbol{K}) \boldsymbol{\chi}_k + \boldsymbol{d}_k^T \boldsymbol{F}_{\boldsymbol{\chi}}^T \boldsymbol{P} \boldsymbol{F}_{\boldsymbol{\chi}} \boldsymbol{d}_k. \end{aligned} \tag{3.34}$$

Assuming that $\delta \boldsymbol{u}_k = -\boldsymbol{K}\boldsymbol{\chi}_k$ stabilizes the closed-loop system (3.31), thus $\Delta V(\boldsymbol{\chi}_k) < 0$, one can consider the following inequality

$$\Delta V(\boldsymbol{\chi}_k) + \boldsymbol{z}_k^T \boldsymbol{z}_k - \gamma^2 \boldsymbol{d}_k^T \boldsymbol{d}_k < 0. \tag{3.35}$$

Substituting (3.34) in (3.35) yields

$$\begin{bmatrix} \boldsymbol{\chi}_k \\ \boldsymbol{d}_k \end{bmatrix}^T \begin{bmatrix} \tilde{\boldsymbol{A}}_{\boldsymbol{\chi}}^T \boldsymbol{P} \tilde{\boldsymbol{A}}_{\boldsymbol{\chi}} - \boldsymbol{P} + \tilde{\boldsymbol{H}}_{\boldsymbol{z}}^T \tilde{\boldsymbol{H}}_{\boldsymbol{z}} & \tilde{\boldsymbol{A}}_{\boldsymbol{\chi}}^T \boldsymbol{P} \boldsymbol{F}_{\boldsymbol{\chi}} + \tilde{\boldsymbol{H}}_{\boldsymbol{z}}^T \boldsymbol{D}_{\boldsymbol{zd}} \\ * & \boldsymbol{F}_{\boldsymbol{\chi}}^T \boldsymbol{P} \boldsymbol{F}_{\boldsymbol{\chi}} + \boldsymbol{D}_{\boldsymbol{zd}}^T \boldsymbol{D}_{\boldsymbol{zd}} - \gamma^2 \mathbb{I} \end{bmatrix} \begin{bmatrix} \boldsymbol{\chi}_k \\ \boldsymbol{d}_k \end{bmatrix} < 0, \tag{3.36}$$

where $\tilde{\boldsymbol{A}}_{\boldsymbol{\chi}} \triangleq (\boldsymbol{A}_{\boldsymbol{\chi}} - \boldsymbol{B}_{\boldsymbol{\chi}}\boldsymbol{K})$ and $\tilde{\boldsymbol{H}}_{\boldsymbol{z}} \triangleq (\boldsymbol{H}_{\boldsymbol{z}} - \boldsymbol{D}_{\boldsymbol{zu}}\boldsymbol{K})$. Inequality (3.36) can be rewritten as

$$\begin{bmatrix} \boldsymbol{P} & \boldsymbol{0} \\ \boldsymbol{0} & \gamma^2 \mathbb{I} \end{bmatrix} - \begin{bmatrix} \tilde{\boldsymbol{A}}_{\boldsymbol{\chi}}^T \boldsymbol{P} & \tilde{\boldsymbol{H}}_{\boldsymbol{z}}^T \\ \boldsymbol{F}_{\boldsymbol{\chi}}^T \boldsymbol{P} & \boldsymbol{D}_{\boldsymbol{zd}}^T \end{bmatrix} \begin{bmatrix} \boldsymbol{P}^{-1} & \boldsymbol{0} \\ \boldsymbol{0} & \mathbb{I} \end{bmatrix} \begin{bmatrix} \boldsymbol{P}\tilde{\boldsymbol{A}}_{\boldsymbol{\chi}} & \boldsymbol{P}\boldsymbol{F}_{\boldsymbol{\chi}} \\ \tilde{\boldsymbol{H}}_{\boldsymbol{z}} & \boldsymbol{D}_{\boldsymbol{zd}} \end{bmatrix} > 0,$$

which, through the Schur complement, is equivalent to

$$\boldsymbol{Z} \triangleq \begin{bmatrix} \boldsymbol{P} & \mathbf{0} & \tilde{\boldsymbol{A}}_{\boldsymbol{\chi}}^T \boldsymbol{P} & \tilde{\boldsymbol{H}}_{\boldsymbol{z}}^T \\ \mathbf{0} & \gamma^2 \mathbb{I} & \boldsymbol{F}_{\boldsymbol{\chi}}^T \boldsymbol{P} & \boldsymbol{D}_{\boldsymbol{zd}}^T \\ \boldsymbol{P}\tilde{\boldsymbol{A}}_{\boldsymbol{\chi}} & \boldsymbol{P}\boldsymbol{F}_{\boldsymbol{\chi}} & \boldsymbol{P} & \mathbf{0} \\ \tilde{\boldsymbol{H}}_{\boldsymbol{z}} & \boldsymbol{D}_{\boldsymbol{zd}} & \mathbf{0} & \mathbb{I} \end{bmatrix} > 0. \tag{3.37}$$

Then, performing a congruence transformation $\bar{\boldsymbol{Z}}^T \boldsymbol{Z} \bar{\boldsymbol{Z}} > 0$, where

$$\bar{\boldsymbol{Z}} \triangleq \begin{bmatrix} \mathbf{0} & \gamma \boldsymbol{P}^{-1} & \mathbf{0} & \mathbf{0} \\ \mathbf{0} & \mathbf{0} & \gamma^{-1}\mathbb{I} & \mathbf{0} \\ \gamma \boldsymbol{P}^{-1} & \mathbf{0} & \mathbf{0} & \mathbf{0} \\ \mathbf{0} & \mathbf{0} & \mathbf{0} & \gamma \mathbb{I} \end{bmatrix},$$

and defining $\boldsymbol{P}_\infty \triangleq \gamma^2 \boldsymbol{P}^{-1}$, yields

$$\begin{bmatrix} \boldsymbol{P}_\infty & \tilde{\boldsymbol{A}}_{\boldsymbol{\chi}} \boldsymbol{P}_\infty & \boldsymbol{F}_{\boldsymbol{\chi}} & \mathbf{0} \\ \boldsymbol{P}_\infty \tilde{\boldsymbol{A}}_{\boldsymbol{\chi}}^T & \boldsymbol{P}_\infty & \mathbf{0} & \boldsymbol{P}_\infty \tilde{\boldsymbol{H}}_{\boldsymbol{z}}^T \\ \boldsymbol{F}_{\boldsymbol{\chi}}^T & \mathbf{0} & \mathbb{I} & \boldsymbol{D}_{\boldsymbol{zd}}^T \\ \mathbf{0} & \tilde{\boldsymbol{H}}_{\boldsymbol{z}} \boldsymbol{P}_\infty & \boldsymbol{D}_{\boldsymbol{zd}} & \gamma^2 \mathbb{I} \end{bmatrix} > 0. \tag{3.38}$$

Finally, similarly to the $\mathcal{H}_2$ control case, by introducing an instrumental variable $\boldsymbol{X}_\infty$ in order to reduce conservativeness, and defining $\boldsymbol{Y} \triangleq -\boldsymbol{K}\boldsymbol{X}_\infty$ and $\tilde{\gamma} \triangleq \gamma^2$, from the condition (3.38) and recalling that $\|\boldsymbol{\Psi}_{\boldsymbol{dz}}(\varsigma)\|_\infty < \gamma$, the problem of computing the sub-optimal solution $\boldsymbol{K}$ that minimizes the upper-bound γ of the $\mathcal{H}_\infty$ norm of the closed-loop system (3.21) is casted into the optimization problem

$$\min_{\boldsymbol{P}_\infty, \boldsymbol{X}_\infty, \boldsymbol{Y}} \tilde{\gamma} \quad \text{subject to}$$

$$\begin{bmatrix} \boldsymbol{P}_\infty & \boldsymbol{A}_{\boldsymbol{\chi}} \boldsymbol{X}_\infty + \boldsymbol{B}_{\boldsymbol{\chi}} \boldsymbol{Y} & \boldsymbol{F}_{\boldsymbol{\chi}} & \mathbf{0} \\ * & \boldsymbol{X}_\infty + \boldsymbol{X}_\infty^T - \boldsymbol{P}_\infty & \mathbf{0} & \boldsymbol{X}_\infty^T \boldsymbol{H}_{\boldsymbol{z}} + \boldsymbol{Y}^T \boldsymbol{D}_{\boldsymbol{zu}}^T \\ * & * & \mathbb{I} & \boldsymbol{D}_{\boldsymbol{zd}}^T \\ * & * & * & \tilde{\gamma} \mathbb{I} \end{bmatrix} > 0. \tag{3.39}$$

with $\boldsymbol{P}_\infty = \boldsymbol{P}_\infty^T$, while no properties are required on $\boldsymbol{Y}$ and $\boldsymbol{X}_\infty$.

Notice that by choosing $\boldsymbol{X}_\infty = \boldsymbol{X}_\infty^T = \boldsymbol{P}_\infty$, the original condition (3.38) is recovered. Asymptotic stability and minimization of the upper-bound γ of the $\mathcal{H}_\infty$ norm are both guaranteed by feasibility of (3.39). The gain matrix $\boldsymbol{K}$ is obtained from $\boldsymbol{K} = -\boldsymbol{Y}\boldsymbol{X}_\infty^{-1}$.

3.4.3 Pole placement in LMI regions

An LMI region is defined as a convex subset $\mathbb{D}$ of the complex plane that can be expressed as (Chilali & Gahinet, 1996)

$$\mathbb{D} \triangleq \{\varsigma \in \mathbb{C} : \boldsymbol{U} + \varsigma \boldsymbol{V} + \varsigma^* \boldsymbol{V}^T < 0\}, \tag{3.40}$$

whose shape is defined by the matrices $\boldsymbol{U} = \boldsymbol{U}^T \in \mathbb{R}^{n_\mathrm{D} \times n_\mathrm{D}}$ and $\boldsymbol{V} \in \mathbb{R}^{n_\mathrm{D} \times n_\mathrm{D}}$. Such regions are symmetric with respect to the real axis, and the intersection between two of them is also an LMI region.

In control design, it is common to have requirements on the time response of the closed-loop system. For instance, when dealing with standard second-order continuous-time linear systems, settling time and percentage overshoot are directly related to the real part and phase angle of their poles, respectively, and requirements on these are guaranteed if the system's poles belong to certain regions, given by $\{s \in \mathbb{C} : \mathrm{Re}(s) < -\varepsilon\}$ and $\{s \in \mathbb{C} : |\mathrm{Im}(s)| < \tan(\phi)|\mathrm{Re}(s)|\}$, with $\varepsilon \in \mathbb{R}$ and $\phi \in [0, \pi/2]$. On the other hand, for discrete-time linear systems, as $\varsigma = e^{sT_c}$ (Phillips & Nagle, 1995), the settling time is related to $\ln|\varsigma|$ and can be characterized by circular regions, while the percentage overshoot depends nonlinearly on both $|\varsigma|$ and phase angles and can be characterized by logarithmic spirals.

Consider now the system (3.9) and the state-feedback control law $\delta \boldsymbol{u}_k = -\boldsymbol{K}\boldsymbol{\chi}_k$. The eigenvalues of the closed-loop system matrix $\tilde{\boldsymbol{A}}_{\boldsymbol{\chi}} \triangleq \boldsymbol{A}_{\boldsymbol{\chi}} - \boldsymbol{B}_{\boldsymbol{\chi}}\boldsymbol{K}$ belong to an LMI region $\mathbb{D}$ if, and only if, there exists a symmetric matrix $\boldsymbol{T} > 0$ such that (Chilali & Gahinet, 1996)

$$\boldsymbol{U} \otimes \boldsymbol{T} + \boldsymbol{V} \otimes (\boldsymbol{T}\tilde{\boldsymbol{A}}_{\boldsymbol{\chi}}) + \boldsymbol{V}^T \otimes (\tilde{\boldsymbol{A}}_{\boldsymbol{\chi}}^T \boldsymbol{T}) < 0, \tag{3.41}$$

where $\otimes$ denotes the Kronecker product of matrices, defined by

$$\boldsymbol{U} \otimes \boldsymbol{T} \triangleq \begin{bmatrix} U_{11}\boldsymbol{T} & U_{12}\boldsymbol{T} & \cdots & U_{1n_\mathrm{D}}\boldsymbol{T} \\ U_{21}\boldsymbol{T} & U_{22}\boldsymbol{T} & \cdots & U_{2n_\mathrm{D}}\boldsymbol{T} \\ \vdots & \vdots & \ddots & \vdots \\ U_{n_\mathrm{D}1}\boldsymbol{T} & U_{n_\mathrm{D}2}\boldsymbol{T} & \cdots & U_{n_\mathrm{D}n_\mathrm{D}}\boldsymbol{T} \end{bmatrix}.$$

If the condition (3.41) is satisfied, the closed-loop system is said to be *D-stable*. This inequality can be used for control design with pole placement constraints, via LMI approach, in which performance requirements are specified in terms of LMI regions.

In this work, two regions are of interest (see Figure 3.1):

Region 1: $\mathbb{D}_1 \triangleq \{\varsigma \in \mathbb{C} : \mathrm{Re}(\varsigma) > \varepsilon \geq 0\}$

Since the settling time is related to $\ln|\varsigma|$, an ideal region to ensure a desired minimum

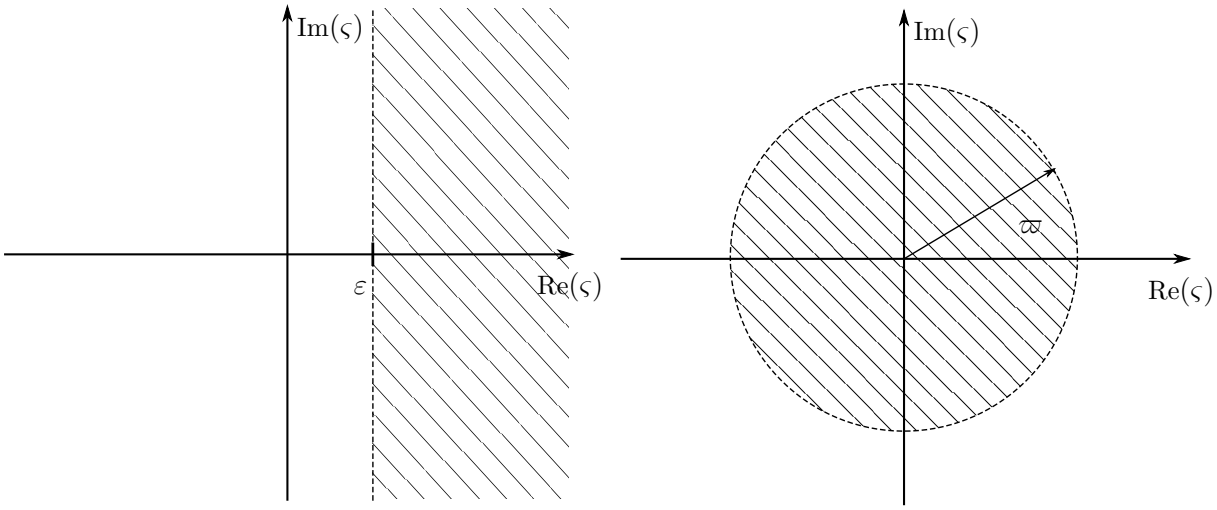

(a) Region 1 (b) Region 2

Figure 3.1: LMI regions.

settling time for the closed-loop system is defined by $\{\varsigma \in \mathbb{C} : |\varsigma| > \varepsilon \geq 0\}$, which corresponds to all the points of the complex plane outside a disc with radius ε, centered at the origin. However, this is not a convex region, thus it cannot be expressed in the form (3.40). Seeking an alternative, we define the region $\{\varsigma \in \mathbb{C} : \text{Re}(\varsigma) > \varepsilon \geq 0\}$, which is convex.

Given that $|\varsigma| \geq |\text{Re}(\varsigma)|$, $\text{Re}(\varsigma) > \varepsilon$ and $\varepsilon \geq 0$, this region guarantees that $|\varsigma| > \varepsilon$, ensuring a desired minimum settling time for the closed-loop system, while also avoiding the ringing effect[7]. It can be expressed in the form (3.40) by recalling that $\varsigma + \varsigma^* = 2\text{Re}(\varsigma)$. Then, the condition $\text{Re}(\varsigma) > \varepsilon$ is equivalent to $\varsigma + \varsigma^* > 2\varepsilon$, which can be rewritten as $2\varepsilon - \varsigma - \varsigma^* < 0$. Hence, its shape is defined by

$$\boldsymbol{U}_1 \triangleq 2\varepsilon, \quad \boldsymbol{V}_1 \triangleq -1. \tag{3.42}$$

Substituting (3.42) in (3.41) yields

$$\boldsymbol{A}_{\boldsymbol{\chi}}^T \boldsymbol{T}_1 + \boldsymbol{T}_1 \boldsymbol{A}_{\boldsymbol{\chi}} - \boldsymbol{K}^T \boldsymbol{B}_{\boldsymbol{\chi}}^T \boldsymbol{T}_1 - \boldsymbol{T}_1 \boldsymbol{B}_{\boldsymbol{\chi}} \boldsymbol{K} - 2\varepsilon \boldsymbol{T}_1 > 0,$$

which, by applying a congruence transformation using $\boldsymbol{T}_1^{-1}$ and defining $\bar{\boldsymbol{T}}_1 \triangleq \boldsymbol{T}_1^{-1}$ and $\boldsymbol{Y} \triangleq -\boldsymbol{K}\bar{\boldsymbol{T}}_1$, leads to the LMI

$$\bar{\boldsymbol{T}}_1 \boldsymbol{A}_{\boldsymbol{\chi}}^T + \boldsymbol{A}_{\boldsymbol{\chi}} \bar{\boldsymbol{T}}_1 + \boldsymbol{Y}^T \boldsymbol{B}_{\boldsymbol{\chi}}^T + \boldsymbol{B}_{\boldsymbol{\chi}} \boldsymbol{Y} - 2\varepsilon \bar{\boldsymbol{T}}_1 > 0. \tag{3.43}$$

The gain matrix $\boldsymbol{K}$ that guarantees that $\text{eig}\{\tilde{\boldsymbol{A}}_{\boldsymbol{\chi}}\} \subset \mathbb{D}_1$ is then given by $\boldsymbol{K} = -\boldsymbol{Y}\bar{\boldsymbol{T}}_1^{-1}$,

[7] The ringing effect is a transient behavior of the system characterized by cycling between positive and negative deviations from the steady-state value. It is caused by the presence of poles with negative real part, being intensified when they are close to the unitary circle (Seborg et al., 2003; Phillips & Nagle, 1995).

where $\text{eig}\{\tilde{\boldsymbol{A}}_{\boldsymbol{\chi}}\}$ denotes the set of eigenvalues of $\tilde{\boldsymbol{A}}_{\boldsymbol{\chi}}$.

Region 2: $\mathbb{D}_2 \triangleq \{\varsigma \in \mathbb{C} : 0 \leq |\varsigma| < \varpi\}$

This region is a disc with radius ϖ, centered at the origin of the complex plane, and guarantees that $|\varsigma| < \varpi$, ensuring a desired maximum settling time for the closed-loop system. It can be expressed in the form (3.40) by rewriting $|\varsigma| < \varpi$ as $\varsigma\varsigma^* < \varpi^2$, which can be further rewritten as $\varpi - \varsigma\varpi^{-1}\varsigma^* > 0$. Through the Schur complement, the latter is equivalent to

$$\begin{bmatrix} \varpi & -\varsigma \\ -\varsigma^* & \varpi \end{bmatrix} > 0,$$

which can be rewritten as

$$\begin{bmatrix} -\varpi & 0 \\ 0 & -\varpi \end{bmatrix} + \varsigma \begin{bmatrix} 0 & 1 \\ 0 & 0 \end{bmatrix} + \varsigma^* \begin{bmatrix} 0 & 0 \\ 1 & 0 \end{bmatrix} < 0.$$

Hence,

$$\boldsymbol{U}_2 = \begin{bmatrix} -\varpi & 0 \\ 0 & -\varpi \end{bmatrix}, \quad \boldsymbol{V}_2 = \begin{bmatrix} 0 & 1 \\ 0 & 0 \end{bmatrix}. \tag{3.44}$$

Substituting (3.44) in (3.41) yields

$$\begin{bmatrix} -\varpi \boldsymbol{T}_2 & \boldsymbol{T}_2\boldsymbol{A}_{\boldsymbol{\chi}} - \boldsymbol{T}_2\boldsymbol{B}_{\boldsymbol{\chi}}\boldsymbol{K} \\ \boldsymbol{A}_{\boldsymbol{\chi}}^T\boldsymbol{T}_2 - \boldsymbol{K}^T\boldsymbol{B}_{\boldsymbol{\chi}}^T\boldsymbol{T}_2 & -\varpi \boldsymbol{T}_2 \end{bmatrix} < 0,$$

which, by applying a congruence transformation using $\boldsymbol{T}_2^{-1}$ and defining $\bar{\boldsymbol{T}}_2 \triangleq \boldsymbol{T}_2^{-1}$ and $\boldsymbol{Y} \triangleq -\boldsymbol{K}\bar{\boldsymbol{T}}_2$, leads to the LMI

$$\begin{bmatrix} -\varpi \bar{\boldsymbol{T}}_2 & \boldsymbol{A}_{\boldsymbol{\chi}}\bar{\boldsymbol{T}}_2 + \boldsymbol{B}_{\boldsymbol{\chi}}\boldsymbol{Y} \\ \bar{\boldsymbol{T}}_2\boldsymbol{A}_{\boldsymbol{\chi}}^T + \boldsymbol{Y}^T\boldsymbol{B}_{\boldsymbol{\chi}}^T & -\varpi \bar{\boldsymbol{T}}_2 \end{bmatrix} < 0. \tag{3.45}$$

The gain matrix $\boldsymbol{K}$ that guarantees that $\text{eig}\{\tilde{\boldsymbol{A}}_{\boldsymbol{\chi}}\} \subset \mathbb{D}_2$ is then given by $\boldsymbol{K} = -\boldsymbol{Y}\bar{\boldsymbol{T}}_2^{-1}$. Minimum and maximum settling times can be both guaranteed if $\text{eig}\{\tilde{\boldsymbol{A}}_{\boldsymbol{\chi}}\} \subset \mathbb{D}_1 \cap \mathbb{D}_2$, which can be achieved by computing a gain matrix $\boldsymbol{K}$ such that (3.43) and (3.45) are simultaneously satisfied, with $\bar{\boldsymbol{T}}_1 = \bar{\boldsymbol{T}}_2 > 0$. Unfortunately, as logarithmic spirals are not convex regions, percentage overshoot requirements cannot be directly specified using LMI regions, thus those are not exploited in this work.

Finally, it is interesting to note that, considering an open-loop system and making $\varpi = 1$ in (3.45) (an unitary circle), by changing the signals of the inequality, performing

the congruence transformation

$$\begin{bmatrix} \mathbf{0} & \mathbb{I} \\ -\mathbb{I} & \mathbf{0} \end{bmatrix} \begin{bmatrix} \bar{\boldsymbol{T}}_2 & -\boldsymbol{A}_{\boldsymbol{\chi}}\bar{\boldsymbol{T}}_2 \\ -\bar{\boldsymbol{T}}_2\boldsymbol{A}_{\boldsymbol{\chi}}^T & \bar{\boldsymbol{T}}_2 \end{bmatrix} \begin{bmatrix} \mathbf{0} & -\mathbb{I} \\ \mathbb{I} & \mathbf{0} \end{bmatrix} > 0,$$

followed by the Schur complement and changing signals again, the Lyapunov stability criterion (3.3) is recovered.

3.4.4 Multi-objective control design

The present mixed $\mathcal{H}_2/\mathcal{H}_\infty$ control paradigm is similar to the one proposed in Chilali & Gahinet (1996).

In order to design a discrete-time mixed $\mathcal{H}_2/\mathcal{H}_\infty$ controller with pole placement constraints, for path tracking of the suspended load with stabilization of the tilt-rotor UAV, consider the discrete-time linear system

$$\begin{aligned} \boldsymbol{\chi}_{k+1} &= \boldsymbol{A}_{\boldsymbol{\chi}}\boldsymbol{\chi}_k + \boldsymbol{B}_{\boldsymbol{\chi}}\delta\boldsymbol{u}_k + \boldsymbol{F}_{\boldsymbol{\chi}}\boldsymbol{d}_k, \\ \boldsymbol{z}_k &= \boldsymbol{H}_{\boldsymbol{z}}\boldsymbol{\chi}_k + \boldsymbol{D}_{\boldsymbol{zu}}\delta\boldsymbol{u}_k + \boldsymbol{D}_{\boldsymbol{zd}}\boldsymbol{d}_k, \\ \tilde{\boldsymbol{z}}_k &= \boldsymbol{H}_{\boldsymbol{z}}\boldsymbol{\chi}_k + \boldsymbol{D}_{\boldsymbol{zu}}\delta\boldsymbol{u}_k, \end{aligned} \tag{3.46}$$

where $\boldsymbol{z}_k, \tilde{\boldsymbol{z}}_k \in \mathbb{R}^{n_z}$ are cost variables, $\boldsymbol{H}_{\boldsymbol{z}} \in \mathbb{R}^{n_z \times 24}$, $\boldsymbol{D}_{\boldsymbol{zu}} \in \mathbb{R}^{n_z \times 4}$ and $\boldsymbol{D}_{\boldsymbol{zd}} \in \mathbb{R}^{n_z \times 3}$ are design weighting matrices.

The objective is to design a state-feedback controller that minimizes the $\mathcal{H}_2$ norm $\|\boldsymbol{\Psi}_{\boldsymbol{d\tilde{z}}}\|_2$, while guaranteeing a specified upper-bound for the $\mathcal{H}_\infty$ norm $\|\boldsymbol{\Psi}_{\boldsymbol{dz}}\|_\infty$ of the closed-loop system. Moreover, it is also desired that the closed-loop system satisfy time response requirements that may be specified in terms of LMI regions.

The solution to this control design problem can be achieved by gathering the LMIs discussed in the previous sections into a single optimization problem. Consider the state-feedback control law $\delta\boldsymbol{u}_k = -\boldsymbol{K}\boldsymbol{\chi}_k$, a prescribed upper-bound[8] $\tilde{\gamma} > \|\boldsymbol{\Psi}_{\boldsymbol{dz}}\|_\infty^2$, and the LMI regions $\mathbb{D}_1 \triangleq \mathrm{Re}(\mathrm{eig}\{\tilde{\boldsymbol{A}}_{\boldsymbol{\chi}}\}) > \varepsilon$ and $\mathbb{D}_2 \triangleq |\mathrm{eig}\{\tilde{\boldsymbol{A}}_{\boldsymbol{\chi}}\}| < \varpi$, where $\tilde{\boldsymbol{A}}_{\boldsymbol{\chi}} \triangleq \boldsymbol{A}_{\boldsymbol{\chi}} - \boldsymbol{B}_{\boldsymbol{\chi}}\boldsymbol{K}$. In order to guarantee convexity in the decision variables, a common solution is searched by making $\boldsymbol{P}_2 = \boldsymbol{P}_\infty = \bar{\boldsymbol{P}}$ and $\boldsymbol{X}_2 = \boldsymbol{X}_\infty = \bar{\boldsymbol{T}}_1 = \bar{\boldsymbol{T}}_2 = \bar{\boldsymbol{X}}$ (Chilali & Gahinet, 1996). Then, the

[8] The upper-bound $\tilde{\gamma}$ can be obtained by first solving the $\mathcal{H}_\infty$ control problem, and incrementing the optimal value obtained.

aforementioned control design objectives are achieved by solving the optimization problem

$$\min_{\bar{\boldsymbol{P}},\bar{\boldsymbol{X}},\boldsymbol{Y},\boldsymbol{N}} \ \text{trace}\{\boldsymbol{N}\} \quad \text{subject to}$$

$$\begin{bmatrix} \boldsymbol{N} & \boldsymbol{H}_{\boldsymbol{z}}\bar{\boldsymbol{X}} + \boldsymbol{D}_{\boldsymbol{zu}}\boldsymbol{Y} \\ * & \bar{\boldsymbol{X}} + \bar{\boldsymbol{X}}^T - \bar{\boldsymbol{P}} \end{bmatrix} > 0,$$

$$\begin{bmatrix} \bar{\boldsymbol{P}} & \boldsymbol{A}_{\boldsymbol{\chi}}\bar{\boldsymbol{X}} + \boldsymbol{B}_{\boldsymbol{\chi}}\boldsymbol{Y} & \boldsymbol{F}_{\boldsymbol{\chi}} \\ * & \bar{\boldsymbol{X}} + \bar{\boldsymbol{X}}^T - \bar{\boldsymbol{P}} & \boldsymbol{0}_{24\times 3} \\ * & * & \mathbb{I}_{3\times 3} \end{bmatrix} > 0,$$

$$\begin{bmatrix} \bar{\boldsymbol{P}} & \boldsymbol{A}_{\boldsymbol{\chi}}\bar{\boldsymbol{X}} + \boldsymbol{B}_{\boldsymbol{\chi}}\boldsymbol{Y} & \boldsymbol{F}_{\boldsymbol{\chi}} & \boldsymbol{0}_{24\times n_z} \\ * & \bar{\boldsymbol{X}} + \bar{\boldsymbol{X}}^T - \bar{\boldsymbol{P}} & \boldsymbol{0}_{24\times 3} & \bar{\boldsymbol{X}}^T\boldsymbol{H}_{\boldsymbol{z}}^T + \boldsymbol{Y}^T\boldsymbol{D}_{\boldsymbol{zu}}^T \\ * & * & \mathbb{I}_{3\times 3} & \boldsymbol{D}_{\boldsymbol{zd}}^T \\ * & * & * & \tilde{\gamma}\mathbb{I}_{n_z\times n_z} \end{bmatrix} > 0,$$

$$\bar{\boldsymbol{X}}\boldsymbol{A}_{\boldsymbol{\chi}}^T + \boldsymbol{A}_{\boldsymbol{\chi}}\bar{\boldsymbol{X}} + \boldsymbol{Y}^T\boldsymbol{B}_{\boldsymbol{\chi}}^T + \boldsymbol{B}_{\boldsymbol{\chi}}\boldsymbol{Y} - 2\varepsilon\bar{\boldsymbol{X}} > 0,$$

$$\begin{bmatrix} -\varpi\bar{\boldsymbol{X}} & \boldsymbol{A}_{\boldsymbol{\chi}}\bar{\boldsymbol{X}} + \boldsymbol{B}_{\boldsymbol{\chi}}\boldsymbol{Y} \\ * & -\varpi\bar{\boldsymbol{X}} \end{bmatrix} < 0,$$

where the additional constraint $\bar{\boldsymbol{X}} = \bar{\boldsymbol{X}}^T > 0$ must be imposed, $\boldsymbol{N} = \boldsymbol{N}^T$ and $\bar{\boldsymbol{P}} = \bar{\boldsymbol{P}}^T$, whilst no properties are required on $\boldsymbol{Y}$. The gain matrix $\boldsymbol{K}$ is obtained from $\boldsymbol{K} = -\boldsymbol{Y}\bar{\boldsymbol{X}}^{-1}$.

Finally, as in the case of the discrete-time linear quadratic regulator, the feedforward term (3.18) is introduced in order to apply the control signals to the tilt-rotor UAV with suspended load.

3.5 Final remarks

This chapter described the design of discrete-time, linear state-feedback control strategies for path tracking of the suspended load with stabilization of the tilt-rotor UAV.

A discrete-time linear quadratic regulator was proposed for path tracking of the suspended load with stabilization of the tilt-rotor UAV. The DLQR minimizes the energy of the tracking error and control signals, and was designed through the solution of a discrete-time algebraic Riccati equation. The controller was designed based on discrete-time linearized error dynamics, obtained from the load's perspective model derived in the previous chapter, and augmented with integral actions for constant disturbances rejection.

A discrete-time mixed $\mathcal{H}_2/\mathcal{H}_\infty$ controller with pole placement constraints was also proposed for path tracking of the suspended load with stabilization of the tilt-rotor UAV. The controller featured constant disturbances rejection due to state augmentation, compensation of external disturbances, and time response guarantees. Its design was performed through linear matrix inequality (LMI) approach.

The described control strategies rely on full information about the system states in

order to achieve their purposes. The next chapter focuses on the design of state estimation strategies, for providing this information when it is not available as required by the state-feedback controllers.

4

State estimation strategies

In the previous chapter, state-feedback control strategies were designed for path tracking control of the suspended load with stabilization of the tilt-rotor UAV, based on dynamic equations formulated from the load's perspective. These strategies rely on availability of full information about the system states, at every time instant. However, in real applications, it is common the case that incomplete state information is available for feedback connection, and available information is often corrupted with noise.

This chapter focuses on the design of state estimators for providing such information from available measurements. Two different scenarios are addressed. In the first one, only a half of the state vector is measured, corresponding to the generalized coordinates, and this measurement is corrupted with zero-mean Gaussian noise. For this situation, a linearized Kalman filter is designed for estimation of the entire state vector. In the second one, the load's position and orientation w.r.t. to the inertial frame are not directly measured. It is assumed that available sensors provide information about the aircraft's position, orientation and angular velocity, and also about the position of the load with respect to the UAV, considering bounded noise without assumptions on probability distributions. Furthermore, the sensors are assumed to have different sampling times. For this last scenario, a deterministic, zonotopic state estimator is proposed.

The chapter is organized as follows: Section 4.1 introduces a background material for the zonotopic state estimation algorithm; Section 4.2 describes the design of the linearized Kalman filter for the first scenario; and Section 4.3 presents the design of the zonotopic state estimator considering the second scenario.

4.1 Preliminaries

4.1.1 Interval analysis

This subsection is mainly based on Moore et al. (2009). Notation and definitions are presented[1].

Interval analysis, mostly introduced by Moore (1966), is based on computation with sets, by regarding real compact intervals as a new number system. It has a wide range of applications, such as reliable computing, global optimization, solution of nonlinear equations and differential equations, state and parameter estimation, robot localization, path planning, and robust control (Jaulin et al., 2001).

Definition 4.1. Let $\mathbb{IR}$ denote the set of real compact intervals. An interval $\lfloor a \rceil \in \mathbb{IR}$ is defined by

$$\lfloor a \rceil = [\underline{a},\, \overline{a}\,] \triangleq \{a \in \mathbb{R} : \underline{a} \leq a \leq \overline{a}\}, \tag{4.1}$$

and $\underline{a},\ \overline{a} \in \mathbb{R}$ are called its endpoints.

A real number can be seen as a special case of an interval. Let $a \in \mathbb{R}$ and $\lfloor a \rceil = [\underline{a}, \overline{a}\,] \in \mathbb{IR}$, such that $a \in \lfloor a \rceil$. If $\underline{a} = \overline{a}$, $\lfloor a \rceil$ is called a *degenerate interval*, which is a singleton. Then, through (4.1), we have that $\underline{a} = \overline{a} = a$, thus

$$[\,a,\ a\,] = a. \tag{4.2}$$

Definition 4.2. Let $\lfloor a \rceil = [\underline{a},\, \overline{a}\,] \in \mathbb{IR}$. The midpoint and the diameter of $\lfloor a \rceil$ are defined by

$$\operatorname{mid}(\lfloor a \rceil) \triangleq \frac{\underline{a} + \overline{a}}{2}, \quad \operatorname{diam}(\lfloor a \rceil) \triangleq \overline{a} - \underline{a},$$

respectively.

Interval arithmetic defines the four basic operations with intervals.

Definition 4.3. Let $\lfloor a \rceil = [\underline{a},\, \overline{a}\,] \in \mathbb{IR}$ and $\lfloor b \rceil = [\underline{b},\, \overline{b}\,] \in \mathbb{IR}$. The sum of two intervals is defined by

$$\lfloor a \rceil + \lfloor b \rceil \triangleq \{a + b : a \in \lfloor a \rceil,\ b \in \lfloor b \rceil\}. \tag{4.3}$$

Definition 4.4. Let $\lfloor a \rceil = [\underline{a},\, \overline{a}\,] \in \mathbb{IR}$ and $\lfloor b \rceil = [\underline{b},\, \overline{b}\,] \in \mathbb{IR}$. The difference of two intervals is defined by

$$\lfloor a \rceil - \lfloor b \rceil \triangleq \{a - b : a \in \lfloor a \rceil,\ b \in \lfloor b \rceil\}. \tag{4.4}$$

Definition 4.5. Let $\lfloor a \rceil = [\underline{a},\, \overline{a}\,] \in \mathbb{IR}$ and $\lfloor b \rceil = [\underline{b},\, \overline{b}\,] \in \mathbb{IR}$. The product of two intervals is defined by

$$\lfloor a \rceil \lfloor b \rceil \triangleq \{ab : a \in \lfloor a \rceil,\ b \in \lfloor b \rceil\}. \tag{4.5}$$

[1] Only the ones necessary for this work. Many other aspects on interval analysis can be found in the cited references.

Definition 4.6. Let $\lfloor a \rceil = [\underline{a},\, \overline{a}\,] \in \mathbb{IR}$ and $\lfloor b \rceil = [\underline{b},\, \overline{b}\,] \in \mathbb{IR}$. The quotient of two intervals is defined by

$$\lfloor a \rceil / \lfloor b \rceil \triangleq \{a/b : a \in \lfloor a \rceil,\ b \in \lfloor b \rceil\}, \tag{4.6}$$

provided that $0 \notin \lfloor b \rceil$.

Endpoint expressions for interval arithmetic operations are given by (Moore et al., 2009)

- $\lfloor a \rceil + \lfloor b \rceil = [\underline{a},\, \overline{a}\,] + [\underline{b},\, \overline{b}\,] = [\underline{a} + \underline{b},\, \overline{a} + \overline{b}\,]$,
- $\lfloor a \rceil - \lfloor b \rceil = [\underline{a},\, \overline{a}\,] - [\underline{b},\, \overline{b}\,] = [\underline{a} - \overline{b},\, \overline{a} - \underline{b}\,]$,
- $\lfloor a \rceil \lfloor b \rceil = [\underline{a},\, \overline{a}\,][\underline{b},\, \overline{b}\,] = [\,\min\{\underline{a}\underline{b},\, \underline{a}\overline{b},\, \overline{a}\underline{b},\, \overline{a}\overline{b}\},\ \max\{\underline{a}\underline{b},\, \underline{a}\overline{b},\, \overline{a}\underline{b},\, \overline{a}\overline{b}\}\,]$,
- $\lfloor a \rceil / \lfloor b \rceil = [\underline{a},\, \overline{a}\,]/[\underline{b},\, \overline{b}\,] = [\underline{a},\, \overline{a}\,][1/\overline{b},\ 1/\underline{b}\,]$ if $0 \notin \lfloor b \rceil$,

which can be applied to real numbers as well, by regarding them as degenerate intervals. Interval addition and multiplication are commutative and associative, i.e.,

$$\lfloor a \rceil + \lfloor b \rceil = \lfloor b \rceil + \lfloor a \rceil, \qquad \lfloor a \rceil + (\lfloor b \rceil + \lfloor c \rceil) = (\lfloor a \rceil + \lfloor b \rceil) + \lfloor c \rceil,$$
$$\lfloor a \rceil \lfloor b \rceil = \lfloor b \rceil \lfloor a \rceil, \qquad \lfloor a \rceil (\lfloor b \rceil \lfloor c \rceil) = (\lfloor a \rceil \lfloor b \rceil) \lfloor c \rceil,$$

for any $\lfloor a \rceil$, $\lfloor b \rceil$, $\lfloor c \rceil \in \mathbb{IR}$. Moreover, the intervals $[\,0,\, 0\,]$ and $[\,1,\, 1\,]$ are the identities of the sum and product, respectively. On the other hand, the difference and quotient are not the inverse operations of the sum and product, respectively. The latter can be concluded by verifying that $\lfloor a \rceil - \lfloor a \rceil \neq [\,0,\, 0\,]$ and $\lfloor a \rceil / \lfloor a \rceil \neq [\,1,\, 1\,]$ for a non-degenerate interval $\lfloor a \rceil \in \mathbb{IR}$.

Any interval $\lfloor a \rceil \in \mathbb{IR}$ can be written in terms of its midpoint and diameter, as

$$\lfloor a \rceil = \mathrm{mid}(\lfloor a \rceil) + \frac{1}{2}\mathrm{diam}(\lfloor a \rceil)\,[-1,\ 1\,]. \tag{4.7}$$

Elementary functions of intervals are defined by their ranges over them, such as $\sin \lfloor a \rceil$, $\lfloor a \rceil^2$, $e^{\lfloor a \rceil}$, $\ln \lfloor a \rceil$ and $\sqrt{\lfloor a \rceil}$.

Definition 4.7. An interval vector $\lfloor \boldsymbol{a} \rceil \in \mathbb{IR}^n$, also called a *box*, is defined by

$$\lfloor \boldsymbol{a} \rceil \triangleq \{\boldsymbol{a} \in \mathbb{R}^n : \underline{a}_i \leq a_i \leq \overline{a}_i,\ i = 1, 2, \ldots, n\},$$

where i denotes the i-th element.

Definition 4.8. An interval matrix $\lfloor \boldsymbol{A} \rceil \in \mathbb{IR}^{n \times m}$ is defined by

$$\lfloor \boldsymbol{A} \rceil \triangleq \{\boldsymbol{A} \in \mathbb{R}^{n \times m} : \underline{a}_{ij} \leq a_{ij} \leq \overline{a}_{ij},\ i = 1, 2, \ldots, n,\ j = 1, 2, \ldots, m\},$$

where i denotes the i-line and j-th column element.

The midpoint and diameter are defined component-wise for boxes and interval matrices, yielding real vectors and real matrices, respectively. On the other hand, real vectors and real matrices can be regarded as degenerate boxes and degenerate matrices, respectively.

Interval extensions of real valued functions play an important role in interval analysis. Some of them are now presented.

Definition 4.9 (Natural interval extension)**.** Let $\lfloor \boldsymbol{a} \rceil \in \mathbb{IR}^n$ and $f(\boldsymbol{x})$ be a real valued function, with $\boldsymbol{x} \in \mathbb{R}^n$, composed of arithmetic operations and elementary functions. Then, the natural interval extension of $f(\boldsymbol{x})$ over $\lfloor \boldsymbol{a} \rceil$, denoted by $\square_{\mathrm{N}} \{f(\boldsymbol{x})\}|_{\boldsymbol{x}=\lfloor \boldsymbol{a} \rceil}$, is computed by replacing every occurrence of x_i by $\lfloor a_i \rceil$, $i = 1, 2, \ldots, n$, arithmetic operations by the corresponding interval arithmetic ones, and evaluating the ranges of the elementary functions over the respective $\lfloor a_i \rceil$.

Definition 4.10 (Mean value extension)**.** Let $\lfloor \boldsymbol{a} \rceil \in \mathbb{IR}^n$ and $f(\boldsymbol{x})$ be a real valued function. The mean value extension of $f(\boldsymbol{x})$ over $\lfloor \boldsymbol{a} \rceil$, denoted by $\square_{\mathrm{MV}} \{f(\boldsymbol{x})\}|_{\boldsymbol{x}=\lfloor \boldsymbol{a} \rceil}$, is defined by

$$\square_{\mathrm{MV}} \{f(\boldsymbol{x})\}|_{\boldsymbol{x}=\lfloor \boldsymbol{a} \rceil} \triangleq f(\mathrm{mid}(\lfloor \boldsymbol{a} \rceil)) + \square \{\nabla_{\boldsymbol{x}} f(\boldsymbol{x})\}|_{\boldsymbol{x}=\lfloor \boldsymbol{a} \rceil} \cdot (\lfloor \boldsymbol{a} \rceil - \mathrm{mid}(\lfloor \boldsymbol{a} \rceil)),$$

where $\nabla_{\boldsymbol{x}} f(\boldsymbol{x})$ denotes the gradient of $f(\boldsymbol{x})$ with respect to $\boldsymbol{x}$ (defined as a column vector), $\square \{f\}$ denotes any interval extension of f, and $\cdot$ denotes scalar product.

At last, an important problem that appears in interval analysis is the so-called *interval dependency*. This phenomenon usually occurs when computing an interval extension of a real valued function in which each variable appears several times, yielding overestimated results. For instance, let $f(x) = x - x$, $g(x) = x \cdot x$ and $\lfloor a \rceil = [\,-1,\ 3\,]$. Then,

$$\square_{\mathrm{N}} \{f(x)\}|_{x=\lfloor a \rceil} = [\,-1,\ 3\,] - [\,-1,\ 3\,] = [\,-1-3,\ 3+1\,] = [\,-4,\ 4\,]$$

and

$$\square_{\mathrm{N}} \{g(x)\}|_{x=\lfloor a \rceil} = [\,-1,\ 3\,][\,-1,\ 3\,] = [\,\min\{1, -3, 9\},\ \max\{1, -3, 9\}\,] = [\,-3,\ 9\,],$$

which are overestimated, since it is clear that $f(x) = 0\ \forall x \in \mathbb{R}$ and $g(x) \in [\,0,\ 9\,]\ \forall x \in [\,-1,\ 3\,]$.

4.1.2 Zonotopes

This subsection is mainly based on Alamo et al. (2005) and Le et al. (2013a).

Zonotopes are a special class of convex, symmetric polytopes that have become popular in set-membership techniques due to several properties. Their applications include set-membership state and parameter estimation, system identification and fault detection.

Definition 4.11. The Minkowski sum of two sets $\mathbb{X}, \mathbb{Y} \subset \mathbb{R}^n$ is defined by

$$\mathbb{X} \oplus \mathbb{Y} \triangleq \{\boldsymbol{x} + \boldsymbol{y} : \boldsymbol{x} \in \mathbb{X},\ \boldsymbol{y} \in \mathbb{Y}\}. \tag{4.8}$$

Definition 4.12. Given a vector $\boldsymbol{c} \in \mathbb{R}^n$ and a set of vectors $\{\boldsymbol{g}_1,\ \boldsymbol{g}_2,\ \ldots,\ \boldsymbol{g}_r\}$, with $\boldsymbol{g}_j \in \mathbb{R}^n$, $j \in \{1, 2, \ldots, r\}$, $r \geq n$, a r-zonotope $\mathbb{Z}$ in $\mathbb{R}^n$ is defined by

$$\mathbb{Z} \triangleq \{\boldsymbol{x} \in \mathbb{R}^n : \boldsymbol{x} = \boldsymbol{c} + \sum_{i=1}^{r} \alpha_i \boldsymbol{g}_i,\ |\alpha_i| \leq 1\}, \tag{4.9}$$

where $\boldsymbol{c}$ is called its center, $\boldsymbol{g}_1, \boldsymbol{g}_2, \ldots, \boldsymbol{g}_r$ its generators, and r its order.

Let $\mathbb{B}$ denote the *unitary interval* $[-1,\ 1]$, and $\mathbb{B}^r$ denote a r-dimensional unitary box, which is the Cartesian product of r unitary intervals. A zonotope can be interpreted in terms of the Minkowski sum of line segments. Define the line segment associated with $\boldsymbol{g}_i$ as $\boldsymbol{g}_i\mathbb{B} \triangleq \{\boldsymbol{x} \in \mathbb{R}^n : x = \alpha_i \boldsymbol{g}_i,\ |\alpha_i| \leq 1\}$. Then,

$$\mathbb{Z} = \boldsymbol{c} \oplus \boldsymbol{g}_1\mathbb{B} \oplus \boldsymbol{g}_2\mathbb{B} \oplus \cdots \oplus \boldsymbol{g}_r\mathbb{B}. \tag{4.10}$$

A third, more compact representation of a zonotope is given by an affine transformation of a unitary box. Let $\boldsymbol{G} \triangleq [\boldsymbol{g}_1\ \ \boldsymbol{g}_2\ \ \cdots\ \ \boldsymbol{g}_r] \in \mathbb{R}^{n \times r}$, then

$$\mathbb{Z} = \boldsymbol{c} \oplus \boldsymbol{G}\mathbb{B}^r, \tag{4.11}$$

where $\boldsymbol{G}$ is called its generator matrix. Figure 4.1 illustrates an example of a zonotope.

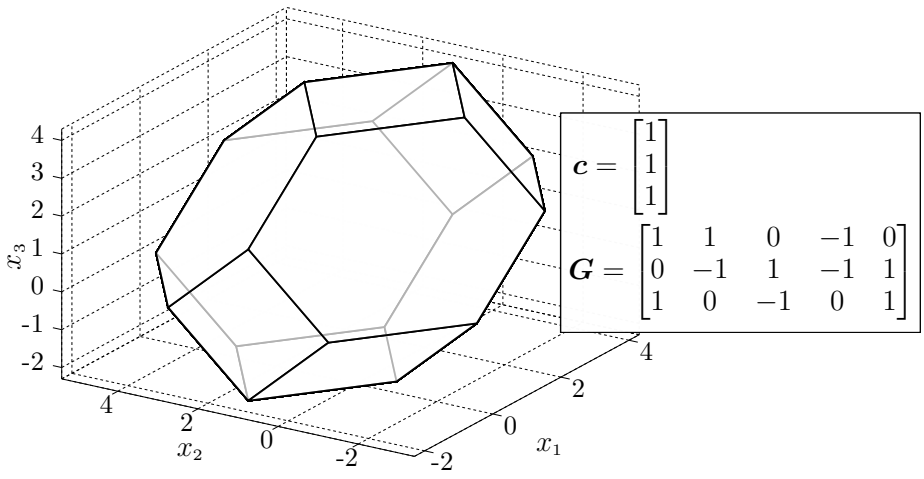

Figure 4.1: A 5-zonotope in $\mathbb{R}^3$.

Zonotopes can represent symmetric polytopes with arbitrary complexity, which increases according to their order. Moreover, they are closed under the Minkowski sum and linear image:

$$\mathbb{Z}_1 \oplus \mathbb{Z}_2 = (\boldsymbol{c}_1 + \boldsymbol{c}_2) \oplus [\boldsymbol{G}_1\ \boldsymbol{G}_2]\mathbb{B}^{r_1+r_2},$$
$$\boldsymbol{A}\mathbb{Z} \triangleq \{\boldsymbol{A}\boldsymbol{x} : \boldsymbol{x} \in \mathbb{Z}\} = (\boldsymbol{A}\boldsymbol{c}) \oplus (\boldsymbol{A}\boldsymbol{G})\mathbb{B}^r.$$

From the commutativity of the Minkowski sum in (4.10), we have also that the columns of the generator matrix of a zonotope can be permuted without modifying the zonotope.

A box is a special case of a zonotope, in which the generator matrix is square and diagonal. Similarly to (4.7), every box $\llcorner \boldsymbol{a} \urcorner \in \mathbb{IR}^n$ can be written as

$$\llcorner \boldsymbol{a} \urcorner = \text{mid}(\llcorner \boldsymbol{a} \urcorner) + \frac{1}{2}\text{diag}(\text{diam}(\llcorner \boldsymbol{a} \urcorner)) \begin{bmatrix} [-1,\ 1] \\ \vdots \\ [-1,\ 1] \end{bmatrix} = \text{mid}(\llcorner \boldsymbol{a} \urcorner) \oplus \frac{1}{2}\text{diag}(\text{diam}(\llcorner \boldsymbol{a} \urcorner))\mathbb{B}^n,$$

where the interval addition was regarded as a Minkowski sum since their definitions are equivalent (see (4.3) and (4.8)).

Theorem 4.1. *(Le et al., 2013a; Kühn, 1998) Consider a zonotope $\mathbb{Z} \triangleq \boldsymbol{c} \oplus \boldsymbol{G}\mathbb{B}^r \subset \mathbb{R}^n$. Then, the smallest box containing $\mathbb{Z}$ is given by $\boldsymbol{c} \oplus rs(\boldsymbol{G})\mathbb{B}^n$, which is also called the* interval hull *of $\mathbb{Z}$, where $rs(\boldsymbol{G})$ (row sum) is a diagonal matrix such that $rs(\boldsymbol{G})_{ii} \triangleq \sum_{j=1}^{r} |\boldsymbol{G}_{ij}|$.*

For convenience, this work regards the interval hull of a zonotope as an "interval extension" of it, i.e.

$$\square\{\mathbb{Z}\} \triangleq \boldsymbol{c} \oplus \text{rs}(\boldsymbol{G})\mathbb{B}^n.$$

Theorem 4.2. *(Alamo et al., 2005) Define a family of zonotopes as $\mathbb{Z}_{\llcorner \urcorner} = \boldsymbol{c} \oplus \llcorner \boldsymbol{G} \urcorner \mathbb{B}^r \triangleq \{\mathbb{Z} = \boldsymbol{c} \oplus \boldsymbol{G}\mathbb{B}^r \subset \mathbb{R}^n : \boldsymbol{G} \in \llcorner \boldsymbol{G} \urcorner\}$, and the* zonotope inclusion *$\diamond\{\mathbb{Z}_{\llcorner \urcorner}\} \triangleq \boldsymbol{c} \oplus [mid(\llcorner \boldsymbol{G} \urcorner)\ \boldsymbol{H}]\mathbb{B}^{n+r}$, where $\boldsymbol{H}_{ii} \triangleq (1/2)\sum_{j=1}^{r} diam\left(\llcorner \boldsymbol{G} \urcorner_{ij}\right)$. Under these definitions, $\diamond\{\mathbb{Z}_{\llcorner \urcorner}\} \supseteq \mathbb{Z}_{\llcorner \urcorner}$.*

4.1.3 Strips

Strips are sets commonly used in set-membership techniques as auxiliary entities.

A strip is a set defined by $\mathbb{S} \triangleq \{\boldsymbol{x} \in \mathbb{R}^n : |\boldsymbol{\rho}^T\boldsymbol{x} - \gamma| \leq \sigma\} \subset \mathbb{R}^n$, bounded by the parallel hyperplanes $\{\boldsymbol{x} \in \mathbb{R}^n : \boldsymbol{\rho}^T\boldsymbol{x} = \gamma + \sigma\}$ and $\{\boldsymbol{x} \in \mathbb{R}^n : \boldsymbol{\rho}^T\boldsymbol{x} = \gamma - \sigma\}$, where γ and σ are real scalars, and $\boldsymbol{\rho} \in \mathbb{R}^n$ (Vicino & Zappa, 1996). Figure 4.2 illustrates an example of a strip in $\mathbb{R}^2$.

4.2 Linearized Kalman filter

This section presents the design of a linearized Kalman filter for the tilt-rotor UAV with suspended load. It is considered a fictitious scenario in which only the first half of the state vector (2.56) is measured, corrupted with additive noise, i.e.,

$$\boldsymbol{y}_k = \boldsymbol{q}_k + \boldsymbol{v}_k = \begin{bmatrix} \mathbb{I}_{10\times 10} & \boldsymbol{0}_{10\times 10} \end{bmatrix} \boldsymbol{x}_k + \boldsymbol{v}_k, \tag{4.12}$$

where $\boldsymbol{v} \in \mathbb{R}^{10}$ corresponds to the measurement noise and $\boldsymbol{q}$ is given by (2.26).

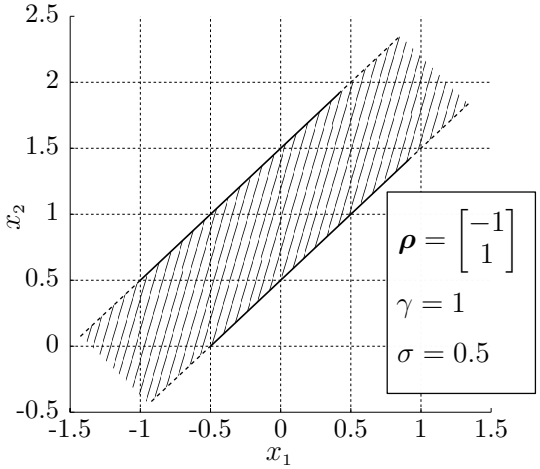

Figure 4.2: A strip in $\mathbb{R}^2$.

4.2.1 State-space equations for Kalman filtering

In order to design a linearized Kalman filter (LKF) to provide the entire state vector, the linearized state-space equations (3.4) are evaluated at an equilibrium point, resulting in a time-invariant system, and discretized using the ZOH method for the controller sampling time T_c, yielding[2]

$$\Delta \boldsymbol{x}_k = \boldsymbol{A}_\mathrm{d} \Delta \boldsymbol{x}_{k-1} + \boldsymbol{B}_\mathrm{d} \Delta \boldsymbol{u}_{k-1} + \boldsymbol{F}_\mathrm{d} \boldsymbol{d}_{k-1} + \boldsymbol{w}_{k-1}, \tag{4.13}$$

with 'd' denoting discrete-time, $\boldsymbol{A}_\mathrm{d} \in \mathbb{R}^{20\times 20}$, $\boldsymbol{B}_\mathrm{d} \in \mathbb{R}^{20\times 4}$, $\boldsymbol{F}_\mathrm{d} \in \mathbb{R}^{20\times 3}$, and $\boldsymbol{w} \in \mathbb{R}^{20}$ represents unmodeled dynamics associated with linearization (truncated terms of the Taylor series expansion).

In order to improve the state estimation, inspired by the work of Rigatos & Raffo (2015), the external disturbances affecting the system are also estimated, by augmenting the state vector $\Delta \boldsymbol{x}$ with the disturbance vector $\boldsymbol{d}$, leading to

$$\underbrace{\begin{bmatrix} \Delta \boldsymbol{x}_k \\ \boldsymbol{d}_k \end{bmatrix}}_{\boldsymbol{\nu}_k} = \underbrace{\begin{bmatrix} \boldsymbol{A}_\mathrm{d} & \boldsymbol{F}_\mathrm{d} \\ \boldsymbol{0}_{3\times 20} & \mathbb{I}_{3\times 3} \end{bmatrix}}_{\boldsymbol{A}_\nu} \underbrace{\begin{bmatrix} \Delta \boldsymbol{x}_{k-1} \\ \boldsymbol{d}_{k-1} \end{bmatrix}}_{\boldsymbol{\nu}_{k-1}} + \underbrace{\begin{bmatrix} \boldsymbol{B}_\mathrm{d} \\ \boldsymbol{0}_{3\times 4} \end{bmatrix}}_{\boldsymbol{B}_\nu} \Delta \boldsymbol{u}_{k-1} + \underbrace{\begin{bmatrix} \boldsymbol{w}_{k-1} \\ \tilde{\boldsymbol{d}}_{k-1} \end{bmatrix}}_{\bar{\boldsymbol{w}}_{k-1}},$$

where $\tilde{\boldsymbol{d}}_{k-1} \triangleq \boldsymbol{d}_k - \boldsymbol{d}_{k-1}$. Moreover, rewriting the measurement equation (4.12) as a function of the augmented state vector yields

$$\Delta \boldsymbol{y}_k = \underbrace{\left[\begin{array}{cc|c} \mathbb{I}_{10\times 10} & \boldsymbol{0}_{10\times 10} & \boldsymbol{0}_{10\times 3} \end{array}\right]}_{\boldsymbol{H}_\nu} \underbrace{\begin{bmatrix} \Delta \boldsymbol{x}_k \\ \boldsymbol{d}_k \end{bmatrix}}_{\boldsymbol{\nu}_k} + \boldsymbol{v}_k,$$

where $\Delta \boldsymbol{y}_k = \boldsymbol{y}_k - \boldsymbol{y}^\mathrm{eq} = \boldsymbol{y}_k - \boldsymbol{q}^\mathrm{eq}$. Therefore, the discrete-time state-space equations to be

[2] In order to avoid misleading, $(\cdot)^\mathrm{tr} \triangleq (\cdot)^\mathrm{eq}$ and $\delta(\cdot) \triangleq \Delta(\cdot)$.

used in the linearized Kalman filter algorithm are given by

$$\boldsymbol{\nu}_k = \boldsymbol{A}_\nu \boldsymbol{\nu}_{k-1} + \boldsymbol{B}_\nu \Delta \boldsymbol{u}_{k-1} + \bar{\boldsymbol{w}}_{k-1}, \tag{4.14}$$

$$\Delta \boldsymbol{y}_k = \boldsymbol{H}_\nu \boldsymbol{\nu}_k + \boldsymbol{v}_k. \tag{4.15}$$

Remark 4.1. *As mentioned in Chapter 3, due to limited computational resources, an analytical expression for $\boldsymbol{A}_c(t)$ could not be obtained. Hence, if the linearization were performed around the desired trajectory or the estimated state vector, instead of an equilibrium point, it would not be possible without making $\boldsymbol{A}_c(t) \approx \boldsymbol{A}_c(t)|_{\boldsymbol{u}^{tr}=\boldsymbol{u}^{eq}}$, which in turn leads to estimation error. The same fact also prevents the use of an Extended Kalman Filter, for instance, since the knowledge of an analytical expression of the Jacobian matrix of the system would be required.*

4.2.2 Filter algorithm

The linear Kalman filter, proposed by Kalman (1960), is a two-step optimal state estimator with predictor-corrector structure, whose algorithm is based on the propagation of mean and covariance of Gaussian distributions through linear discrete-time dynamic systems.

To design a LKF based on the state-space equations (4.14)-(4.15), the unmodelled dynamics $\bar{\boldsymbol{w}}$ are regarded as process noise. Moreover, $\bar{\boldsymbol{w}}$ and $\boldsymbol{v}$ are assumed to be white, uncorrelated signals with zero-mean Gaussian distribution, and known, constant covariance matrices denoted by $\boldsymbol{P}^{\boldsymbol{w}} \in \mathbb{R}^{23\times 23}$ and $\boldsymbol{P}^{\boldsymbol{v}} \in \mathbb{R}^{10\times 10}$, respectively.

Let $\hat{(\cdot)}$ denote estimated variables, and $(\cdot)_{m|n}$ denote information at time instant m given measurements up to instant n. Furthermore, suppose that previously estimated states $\hat{\boldsymbol{\nu}}_{k-1|k-1}$ are available. Then, the state vector $\hat{\boldsymbol{\nu}}_{k|k-1}$ is given through propagation of mean values in (4.14), yielding the *prediction step*

$$\hat{\boldsymbol{\nu}}_{k|k-1} = \boldsymbol{A}_\nu \hat{\boldsymbol{\nu}}_{k-1|k-1} + \boldsymbol{B}_\nu \Delta \boldsymbol{u}_{k-1},$$

whilst $\hat{\boldsymbol{\nu}}_{k|k}$ is given by the *correction step*, defined as

$$\hat{\boldsymbol{\nu}}_{k|k} = \hat{\boldsymbol{\nu}}_{k|k-1} + \boldsymbol{N}_k(\Delta \boldsymbol{y}_k - \boldsymbol{H}_\nu \hat{\boldsymbol{\nu}}_{k|k-1}),$$

being $\boldsymbol{N}_k$ the so-called *Kalman gain*.

Define $\tilde{\boldsymbol{\nu}}_k \triangleq \boldsymbol{\nu}_k - \hat{\boldsymbol{\nu}}_{k|k}$ as the estimation error, and let $\boldsymbol{P}^{\nu}_{k|k} \triangleq \mathcal{E}\left[\tilde{\boldsymbol{\nu}}_k \tilde{\boldsymbol{\nu}}_k^T\right]$, where $\mathcal{E}[\cdot]$ denotes expected value. Then, propagation of covariances in (4.14) yields

$$\boldsymbol{P}^{\nu}_{k|k-1} = \boldsymbol{A}_\nu \boldsymbol{P}^{\nu}_{k-1|k-1} \boldsymbol{A}_\nu^T + \boldsymbol{P}^{\boldsymbol{w}},$$

whilst propagation of covariances in the correction step yields

$$\boldsymbol{P}^{\boldsymbol{\nu}}_{k|k} = (\mathbb{I}_{20\times 20} - \boldsymbol{N}_k \boldsymbol{H}_{\boldsymbol{\nu}}) \boldsymbol{P}^{\boldsymbol{\nu}}_{k|k-1} (\mathbb{I}_{20\times 20} - \boldsymbol{N}_k \boldsymbol{H}_{\boldsymbol{\nu}})^T + \boldsymbol{N}_k \boldsymbol{P}^{\boldsymbol{v}} \boldsymbol{N}_k^T.$$

The Kalman gain is computed in such a way that the LKF provides estimates with minimum-variance error, i.e., the cost function

$$J_{\text{LKF}} = \text{tr}\left\{\boldsymbol{P}^{\boldsymbol{\nu}}_{k|k}\right\}$$

is minimized. The solution of this optimization problem is given by the gain update equation (Simon, 2006)

$$\boldsymbol{N}_k = \boldsymbol{P}^{\boldsymbol{\nu}}_{k|k-1} \boldsymbol{H}^T_{\boldsymbol{\nu}} (\boldsymbol{H}_{\boldsymbol{\nu}} \boldsymbol{P}^{\boldsymbol{\nu}}_{k|k-1} \boldsymbol{H}^T_{\boldsymbol{\nu}} + \boldsymbol{P}^{\boldsymbol{v}})^{-1}.$$

The design of the LKF lies in the appropriate choice of the covariance matrices $\boldsymbol{P}^{\boldsymbol{w}}$, $\boldsymbol{P}^{\boldsymbol{v}}$, and $\boldsymbol{P}^{\boldsymbol{\nu}}_{0|0}$, and also the initial estimate $\hat{\boldsymbol{\nu}}_{0|0}$. In the case of the tilt-rotor UAV with suspended load, for the considered scenario, $\boldsymbol{P}^{\boldsymbol{v}}$ is given according to the measurement noise $\boldsymbol{v}_k$, while $\boldsymbol{P}^{\boldsymbol{w}}$ and $\boldsymbol{P}^{\boldsymbol{\nu}}_{0|0}$ must be chosen by trial and error. For instance, $\boldsymbol{P}^{\boldsymbol{\nu}}_{0|0}$ should be chosen such that $\boldsymbol{P}^{\boldsymbol{\nu}}_{k|k}$ does not significantly changes over time (Simon, 2006, p. 140), and $\boldsymbol{P}^{\boldsymbol{w}}$ can first be chosen sufficiently small and adjusted incrementally by verifying the estimation error consistency of innovation whiteness (Candy, 2009, Section 5.7). The LKF algorithm based on the dynamic system (4.14)-(4.15) is summarized in Algorithm 4.1.

Algorithm 4.1 Linearized Kalman filter algorithm

procedure LKF($\hat{\boldsymbol{\nu}}_{k-1|k-1}, \Delta\boldsymbol{u}_{k-1}, \boldsymbol{y}_k, \boldsymbol{P}^{\boldsymbol{w}}, \boldsymbol{P}^{\boldsymbol{v}}, \boldsymbol{P}^{\boldsymbol{\nu}}_{k-1|k-1}$)
  $\hat{\boldsymbol{\nu}}_{k|k-1} \leftarrow \boldsymbol{A}_{\boldsymbol{\nu}} \hat{\boldsymbol{\nu}}_{k-1|k-1} + \boldsymbol{B}_{\boldsymbol{\nu}} \Delta\boldsymbol{u}_{k-1}$
  $\boldsymbol{P}^{\boldsymbol{\nu}}_{k|k-1} \leftarrow \boldsymbol{A}_{\boldsymbol{\nu}} \boldsymbol{P}^{\boldsymbol{\nu}}_{k-1|k-1} \boldsymbol{A}^T_{\boldsymbol{\nu}} + \boldsymbol{P}^{\boldsymbol{w}}$
  $\boldsymbol{N}_k \leftarrow \boldsymbol{P}^{\boldsymbol{\nu}}_{k|k-1} \boldsymbol{H}^T_{\boldsymbol{\nu}} (\boldsymbol{H}_{\boldsymbol{\nu}} \boldsymbol{P}^{\boldsymbol{\nu}}_{k|k-1} \boldsymbol{H}^T_{\boldsymbol{\nu}} + \boldsymbol{P}^{\boldsymbol{v}})^{-1}$
  $\hat{\boldsymbol{\nu}}_{k|k} \leftarrow \hat{\boldsymbol{\nu}}_{k|k-1} + \boldsymbol{N}_k (\Delta\boldsymbol{y}_k - \boldsymbol{H}_{\boldsymbol{\nu}} \hat{\boldsymbol{\nu}}_{k|k-1})$
  $\boldsymbol{P}^{\boldsymbol{\nu}}_{k|k} \leftarrow (\mathbb{I}_{20\times 20} - \boldsymbol{N}_k \boldsymbol{H}_{\boldsymbol{\nu}}) \boldsymbol{P}^{\boldsymbol{\nu}}_{k|k-1} (\mathbb{I}_{20\times 20} - \boldsymbol{N}_k \boldsymbol{H}_{\boldsymbol{\nu}})^T + \boldsymbol{N}_k \boldsymbol{P}^{\boldsymbol{v}} \boldsymbol{N}_k^T$
  return $\hat{\boldsymbol{\nu}}_{k|k}$, $\boldsymbol{P}^{\boldsymbol{\nu}}_{k|k}$
end procedure

4.3 Zonotopic state estimator

This section presents the design of a zonotopic state estimator (ZSE) for the tilt-rotor UAV with suspended load. A more realistic scenario is considered, in which the load's position and orientation are not directly measured. The following sensors are assumed to be available:

- A Global Positioning System (GPS) equipment, providing the position of the UAV[3]

[3]In this work, the position and orientation of the UAV refer to the origin and orientation of the

with respect to the inertial reference frame $\mathcal{I}$, along axes x and y;

- A barometer, providing the position of the UAV with respect to $\mathcal{I}$, along axis z;
- An Inertial Measurement Unit (IMU), providing the orientation and angular velocity of the UAV with respect to $\mathcal{I}$, the latter expressed in the geometric center frame $\mathcal{B}$;
- A camera, providing the position of the load with respect to the UAV, expressed in $\mathcal{B}$;
- Embedded sensors at the servomotors, providing the tilting angles and their time derivatives.

Moreover, the provided information is assumed to be corrupted with additive noise, and each sensor has its own sampling time.

4.3.1 Measurement equation

The objective of this subsection is to obtain an equation of the form $\boldsymbol{y}_k = \boldsymbol{\pi}(\boldsymbol{x}_k) + \boldsymbol{v}_k$, to be used in the zonotopic state estimation algorithm, where $\boldsymbol{y}_k$ is the measured vector at time instant k, and $\boldsymbol{v}_k$ correspond to measurement noise.

Let $\boldsymbol{\xi}_{\mathcal{B}} \triangleq [x_{\mathcal{B}}\ y_{\mathcal{B}}\ z_{\mathcal{B}}]^T$ denote the position of the UAV with respect to $\mathcal{I}$, shown in Figure 4.3. Then, the following holds

$$\boldsymbol{\xi}_{\mathcal{B}}(\boldsymbol{\xi}, \boldsymbol{\eta}) = \boldsymbol{\xi} + \boldsymbol{R}^{\mathcal{I}}_{\mathcal{L}} \boldsymbol{d}^{\mathcal{L}}_{\mathcal{B}}. \tag{4.16}$$

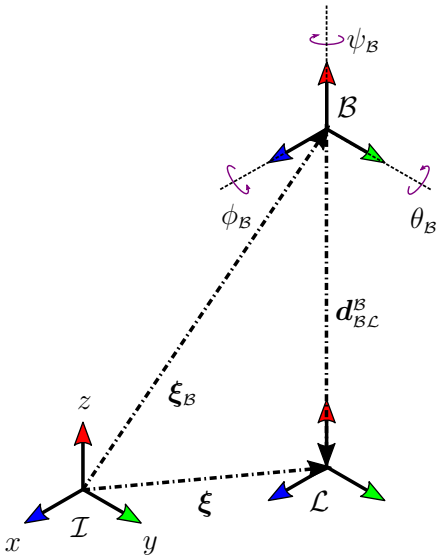

Figure 4.3: Position and orientation of the tilt-rotor UAV, and load's position, as measured from the available sensors.

geometric center frame $\mathcal{B}$, respectively.

The orientation of the aircraft with respect to $\mathcal{I}$, analogously to the load's one, is assumed to be parametrized by Euler angles, denoted by $\boldsymbol{\eta}_{\mathcal{B}} \triangleq [\phi_{\mathcal{B}}\ \theta_{\mathcal{B}}\ \psi_{\mathcal{B}}]^T$, using the local roll-pitch-yaw convention. Therefore,

$$\boldsymbol{R}_{\mathcal{B}}^{\mathcal{I}} \triangleq \boldsymbol{R}_{z,\psi_{\mathcal{B}}}\boldsymbol{R}_{y,\theta_{\mathcal{B}}}\boldsymbol{R}_{x,\phi_{\mathcal{B}}} = \begin{bmatrix} \mathrm{c}_{\psi_{\mathcal{B}}}\mathrm{c}_{\theta_{\mathcal{B}}} & \mathrm{c}_{\psi_{\mathcal{B}}}\mathrm{s}_{\theta_{\mathcal{B}}}\mathrm{s}_{\phi_{\mathcal{B}}} - \mathrm{s}_{\psi_{\mathcal{B}}}\mathrm{c}_{\phi_{\mathcal{B}}} & \mathrm{c}_{\psi_{\mathcal{B}}}\mathrm{s}_{\theta_{\mathcal{B}}}\mathrm{c}_{\phi_{\mathcal{B}}} + \mathrm{s}_{\psi_{\mathcal{B}}}\mathrm{s}_{\phi_{\mathcal{B}}} \\ \mathrm{s}_{\psi_{\mathcal{B}}}\mathrm{c}_{\theta_{\mathcal{B}}} & \mathrm{s}_{\psi_{\mathcal{B}}}\mathrm{s}_{\theta_{\mathcal{B}}}\mathrm{s}_{\phi_{\mathcal{B}}} + \mathrm{c}_{\psi_{\mathcal{B}}}\mathrm{c}_{\phi_{\mathcal{B}}} & \mathrm{s}_{\psi_{\mathcal{B}}}\mathrm{s}_{\theta_{\mathcal{B}}}\mathrm{c}_{\phi_{\mathcal{B}}} - \mathrm{c}_{\psi_{\mathcal{B}}}\mathrm{s}_{\phi_{\mathcal{B}}} \\ -\mathrm{s}_{\theta_{\mathcal{B}}} & \mathrm{c}_{\theta_{\mathcal{B}}}\mathrm{s}_{\phi_{\mathcal{B}}} & \mathrm{c}_{\theta_{\mathcal{B}}}\mathrm{c}_{\phi_{\mathcal{B}}} \end{bmatrix}.$$

However, we have also that $\boldsymbol{R}_{\mathcal{B}}^{\mathcal{I}} = \boldsymbol{R}_{\mathcal{L}}^{\mathcal{I}}\boldsymbol{R}_{\mathcal{B}}^{\mathcal{L}}$. Hence, if $\theta_{\mathcal{B}} \neq \pm\pi/2$,

$$\phi_{\mathcal{B}}(\boldsymbol{\eta},\boldsymbol{\gamma}) = \arctan\left(\frac{(\boldsymbol{R}_{\mathcal{L}}^{\mathcal{I}}\boldsymbol{R}_{\mathcal{B}}^{\mathcal{L}})_{32}}{(\boldsymbol{R}_{\mathcal{L}}^{\mathcal{I}}\boldsymbol{R}_{\mathcal{B}}^{\mathcal{L}})_{33}}\right), \tag{4.17}$$

$$\theta_{\mathcal{B}}(\boldsymbol{\eta},\boldsymbol{\gamma}) = \arcsin\left(-(\boldsymbol{R}_{\mathcal{L}}^{\mathcal{I}}\boldsymbol{R}_{\mathcal{B}}^{\mathcal{L}})_{31}\right), \tag{4.18}$$

$$\psi_{\mathcal{B}}(\boldsymbol{\eta},\boldsymbol{\gamma}) = \arctan\left(\frac{(\boldsymbol{R}_{\mathcal{L}}^{\mathcal{I}}\boldsymbol{R}_{\mathcal{B}}^{\mathcal{L}})_{21}}{(\boldsymbol{R}_{\mathcal{L}}^{\mathcal{I}}\boldsymbol{R}_{\mathcal{B}}^{\mathcal{L}})_{11}}\right). \tag{4.19}$$

The angular velocity provided by the IMU is given by

$$\boldsymbol{\omega}_{\mathcal{I}\mathcal{B}}^{\mathcal{B}}(\boldsymbol{\eta},\boldsymbol{\gamma},\dot{\boldsymbol{\eta}},\dot{\boldsymbol{\gamma}}) = \boldsymbol{\omega}_{\mathcal{I}\mathcal{L}}^{\mathcal{B}} + \boldsymbol{\omega}_{\mathcal{L}\mathcal{B}}^{\mathcal{B}} = (\boldsymbol{R}_{\mathcal{B}}^{\mathcal{L}})^T\boldsymbol{W}_{\boldsymbol{\eta}}\dot{\boldsymbol{\eta}} + \boldsymbol{Q}\dot{\boldsymbol{\gamma}}, \tag{4.20}$$

where $\boldsymbol{\eta} = [\phi\ \theta\ \psi]^T$ are the Euler angles parametrizing the orientation of the load with respect to $\mathcal{I}$, $\boldsymbol{\gamma} = [\gamma_1\ \gamma_2]^T$ are the angles describing the orientation of the UAV with respect to the rod, $\boldsymbol{W}_{\boldsymbol{\eta}}$ and $\boldsymbol{Q}$ are defined in (2.17) and (2.18), respectively.

Let $\boldsymbol{d}_{\mathcal{B}\mathcal{L}}^{\mathcal{B}}$ denotes the displacement vector from $\mathcal{B}$ to $\mathcal{L}$, expressed in $\mathcal{B}$, which is the measurement provided by the camera (see Figure 4.3). Therefore,

$$\boldsymbol{d}_{\mathcal{B}\mathcal{L}}^{\mathcal{B}}(\boldsymbol{\gamma}) = -\boldsymbol{d}_{\mathcal{L}\mathcal{B}}^{\mathcal{B}} = -(\boldsymbol{R}_{\mathcal{B}}^{\mathcal{L}})^T\boldsymbol{d}_{\mathcal{L}\mathcal{B}}^{\mathcal{L}} \triangleq -(\boldsymbol{R}_{\mathcal{B}}^{\mathcal{L}})^T\boldsymbol{d}_{\mathcal{B}}^{\mathcal{L}}. \tag{4.21}$$

Gathering (4.16)-(4.21) along with the system states α_{R}, α_{L}, $\dot{\alpha}_{\mathrm{R}}$ and $\dot{\alpha}_{\mathrm{L}}$, and adding the measurement noise $\boldsymbol{v}_k$, leads to the nonlinear measurement equation

$$\boldsymbol{y}_k = \boldsymbol{\pi}(\boldsymbol{x}_k) + \boldsymbol{v}_k \triangleq \begin{bmatrix} \boldsymbol{\xi}_{\mathcal{B}}(\boldsymbol{\xi},\boldsymbol{\eta}) \\ \phi_{\mathcal{B}}(\boldsymbol{\eta},\boldsymbol{\gamma}) \\ \theta_{\mathcal{B}}(\boldsymbol{\eta},\boldsymbol{\gamma}) \\ \psi_{\mathcal{B}}(\boldsymbol{\eta},\boldsymbol{\gamma}) \\ \boldsymbol{\omega}_{\mathcal{I}\mathcal{B}}^{\mathcal{B}}(\boldsymbol{\eta},\boldsymbol{\gamma},\dot{\boldsymbol{\eta}},\dot{\boldsymbol{\gamma}}) \\ \boldsymbol{d}_{\mathcal{B}\mathcal{L}}^{\mathcal{B}}(\boldsymbol{\gamma}) \\ \alpha_{\mathrm{R}} \\ \alpha_{\mathrm{L}} \\ \dot{\alpha}_{\mathrm{R}} \\ \dot{\alpha}_{\mathrm{L}} \end{bmatrix} + \boldsymbol{v}_k = \begin{bmatrix} \boldsymbol{\xi} + \boldsymbol{R}_{\mathcal{B}}^{\mathcal{I}}\boldsymbol{d}_{\mathcal{B}}^{\mathcal{L}} \\ \arctan\left((\boldsymbol{R}_{\mathcal{L}}^{\mathcal{I}}\boldsymbol{R}_{\mathcal{B}}^{\mathcal{L}})_{32}/(\boldsymbol{R}_{\mathcal{L}}^{\mathcal{I}}\boldsymbol{R}_{\mathcal{B}}^{\mathcal{L}})_{33}\right) \\ \arcsin\left(-(\boldsymbol{R}_{\mathcal{L}}^{\mathcal{I}}\boldsymbol{R}_{\mathcal{B}}^{\mathcal{L}})_{31}\right) \\ \arctan\left((\boldsymbol{R}_{\mathcal{L}}^{\mathcal{I}}\boldsymbol{R}_{\mathcal{B}}^{\mathcal{L}})_{21}/(\boldsymbol{R}_{\mathcal{L}}^{\mathcal{I}}\boldsymbol{R}_{\mathcal{B}}^{\mathcal{L}})_{11}\right) \\ (\boldsymbol{R}_{\mathcal{B}}^{\mathcal{L}})^T\boldsymbol{W}_{\boldsymbol{\eta}}\dot{\boldsymbol{\eta}} + \boldsymbol{Q}\dot{\boldsymbol{\gamma}} \\ -(\boldsymbol{R}_{\mathcal{B}}^{\mathcal{L}})^T\boldsymbol{d}_{\mathcal{B}}^{\mathcal{L}} \\ \alpha_{\mathrm{R}} \\ \alpha_{\mathrm{L}} \\ \dot{\alpha}_{\mathrm{R}} \\ \dot{\alpha}_{\mathrm{L}} \end{bmatrix} + \boldsymbol{v}_k, \tag{4.22}$$

with $\boldsymbol{y}_k, \boldsymbol{v}_k \in \mathbb{R}^{16}$.

4.3.2 Zonotopic state estimation algorithm

This subsection presents the state estimation algorithm proposed by Alamo et al. (2005) for nonlinear, single-output discrete-time systems, based on zonotopes and strips. According to Kühn (1998), orbits of discrete-time systems can be bounded by zonotopes with sub-exponential overestimation.

Consider the nonlinear discrete-time system

$$\begin{aligned} \boldsymbol{x}_k &= \boldsymbol{f}(\boldsymbol{x}_{k-1}, \boldsymbol{w}_{k-1}), \\ y_k &= g(\boldsymbol{x}_k, \boldsymbol{v}_k), \end{aligned} \tag{4.23}$$

where $\boldsymbol{x}_k \in \mathbb{R}^{n_x}$ are the system states, $y_k \in \mathbb{R}$ is the system measurement, $\boldsymbol{w}_k \in \mathbb{R}^{n_w}$ represents process disturbances and parametric uncertainties, and $\boldsymbol{v}_k \in \mathbb{R}^{n_v}$ represents measurement noise. Assume that $\boldsymbol{w}_k$, $\boldsymbol{v}_k$, and $\boldsymbol{x}_0$ belong to known compact sets $\mathbb{W}$, $\mathbb{V}$ and $\mathbb{X}_0$, respectively.

Given the compact set $\mathbb{X}_{k-1}$, such that $\boldsymbol{x}_{k-1} \in \mathbb{X}_{k-1}$, the *uncertain trajectory* of the system (4.23) is defined as the set of values that the time update equation $\boldsymbol{f}$ achieve for all possible $\boldsymbol{x}_{k-1} \in \mathbb{X}_{k-1}$ and $\boldsymbol{w} \in \mathbb{W}$, denoted by $\boldsymbol{f}(\mathbb{X}_{k-1}, \mathbb{W})$. Moreover, given the measured output y_k, the *consistent state set* is defined as $\mathbb{X}_{y_k} \triangleq \{\boldsymbol{x} \in \mathbb{R}^{n_x} : y_k \in g(\boldsymbol{x}, \mathbb{V})\}$, and the *exact uncertain state set* is defined as the intersection between the uncertain trajectory of the system and the consistent state set, denoted as $\mathbb{X}_k \triangleq \boldsymbol{f}(\mathbb{X}_{k-1}, \mathbb{W}) \cap \mathbb{X}_{y_k}$.

Suppose that a previously estimated set $\hat{\mathbb{X}}_{k-1}$ is available. Then, a zonotope $\bar{\mathbb{X}}_k$ bounding the uncertain trajectory $\boldsymbol{f}(\hat{\mathbb{X}}_{k-1}, \mathbb{W})$ can be obtained through the following theorem.

Theorem 4.3 (Generalization of Kühn's method)**.** *(Alamo et al., 2005) Given a function $\boldsymbol{f}(\boldsymbol{x}, \boldsymbol{w})$ with $\boldsymbol{x} \in \mathbb{X} \subset \mathbb{R}^{n_x}$ and $\boldsymbol{w} \in \mathbb{W} \subset \mathbb{R}^{n_w}$, in which $\mathbb{X} \triangleq \boldsymbol{c}_x \oplus \boldsymbol{G}_x \mathbb{B}^{r_x}$ and $\mathbb{W} \triangleq \boldsymbol{c}_w \oplus \boldsymbol{G}_w \mathbb{B}^{r_w}$ are known zonotopes. Define*

- *A zonotope $\mathbb{Z}_q \triangleq \boldsymbol{c}_q \oplus \boldsymbol{G}_q \mathbb{B}^{r_q}$ such that $\boldsymbol{f}(\boldsymbol{c}_x, \mathbb{W}) \subseteq \mathbb{Z}_q$;*
- *An interval matrix $\llcorner \boldsymbol{M} \urcorner \triangleq \square\{\nabla_{\boldsymbol{x}} \boldsymbol{f}(\mathbb{X}, \mathbb{W})\}\boldsymbol{G}_x$;*
- *A zonotope $\mathbb{Z}_\Psi \triangleq \mathbb{Z}_q \oplus \diamond\{\llcorner \boldsymbol{M} \urcorner \mathbb{B}^{r_x}\}$.*

Then, $\mathbb{Z}_\Psi \supseteq \boldsymbol{f}(\mathbb{X}, \mathbb{W})$.

This operation is called *prediction step*, as an analogy to the Kalman filter algorithm. Moreover, given the measured output y_k and the zonotope $\bar{\mathbb{X}}_k$, a strip $\bar{\mathbb{X}}_{y_k}$, such that $\bar{\mathbb{X}}_k \cap \mathbb{X}_{y_k} \subseteq \bar{\mathbb{X}}_k \cap \bar{\mathbb{X}}_{y_k}$, can be computed through the following theorem.

Theorem 4.4. *(Alamo et al., 2005) Given the zonotope $\bar{\mathbb{X}}_k \subset \mathbb{R}^{n_x}$ and the measured output y_k, compute by means of interval arithmetic, $\boldsymbol{\rho} \in \mathbb{R}^{n_x}$, $s \in \mathbb{R}$ and $\sigma \in \mathbb{R}$, such that*

- $\boldsymbol{\rho} = mid\Big(\square\{\nabla_{\boldsymbol{x}} g(\bar{\mathbb{X}}_k, \mathbb{V})\}\Big)$;
- $\boldsymbol{\rho}^T \bar{\mathbb{X}}_k - g(\bar{\mathbb{X}}_k, \mathbb{V}) \subseteq [s - \sigma,\ s + \sigma]$.

Then, $\bar{\mathbb{X}}_k \cap \mathbb{X}_{y_k} \subseteq \bar{\mathbb{X}}_k \cap \bar{\mathbb{X}}_{y_k}$, *where* $\bar{\mathbb{X}}_{y_k} \triangleq \{\boldsymbol{x} \in \mathbb{R}^{n_x} : |\boldsymbol{\rho}^T \boldsymbol{x} - y_k - s| \leq \sigma\}$.

A zonotope bounding the intersection $\bar{\mathbb{X}}_k \cap \bar{\mathbb{X}}_{y_k}$ is obtained through the next theorem.

Theorem 4.5. *(Alamo et al., 2005) Given a zonotope* $\mathbb{Z} \triangleq \boldsymbol{c} \oplus \boldsymbol{G}\mathbb{B}^r \subset \mathbb{R}^n$, *a strip* $\mathbb{S} \triangleq \{\boldsymbol{x} \in \mathbb{R}^n : |\boldsymbol{\rho}^T \boldsymbol{x} - \gamma| \leq \sigma\}$ *and a vector* $\boldsymbol{\lambda} \in \mathbb{R}^n$. *Define*

- $\boldsymbol{c}_I(\boldsymbol{\lambda}) \triangleq \boldsymbol{c} + \boldsymbol{\lambda}(\gamma - \boldsymbol{\rho}^T \boldsymbol{c})$;
- $\boldsymbol{G}_I(\boldsymbol{\lambda}) \triangleq [(\mathbb{I}_{n\times n} - \boldsymbol{\lambda}\boldsymbol{\rho}^T)\boldsymbol{G}\ \ \sigma\boldsymbol{\lambda}]$.

Then, $\mathbb{Z} \cap \mathbb{S} \subseteq \mathbb{Z}_I(\boldsymbol{\lambda}) \triangleq \boldsymbol{c}_I(\boldsymbol{\lambda}) \oplus \boldsymbol{G}_I(\boldsymbol{\lambda})\mathbb{B}^{r+1}$.

The last two operations together are called *update step*[4]. The resulting zonotope is parametrized by a vector $\boldsymbol{\lambda} \in \mathbb{R}^{n_x}$, which is chosen according to specific criteria. A choice that minimizes the Frobenius norm of its generator matrix is given by the next theorem.

Theorem 4.6. *(Alamo et al., 2005) Let* $\mathbb{Z}_I(\boldsymbol{\lambda}) = \boldsymbol{c}_I(\boldsymbol{\lambda}) \oplus \boldsymbol{G}_I(\boldsymbol{\lambda})\mathbb{B}^{r+1} \subset \mathbb{R}^n$, *where* $\boldsymbol{c}_I(\boldsymbol{\lambda}) \triangleq \boldsymbol{c} + \boldsymbol{\lambda}(\gamma - \boldsymbol{\rho}^T \boldsymbol{c})$ *and* $\boldsymbol{G}_I(\boldsymbol{\lambda}) \triangleq [(\mathbb{I}_{n\times n} - \boldsymbol{\lambda}\boldsymbol{\rho}^T)\boldsymbol{G}\ \ \sigma\boldsymbol{\lambda}]$. *Then,* $\boldsymbol{\lambda} = (\boldsymbol{G}\boldsymbol{G}^T\boldsymbol{\rho})/(\boldsymbol{\rho}^T\boldsymbol{G}\boldsymbol{G}^T\boldsymbol{\rho} + \sigma^2)$ *minimizes the Frobenius norm of* $\boldsymbol{G}_I(\boldsymbol{\lambda})$.

The ZSE algorithm is composed of the aforementioned steps, being summarized in the Algorithm 4.2. Although formulated for single-output systems, the ZSE can be applied to multi-output systems, by performing the update step using each element of the measurement vector in an iterative manner (Le et al., 2013b). Moreover, the ability of dealing with measurements individually allows it to handle situations in which the measurement vector is incomplete, which happens, for instance, when available sensors have different sampling times.

Algorithm 4.2 Zonotopic state estimator algorithm

1: Compute the zonotope $\bar{\mathbb{X}}_k \supseteq \boldsymbol{f}(\hat{\mathbb{X}}_{k-1}, \mathbb{W})$ by means of Theorem 4.3
2: Compute the strip $\bar{\mathbb{X}}_{y_k}$ by means of Theorem 4.4
3: Compute the zonotope $\hat{\mathbb{X}}_k(\boldsymbol{\lambda}) \supseteq \bar{\mathbb{X}}_k \cap \bar{\mathbb{X}}_{y_k}$ by means of Theorem 4.5

[4]The terminologies *prediction step* and *update step* are not used in Alamo et al. (2005), but in the more recent work of Le et al. (2013b).

4.3.3 ZSE for the tilt-rotor UAV with suspended load

Despite the state estimator being formulated for nonlinear systems, the computational burden of bounding the uncertain trajectory for (2.57) through Theorem 4.3 is very high[5]. Therefore, the linear discrete-time system (4.13) is used instead. Moreover, as well as in the linearized Kalman filter design, the state vector $\Delta\boldsymbol{x}$ is augmented with the disturbances vector $\boldsymbol{d}$, thus the time update equation to be used in the prediction step is given by

$$\boldsymbol{\nu}_k = \boldsymbol{A}_{\boldsymbol{\nu}}\boldsymbol{\nu}_{k-1} + \boldsymbol{B}_{\boldsymbol{\nu}}\Delta\boldsymbol{u}_{k-1} + \bar{\boldsymbol{w}}_{k-1}, \tag{4.24}$$

with $\boldsymbol{\nu} \in \mathbb{R}^{23}$, $\boldsymbol{A}_{\boldsymbol{\nu}} \in \mathbb{R}^{23\times 23}$, $\boldsymbol{B}_{\boldsymbol{\nu}} \in \mathbb{R}^{23\times 4}$ and $\bar{\boldsymbol{w}} \in \mathbb{R}^{23}$.

Assume that $\boldsymbol{\nu}_{k-1}$ and $\bar{\boldsymbol{w}}$ belong to zonotopes $\hat{\mathbb{X}}_{k-1} \triangleq \boldsymbol{c}_{\hat{x}_{k-1}} \oplus \boldsymbol{G}_{\hat{x}_{k-1}}\mathbb{B}^{r_{\hat{x}_{k-1}}}$ and $\bar{\mathbb{W}} \triangleq \boldsymbol{c}_{\bar{w}} \oplus \boldsymbol{G}_{\bar{w}}\mathbb{B}^{r_{\bar{w}}}$, respectively. Applying Theorem 4.3 to equation (4.24) yields

$$\begin{aligned}
\mathbb{Z}_q &= (\boldsymbol{A}_{\boldsymbol{\nu}}\boldsymbol{\nu}_{k-1} + \boldsymbol{B}_{\boldsymbol{\nu}}\Delta\boldsymbol{u}_{k-1} + \bar{\boldsymbol{w}}_{k-1})\big|_{\bar{\boldsymbol{w}}_k=\bar{\mathbb{W}}}^{\boldsymbol{\nu}_{k-1}=\boldsymbol{c}_{\hat{x}_{k-1}}} \\
&= \boldsymbol{A}_{\boldsymbol{\nu}}\boldsymbol{c}_{\hat{x}_{k-1}} \oplus \boldsymbol{B}_{\boldsymbol{\nu}}\Delta\boldsymbol{u}_{k-1} \oplus \bar{\mathbb{W}} \\
&= \boldsymbol{A}_{\boldsymbol{\nu}}\boldsymbol{c}_{\hat{x}_{k-1}} \oplus \boldsymbol{B}_{\boldsymbol{\nu}}\Delta\boldsymbol{u}_{k-1} \oplus \boldsymbol{c}_{\bar{w}} \oplus \boldsymbol{G}_{\bar{w}}\mathbb{B}^{r_{\bar{w}}} \\
&= (\boldsymbol{A}_{\boldsymbol{\nu}}\boldsymbol{c}_{\hat{x}_{k-1}} + \boldsymbol{B}_{\boldsymbol{\nu}}\Delta\boldsymbol{u}_{k-1} + \boldsymbol{c}_{\bar{w}}) \oplus \boldsymbol{G}_{\bar{w}}\mathbb{B}^{r_{\bar{w}}},
\end{aligned}$$

$$\begin{aligned}
{}_{\llcorner}\boldsymbol{M}^{\urcorner} &= \square\left\{\nabla_{\boldsymbol{\nu}}(\boldsymbol{A}_{\boldsymbol{\nu}}\boldsymbol{\nu}_{k-1} + \boldsymbol{B}_{\boldsymbol{\nu}}\Delta\boldsymbol{u}_{k-1} + \bar{\boldsymbol{w}}_{k-1})\right\}\big|_{\bar{\boldsymbol{w}}_{k-1}=\bar{\mathbb{W}}}^{\boldsymbol{\nu}_{k-1}=\hat{\mathbb{X}}_{k-1}}\boldsymbol{G}_{\hat{x}_{k-1}} \\
&= \square\left\{\boldsymbol{A}_{\boldsymbol{\nu}}\right\}\big|_{\bar{\boldsymbol{w}}_{k-1}=\bar{\mathbb{W}}}^{\boldsymbol{\nu}_{k-1}=\hat{\mathbb{X}}_{k-1}}\boldsymbol{G}_{\hat{x}_{k-1}} = \boldsymbol{A}_{\boldsymbol{\nu}}\boldsymbol{G}_{\hat{x}_{k-1}},
\end{aligned}$$

$$\diamond\{{}_{\llcorner}\boldsymbol{M}^{\urcorner}\mathbb{B}^{r_{\hat{x}_{k-1}}}\} = \diamond\{\boldsymbol{A}_{\boldsymbol{\nu}}\boldsymbol{G}_{\hat{x}_{k-1}}\mathbb{B}^{r_{\hat{x}_{k-1}}}\} = \boldsymbol{A}_{\boldsymbol{\nu}}\boldsymbol{G}_{\hat{x}_{k-1}}\mathbb{B}^{r_{\hat{x}_{k-1}}},$$

$$\begin{aligned}
\bar{\mathbb{X}}_k &= \mathbb{Z}_q \oplus \diamond\{{}_{\llcorner}\boldsymbol{M}^{\urcorner}\mathbb{B}^{r_{\hat{x}_{k-1}}}\} = (\boldsymbol{A}_{\boldsymbol{\nu}}\boldsymbol{c}_{\hat{x}_{k-1}} + \boldsymbol{B}_{\boldsymbol{\nu}}\Delta\boldsymbol{u}_{k-1} + \boldsymbol{c}_{\bar{w}}) \oplus \boldsymbol{G}_{\bar{w}}\mathbb{B}^{r_{\bar{w}}} \oplus \boldsymbol{A}_{\boldsymbol{\nu}}\boldsymbol{G}_{\hat{x}_{k-1}}\mathbb{B}^{r_{\hat{x}_{k-1}}} \\
&= (\boldsymbol{A}_{\boldsymbol{\nu}}\boldsymbol{c}_{\hat{x}_{k-1}} + \boldsymbol{B}_{\boldsymbol{\nu}}\Delta\boldsymbol{u}_{k-1} + \boldsymbol{c}_{\bar{w}}) \oplus [\boldsymbol{G}_{\bar{w}} \;\; \boldsymbol{A}_{\boldsymbol{\nu}}\boldsymbol{G}_{\hat{x}_{k-1}}]\mathbb{B}^{r_{\bar{w}}+r_{\hat{x}_{k-1}}}
\end{aligned} \tag{4.25}$$

Hence, the prediction step is performed through equation (4.25). For the update step, the nonlinear mapping (4.22) can be used for obtaining the strip $\bar{\mathbb{X}}_{\boldsymbol{y}_k(i)}$, by means of Theorem 4.4, where $\boldsymbol{y}_k(i)$ stands for i-th element of $\boldsymbol{y}_k$. The whole predicted set $\bar{\mathbb{X}}_k$ appears at least twice in the computation of the parameters s and σ, which is made through interval arithmetic. Therefore, due to interval dependency, it may result in a very large strip such that the intersection is $\bar{\mathbb{X}}_k$ itself. The following theorem shows that this problem can be avoided if the measurement equation is linear.

[5]It is necessary to perform interval extensions on the gradient of the time-update equation (obtained through Euler approximation of (2.57), for instance) at each time step. As mentioned in Chapter 3, due to limited computational resources, an analytical expression for $\boldsymbol{M}(\boldsymbol{q})^{-1}$ could not be obtained, hence neither for $\boldsymbol{\varphi}(\boldsymbol{x}, \boldsymbol{u}, \boldsymbol{d})$, which is needed for computing an analytical expression for the gradient.

Lemma 4.1. *Consider the predicted zonotope* $\bar{\mathbb{X}}_k$ *and the linear measurement equation* $\boldsymbol{y}_k = \boldsymbol{g}(\boldsymbol{x}_k, \boldsymbol{v}_k) \triangleq \boldsymbol{H}\boldsymbol{x}_k + \boldsymbol{v}_k$*, where* $\boldsymbol{y} \in \mathbb{R}^{n_y}$ *are the measured outputs,* $\boldsymbol{x} \in \mathbb{R}^{n_x}$ *are the system states,* $\boldsymbol{v} \in \mathbb{V}$*,* $\mathbb{V} \triangleq \boldsymbol{c}_v \oplus \boldsymbol{G}_v \mathbb{B}^{r_v} \subset \mathbb{R}^{n_y}$ *corresponds to measurement noise, and* $\boldsymbol{H} \in \mathbb{R}^{n_y \times n_x}$*. If interval extensions are performed properly, the strip obtained through Theorem 4.4 using the* i*-th element of the measured vector does not depend on* $\bar{\mathbb{X}}_k$*.*

Proof. Consider the measurement equation $\boldsymbol{y}_k(i) = \boldsymbol{g}(i)(\boldsymbol{x}_k, \boldsymbol{v}_k)$, where (i) denotes i-th line. From Theorem 4.4,

$$\begin{aligned}\boldsymbol{\rho} &= \operatorname{mid}\Big(\square\left\{\nabla_{\boldsymbol{x}}(\boldsymbol{g}(i)(\boldsymbol{x}_k, \boldsymbol{v}_k))\right\}|_{\boldsymbol{v}_k=\mathbb{V}}^{\boldsymbol{x}_k=\bar{\mathbb{X}}_k}\Big) = \operatorname{mid}\Big(\square\left\{\nabla_{\boldsymbol{x}}(\boldsymbol{H}(i)\boldsymbol{x}_k + \boldsymbol{v}_k(i))\right\}|_{\boldsymbol{v}_k=\mathbb{V}}^{\boldsymbol{x}_k=\bar{\mathbb{X}}_k}\Big) \\ &= \operatorname{mid}\Big(\square\left\{\boldsymbol{H}(i)^T\right\}|_{\boldsymbol{v}_k=\mathbb{V}}^{\boldsymbol{x}_k=\bar{\mathbb{X}}_k}\Big) = \operatorname{mid}(\boldsymbol{H}(i)^T) = \boldsymbol{H}(i)^T.\end{aligned}$$

Moreover, define $\boldsymbol{h}(\boldsymbol{x}_k, \boldsymbol{v}_k) \triangleq \boldsymbol{\rho}^T\boldsymbol{x}_k - \boldsymbol{g}(i)(\boldsymbol{x}_k, \boldsymbol{v}_k)$. Then,

$$\square\left\{\boldsymbol{h}(\boldsymbol{x}_k, \boldsymbol{v}_k)\right\}|_{\boldsymbol{v}_k=\mathbb{V}}^{\boldsymbol{x}_k=\bar{\mathbb{X}}_k} = \square\left\{\boldsymbol{\rho}^T\boldsymbol{x}_k - (\boldsymbol{H}(i)\boldsymbol{x}_k + \boldsymbol{v}_k(i))\right\}|_{\boldsymbol{v}_k=\mathbb{V}}^{\boldsymbol{x}_k=\bar{\mathbb{X}}_k} = \square\left\{\boldsymbol{H}(i)\boldsymbol{x}_k - \boldsymbol{H}(i)\boldsymbol{x}_k - \boldsymbol{v}_k(i)\right\}|_{\boldsymbol{v}_k=\mathbb{V}}^{\boldsymbol{x}_k=\bar{\mathbb{X}}_k}.$$

Depending on the adopted interval extension, interval dependency may occur due to $\boldsymbol{H}(i)\boldsymbol{x}_k - \boldsymbol{H}(i)\boldsymbol{x}_k$, which is not zero in interval arithmetic. This issue is avoided by performing the subtraction *before* the interval extension, yielding

$$\begin{aligned}\square\left\{-\boldsymbol{v}_k(i)\right\}|_{\boldsymbol{v}_k=\mathbb{V}}^{\boldsymbol{x}_k=\bar{\mathbb{X}}_k} &= -\left(\boldsymbol{c}_v \oplus \operatorname{rs}\left(\boldsymbol{G}_v\right)\mathbb{B}^{r_v}\right)(i) = -\left(\boldsymbol{c}_v(i) \oplus \sum_{j=1}^{r_v}|\boldsymbol{G}_v(i,j)|\mathbb{B}\right) \\ &= \left[-\boldsymbol{c}_v(i) - \sum_{j=1}^{r_v}|\boldsymbol{G}_v(i,j)|,\ \ -\boldsymbol{c}_v(i) + \sum_{j=1}^{r_v}|\boldsymbol{G}_v(i,j)|\right] \triangleq [s-\sigma,\ s+\sigma],\end{aligned}$$

where (i,j) denotes the element from the i-th line and j-th column. Hence, the strip parameters are given by $\boldsymbol{\rho} = \boldsymbol{H}(i)^T$, $s = -\boldsymbol{c}_v(i)$, and $\sigma = \sum_{j=1}^{r_v}|\boldsymbol{G}_v(i,j)|$, which do not depend on any parameter of the predicted zonotope $\bar{\mathbb{X}}_k$. ■

Based on this fact, the measurement equations (4.22) are also linearized around an equilibrium point, yielding

$$\boldsymbol{y}_k - \boldsymbol{\pi}(\boldsymbol{x}^{\text{eq}}) = \boldsymbol{H}_{\text{d}}\Delta\boldsymbol{x}_k + \boldsymbol{v}_k, \quad \boldsymbol{H}_{\text{d}} \triangleq \left.\frac{\partial\boldsymbol{\pi}(\boldsymbol{x})}{\partial\boldsymbol{x}}\right|_{\boldsymbol{x}=\boldsymbol{x}^{\text{eq}}} \in \mathbb{R}^{16\times 20},$$

with $\boldsymbol{v}$ now including unmodeled dynamics due to linearization. The last equation can be rewritten as

$$\boldsymbol{y}_k = \underbrace{\begin{bmatrix}\boldsymbol{H}_{\text{d}} & \boldsymbol{0}_{16\times 3}\end{bmatrix}}_{\boldsymbol{H}_{\boldsymbol{\nu}}}\underbrace{\begin{bmatrix}\Delta\boldsymbol{x}_k \\ \boldsymbol{d}_k\end{bmatrix}}_{\boldsymbol{\nu}_k} + \underbrace{\boldsymbol{\pi}(\boldsymbol{x}^{\text{eq}}) + \boldsymbol{v}_k}_{\bar{\boldsymbol{v}}_k}.$$

Therefore, the measurement equations to be used in the update step are given by

$$\boldsymbol{y}_k = \boldsymbol{H}_{\boldsymbol{\nu}}\boldsymbol{\nu}_k + \bar{\boldsymbol{v}}_k, \tag{4.26}$$

with $\boldsymbol{H_\nu} \in \mathbb{R}^{16\times 23}$.

Consider the predicted zonotope $\bar{\mathbb{X}}_k \triangleq \boldsymbol{c}_{\bar{x}_k} \oplus \boldsymbol{G}_{\bar{x}_k}\mathbb{B}^{r_{\bar{x}_k}}$, and assume that $\bar{\boldsymbol{v}} \in \bar{\mathbb{V}}$, where $\bar{\mathbb{V}} \triangleq \boldsymbol{c}_{\bar{v}} \oplus \boldsymbol{G}_{\bar{v}}\mathbb{B}^{r_{\bar{v}}}$. Hence, Theorems 4.4, 4.5, and 4.6, and equation (4.26), yield the update step for the i-th element of the measured vector $\boldsymbol{y}_k$,

$$\hat{\mathbb{X}}_k = (\boldsymbol{c}_{\bar{x}_k} + \boldsymbol{\lambda}(\boldsymbol{y}_k(i) + s - \boldsymbol{\rho}^T\boldsymbol{c}_{\bar{x}_k})) \oplus [(\mathbb{I}_{23\times 23} - \boldsymbol{\lambda}\boldsymbol{\rho}^T)\boldsymbol{G}_{\bar{x}_k} \;\; \sigma\boldsymbol{\lambda}]\mathbb{B}^{r_{\bar{x}_k}+1}, \tag{4.27}$$

with $\boldsymbol{\rho} = \boldsymbol{H_\nu}(i)^T$, $s = -\boldsymbol{c}_{\bar{v}}(i)$, $\sigma = \sum_{j=1}^{r_{\bar{v}}} |\boldsymbol{G}_{\bar{v}}(i,j)|$ and

$$\boldsymbol{\lambda} = \frac{\boldsymbol{G}_{\bar{x}_k}\boldsymbol{G}_{\bar{x}_k}^T\boldsymbol{\rho}}{\boldsymbol{\rho}^T\boldsymbol{G}_{\bar{x}_k}\boldsymbol{G}_{\bar{x}_k}^T\boldsymbol{\rho} + \sigma^2}.$$

Note from (4.25) and (4.27) that the order of $\hat{\mathbb{X}}_k$ increases at each time step. Algorithm 4.3, proposed by Combastel (2003), corresponds to an order reduction technique that can be used in order to prevent it from increasing indefinitely, by computing a lower-order zonotope bounding $\hat{\mathbb{X}}_k$.

Algorithm 4.3 Zonotope order reduction algorithm

```
procedure ORDER_REDUCTION(X̂_k, r_max)
    H ← columns of G_{x̂_k} ordered in decreasing Euclidean norm
    H_T ← first r_max − n_x columns of H
    for i = 1, ..., n_x do
        Q_ii ← Σ_{j=r_max−n_x+1}^{r_{x̂_k}} |H_ij|
    end for
    X̂_k ← c_{x̂_k} ⊕ [H_T Q]B^{r_max}
    return X̂_k
end procedure
```

Denote $\mathbb{I}_k$ as the set of available measurements at time instant k, which is given according to the sensors' sampling times. Then, gathering (4.25) for performing the prediction step, and (4.27) for performing the update step, the latter iteratively for all $i \in \mathbb{I}_k$, yields the Algorithm 4.4.

The design of the zonotopic state estimator lies in the appropriate choice of the zonotopes $\bar{\mathbb{W}}$ and $\bar{\mathbb{V}}$. On the other hand, a zonotope containing the system's initial states, $\bar{\mathbb{X}}_0$, must also be proposed, to which an *initial update step* must be applied, using initial measurements $\boldsymbol{y}_0$, in order to obtain $\hat{\mathbb{X}}_0$.

Finally, as a drawback from using linearized state-space equations in the zonotopic state estimation algorithm, the property $\boldsymbol{\nu}_k \in \hat{\mathbb{X}}_k$ is guaranteed only if the chosen zonotopes $\bar{\mathbb{W}}$ and $\bar{\mathbb{V}}$ contain all the linearization effects. Moreover, by augmenting the state vector with the external disturbances, bounds must be assumed on their variations within the controller sampling time, instead of bounds on their magnitudes.

Algorithm 4.4 Zonotopic state estimator for the tilt-rotor UAV with suspended load

procedure ZSE($\hat{\mathbb{X}}_{k-1}, \Delta\boldsymbol{u}_{k-1}, \boldsymbol{y}_k, \bar{\mathbb{W}}, \bar{\mathbb{V}}, \mathbb{I}_k, r_{\max}$)
  $\bar{\mathbb{X}}_k \leftarrow (\boldsymbol{A_\nu} \boldsymbol{c}_{\hat{x}_{k-1}} + \boldsymbol{B_\nu} \Delta\boldsymbol{u}_{k-1} + \boldsymbol{c}_{\bar{w}}) \oplus [\boldsymbol{G}_{\bar{w}} \;\; \boldsymbol{A_\nu} \boldsymbol{G}_{\hat{x}_{k-1}}] \mathbb{B}^{r_{\bar{w}} + r_{\hat{x}_{k-1}}}$
  $\tilde{\mathbb{X}}_k \leftarrow \bar{\mathbb{X}}_k$
  for all $i \in \mathbb{I}_k$ **do**
    $\boldsymbol{\rho} \leftarrow \boldsymbol{H_\nu}(i)^T$
    $s \leftarrow -\boldsymbol{c}_{\bar{v}}(i)$
    $\sigma \leftarrow \sum_{j=1}^{r_{\bar{v}}} |\boldsymbol{G}_{\bar{v}}(i,j)|$
    $\boldsymbol{\lambda} \leftarrow (\boldsymbol{G}_{\tilde{x}_k} \boldsymbol{G}_{\tilde{x}_k}^T \boldsymbol{\rho}) / (\boldsymbol{\rho}^T \boldsymbol{G}_{\tilde{x}_k} \boldsymbol{G}_{\tilde{x}_k}^T \boldsymbol{\rho} + \sigma^2)$
    $\tilde{\mathbb{X}}_k \leftarrow (\boldsymbol{c}_{\tilde{x}_k} + \boldsymbol{\lambda}(\boldsymbol{y}_k(i) + s - \boldsymbol{\rho}^T \boldsymbol{c}_{\tilde{x}_k})) \oplus [(\mathbb{I}_{23\times 23} - \boldsymbol{\lambda}\boldsymbol{\rho}^T)\boldsymbol{G}_{\tilde{x}_k} \;\; \sigma\boldsymbol{\lambda}] \mathbb{B}^{r_{\tilde{x}_k}+1}$
  end for
  $\hat{\mathbb{X}}_k \leftarrow \tilde{\mathbb{X}}_k$
  $\hat{\mathbb{X}}_k \leftarrow$ order_reduction($\hat{\mathbb{X}}_k, r_{\max}$)
  return $\hat{\mathbb{X}}_k$
end procedure

4.4 Final remarks

This chapter described the design of state estimFators for providing full information about the system states to the state-feedback controllers, considering scenarios in which incomplete and corrupted with noise state information is available.

Assuming a scenario in which only the generalized coordinates are measured, corrupted with zero-mean Gaussian noise, a linearized Kalman filter was proposed for estimation of the entire state vector. The filter was designed based on discrete-time linearized dynamics, augmented with external disturbances for improved state estimation, in which unmodeled dynamics due to linearization were regarded as process noise.

A second scenario was considered, in which the load's position and orientation w.r.t. to the inertial frame are not directly measured. Available sensors provided information about the aircraft's position, orientation and angular velocity, and the position of the load with respect to the UAV. Unknown but bounded noise was considered, without assumptions on probability distributions, and sensors were assumed to have different sampling times. A zonotopic state estimator was proposed for estimation of the entire state vector.

The next chapter presents simulation results to evaluate the control and state estimation strategies developed so far, in which different trajectories are tracked by the suspended load, in the presence of external disturbances.

5 Simulation results

In the previous chapters, dynamic equations were obtained for the tilt-rotor UAV with suspended load, formulated from the load's perspective, and state-feedback control strategies were designed for path tracking control of the suspended load. Furthermore, state estimation algorithms were also proposed, considering different situations with respect to available measurements.

This chapter evaluates the proposed control and state estimation strategies through simulations in MATLAB/Simulink® environment. Three scenarios are addressed, concerning available measurements: (i) full state information, in which the entire state vector is measured without noise, at every time instant; (ii) the linearized Kalman filter scenario, described in Section 4.2; and (iii) the zonotopic state estimator scenario, described in Section 4.3. Two trajectories are explored, and the suspended load is subject to external disturbances.

The chapter is organized as follows: Section 5.1 presents the physical parameters of the tilt-rotor UAV with suspended load, desired trajectories, external disturbances and performance indexes considered in the simulations; Sections 5.2, 5.3, and 5.4 present and discuss simulation results for the first, second and third scenarios, respectively; and Section 5.5 discusses comparative results between scenarios.

5.1 Simulation specifications

5.1.1 System parameters

Table 5.1 shows the physical parameters of the tilt-rotor UAV with suspended load, for the dynamic model (2.55) (see also Figure 2.4). The UAV's mass, inertia and displacement parameters were obtained from a Computed Aided Design (CAD) model of the ProVANT UAV 2.0, designed in Solidworks® software, illustrated in Figure 2.3. The gravitational acceleration was considered constant, and the parameters k_τ and b are the same considered in Almeida (2014) and Donadel (2015). The parameters λ_{R} and λ_{L} are given according to the direction of rotation of the UAV's propellers: the right propeller rotates counter-clockwise, and the left propeller rotates clockwise. The parameters related to the suspended load, i.e., its mass and inertia matrix, as well as the rod's length and the viscous friction constant, are the same considered in Almeida (2014).

Table 5.1: Physical parameters of the tilt-rotor UAV with suspended load.

Parameter	Value
$m_{\mathcal{L}}$	0.05000 Kg
m_1	1.70249 Kg
m_2, m_3	0.13973 Kg
$\boldsymbol{d}^{\mathcal{L}}_{\mathcal{B}}$	$[0 \;\; 0 \;\; 0.5]^T$ m
$\boldsymbol{d}^{\mathcal{B}}_{\mathcal{C}_1}$	$[-0.00433 \;\; 0.00060 \;\; -0.04559]^T$ m
$\boldsymbol{d}^{\mathcal{B}}_{\mathcal{C}_2}$	$[0.00002 \;\; -0.27761 \;\; 0.05493]^T$ m
$\boldsymbol{d}^{\mathcal{B}}_{\mathcal{C}_3}$	$[0.00077 \;\; 0.27761 \;\; 0.05493]^T$ m
$\boldsymbol{I}_{\mathcal{L}}$	$2.645 \cdot 10^{-6} \cdot \mathbb{I}_{3\times 3}$ Kg·m^2
$\boldsymbol{I}_1$	$\begin{bmatrix} 3697.66749 & 0.36342 & -9.51029 \\ * & 840.10403 & 0.61804 \\ * & * & 3865.05354 \end{bmatrix} \cdot 10^{-6}$ Kg·m^2
$\boldsymbol{I}_2$	$\begin{bmatrix} 441.68245 & 0 & 0 \\ * & 441.67985 & -1.07006 \\ * & * & 0.64418 \end{bmatrix} \cdot 10^{-6}$ Kg·m^2
$\boldsymbol{I}_3$	$\begin{bmatrix} 441.68245 & 0 & 0 \\ * & 441.67985 & 1.07006 \\ * & * & 0.64418 \end{bmatrix} \cdot 10^{-6}$ Kg·m^2
$\hat{\boldsymbol{g}}$	$[0 \;\; 0 \;\; -9.81]^T$ m/s^2
k_τ	$1.7 \cdot 10^{-7}$ N·m·s^2
b	$9.5 \cdot 10^{-6}$ N·s^2
$(\lambda_{\mathrm{R}}, \lambda_{\mathrm{L}})$	$(1, -1)$
β	5^{o}
μ_γ	0.005 N·m/(rad/s)

These physical parameters resulted in the following equilibrium point[1]:

[1] Computed using Simulink's linear analysis tool, which implements optimization algorithms to find an equilibrium point of the system based on specified constraints.

$$\begin{aligned} \boldsymbol{q}^{\text{eq}} &= [0\ \ 0\ \ 0\ \ 0\ \ 0\ \ 0\ \ 0.00015321\ \ 0.02808172\ \ 0.02820590\ \ 0.02774474]^T, \\ \dot{\boldsymbol{q}}^{\text{eq}} &= \mathbf{0}_{10\times 1}, \quad \boldsymbol{u}^{\text{eq}} = [9.98729372\ \ 10.02221862\ \ 0\ \ 0]^T. \end{aligned} \tag{5.1}$$

The equilibrium values were used to obtain the linearized state-space equations described in Chapters 3 and 4. Moreover, the actuators of the aircraft are assumed to saturate at given values, as shown in Table 5.2.

Table 5.2: Saturation levels of the aircraft's actuators.

Control input	Minimum value	Maximum value
f_{R}	0 N	30 N
f_{L}	0 N	30 N
$\tau_{\alpha_{\text{R}}}$	-2 N·m	2 N·m
$\tau_{\alpha_{\text{L}}}$	-2 N·m	2 N·m

The controller sampling time was chosen as $T_c = 12$ ms, which is the highest sampling time of the actuators available for the ProVANT UAV 2.0. For this sampling time and the physical parameters in Table 5.1, using the theorems presented in Section 3.1.2, the discrete-time system (3.9) is controllable, and system (4.14)-(4.15) is observable. On the other hand, the observability of system (4.24)-(4.26), which corresponds to the scenario with different sampling times, could not be verified using theorem (3.2), since not every measurement is available at each time instant. However, considering linear state-space equations obtained from removing elements from the measurement vector, only the linear system associated with the complete measurement vector was verified to be observable.

5.1.2 Desired trajectories

Two reference trajectories were specified for path tracking of the suspended load. The first one is a circular trajectory in the three-dimensional Euclidean space, defined by

$$x^{\text{tr}}(t) = 2\cos\left(\frac{\pi t}{20}\right)\text{m}, \quad y^{\text{tr}}(t) = 2\sin\left(\frac{\pi t}{20}\right)\text{m}, \quad z^{\text{tr}}(t) = 9 - 8\cos\left(\frac{\pi t}{20}\right)\text{m},$$

in which the initial position of the load is displaced by 30 cm from the desired trajectory in each axis: $x(0) = 1.7$ m, $y(0) = 0.3$ m and $z(0) = 0.7$ m. This trajectory was proposed in order to evaluate the performance of the designed control and state estimation strategies in a scenario without aggressive maneuvers. Figure 5.1 illustrates this trajectory.

The second trajectory, defined in Table 5.3, is composed of several connected paths. The initial position of the load is displaced by 30 cm from the desired trajectory along axes x and y: $x(0) = 0.3$ m, $y(0) = -0.3$ m and $z(0) = 0$ m. This trajectory was proposed to evaluate the performance of the designed strategies in a more diversified scenario, starting with vertical take-off in a spiral path, straight line following with rapid changing

in direction, and vertical landing. Figure 5.2 illustrates the second trajectory. In both cases, the initial conditions of the remaining states are equilibrium values, and $\psi^{\text{tr}} = 0$ rad.

Table 5.3: Paths composing the second reference trajectory.

Time (sec)	$x^{\text{tr}}(t)$ (m)	$y^{\text{tr}}(t)$ (m)	$z^{\text{tr}}(t)$ (m)
$0 \leq t < 10$	$0.01t^2 \cos\left(\frac{\pi t}{4}\right)$	$\sin\left(\frac{\pi t}{20}\right) \sin\left(\frac{\pi t}{4}\right)$	$2.5 - 2.5\cos\left(\frac{\pi t}{10}\right)$
$10 \leq t < 19$	$-\frac{\pi}{4}(t-10)$	1	5
$19 \leq t < 20$	$-\frac{9\pi}{4} - 0.5\sin\left(\frac{\pi}{2}(t-19)\right)$	$1.5 - 0.5\cos\left(\frac{\pi}{2}(t-19)\right)$	5
$20 \leq t < 29$	$-\frac{9\pi}{4} - 0.5$	$1.5 + \frac{\pi}{4}(t-20)$	5
$29 \leq t < 30$	$-\frac{9\pi}{4} - 0.5\cos\left(\frac{\pi}{2}(t-29)\right)$	$1.5 + \frac{9\pi}{4} + 0.5\sin\left(\frac{\pi}{2}(t-29)\right)$	5
$30 \leq t < 40$	$-\frac{9\pi}{4} + \frac{\pi}{4}(t-30)$	$2 + \frac{9\pi}{4}$	5
$40 \leq t$	$-\frac{pi}{80}t^2 + \frac{5\pi}{4}t - \frac{119\pi}{4}$	$2 + \frac{9\pi}{4}$	$2.5 + 2.5\cos\left(\frac{\pi}{10}(t-40)\right)$

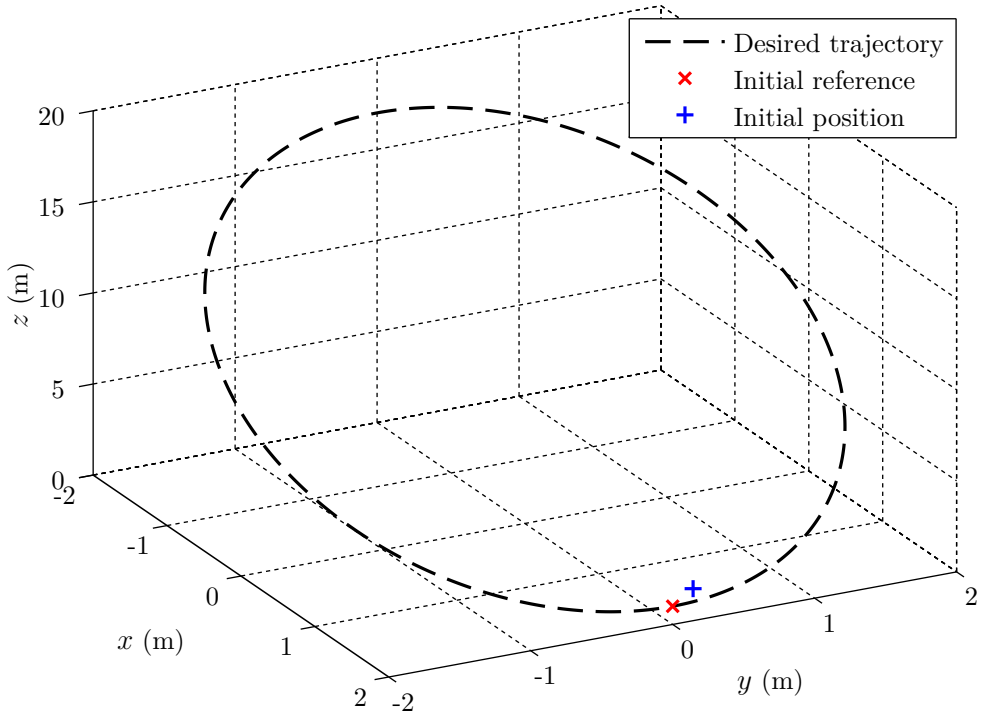

Figure 5.1: The first reference trajectory. The initial reference position and initial position of the load are also depicted.

5.1.3 External disturbances

In order to evaluate the disturbance compensation capabilities of the proposed strategies, external forces are applied to the suspended load as the path tracking is performed. Figures 5.3 and 5.4 show the disturbance profiles for the desired trajectories, which represent sustained wind gusts affecting the load, and consist of steps filtered by first order filters with time constant equal to 0.5 seconds[2]. The profiles differ one from another only by the

[2]Filtering was necessary since the disturbance variations within the controller sampling time must be bounded in order to design the zonotopic state estimator.

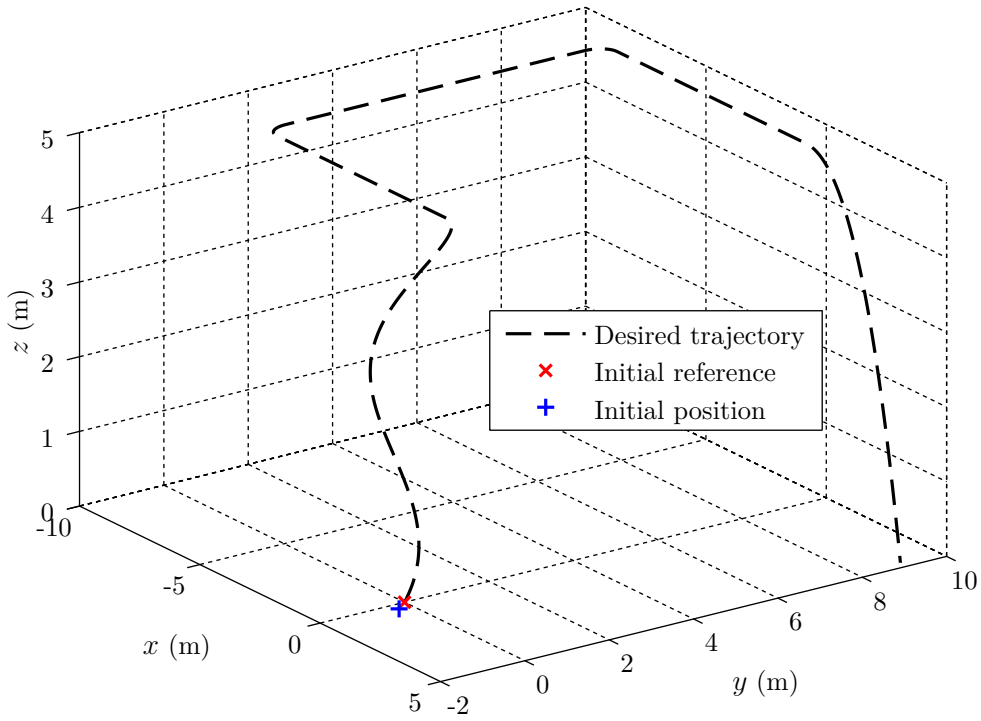

Figure 5.2: The second reference trajectory. The initial reference position and initial position of the load are also depicted.

time of application of the disturbances, which is given according to the simulation total time.

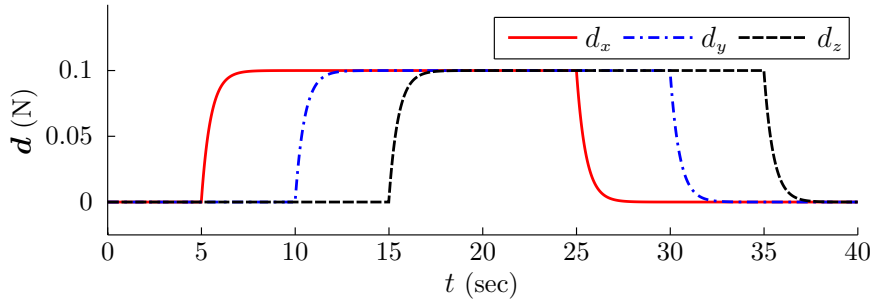

Figure 5.3: Disturbance profile for the first reference trajectory.

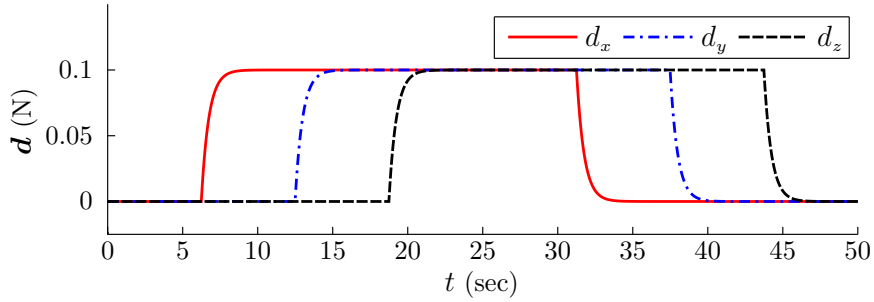

Figure 5.4: Disturbance profile for the second reference trajectory.

The magnitude of the disturbances may look low at a first glance, however the mass of

the load is very small (0.05 Kg), as shown in Table 5.1. Therefore, the resulting acceleration is somewhat considerable[3].

5.1.4 Performance indexes

In order to analyze the performance of the designed controllers, two indexes are employed. The first one is the Integral Square Error (ISE) index, defined by

$$\text{ISE} \triangleq \int_0^{t_\text{f}} e^2 \, \mathrm{d}t,$$

where e denotes the tracking error over the variable of interest, and t_f denotes final time. The ISE index is a measure of the energy of the tracking error accumulated over time, and will be used to analyze which controller performed a more accurate trajectory tracking. The second one is the Integrated Absolute Derivative of the Control signal (IADU) index, defined by

$$\text{IADU} \triangleq \int_0^{t_\text{f}} \left| \frac{\mathrm{d}u}{\mathrm{d}t} \right| \, \mathrm{d}t,$$

where u denotes the control signal of interest. The IADU is a measure of the control effort necessary to perform the trajectory tracking, and will be used to conclude which controller generated smoother control signals for the aircraft actuators.

5.2 Full state information scenario

To evaluate the performance of the proposed controllers for the ideal conditions based on which they were designed, this section presents simulation results considering a scenario in which the whole state vector (2.56) is measured, at every time instant and without noise. It is further referenced as the full state information (FSI) scenario.

The adopted control structure is shown in Figure 5.5. The feedback connection is made with the system states, which are sampled by a zero-order-holder. Blocks denoted by "$\boldsymbol{\chi}$ builder" and "Feed-forward" implement equations (3.7) and (3.18), respectively, and $\boldsymbol{K}$ stands for the gain matrix of either the DLQR or the mixed $\mathcal{H}_2/\mathcal{H}_\infty$ controller.

The Bryson's rule (Johnson & Grimble, 1987) was used as starting point to synthesize the weighting matrices of the DLQR, which are given by

$$\begin{aligned}
\boldsymbol{\Omega}_{\boldsymbol{\chi}} = \text{diag}\Bigg(& \frac{20}{2^2}, \frac{20}{2^2}, \frac{20}{2^2}, \frac{1}{(\pi/2)^2}, \frac{1}{(\pi/2)^2}, \frac{15}{\pi^2}, \frac{10}{(\pi/2)^2}, \frac{10}{(\pi/2)^2}, \frac{0.01}{(\pi/2)^2}, \frac{0.01}{(\pi/2)^2}, \frac{1}{2^2}, \frac{1}{2^2}, \frac{1}{2^2}, \\
& \frac{1}{(\pi/3)^2}, \frac{1}{(\pi/3)^2}, \frac{1}{(\pi/4)^2}, \frac{5}{(3\pi)^2}, \frac{5}{(3\pi)^2}, \frac{0.01}{(3\pi)^2}, \frac{0.01}{(3\pi)^2}, 50, 50, 50, 1 \Bigg), \\
\boldsymbol{\Omega}_{\boldsymbol{u}} = \text{diag}\Bigg(& \frac{150}{(30 - f_\text{L}^\text{eq})^2}, \frac{150}{(30 - f_\text{L}^\text{eq})^2}, \frac{1000}{2^2}, \frac{1000}{2^2} \Bigg),
\end{aligned}$$

[3] 2 m/s^2 for 0.1 N, from Newton's second law.

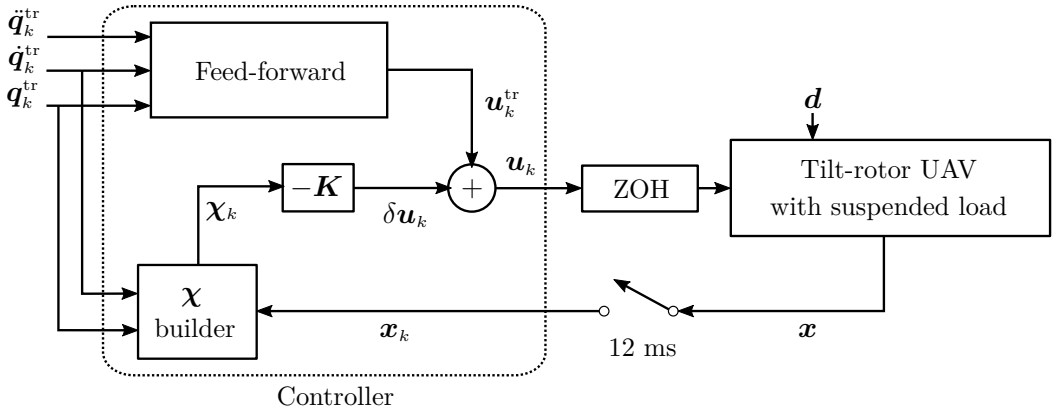

Figure 5.5: Control structure for the full state information scenario.

where $f_{\mathrm{R}}^{\mathrm{eq}}$ and $f_{\mathrm{L}}^{\mathrm{eq}}$ are equilibrium values from (5.1).

The mixed $\mathcal{H}_2/\mathcal{H}_\infty$ control design was performed using the Yalmip toolbox (Löfberg, 2004) with the SDPT3 solver (Toh et al., 1999). The design parameters for the LMI regions are given by $\varepsilon = 0.55$, $\varpi = 0.99402$, which were adjusted such that $-50 < \mathrm{Re}(s) < -0.5$ in continuous time, then mapped through $|\varsigma| = e^{\mathrm{Re}(s)T_c}$. The gain matrices of the mixed $\mathcal{H}_2/\mathcal{H}_\infty$ controller are given by

$$\boldsymbol{H_z} = \mathrm{diag}\left(\frac{\sqrt{20}}{2}, \frac{\sqrt{20}}{2}, \frac{\sqrt{20}}{2}, \frac{1}{\pi/2}, \frac{1}{\pi/2}, \frac{\sqrt{15}}{\pi}, \frac{\sqrt{10}}{\pi/2}, \frac{\sqrt{10}}{\pi/2}, \frac{0.1}{\pi/2}, \frac{0.1}{\pi/2}, \frac{1}{2}, \frac{1}{2}, \frac{1}{2}, \right.$$
$$\left. \frac{1}{\pi/3}, \frac{1}{\pi/3}, \frac{1}{\pi/4}, \frac{\sqrt{5}}{3\pi}, \frac{\sqrt{5}}{3\pi}, \frac{0.1}{3\pi}, \frac{0.1}{3\pi}, \sqrt{50}, \sqrt{50}, \sqrt{50}, 1\right),$$

$$\boldsymbol{D_{zu}} = \begin{bmatrix} \frac{\sqrt{150}}{30 - f_{\mathrm{R}}^{\mathrm{eq}}} & 0 & 0 & 0 \\ 0 & \frac{\sqrt{150}}{30 - f_{\mathrm{R}}^{\mathrm{eq}}} & 0 & 0 \\ 0 & 0 & \frac{\sqrt{1000}}{2} & 0 \\ \mathbf{0}_{2\times1} & \mathbf{0}_{2\times1} & \mathbf{0}_{2\times1} & \mathbf{0}_{2\times1} \\ 0 & 0 & 0 & \frac{\sqrt{1000}}{2} \\ \mathbf{0}_{18\times1} & \mathbf{0}_{18\times1} & \mathbf{0}_{18\times1} & \mathbf{0}_{18\times1} \end{bmatrix}, \quad \boldsymbol{D_{zd}} = \begin{bmatrix} \mathbf{0}_{10\times3} \\ \mathbb{I}_{3\times3} \\ \boldsymbol{N} \\ 0.5\cdot\mathbf{1}_{1\times3} \\ \boldsymbol{N} \\ \mathbf{0}_{2\times3} \\ \mathbb{I}_{3\times3} \\ 0.5\cdot\mathbf{1}_{1\times3} \end{bmatrix},$$

with $\boldsymbol{N} \triangleq \begin{bmatrix} 0 & 1 & 0 \\ 1 & 0 & 0 \end{bmatrix}$, and $\mathbf{1}_{\cdot\times\cdot}$ denotes a matrix of 1's. Matrices $\boldsymbol{H_z}$ and $\boldsymbol{D_{zu}}$ were chosen such that $\boldsymbol{H_z}^T\boldsymbol{H_z} = \boldsymbol{\Omega_\chi}$ and $\boldsymbol{D_{zu}}^T\boldsymbol{D_{zu}} = \boldsymbol{\Omega_u}$, whilst $\boldsymbol{D_{zd}}$ was adjusted by trial and error. A pure $\mathcal{H}_\infty$ controller with pole placement constraints was designed, i.e., the optimization problem described in Section 3.4.2, considering also the constraints described in Section 3.4.3, was solved, in order to obtain an optimal upper bound for the $\mathcal{H}_\infty$ norm, given by $\|\boldsymbol{\Psi_{dz}}(\varsigma)\|_\infty < 17.4617$. Then, the mixed $\mathcal{H}_2/\mathcal{H}_\infty$ controller was designed by choosing $\|\boldsymbol{\Psi_{dz}}(\varsigma)\|_\infty^2 < \tilde{\gamma} = 24^2$, which is slightly greater than the optimal upper bound of the $\mathcal{H}_\infty$

norm, yielding $\|\boldsymbol{\Psi}_{d\tilde{z}}(\varsigma)\|_2 < \sqrt{33.1099}$.

Figure 5.6 illustrates the open-loop and closed-loop poles of the discrete-time system (3.9) for both controllers. Note that, for the chosen design parameters, the pole placement using both controllers were quite similar. Then, at least in the vicinity of the desired operation point, the behavior of the closed-loop system is expected to be not so different from one to another.

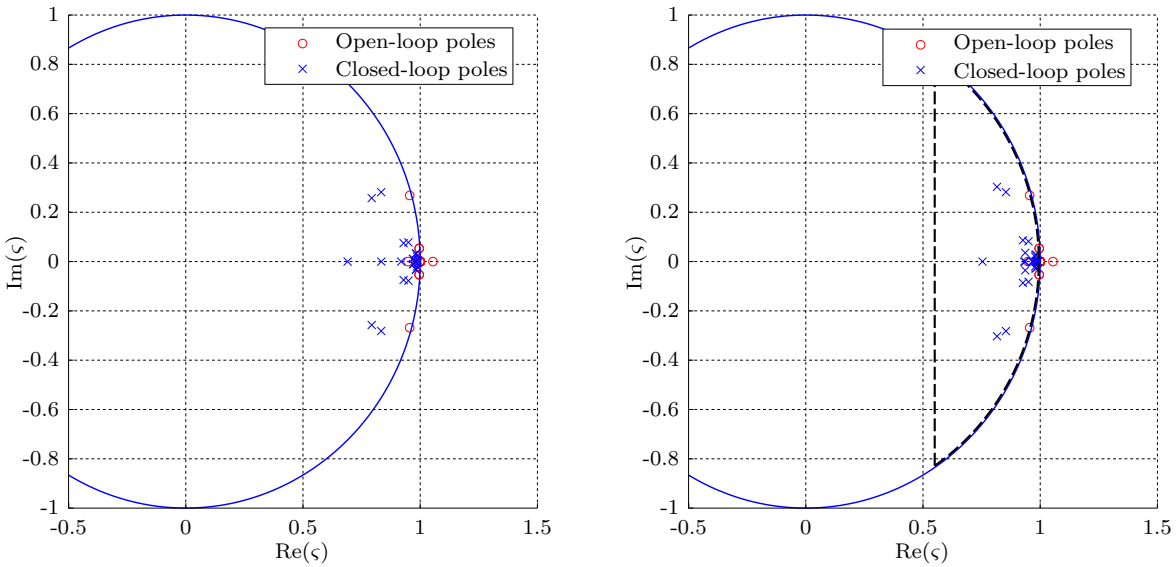

(a) DLQR (b) Mixed $\mathcal{H}_2/\mathcal{H}_\infty$

Figure 5.6: Pole placement using the designed controllers. Solid lines denote the unitary circle and dashed lines denote LMI region boundaries.

First trajectory

The trajectories performed by the tilt-rotor UAV and the suspended load for both controllers are shown in Figure 5.7. The tracking error is shown in Figure 5.8. Note that the path tracking was performed successfully, and that the external disturbances were rejected by both controllers. Also, the closed-loop system behavior was almost the same for the designed controllers, as corroborated through the performance indexes presented in Table 5.4. The distinct behavior of the tracking error over ψ can be explained by the fact that, despite the state-space equations (3.9) being valid for all x, y and z (recall the discussion presented in Section 3.2 about the dependence of the system on these variables), is valid only in the vicinity of $\psi = \psi^{\text{tr}} = 0$. Thus, the behavior of the controllers is expected to be different for $\psi \neq 0$.

Figure 5.9 shows the time evolution of the remaining degrees of freedom, which kept stable as the trajectory was performed, for both controllers. Note that their equilibrium values changed over time, which is due to the presence of external disturbances. Since the

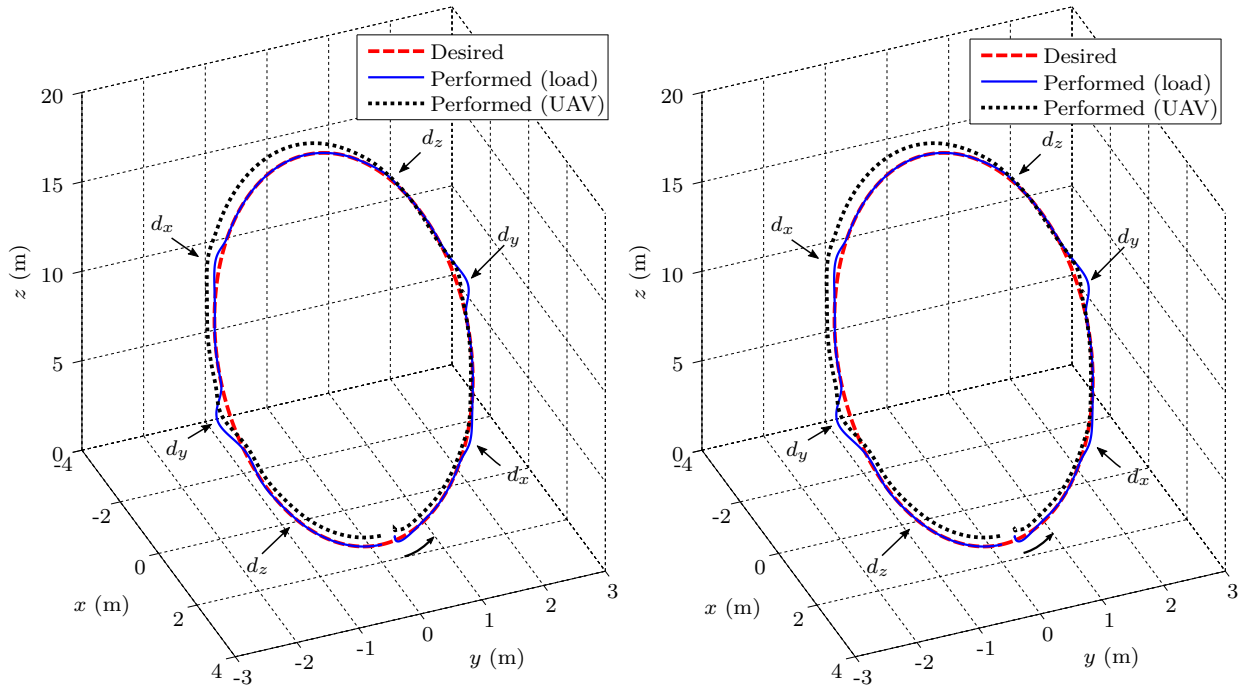

(a) DLQR (b) Mixed $\mathcal{H}_2/\mathcal{H}_\infty$

Figure 5.7: Trajectories performed by the UAV and the suspended load using the designed controllers, for the first desired trajectory, FSI scenario.

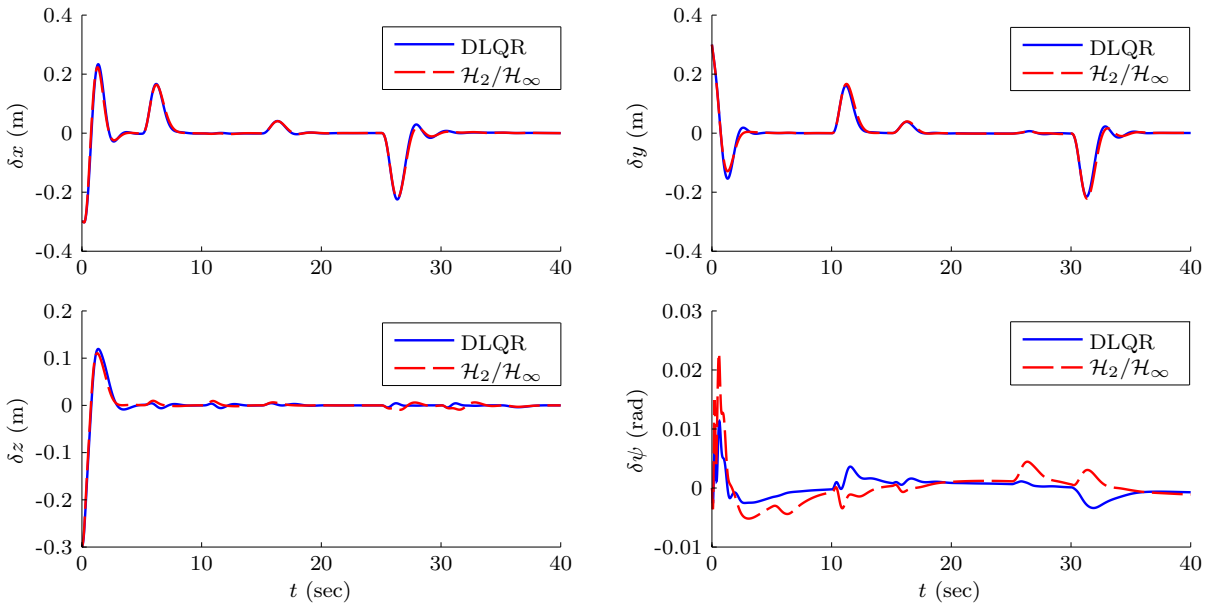

Figure 5.8: Tracking error for the first trajectory, FSI scenario.

orientation of the suspended load with respect to the inertial frame and the orientation of the UAV with respect to the load remained stable, and also from the trajectory performed by the aircraft shown in Figure 5.7, it can be concluded that the tilt-rotor UAV remained stable as well[4]. Figure 5.10 shows the control signals applied by the aircraft's actuators,

[4]As mentioned in Chapter 3, since the UAV's behavior is implicit in the state-space equations,

which were also similar for both controllers, and did not saturate the actuators during the simulation.

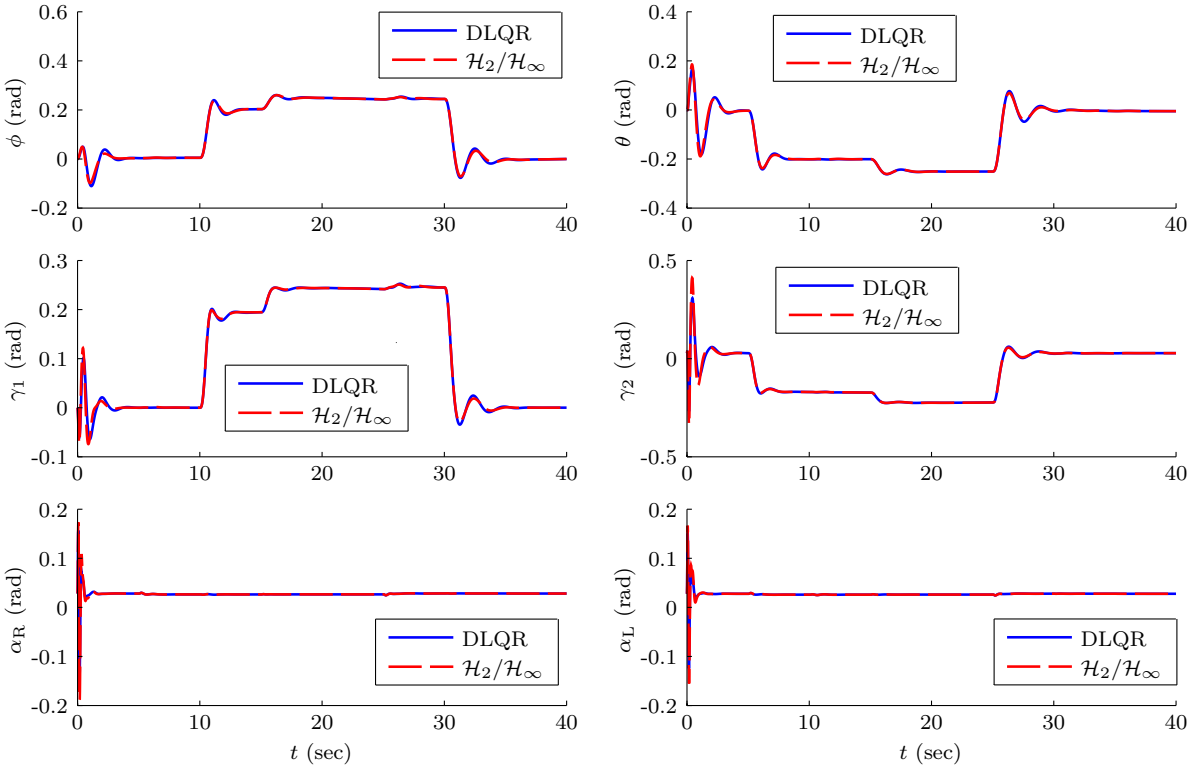

Figure 5.9: Time evolution of the remaining degrees of freedom for the first trajectory, FSI scenario.

Table 5.4 shows the performance indexes for the first trajectory. The DLQR and the mixed $\mathcal{H}_2/\mathcal{H}_\infty$ controller presented very similar ISE and IADU indexes, as expected from the pole placement results. The mixed $\mathcal{H}_2/\mathcal{H}_\infty$ controller performed better path tracking in variables x and z, while the DLQR performed better in y and ψ. The thrusters control signals were smoother using the DLQR, while the servomotor control signals were smoother using the mixed $\mathcal{H}_2/\mathcal{H}_\infty$ controller. The mixed $\mathcal{H}_2/\mathcal{H}_\infty$ is expected to be more aggressive due to its disturbance compensation capabilities. Since the servomotor torques affect only the tilting angles directly (see their mappings to generalized forces in Chapter 2), to attenuate external disturbances affecting the load, less control effort is directed to the servomotor torques, while more control effort is directed to the thrust forces.

Second trajectory

The performed trajectories are shown in Figure 5.11, whist the tracking error is shown in Figure 5.12. As in the previous case, the path tracking was performed successfully, and the external disturbances were rejected. The behavior of the closed-loop system was, again,

stabilization of system implies stabilization of the tilt-rotor UAV.

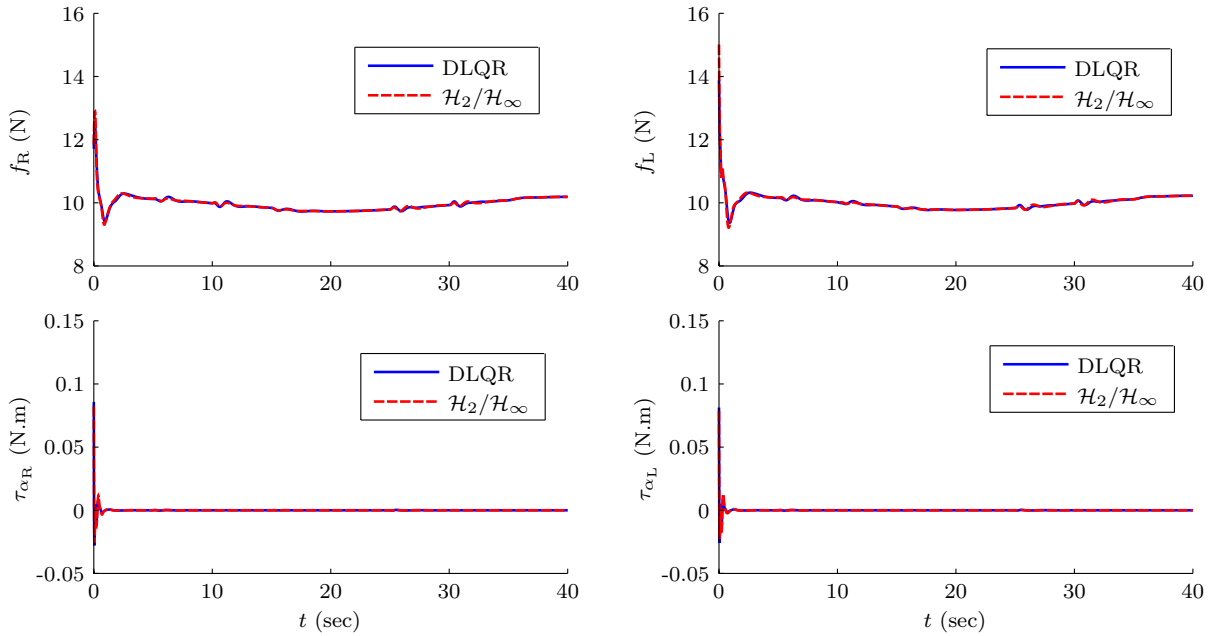

Figure 5.10: Actuator signals for the first trajectory, FSI scenario. Saturation levels are $0 \leq f_R \leq 30$ N, $0 \leq f_L \leq 30$ N, $-2 \leq \tau_{\alpha_R} \leq 2$ N·m and $-2 \leq \tau_{\alpha_L} \leq 2$ N·m.

Table 5.4: Performance indexes for the first trajectory, FSI scenario.

Index	DLQR	$\mathcal{H}_2/\mathcal{H}_\infty$	$\frac{\mathcal{H}_2/\mathcal{H}_\infty}{\text{DLQR}}$
ISE(x)	0.1571	0.1521	0.9691
ISE(y)	0.1111	0.1167	1.0509
ISE(z)	0.0428	0.0385	0.8992
ISE(ψ)	$1.1519{\cdot}10^{-4}$	$3.6213{\cdot}10^{-4}$	3.1438
IADU(f_R)	7.1486	7.9463	1.1116
IADU(f_L)	7.7712	9.6864	1.2465
IADU(τ_{α_R})	0.1984	0.1966	0.9906
IADU(τ_{α_L})	0.1982	0.1978	0.9984

very similar for the DLQR and the mixed $\mathcal{H}_2/\mathcal{H}_\infty$ controller, which was already expected. The transient responses of the system due to path changing are also depicted.

The time evolution of the remaining degrees of freedom is shown in Figure 5.13. As in the previous case, they kept stable as the path tracking was performed, and stability of the tilt-rotor UAV can also be concluded. Once more, their equilibrium values changed over time due to the presence of external disturbances. Figure 5.14 shows the control signals, depicting transient responses necessary to perform path changing. Once again, the control signals did not saturate the aircraft's actuators.

Table 5.5 shows the performance indexes for the second trajectory. Once again, the DLQR and the mixed $\mathcal{H}_2/\mathcal{H}_\infty$ controller presented very similar ISE and IADU indexes. The mixed $\mathcal{H}_2/\mathcal{H}_\infty$ controller performed better path tracking in variables x and y, while the DLQR performed better in z and ψ. For this trajectory, all the control signals were

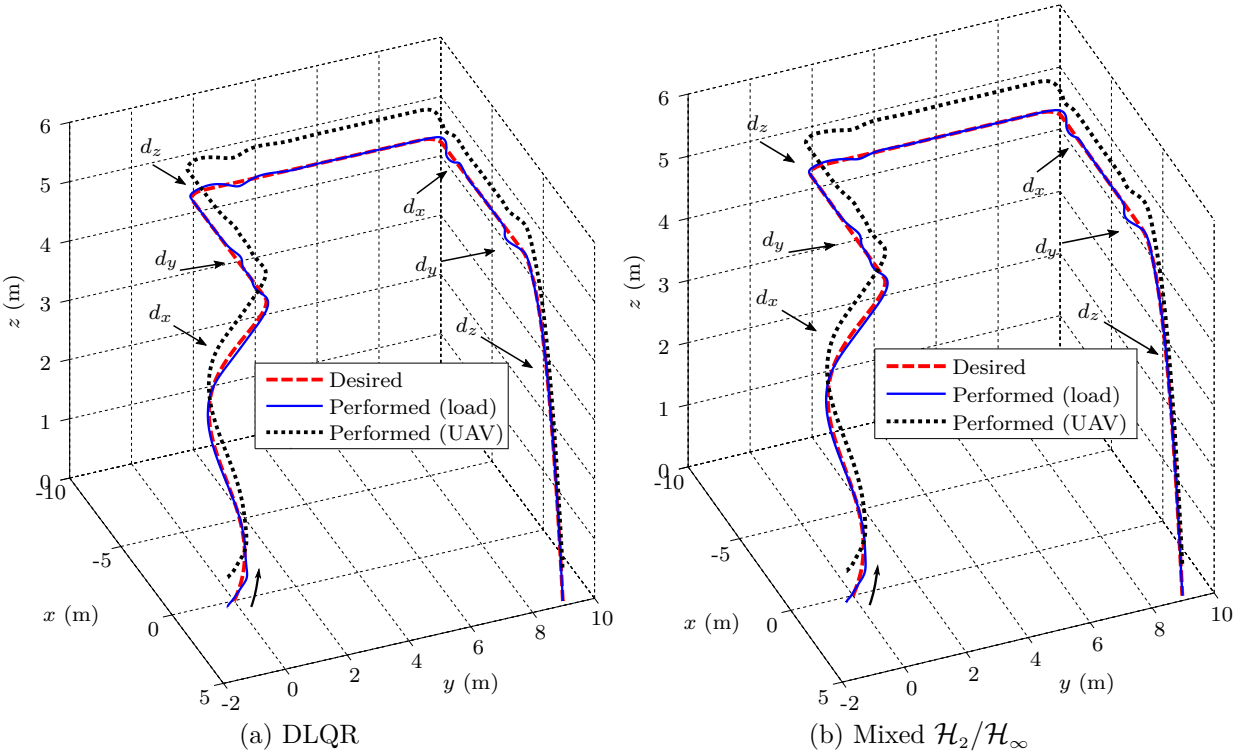

(a) DLQR (b) Mixed $\mathcal{H}_2/\mathcal{H}_\infty$

Figure 5.11: Trajectories performed by the UAV and the suspended load using the designed controllers, for the second desired trajectory, FSI scenario.

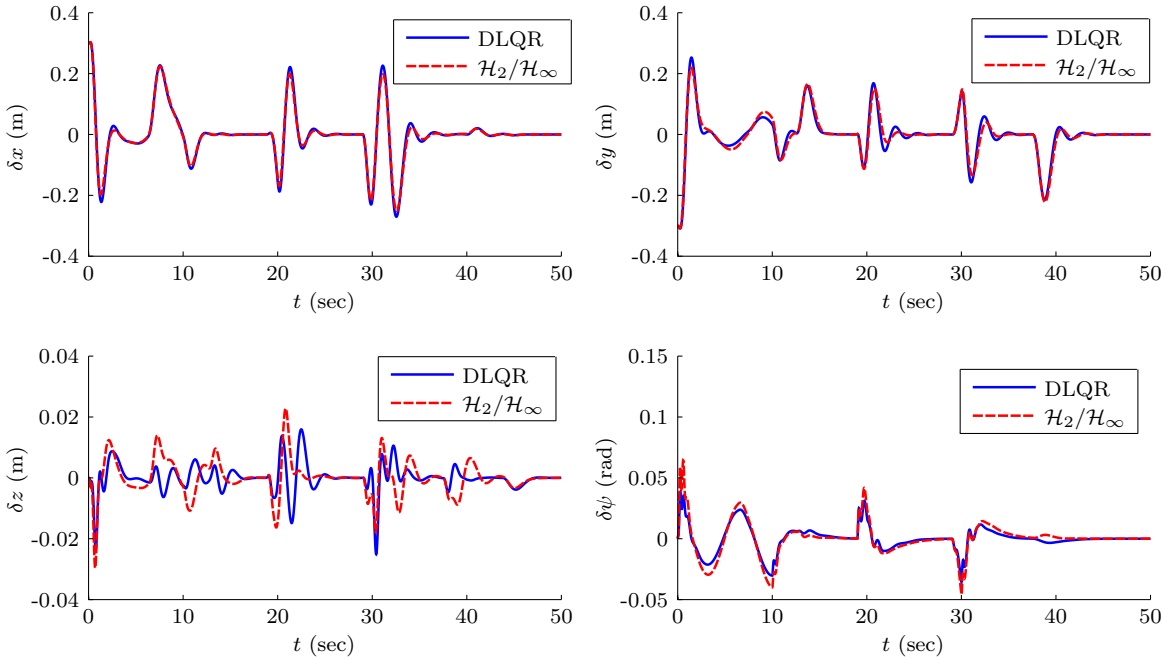

Figure 5.12: Tracking error for the second trajectory, FSI scenario.

smoother using the DLQR. The trajectory requires thruster tilting in order to perform path changing at 19 and 39 seconds (see Figure 5.13), thus due to transient response, the

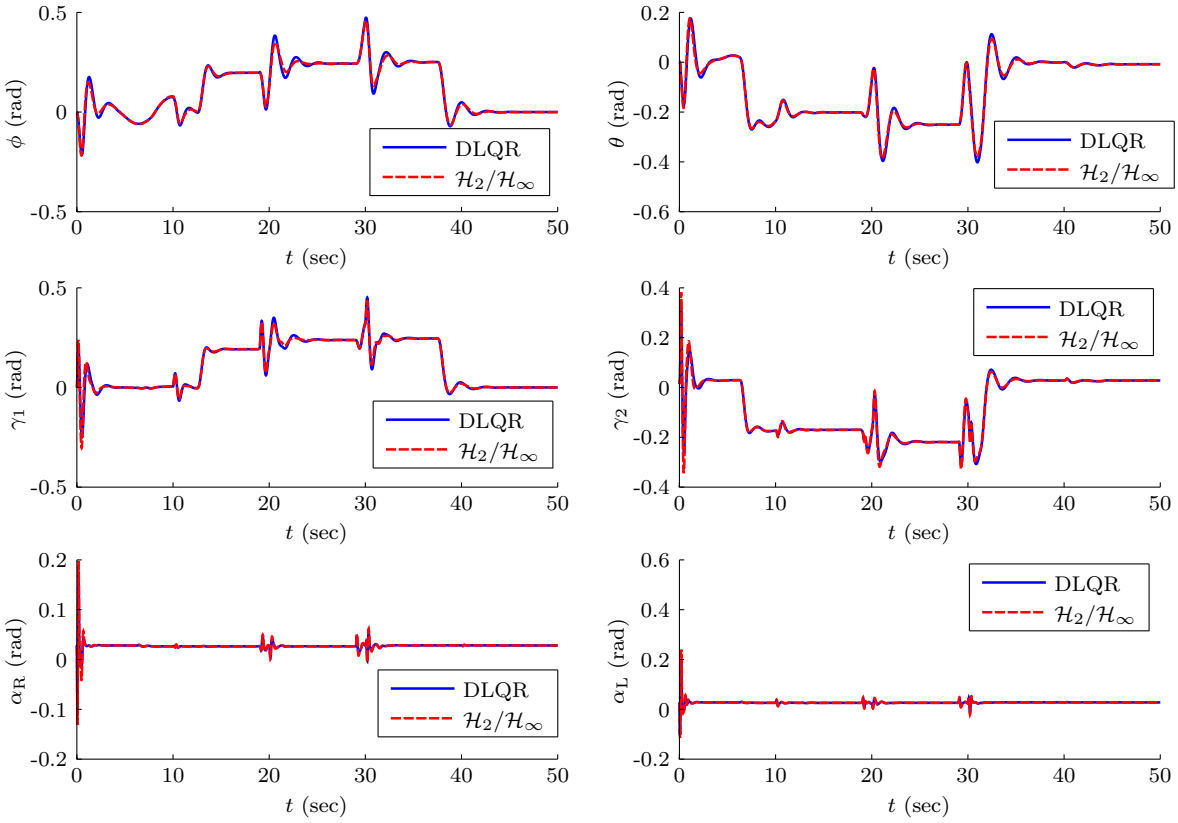

Figure 5.13: Time evolution of the remaining degrees of freedom for the second trajectory, FSI scenario.

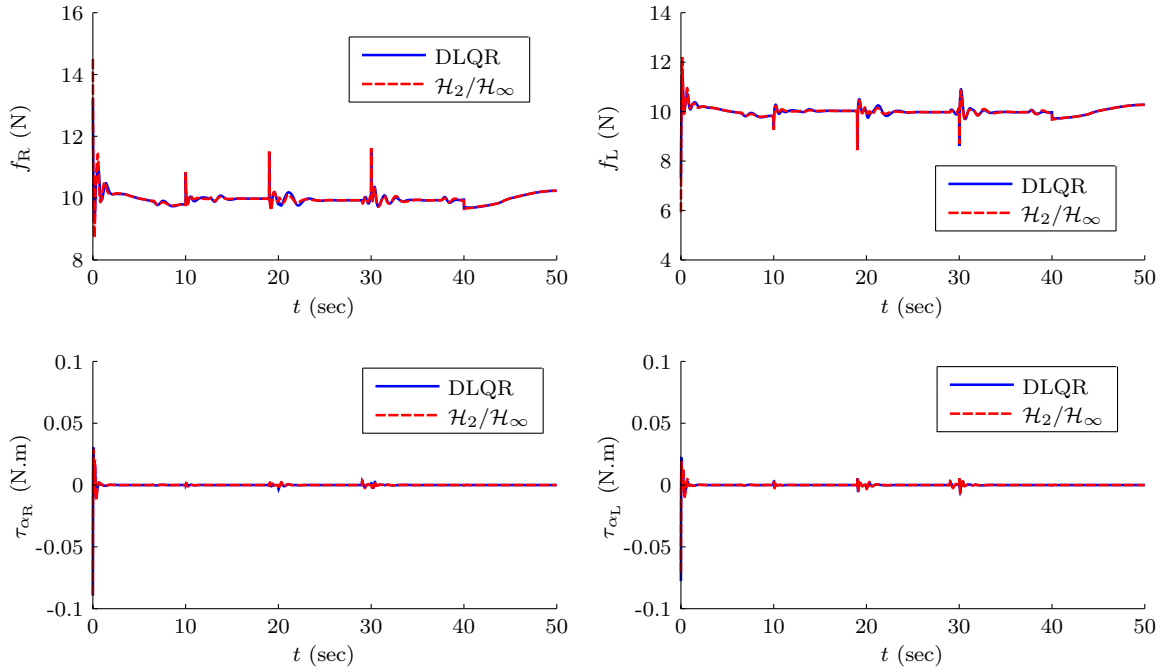

Figure 5.14: Actuator signals for the second trajectory, FSI scenario. Saturation levels are $0 \leq f_R \leq 30$ N, $0 \leq f_L \leq 30$ N, $-2 \leq \tau_{\alpha_R} \leq 2$ N·m and $-2 \leq \tau_{\alpha_L} \leq 2$ N·m.

mixed $\mathcal{H}_2/\mathcal{H}_\infty$ controller was more aggressive also with respect to the servomotor torques.

Table 5.5: Performance indexes for the second trajectory, FSI scenario.

Index	DLQR	$\mathcal{H}_2/\mathcal{H}_\infty$	$\frac{\mathcal{H}_2/\mathcal{H}_\infty}{\text{DLQR}}$
ISE(x)	0.3358	0.2987	0.8896
ISE(y)	0.2330	0.2326	0.9981
ISE(z)	$1.0441{\cdot}10^{-3}$	$1.6637{\cdot}10^{-3}$	1.5935
ISE(ψ)	$5.1167{\cdot}10^{-3}$	$9.4917{\cdot}10^{-3}$	1.8551
IADU(f_R)	24.2162	27.2654	1.1259
IADU(f_L)	24.1251	26.8009	1.1109
IADU(τ_{α_R})	0.2849	0.3020	1.0600
IADU(τ_{α_L})	0.2716	0.2867	1.0553

In both desired trajectories, the load's initial position was displaced from the initial reference position. During the initial convergence, the system trajectory did not deviate significantly from the operation point based on which the discrete-time linearized model (3.9) was obtained, hence both controllers were able to perform the convergence of the system to the desired trajectory. However, for very large displacements, the initial convergence requires harsher control signals and the system trajectory greatly deviates from the operation point, hence the linear controllers are not able to perform the initial convergence, destabilizing the system. Moreover, harsher disturbances also leads to the same result.

5.3 Linearized Kalman filter scenario

This section presents simulation results considering the scenario described in Section 4.2, in which only a half of the state vector (2.56) is measured, at every time instant with additive noise. It is further referenced as the LKF scenario.

The control structure is shown in Figure 5.15. The system's outputs, $\boldsymbol{q}$, are sampled by noisy sensors, whose measurements along with the system's inputs, $\boldsymbol{u}_k$, are provided to the estimator. In the latter, equilibrium values are added or subtracted from these signals to adapt them for the linearized Kalman filter algorithm. The same is done to the state vector estimated by the filter, to recover the estimated state vector of the nonlinear system and make the feedback connection with the controller. The LKF block implements the Algorithm 4.1, whilst the Controller block corresponds to the subsystem with same name presented in the control structure of the FSI scenario (see Figure 5.5).

It is assumed that the initial state is precisely known, i.e., $\Delta\hat{\boldsymbol{x}}_{0|0} = \Delta\boldsymbol{x}_0$. For simulation, the load's position is measured with precision $3\sigma = 15$cm, where σ is the standard deviation, while the remaining generalized coordinates are measured precisely, i.e., $\sigma = 0$. Although some of these assumptions may simplify the problem, it must be depicted that only the generalized coordinates are measured, while their derivatives must be estimated by the

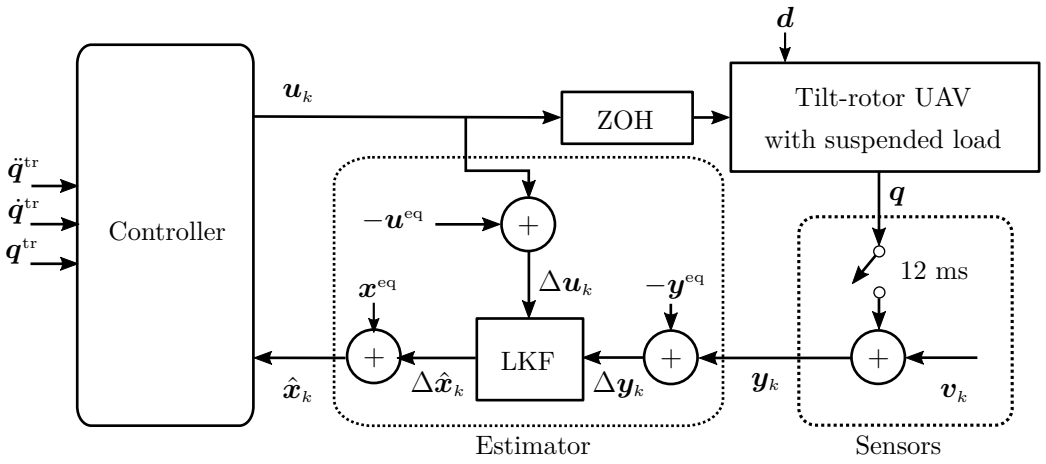

Figure 5.15: Control structure for the linearized Kalman filter scenario.

filter. The covariance matrices used in the filter design are then given by

$$\boldsymbol{P}^{\boldsymbol{\nu}}_{0|0} = 0.01 \cdot \mathbb{I}_{23\times 23}, \quad \boldsymbol{P}^{\boldsymbol{w}} = 1.0 \cdot 10^{-5} \cdot \mathbb{I}_{23\times 23}, \quad \boldsymbol{P}^{\boldsymbol{v}} = \begin{bmatrix} (0.05)^2 \cdot \mathbb{I}_{3\times 3} & \mathbf{0}_{3\times 7} \\ \mathbf{0}_{7\times 3} & \mathbf{0}_{7\times 7} \end{bmatrix},$$

in which $\boldsymbol{P}^{\boldsymbol{\nu}}_{0|0}$ and $\boldsymbol{P}^{\boldsymbol{w}}$ were adjusted empirically, by verifying the estimation error consistency, i.e., if the estimation error was inside the filter's confidence limits.

First trajectory

The trajectories performed by the tilt-rotor UAV and the suspended load are shown in Figure 5.16, and the tracking error is shown in Figure 5.17. The path tracking was performed successfully for the LKF scenario, demonstrating the joint performance of the designed controllers and the linearized Kalman filter, using the adopted control structure. Despite noise, the closed-loop system behavior is very similar for the designed controllers.

Figure 5.18 shows the time evolution of the remaining degrees of freedom, which kept stable as the trajectory was performed. As in the previous scenario, the orientation of the load with respect to the inertial frame and the orientation of the UAV with respect to the load were kept stable, then it can be concluded that the tilt-rotor UAV remained stable as well. Figure 5.19 shows the control signals, which, although noisy, did not saturate the aircraft's actuators.

Table 5.6 shows the IADU and ISE performance indexes. The mixed $\mathcal{H}_2/\mathcal{H}_\infty$ controller performed better path tracking in z, while the DLQR performed better in x, y and ψ. Due to disturbance compensation, the mixed $\mathcal{H}_2/\mathcal{H}_\infty$ controller demonstrated to be way more aggressive than the DLQR, concerning the thrusters control signals (32.07% and 43.35% greater IADU indexes for the right and left thrusters, respectively), while the servomotor control signals were slightly harsher using the DLQR.

For simplicity, estimation results are shown only for simulations with the mixed $\mathcal{H}_2/\mathcal{H}_\infty$

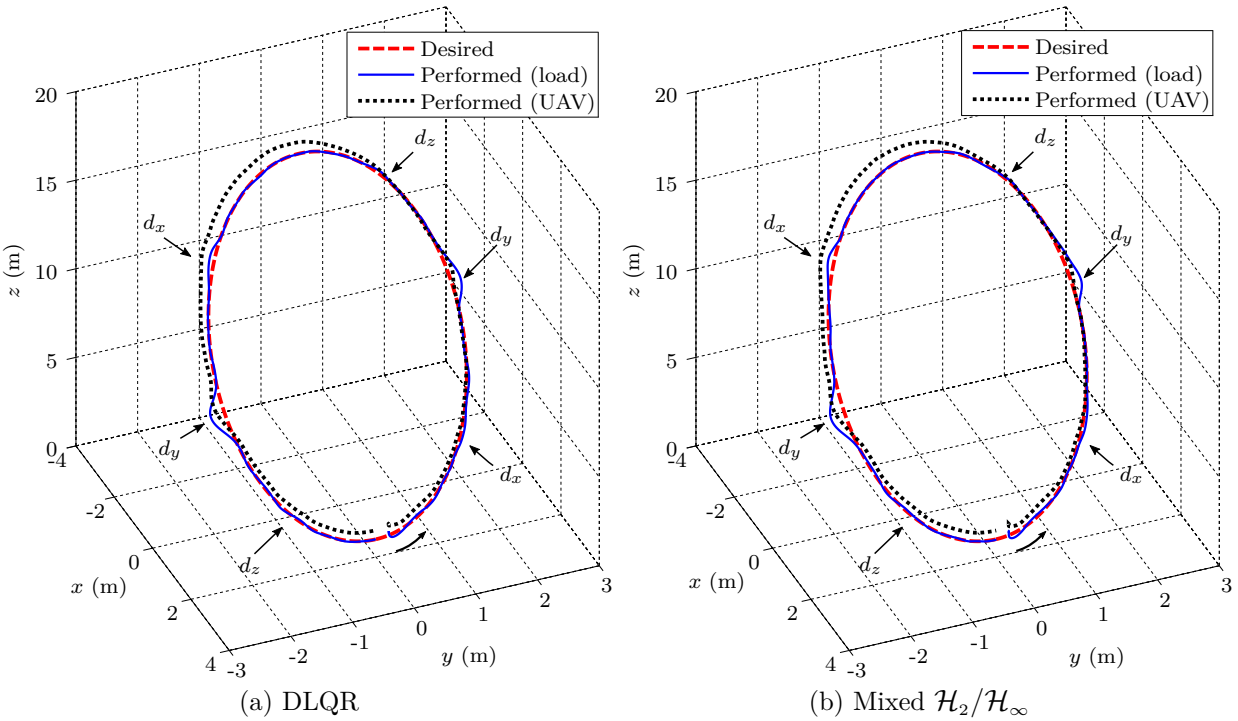

(a) DLQR (b) Mixed $\mathcal{H}_2/\mathcal{H}_\infty$

Figure 5.16: Trajectories performed by the UAV and the suspended load using the designed controllers, for the first desired trajectory, LKF scenario.

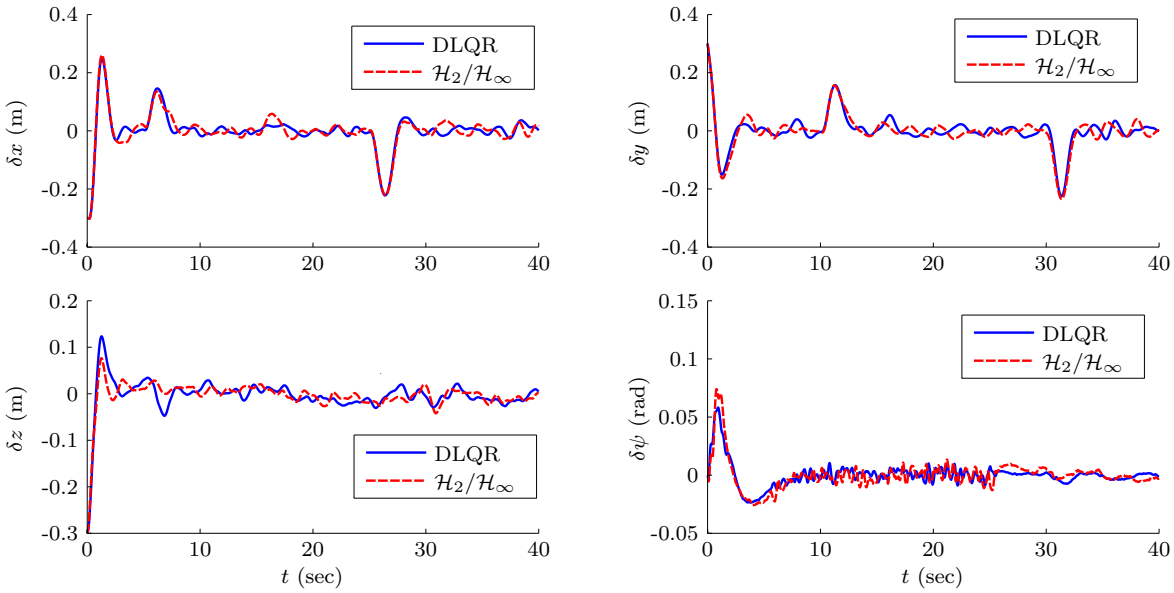

Figure 5.17: Tracking error for the first trajectory, LKF scenario.

controller. Figure 5.20 shows the estimation error of the load's position, along with the linearized Kalman filter confidence limits (i.e., three times the standard deviation) and the measured signals. The linearized Kalman filter reduced the standard deviation of these signals from 5 cm to approximately 1.37 cm.

Figure 5.21 shows the estimation error of the velocities along with the linearized

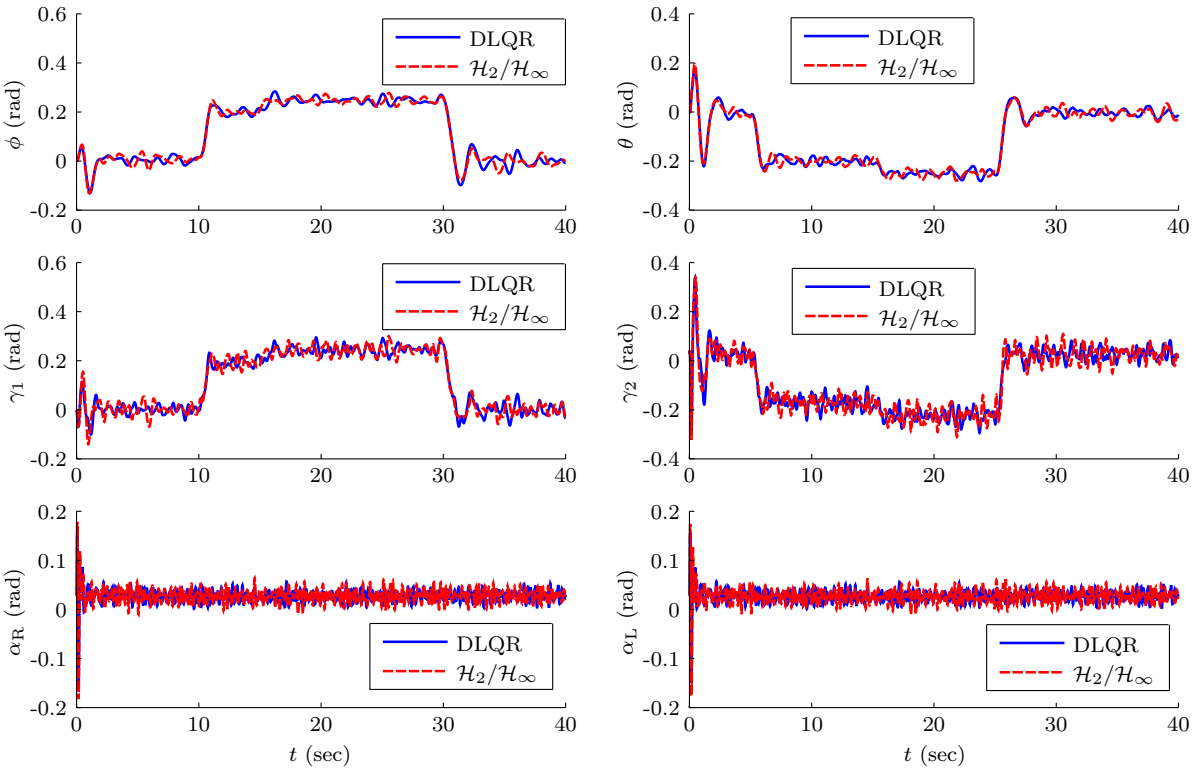

Figure 5.18: Time evolution of the remaining degrees of freedom for the first trajectory, LKF scenario.

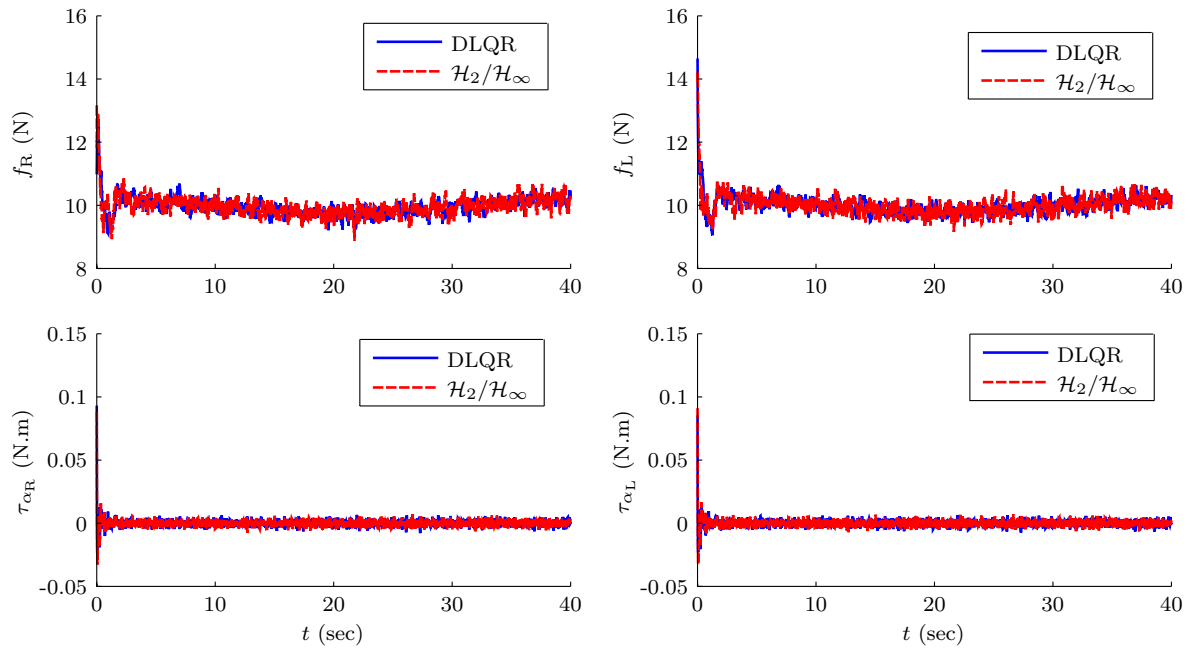

Figure 5.19: Actuator signals for the first trajectory, LKF scenario. Saturation levels are $0 \leq f_R \leq 30$ N, $0 \leq f_L \leq 30$ N, $-2 \leq \tau_{\alpha_R} \leq 2$ N·m and $-2 \leq \tau_{\alpha_L} \leq 2$ N·m.

Kalman filter confidence limits. These variables are not measured. The estimation errors remained in the respective confidence regions for the most time of the simulation, however at some instants they left, mainly at the beginning of the simulation. This comes from the

Table 5.6: Performance indexes for the first trajectory, LKF scenario.

Index	DLQR	$\mathcal{H}_2/\mathcal{H}_\infty$	$\frac{\mathcal{H}_2/\mathcal{H}_\infty}{\text{DLQR}}$
ISE(x)	0.1624	0.1700	1.0473
ISE(y)	0.1196	0.1385	1.1579
ISE(z)	0.0493	0.0380	0.7700
ISE(ψ)	$4.2886{\cdot}10^{-3}$	$6.4845{\cdot}10^{-3}$	1.5120
IADU(f_{R})	208.6821	275.6098	1.3207
IADU(f_{L})	207.4649	297.4057	1.4335
IADU($\tau_{\alpha_{\text{R}}}$)	5.4937	5.1566	0.9386
IADU($\tau_{\alpha_{\text{L}}}$)	5.4901	5.3431	0.9732

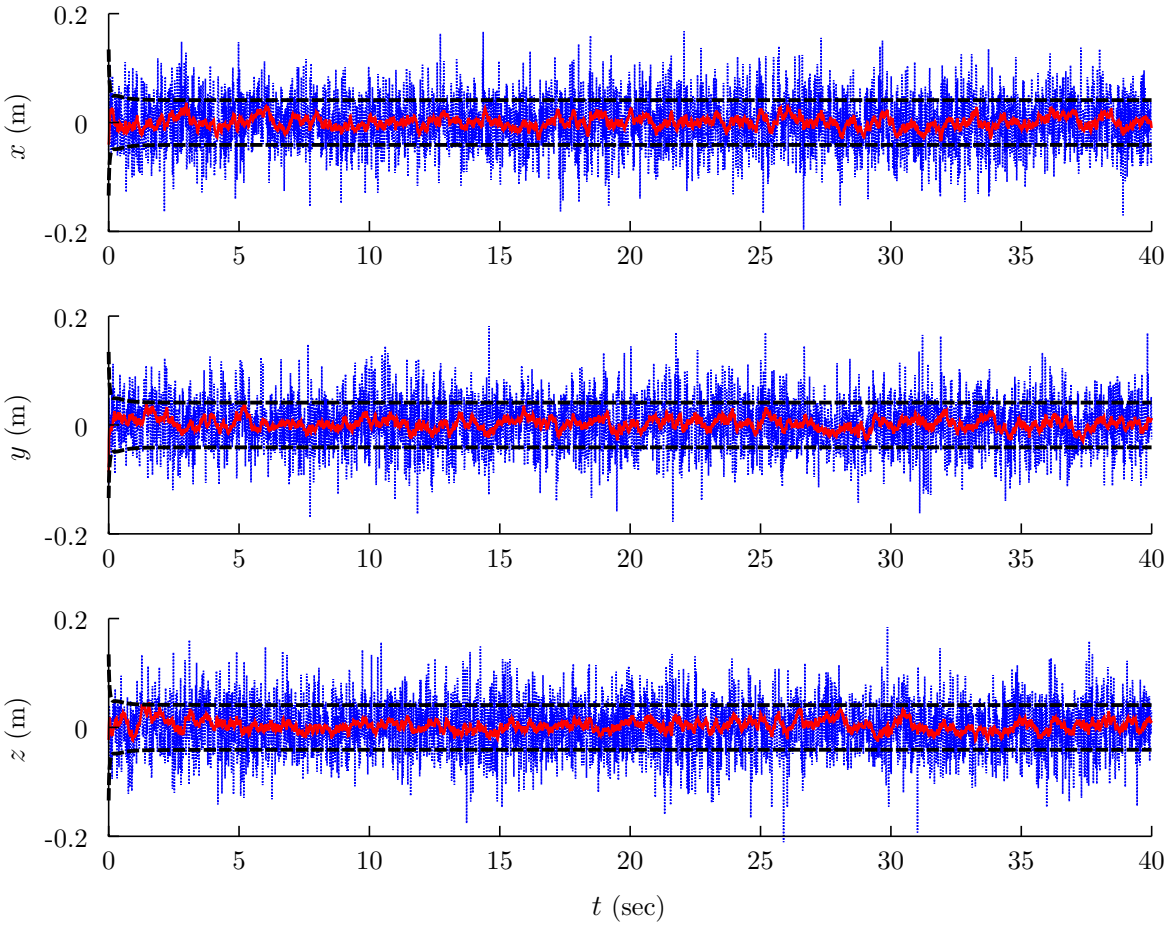

Figure 5.20: Estimation error of x, y and z, for the first trajectory with the mixed $\mathcal{H}_2/\mathcal{H}_\infty$ controller. Solid lines denote estimation error, dashed lines denote confidence limits and dotted lines denote measured signals.

fact that the tilt-rotor UAV with suspended load is a nonlinear system, being the designed linearized Kalman filter valid only in the vicinity of its equilibrium point. It can be noted also that the estimation is biased at some instants, due to the nonlinearities of the system, and since the equilibrium point changes in the presence of external disturbances.

Figure 5.22 shows the estimation error of the external disturbances affecting the suspended load. As in the case of the velocities, the estimation errors remained in the

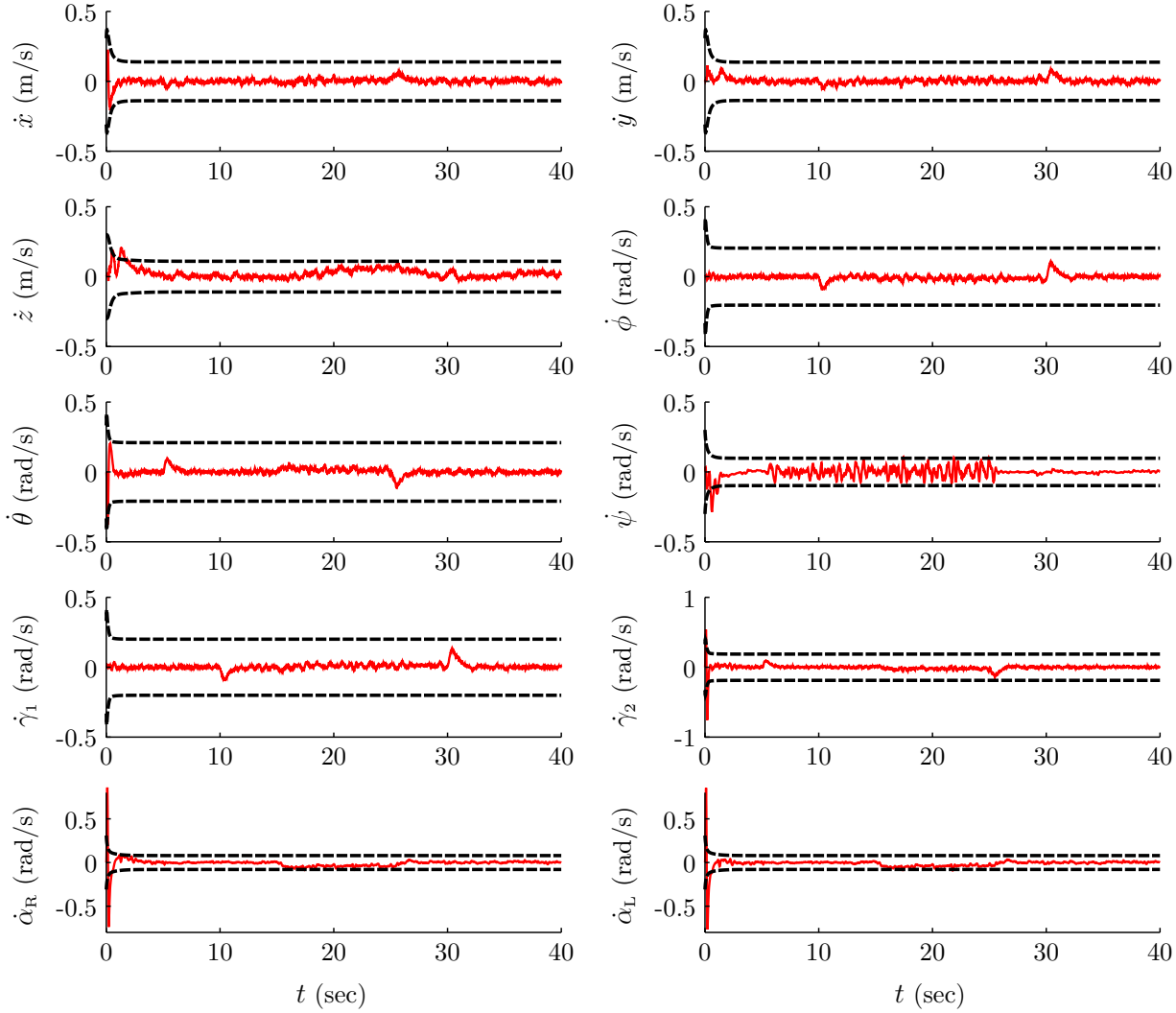

Figure 5.21: Estimation error of the velocities, for the first trajectory with the mixed $\mathcal{H}_2/\mathcal{H}_\infty$ controller. Solid lines denote estimation error, while dashed lines denote confidence limits.

respective confidence regions for the most time of the simulation, at some instants leaving them and also being biased. Nevertheless, the estimation of the disturbances in x and y had standard deviation of 0.0128 N and 0.01274 N, respectively, which is far smaller than the magnitudes of the applied disturbances (0.1 N). On the other hand, the estimation of the disturbances in z had not the same performance. This fact can be explained through the mechanical properties of the system: external forces applied to the load along axes x and y can be easily perceived through the resulting angular displacement of the load with respect to the tilt-rotor UAV, and only the load's mass prevents the motion. In the case of forces applied along axis z, due to the rod, the mass of the UAV also prevents the motion, being more difficult to be perceived. Thus, disturbances along axis z are expected to be less observable.

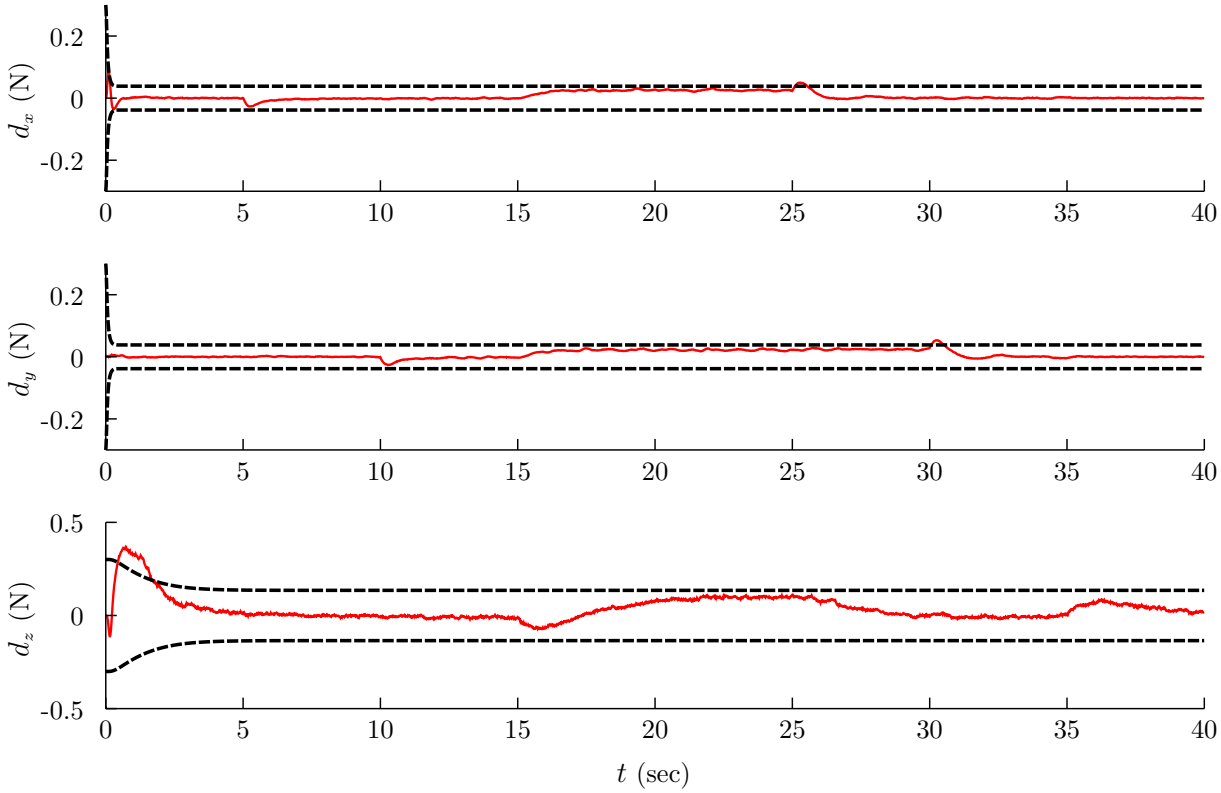

Figure 5.22: Estimation error of the disturbances, for the first trajectory with the mixed $\mathcal{H}_2/\mathcal{H}_\infty$ controller. Solid lines denote estimation error, while dashed lines denote confidence limits.

Second trajectory

The trajectories performed by the tilt-rotor UAV and the suspended load are shown in Figure 5.23, and the tracking error is shown in Figure 5.24. As in the previous case, the path tracking was performed successfully, demonstrating again the joint performance of the designed controllers and the linearized Kalman filter.

Figure 5.25 shows the time evolution of the remaining degrees of freedom, which kept stable as the trajectory was performed. Once again, it can be concluded that the tilt-rotor UAV remained stable as well. Figure 5.26 shows the control signals, which did not saturate the aircraft's actuators.

Table 5.7 shows the IADU and ISE performance indexes for the second trajectory. The mixed $\mathcal{H}_2/\mathcal{H}_\infty$ controller performed better path tracking in x, while the DLQR performed better in y, z and ψ. As in the simulation of the first trajectory, due to disturbance compensation, the mixed $\mathcal{H}_2/\mathcal{H}_\infty$ controller was found to be more aggressive than the DLQR, concerning the thrusters control signals (35.58% and 42.38% greater IADU indexes for the right and left thrusters, respectively), while the servomotor control signals were slightly harsher using the DLQR.

Figure 5.27 shows the estimation error of the load's position, along with the linearized Kalman filter confidence limits and the measured signals. Figure 5.28 shows the estimation

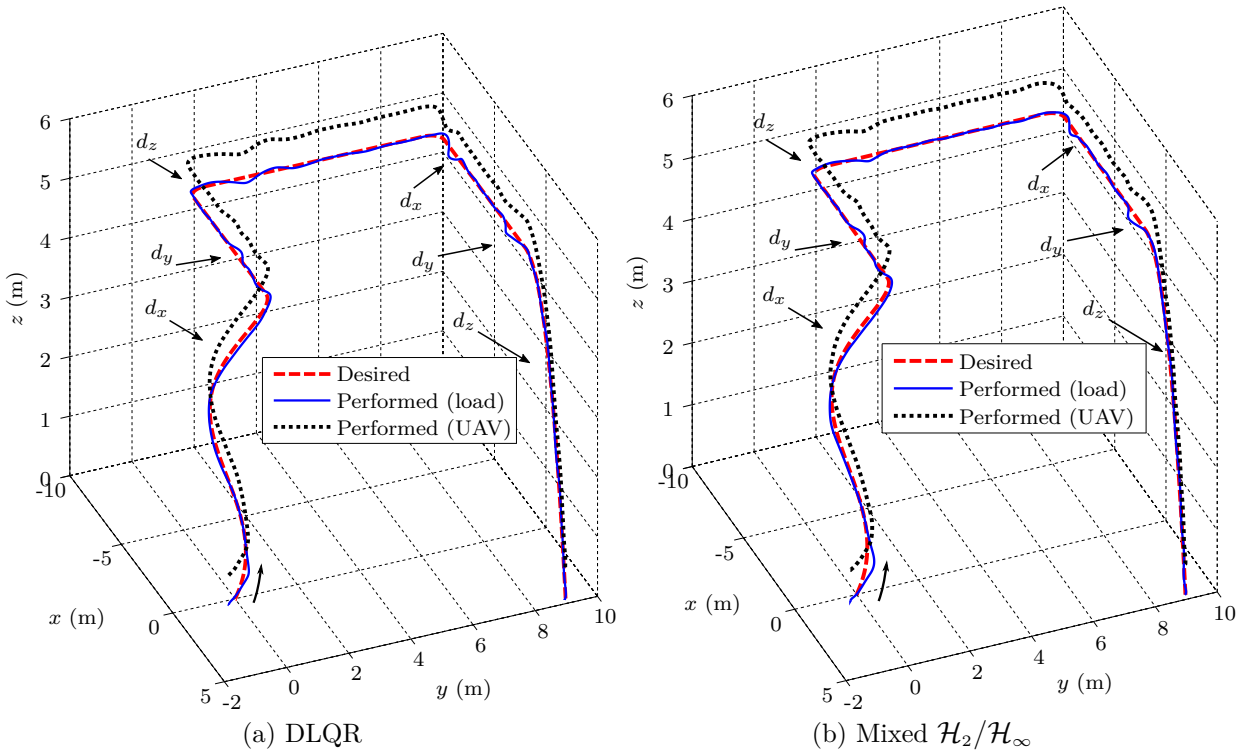

(a) DLQR (b) Mixed $\mathcal{H}_2/\mathcal{H}_\infty$

Figure 5.23: Trajectories performed by the UAV and the suspended load using the designed controllers, for the second desired trajectory, LKF scenario.

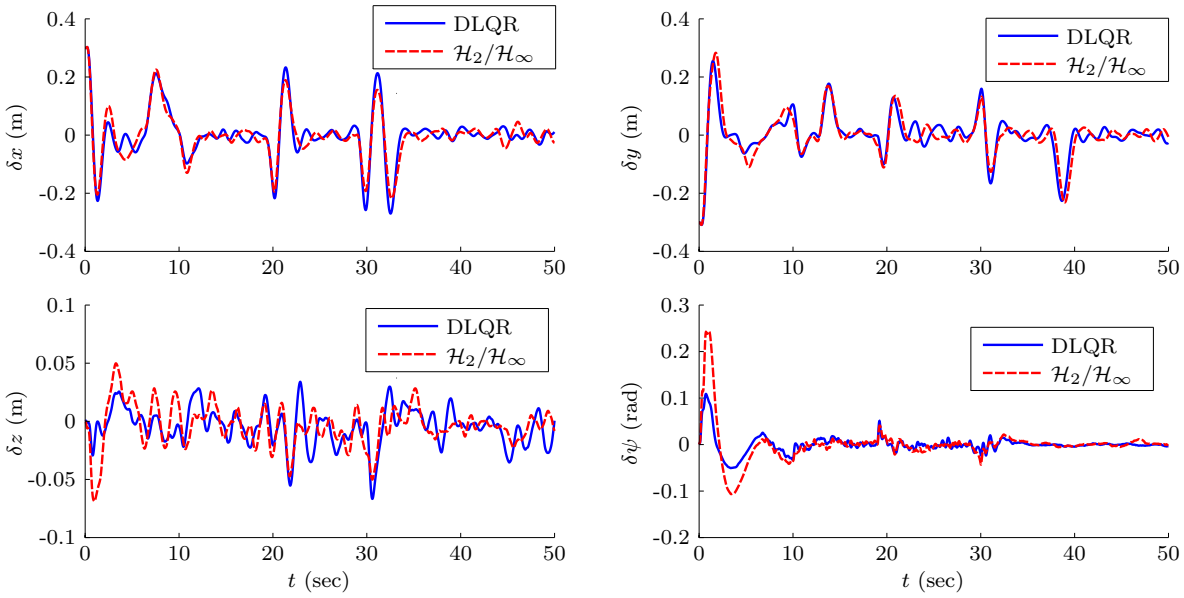

Figure 5.24: Tracking error for the second trajectory, LKF scenario.

error of the velocities along with confidence limits, and Figure 5.29 shows the estimation error of the external disturbances. The discussion on the estimation results for the first trajectory also applies to these results.

As in the previous scenario, in both desired trajectories the load's initial position was

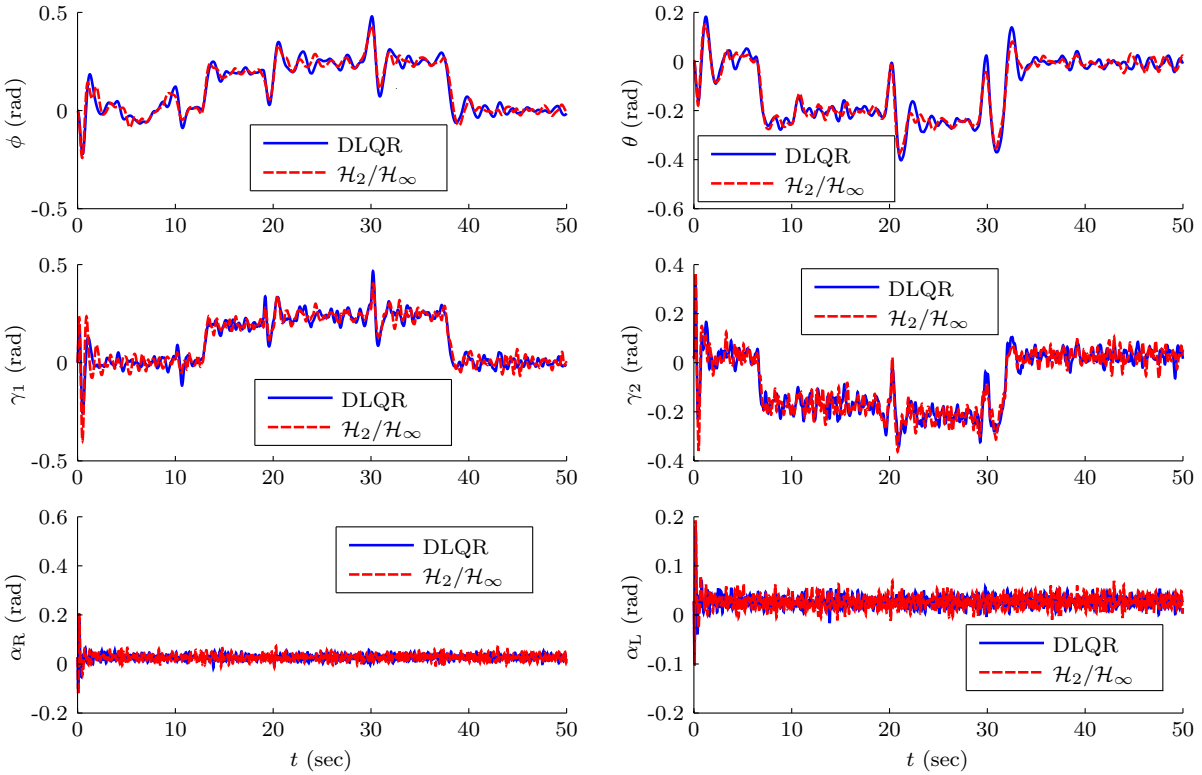

Figure 5.25: Time evolution of the remaining degrees of freedom for the second trajectory, LKF scenario.

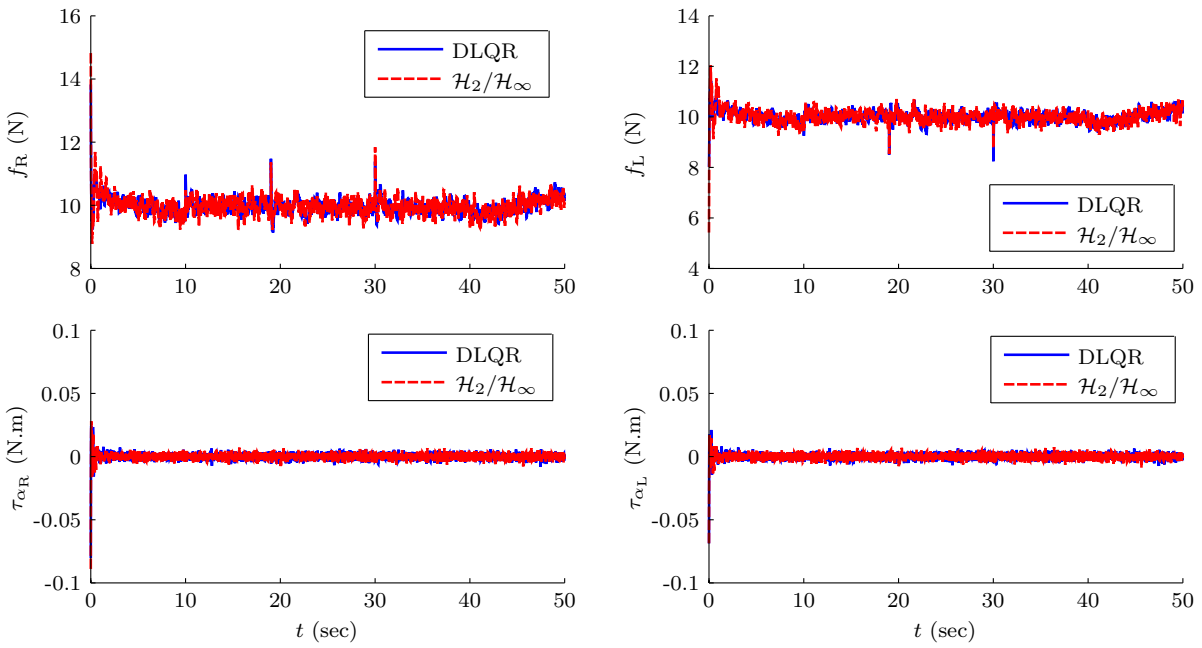

Figure 5.26: Actuator signals for the second trajectory, LKF scenario. Saturation levels are $0 \leq f_R \leq 30$ N, $0 \leq f_L \leq 30$ N, $-2 \leq \tau_{\alpha_R} \leq 2$ N·m and $-2 \leq \tau_{\alpha_L} \leq 2$ N·m.

displaced from the initial reference position. The linear controllers along with the linearized Kalman filter were able to perform the convergence of the system to the desired trajectory. However, for larger displacements, during the initial convergence, the linearized Kalman

Table 5.7: Performance indexes for the second trajectory, LKF scenario.

Index	DLQR	$\mathcal{H}_2/\mathcal{H}_\infty$	$\frac{\mathcal{H}_2/\mathcal{H}_\infty}{\text{DLQR}}$
ISE(x)	0.3523	0.2977	0.8451
ISE(y)	0.2519	0.2799	1.1113
ISE(z)	0.0139	0.0165	1.1871
ISE(ψ)	0.0178	0.0813	4.5737
IADU(f_{R})	270.2537	366.4055	1.3558
IADU(f_{L})	268.2610	381.9623	1.4238
IADU($\tau_{\alpha_{\text{R}}}$)	6.8655	6.3388	0.9233
IADU($\tau_{\alpha_{\text{L}}}$)	6.8335	6.4827	0.9487

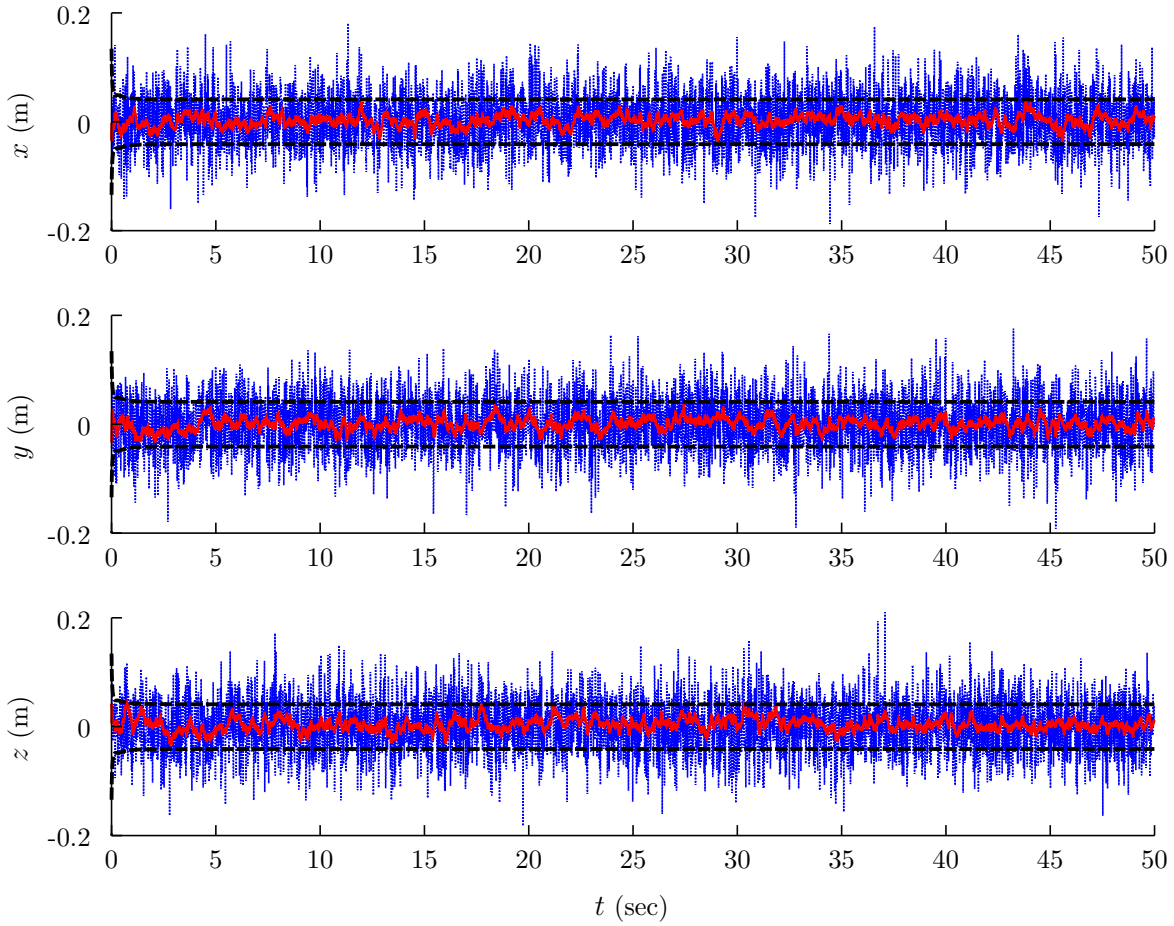

Figure 5.27: Estimation error of x, y and z, for the second trajectory with the mixed $\mathcal{H}_2/\mathcal{H}_\infty$ controller. Solid lines denote estimation error, dashed lines denote confidence limits and dotted lines denote measured signals.

filter provides estimates whose error significantly leaves its confidence limits, resulting in worst situations in comparison with the FSI scenario, destabilizing the system. Harsher disturbances also leads to the same result.

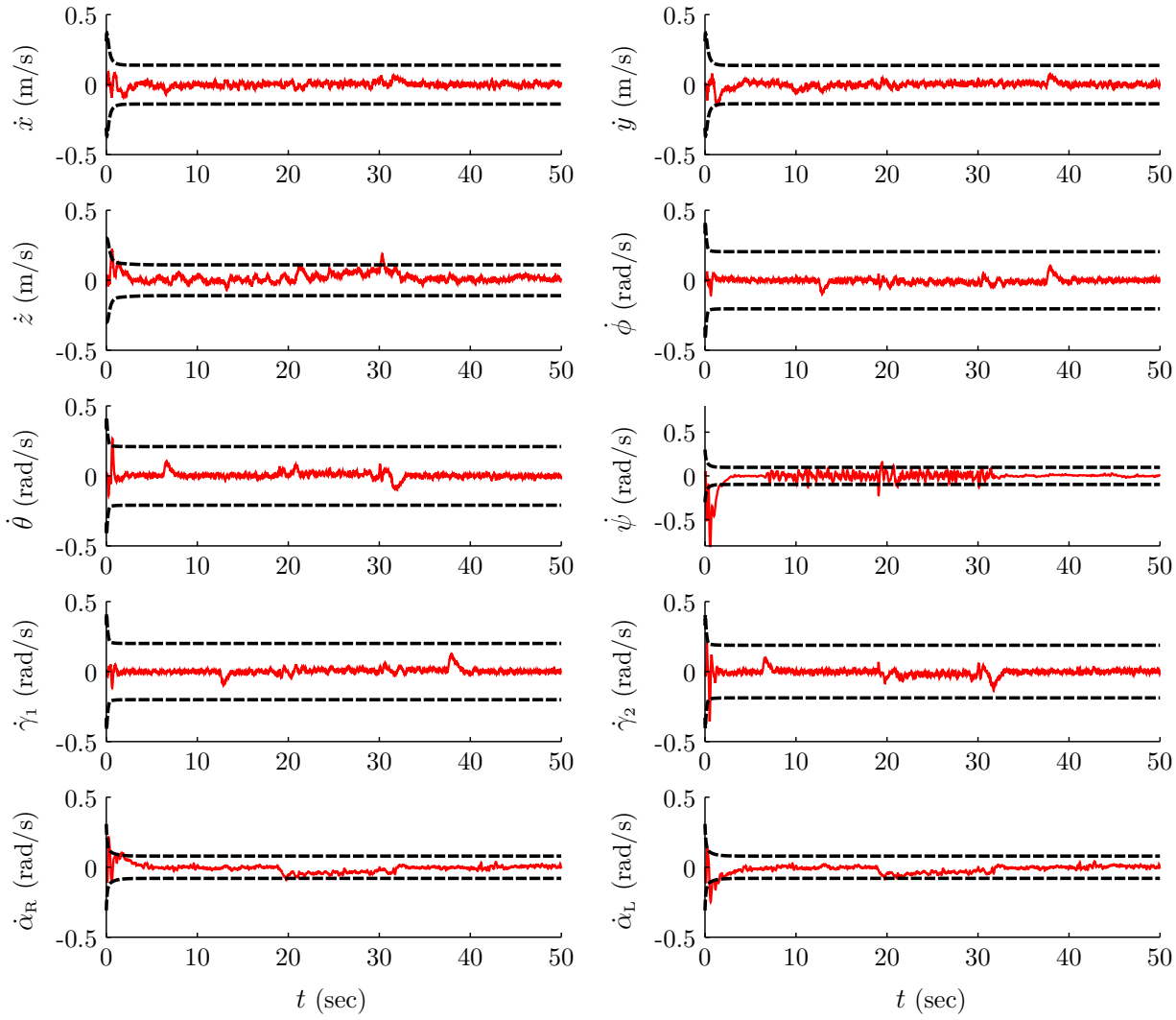

Figure 5.28: Estimation error of the velocities, for the second trajectory with the mixed $\mathcal{H}_2/\mathcal{H}_\infty$ controller. Solid lines denote estimation error, while dashed lines denote confidence limits.

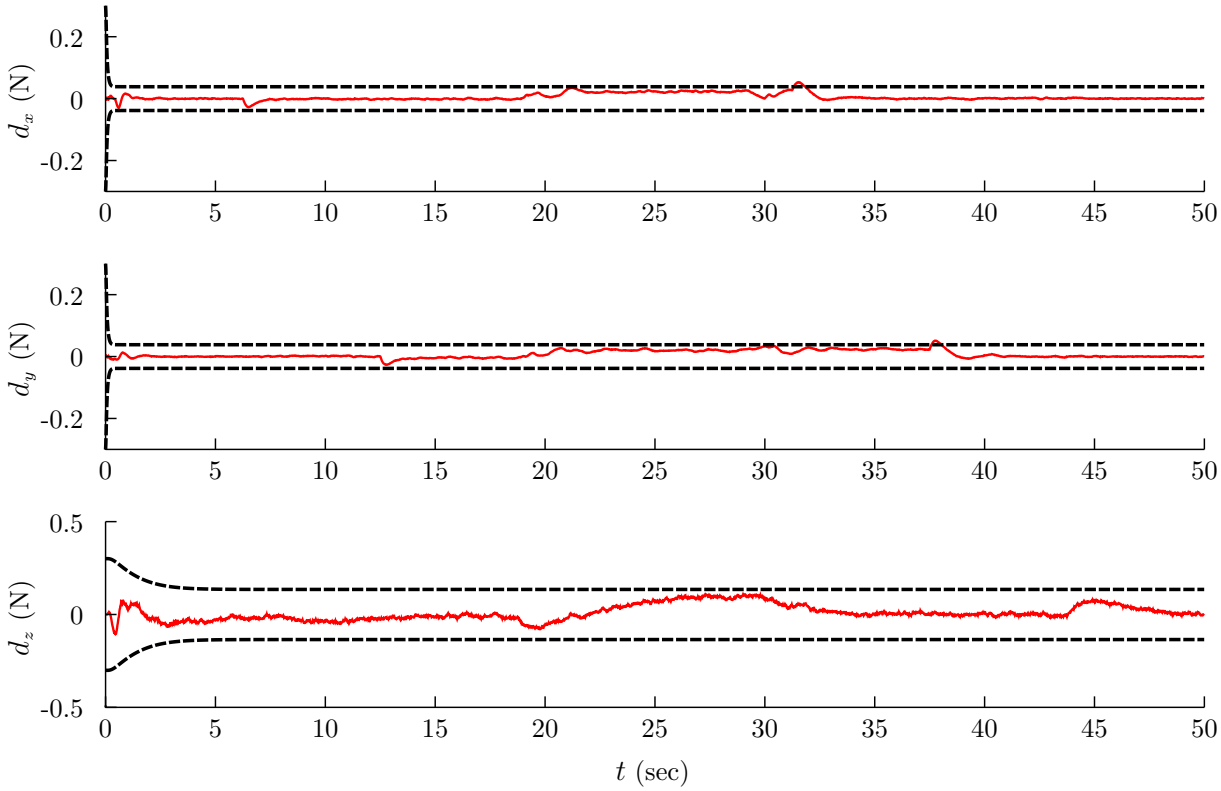

Figure 5.29: Estimation error of the disturbances, for the second trajectory with the mixed $\mathcal{H}_2/\mathcal{H}_\infty$ controller. Solid lines denote estimation error, while dashed lines denote confidence limits.

5.4 Zonotopic state estimator scenario

This section presents simulation results considering the scenario described in Section 4.3, in which measurements are provided by a GPS, a barometer, an IMU, a camera, and sensors embedded at the servomotors. The sensors have different sampling times, and available measurements are corrupted with additive noise. It is further referenced as the ZSE scenario.

The control structure is shown in Figure 5.30. The system's outputs, $\boldsymbol{\pi}(\boldsymbol{x})$, are sampled by the mentioned sensors, whose measurements along with the system's inputs, $\boldsymbol{u}_k$, are provided to the estimator. Equilibrium values are subtracted from control signals in order to adapt them for the zonotopic state estimator algorithm, which provides the first 20 elements of the center of the zonotope $\hat{\mathbb{X}}_k$ as estimated states. Equilibrium values are then added to the latter to recover the estimated state vector of the nonlinear system and make the feedback connection with the controller. The ZSE block implements the Algorithm 4.4, whilst the Controller block, as in the LKF scenario, corresponds to the subsystem with same name presented in the control structure of the FSI scenario.

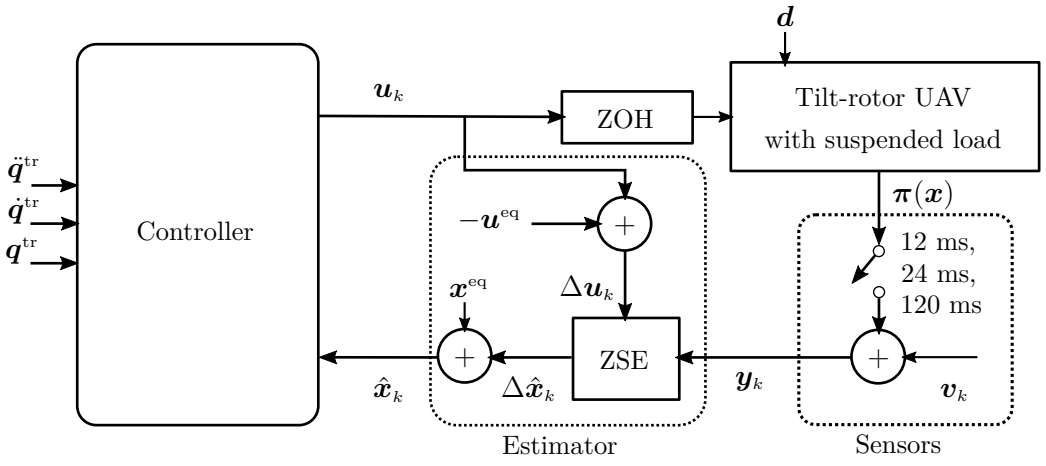

Figure 5.30: Control structure for the zonotopic state estimator scenario.

Table 5.8 shows the sensors parameters for this scenario. The noise bounds of the GPS, barometer/IMU, and the servos' sensors were taken from the Novatel OEMStar GPS receiver, Xsens MTi-G, and Herkulex DRS-0101/DRS-0201 sensors datasheets, respectively. The noise bounds of the camera were chosen empirically. The assumptions on probability density functions were made for simulation purposes, being only the knowledge on the noise bounds used for the design of the zonotopic state estimator. For Gaussian distributions, 'noise bound' means three times the standard deviation. The sets $\mathbb{I}$ correspond to the indexes of the measurement vector $\boldsymbol{y}_k$, associated with the elements that are provided by the corresponding sensor[5]. The union of all sets $\mathbb{I}$ of sensors whose measurements are

[5] $\{1,2,3\} \equiv \boldsymbol{\xi}_{\mathcal{B}}$, $\{4,5,6\} \equiv \boldsymbol{\eta}_{\mathcal{B}}$, $\{7,8,9\} \equiv \boldsymbol{\omega}^{\mathcal{B}}_{\mathcal{IB}}$, $\{10,11,12\} \equiv \boldsymbol{d}^{\mathcal{B}}_{\mathcal{BC}}$, $\{13\} \equiv \alpha_{\mathrm{R}}$, $\{14\} \equiv \alpha_{\mathrm{L}}$, $\{15\} \equiv \dot{\alpha}_{\mathrm{R}}$ and $\{16\} \equiv \dot{\alpha}_{\mathrm{L}}$. See equation (4.22).

available at time instant k yields the set $\mathbb{I}_k$ employed in the zonotopic state estimator algorithm.

Table 5.8: Sensors parameters for the ZSE scenario

Sensor	$\mathbb{I}$	Noise bound	Sampling time	PDF (for simulation)
GPS	$\{1, 2\}$	$\pm 0.15\,\text{m}$	120 ms	Gaussian
Barometer	$\{3\}$	$\pm 0.51\,\text{m}$	12 ms	Gaussian
IMU	$\{4, 5, 6\}$ $\{7, 8, 9\}$	$\pm 2.618{\cdot}10^{-3}\,\text{rad}$ $\pm 16.558{\cdot}10^{-3}\,\text{rad/s}$	12 ms	Gaussian
Camera	$\{10, 11\}$ $\{12\}$	$\pm 0.005\,\text{m}$ $\pm 0.02\,\text{m}$	24 ms	Uniform
Servos	$\{13, 14\}$ $\{15, 16\}$	$\pm 5.67{\cdot}10^{-3}\,\text{rad}$ $\pm 0.50772\,\text{rad/s}$	12 ms	Uniform

The initial predicted zonotope $\bar{\mathbb{X}}_0$ was chosen as a box centered at the desired trajectory, given by $\bar{\mathbb{X}}_0 = [(\boldsymbol{\xi}_0^{\text{tr}})^T \ \mathbf{0}_{1\times 20}]^T \oplus \boldsymbol{G}_{\bar{x}_0}\mathbb{B}^{23}$, with

$$\boldsymbol{G}_{\bar{x}_0} = \text{diag}(0.5{\cdot}\mathbf{1}_{3\times 1}, 0.2{\cdot}|\phi^{\text{eq}}|, 0.2{\cdot}|\theta^{\text{eq}}|, \pi/180, 0.2{\cdot}|{\gamma_1}^{\text{eq}}|, 0.2{\cdot}|{\gamma_2}^{\text{eq}}|, 0.2{\cdot}|{\alpha_{\text{R}}}^{\text{eq}}|, 0.2{\cdot}|{\alpha_{\text{L}}}^{\text{eq}}|, 0.02{\cdot}\mathbf{1}_{13\times 1}).$$

The zonotopes $\bar{\mathbb{W}}$ and $\bar{\mathbb{V}}$ were adjusted by trial and error[6], and are given by $\bar{\mathbb{W}} = \mathbf{0}_{23\times 1} \oplus \boldsymbol{G}_{\bar{w}}\mathbb{B}^{23}$ and $\bar{\mathbb{V}} = \boldsymbol{\pi}(\boldsymbol{x}^{\text{eq}}) \oplus \boldsymbol{G}_{\bar{v}}\mathbb{B}^{16}$, with

$$\begin{aligned}\boldsymbol{G}_{\bar{w}} =& \text{diag}(0.0001{\cdot}\mathbf{1}_{13\times 1}, 0.01{\cdot}\mathbf{1}_{3\times 1}, 0.05{\cdot}\mathbf{1}_{2\times 1}, 0.0001{\cdot}\mathbf{1}_{2\times 1}, 0.01{\cdot}\mathbf{1}_{3\times 1}),\\ \boldsymbol{G}_{\bar{v}} =& \text{diag}(0.18{\cdot}\mathbf{1}_{2\times 1}, 0.612, 3.1416{\cdot}10^{-3}, 3.1416{\cdot}10^{-3}, 0.03, 19.872{\cdot}10^{-3}, 19.872{\cdot}10^{-3}, 0.24,\\ & 0.006{\cdot}\mathbf{1}_{2\times 1}, 0.06, 6.8067{\cdot}10^{-3}{\cdot}\mathbf{1}_{2\times 1}, 0.6093{\cdot}\mathbf{1}_{2\times 1}).\end{aligned}$$

Moreover, the order of $\hat{\mathbb{X}}_k$ was limited to 75 times its dimension.

First trajectory

The trajectories performed by the tilt-rotor UAV and the suspended load are shown in Figure 5.31. The tracking error, shown in Figure 5.32 is not as small as in the previous scenarios, due to the presence of sensors with different sampling times, non-Gaussian noise, and also due to the choice of the center of the estimated zonotope to perform the feedback connection. However, the path tracking was also performed successfully for this scenario, demonstrating the joint performance of the designed controllers and the zonotopic state estimator, using the adopted control structure.

Figure 5.33 shows the time evolution of the remaining degrees of freedom, which kept stable, from which can be concluded that the tilt-rotor UAV remained stable. Figure 5.34 shows the control signals, which, despite being noisier than the ones from the LKF scenario, also did not saturate the aircraft's actuators.

[6]The zonotope $\bar{\mathbb{V}}$ was chosen using the noise bounds from Table 5.8 as starting point, then adjusted empirically in order to accommodate the unmodeled dynamics due to linearization.

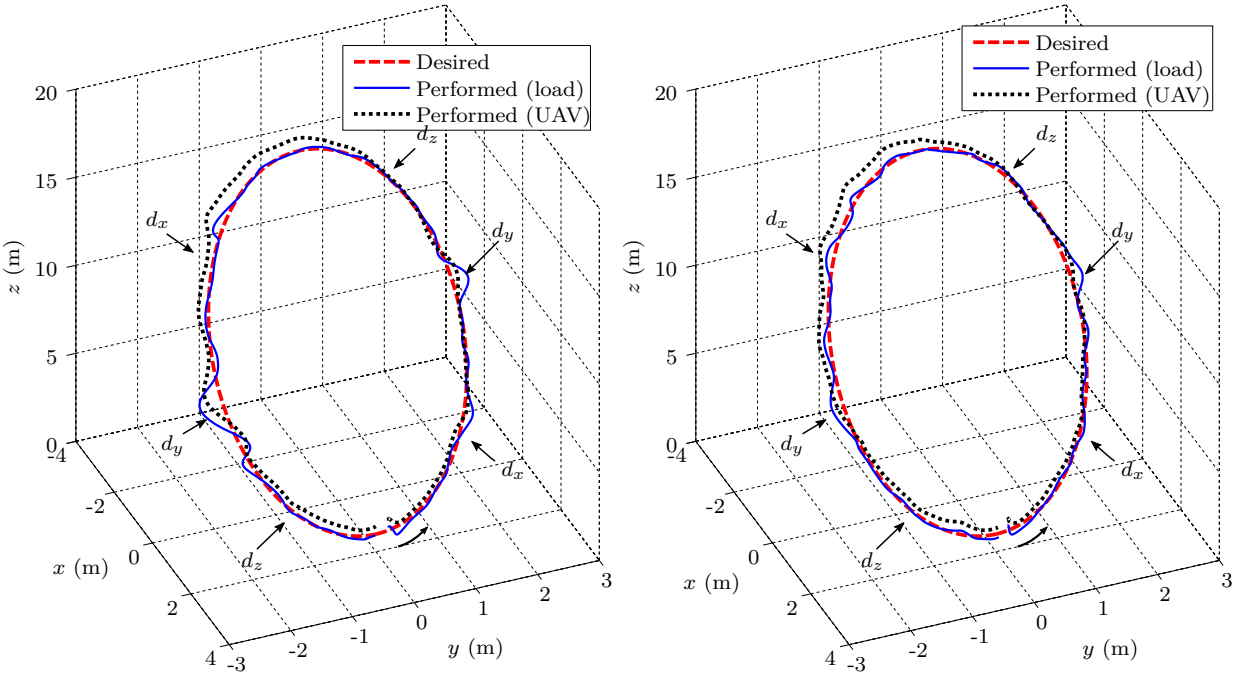

(a) DLQR (b) Mixed $\mathcal{H}_2/\mathcal{H}_\infty$

Figure 5.31: Trajectories performed by the UAV and the suspended load using the designed controllers, for the first desired trajectory, ZSE scenario.

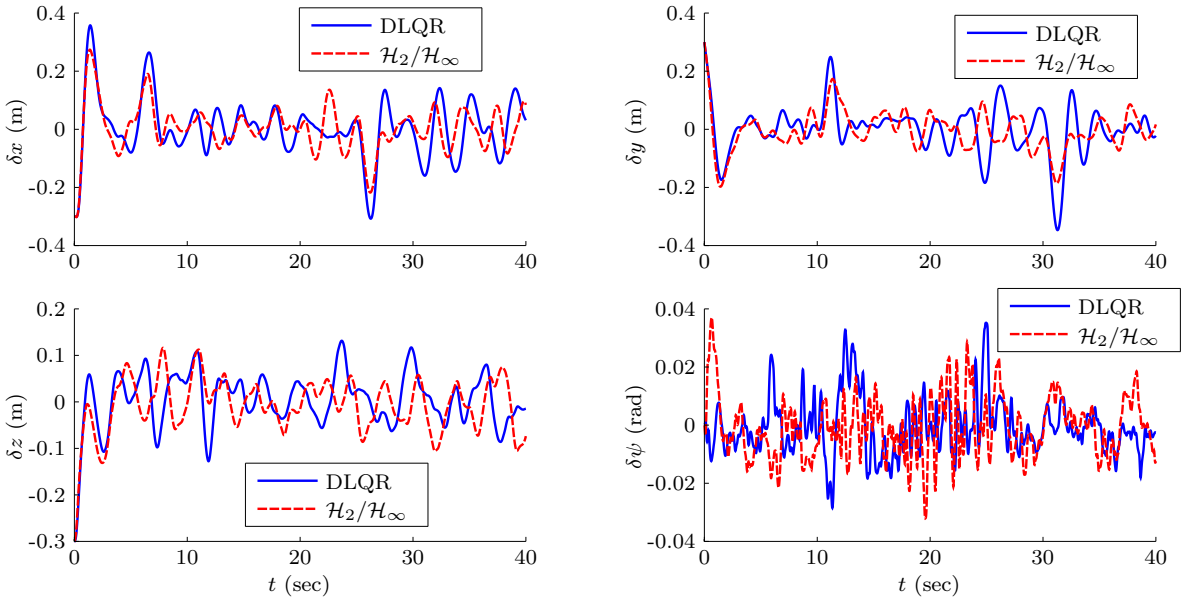

Figure 5.32: Tracking error for the first trajectory, ZSE scenario.

Table 5.9 shows the IADU and ISE performance indexes. Due to disturbance compensation, the mixed $\mathcal{H}_2/\mathcal{H}_\infty$ controller performed much better path tracking in x and y (ISE indexes only 62.23% and 62.19% of the respective ones from the DLQR), and slightly better in z, while the DLQR performed better in ψ. As in the LKF scenario, the mixed $\mathcal{H}_2/\mathcal{H}_\infty$ controller demonstrated to be way more aggressive than the DLQR with

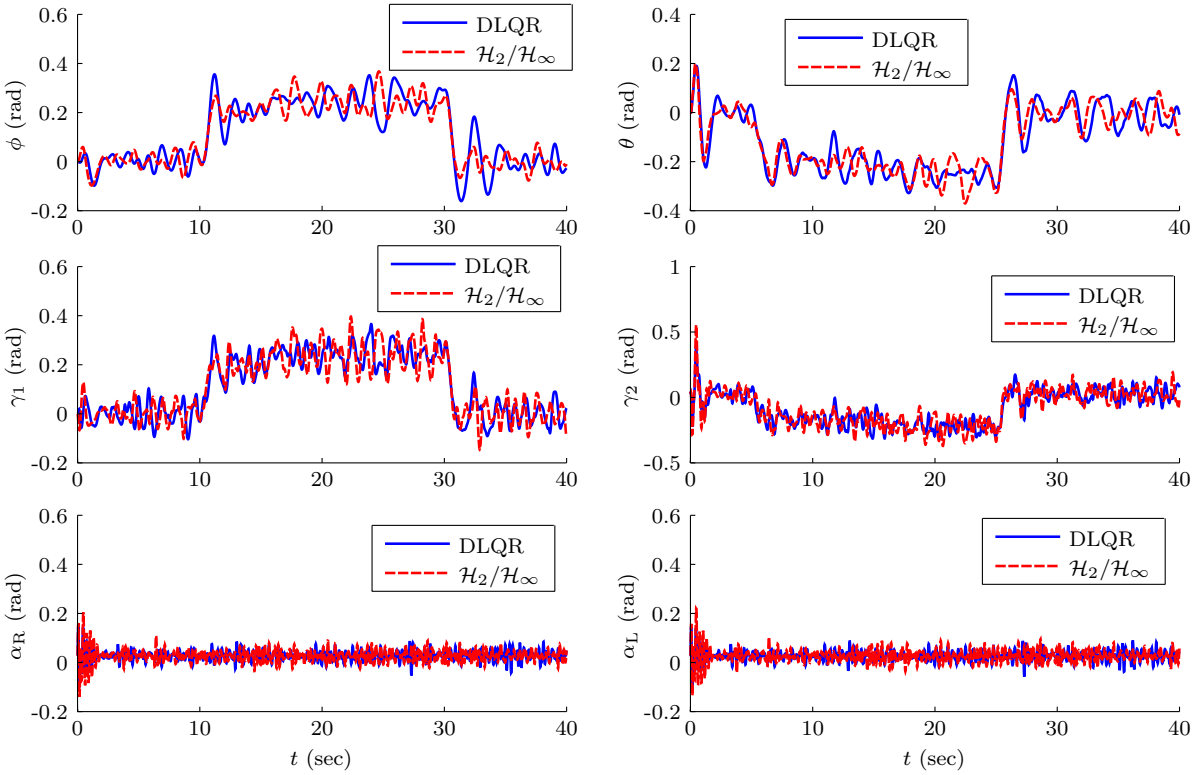

Figure 5.33: Time evolution of the remaining degrees of freedom for the first trajectory, ZSE scenario.

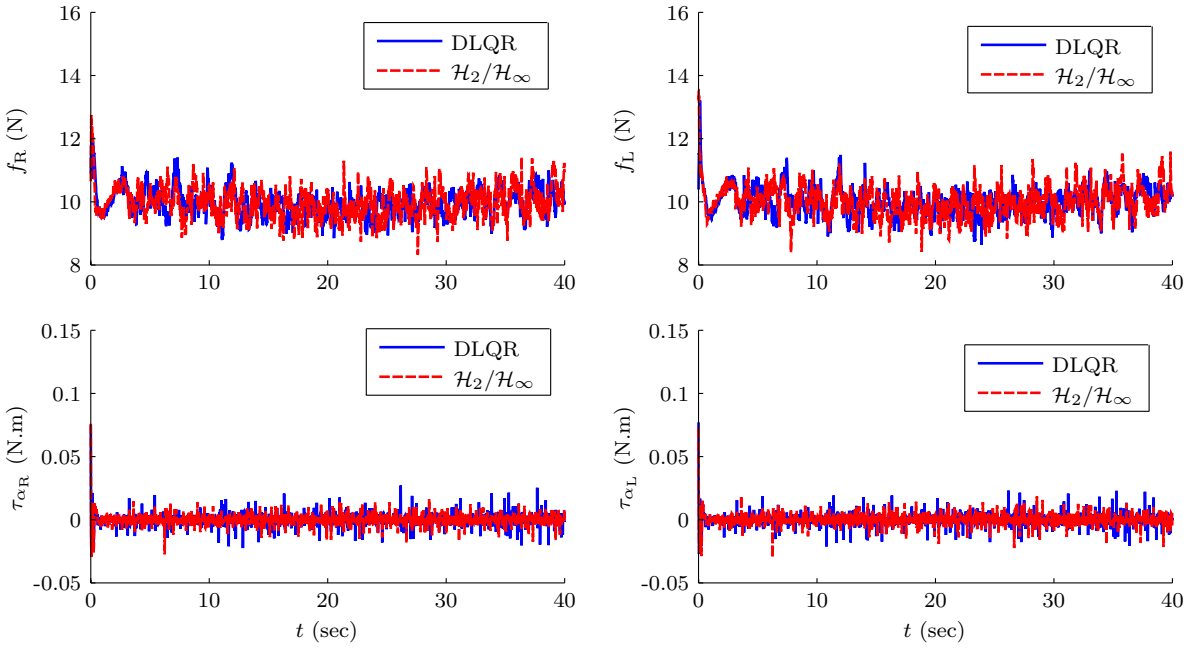

Figure 5.34: Actuator signals for the first trajectory, ZSE scenario. Saturation levels are $0 \leq f_R \leq 30$ N, $0 \leq f_L \leq 30$ N, $-2 \leq \tau_{\alpha_R} \leq 2$ N·m and $-2 \leq \tau_{\alpha_L} \leq 2$ N·m.

respect to the thrusters signals (35.04% and 29.6% greater IADU indexes for the right and left thrusters, respectively), while the servomotor control signals were harsher using the DLQR.

Table 5.9: Performance indexes for the first trajectory, ZSE scenario.

Index	DLQR	$\mathcal{H}_2/\mathcal{H}_\infty$	$\frac{\mathcal{H}_2/\mathcal{H}_\infty}{\text{DLQR}}$
ISE(x)	0.4146	0.2580	0.6223
ISE(y)	0.2895	0.1801	0.6219
ISE(z)	0.1389	0.1326	0.9542
ISE(ψ)	$3.8434{\cdot}10^{-3}$	$4.4799{\cdot}10^{-3}$	1.1656
IADU(f_R)	302.6595	408.7079	1.3504
IADU(f_L)	314.6170	407.7327	1.2960
IADU(τ_{α_R})	7.3176	6.0647	0.8288
IADU(τ_{α_L})	7.3531	6.4135	0.8722

For this scenario as well, estimation results are shown only for simulations with the mixed $\mathcal{H}_2/\mathcal{H}_\infty$ controller. Figure 5.35 shows the estimation error of the generalized coordinates, along with the zonotopic state estimator confidence limits (obtained by computing $\square\left\{\hat{\mathbb{X}}_k - \boldsymbol{c}_{\hat{x}_k}\right\}$). The confidence regions were large for some variables (around ± 1 m for x and y, and ± 2 m for z), but the estimation error was close to zero. Some patterns arised in the confidence limits due to the greater sampling times of the GPS and the camera, whose measurements were available only every 120 ms and 24 ms for performing the update step, respectively, while the other sensors' data were available every 12 ms, which is the controller sampling time. Moreover, note that the estimation errors of α_R and α_L left their respective confidence regions at the beginning of the simulation, due to nonlinearities that appeared during the initial convergence of the system to the reference trajectory.

Figure 5.36 shows the estimation error of the velocities along with the respective confidence limits. As in the previous case, the confidence regions were large for some variables (around ± 3.25 m/s for $\dot{x}$, ± 2.9 m/s for $\dot{y}$ and ± 5.1 m/s for $\dot{z}$), but the estimation error was also close to zero, and patterns arised in the confidence limits due to the greater sampling times of the GPS and the camera. The estimation errors of $\dot{\alpha}_\text{R}$ and $\dot{\alpha}_\text{L}$ left their respective confidence regions at the beginning of the simulation, due to the initial convergence of the system to the reference trajectory.

Figure 5.37 shows the estimation error of the external disturbances and the respective confidence limits. The confidence regions were much larger than the disturbances affecting the system (around ± 0.325 N for d_x, ± 0.285 N for d_y and ± 8.25 N for d_z, while the magnitudes of the disturbances were 0.1 N). However, the estimation error of d_x and d_y deviated from zero at most by around 0.06 N. On the other hand, as in the case of the LKF, the estimation error of d_z had not the same performance, deviating from zero by values much greater than 0.1 N.

Notice that, although dealing with different scenarios, the confidence regions provided by the zonotopic state estimator were very large if compared to the linearized Kalman filter confidence regions. Unlike the LKF algorithm, which propagates means and covariances

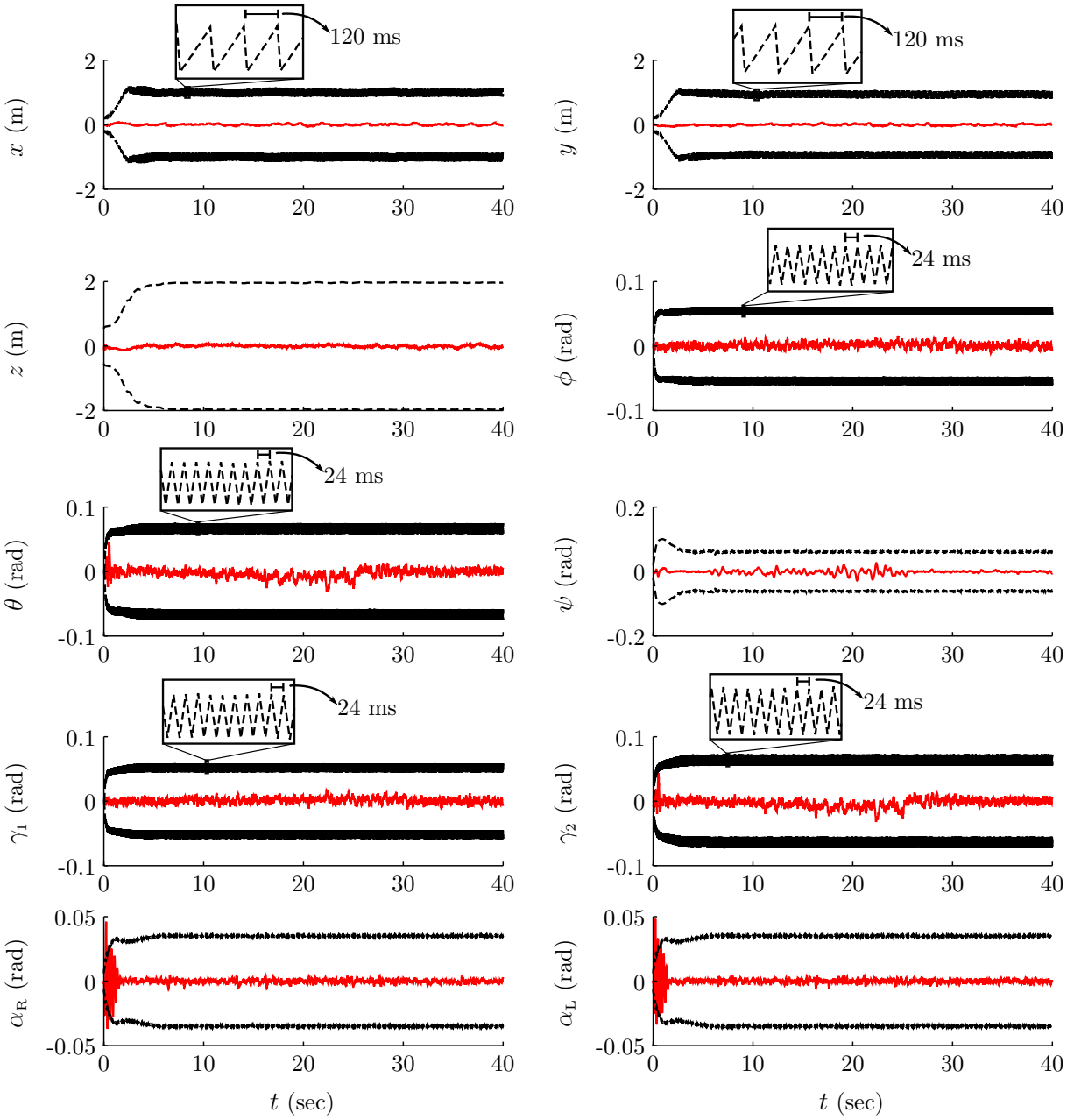

Figure 5.35: Estimation error of the generalized coordinates with the ZSE, for the first trajectory with the mixed $\mathcal{H}_2/\mathcal{H}_\infty$ controller. Solid lines denote estimation error, while dashed lines denote confidence limits.

through the linearized model and minimizes the variance of the estimation error, the ZSE algorithm propagates the estimated sets taking into account the worst case for noise and disturbances affecting the system. Moreover, the zonotopes $\bar{\mathbb{W}}$ and $\bar{\mathbb{V}}$ had to be overestimated empirically in order to accommodate unmodelled dynamics due to linearization.

Figure 5.38 shows the Frobenius norm of the generator matrix of the estimated zonotope $\hat{\mathbb{X}}_k$. The same patterns due to the sampling times of the GPS and the camera arised in the time evolution of the Frobenius norm.

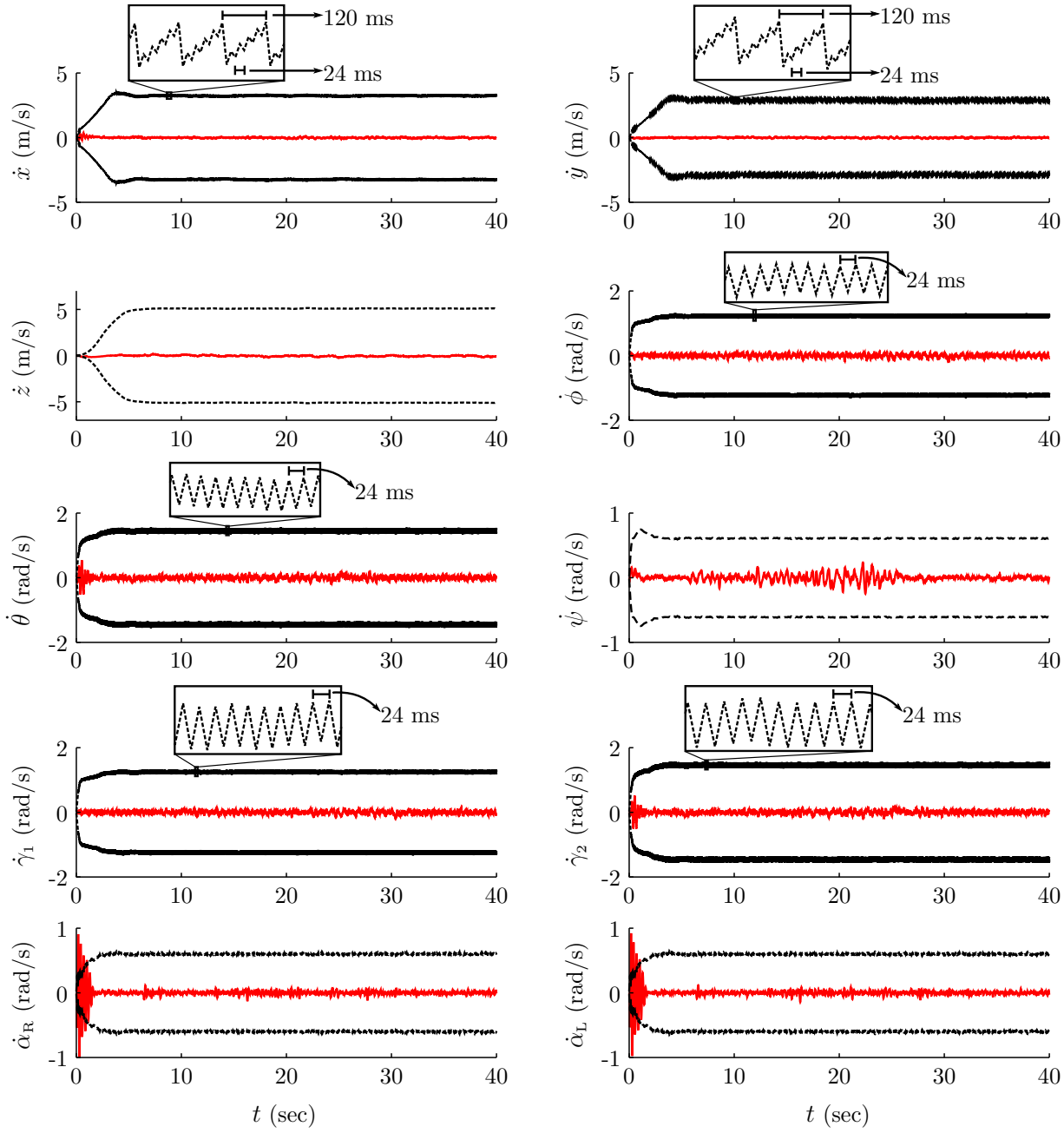

Figure 5.36: Estimation error of the velocities with the ZSE, for the first trajectory with the mixed $\mathcal{H}_2/\mathcal{H}_\infty$ controller. Solid lines denote estimation error, while dashed lines denote confidence limits.

Second trajectory

The trajectories performed by the tilt-rotor UAV and the suspended load are shown in Figure 5.39. The tracking error is shown in Figure 5.40. The path tracking was also performed successfully for this trajectory, demonstrating again the joint performance of the designed controllers and the zonotopic state estimator, using the adopted control structure.

Figure 5.41 shows the time evolution of the remaining degrees of freedom, which kept

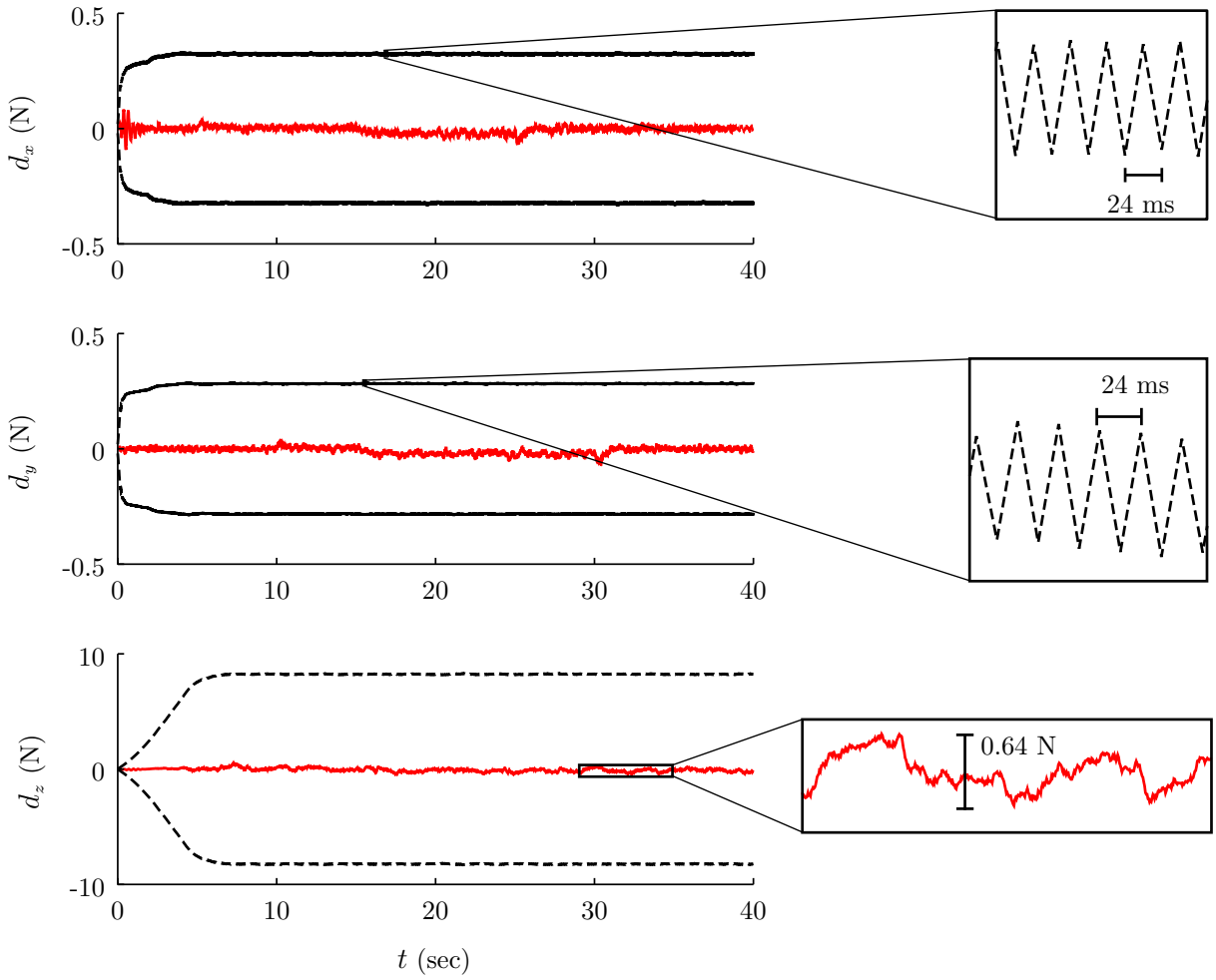

Figure 5.37: Estimation error of the disturbances with the ZSE, for the first trajectory with the mixed $\mathcal{H}_2/\mathcal{H}_\infty$ controller. Solid lines denote estimation error, while dashed lines denote confidence limits.

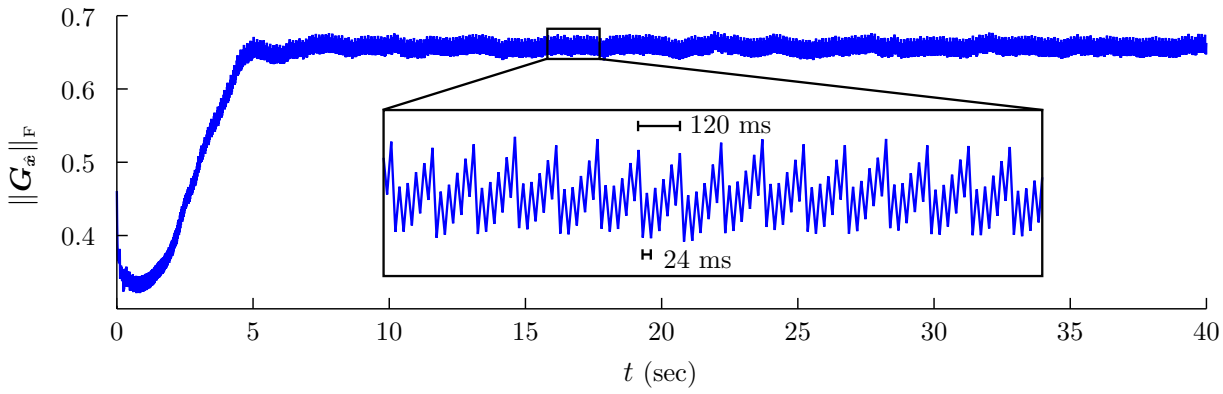

Figure 5.38: Frobenius norm of the estimated zonotope's generator matrix, for the first trajectory with the mixed $\mathcal{H}_2/\mathcal{H}_\infty$ controller.

stable, from which can be concluded that the tilt-rotor UAV remained stable. Figure 5.42 shows the control signals, which did not saturate the aircraft's actuators.

Table 5.10 shows the IADU and ISE performance indexes. The mixed $\mathcal{H}_2/\mathcal{H}_\infty$ controller

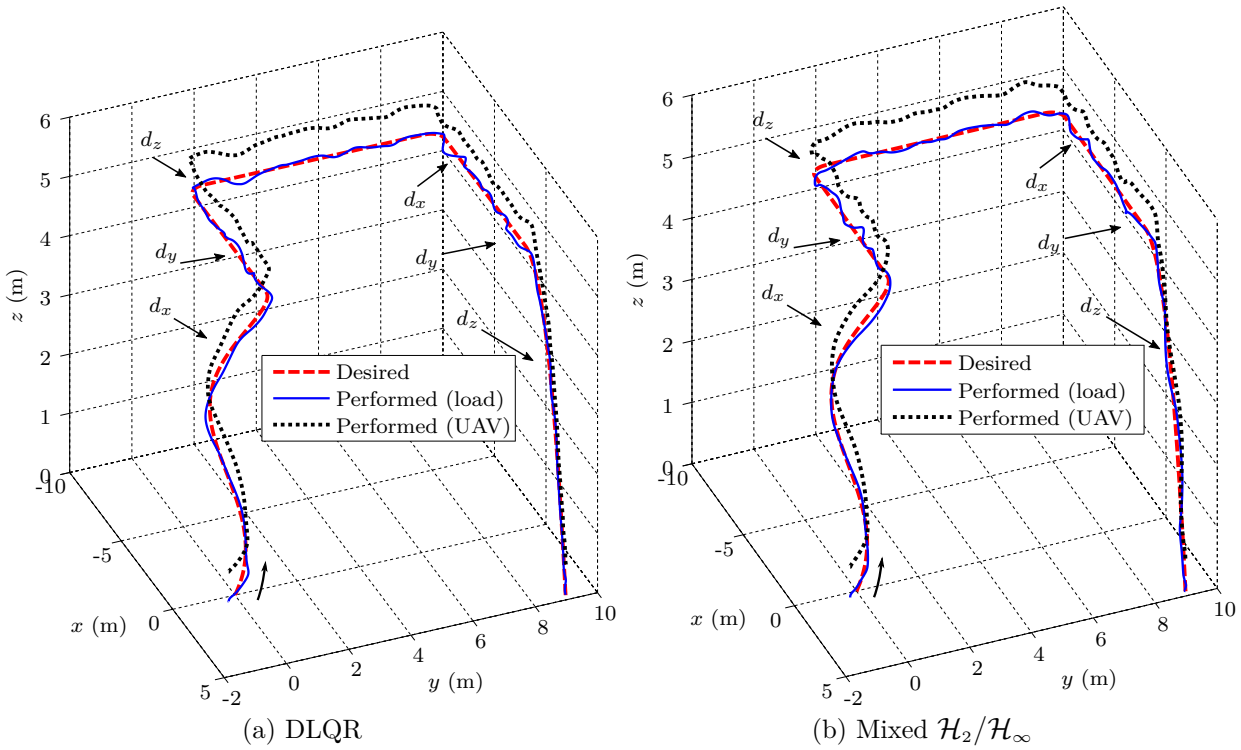

(a) DLQR (b) Mixed $\mathcal{H}_2/\mathcal{H}_\infty$

Figure 5.39: Trajectories performed by the UAV and the suspended load using the designed controllers, for the second desired trajectory, ZSE scenario.

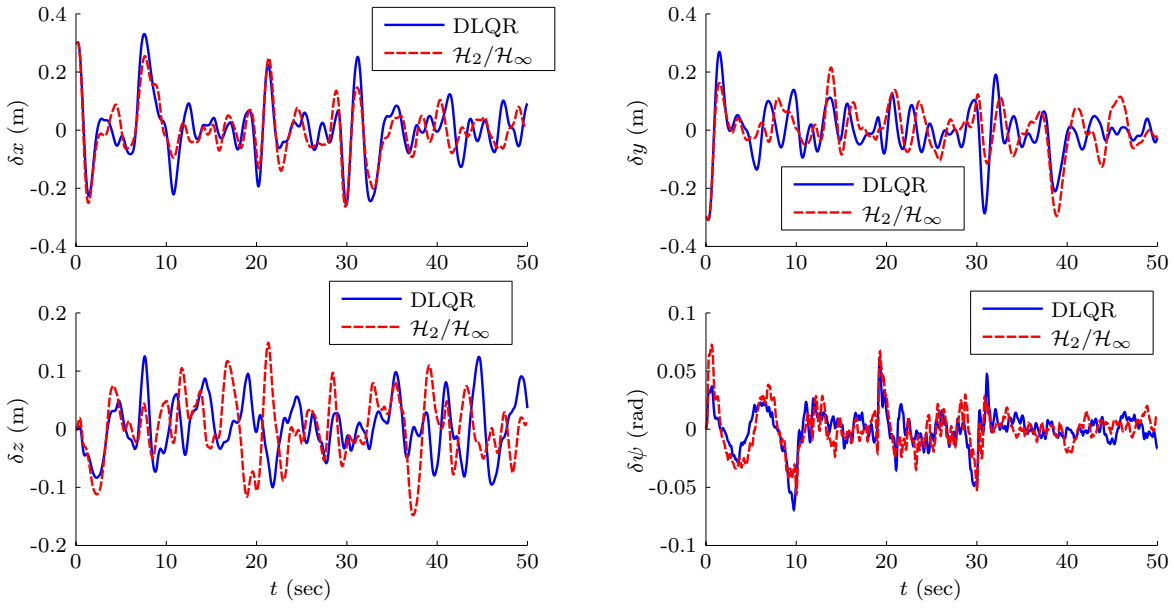

Figure 5.40: Tracking error for the second trajectory, ZSE scenario.

performed better path tracking in x (ISE index 80.59% of the respective one from the DLQR), while the DLQR performed better in y, z and ψ. The mixed $\mathcal{H}_2/\mathcal{H}_\infty$ controller was again more aggressive than the DLQR with respect to the thrusters signals (27.39% and 27.78% greater IADU indexes for the right and left thrusters, respectively), while the

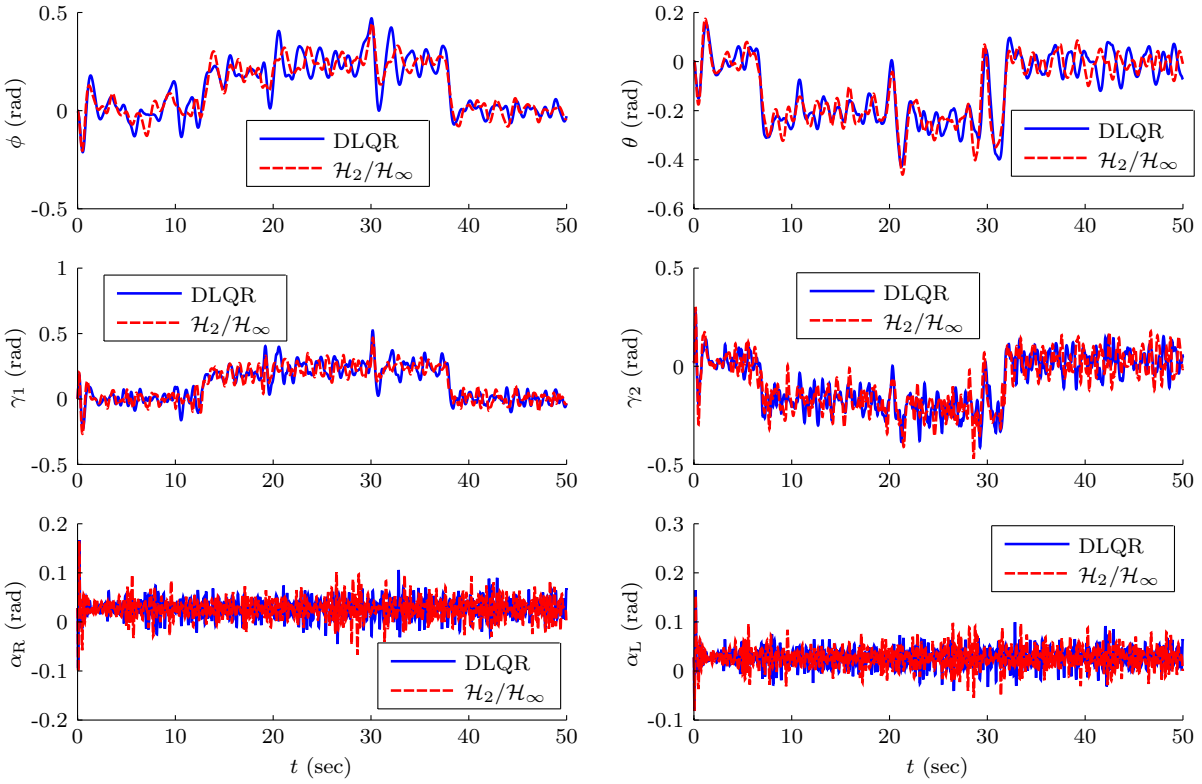

Figure 5.41: Time evolution of the remaining degrees of freedom for the second trajectory, ZSE scenario.

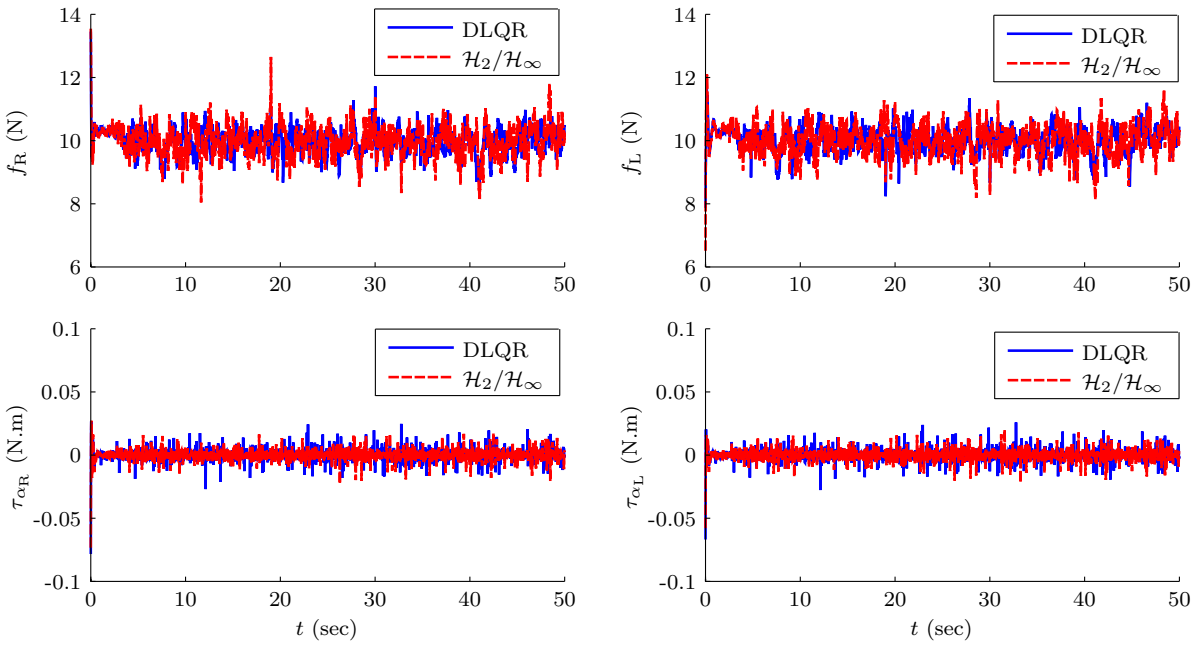

Figure 5.42: Actuator signals for the second trajectory, ZSE scenario. Saturation levels are $0 \leq f_R \leq 30$ N, $0 \leq f_L \leq 30$ N, $-2 \leq \tau_{\alpha_R} \leq 2$ N·m and $-2 \leq \tau_{\alpha_L} \leq 2$ N·m.

servomotor control signals were harsher using the DLQR.

Figure 5.43 shows the estimation error of the generalized coordinates, along with the respective confidence limits. The discussion on the confidence regions presented for the

Table 5.10: Performance indexes for the second trajectory, ZSE scenario.

Index	DLQR	$\mathcal{H}_2/\mathcal{H}_\infty$	$\frac{\mathcal{H}_2/\mathcal{H}_\infty}{\text{DLQR}}$
ISE(x)	0.5242	0.4225	0.8059
ISE(y)	0.3347	0.3443	1.0285
ISE(z)	0.1123	0.1529	1.3608
ISE(ψ)	0.0123	0.0161	1.3094
IADU(f_{R})	406.9815	518.4401	1.2739
IADU(f_{L})	404.0254	516.2678	1.2778
IADU($\tau_{\alpha_{\text{R}}}$)	8.9879	7.4309	0.8268
IADU($\tau_{\alpha_{\text{L}}}$)	9.0586	7.7548	0.8561

first trajectory results also applies here. The patterns in the confidence limits due to the sampling times of the GPS and the camera can also be observed.

Figure 5.44 shows the estimation error of the velocities along with confidence limits, and Figure 5.45 shows the estimation error of the external disturbances. Again, the patterns in the confidence limits can be observed, and the discussion of the first trajectory results also applies here. Figure 5.46 shows the time evolution of the Frobenius norm of the generator matrix of $\hat{\mathbb{X}}_k$.

Regarding the initial displacement of the load, the ZSE algorithm was also designed based on linearized dynamic equations. Then, for larger initial displacements and harsher disturbances, the estimation error associated with the center of the estimated zonotope significantly leaves the confidence limits, destabilizing the system.

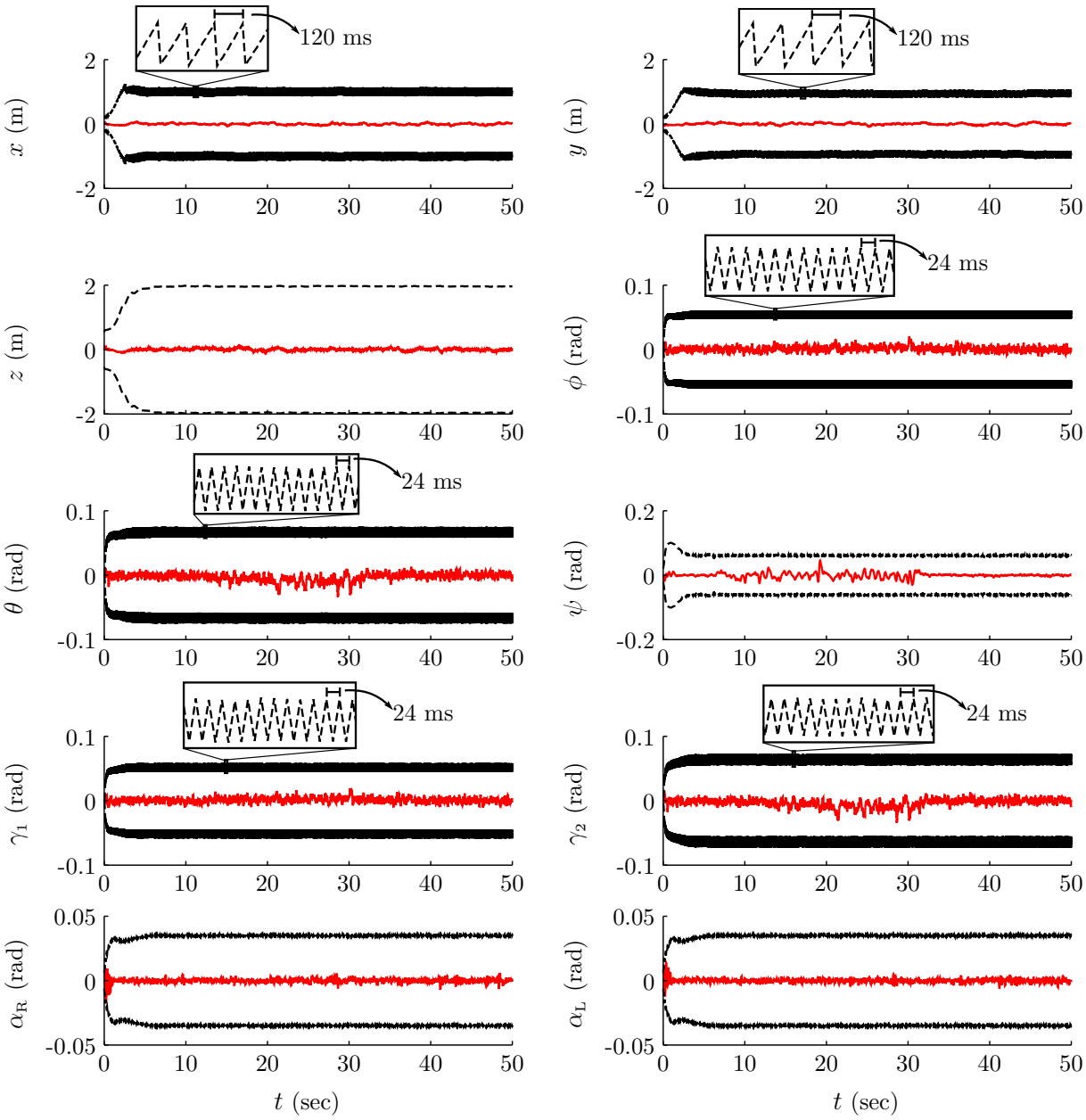

Figure 5.43: Estimation error of the generalized coordinates with the ZSE, for the second trajectory with the mixed $\mathcal{H}_2/\mathcal{H}_\infty$ controller. Solid lines denote estimation error, while dashed lines denote confidence limits.

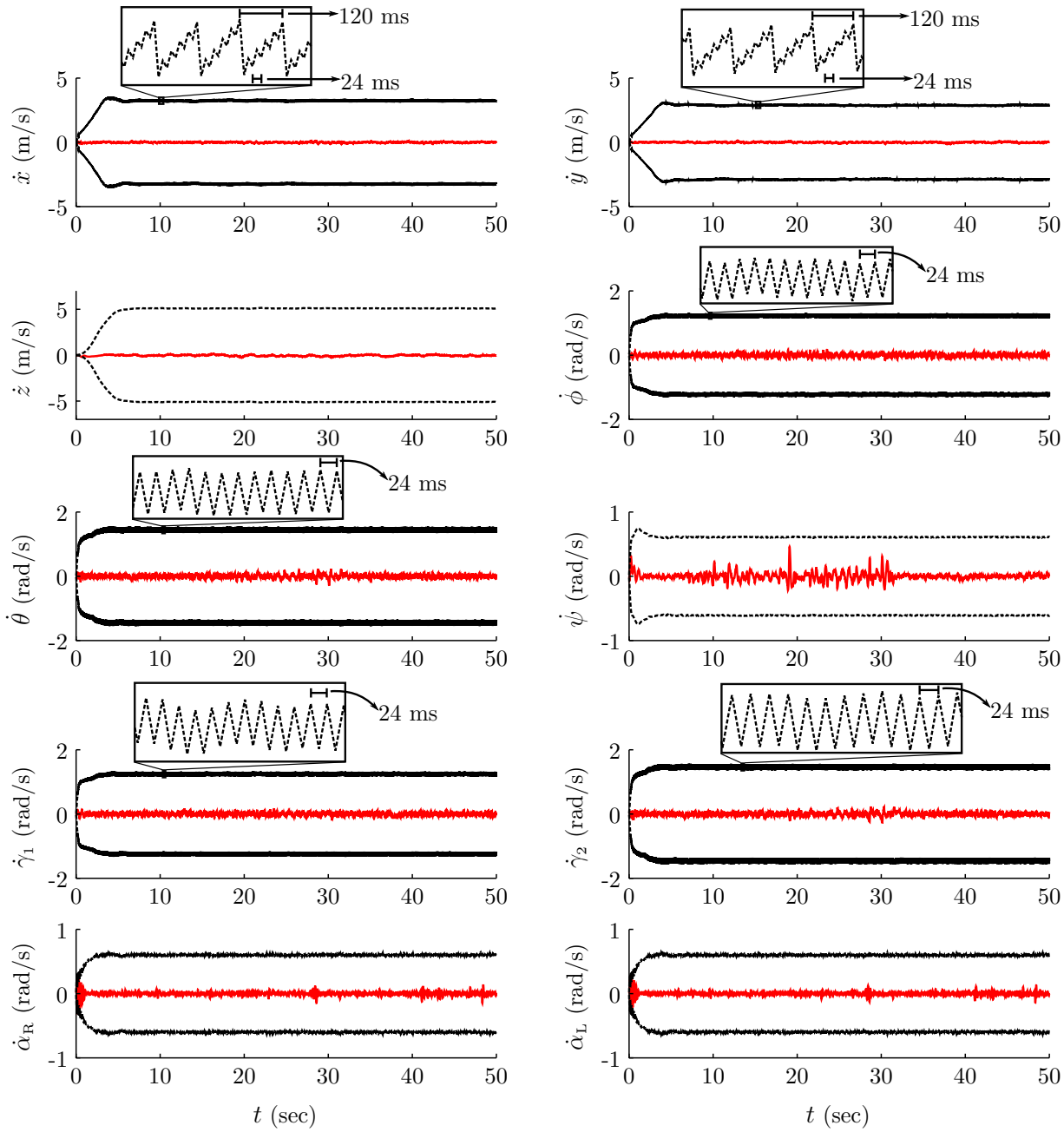

Figure 5.44: Estimation error of the velocities with the ZSE, for the second trajectory with the mixed $\mathcal{H}_2/\mathcal{H}_\infty$ controller. Solid lines denote estimation error, while dashed lines denote confidence limits.

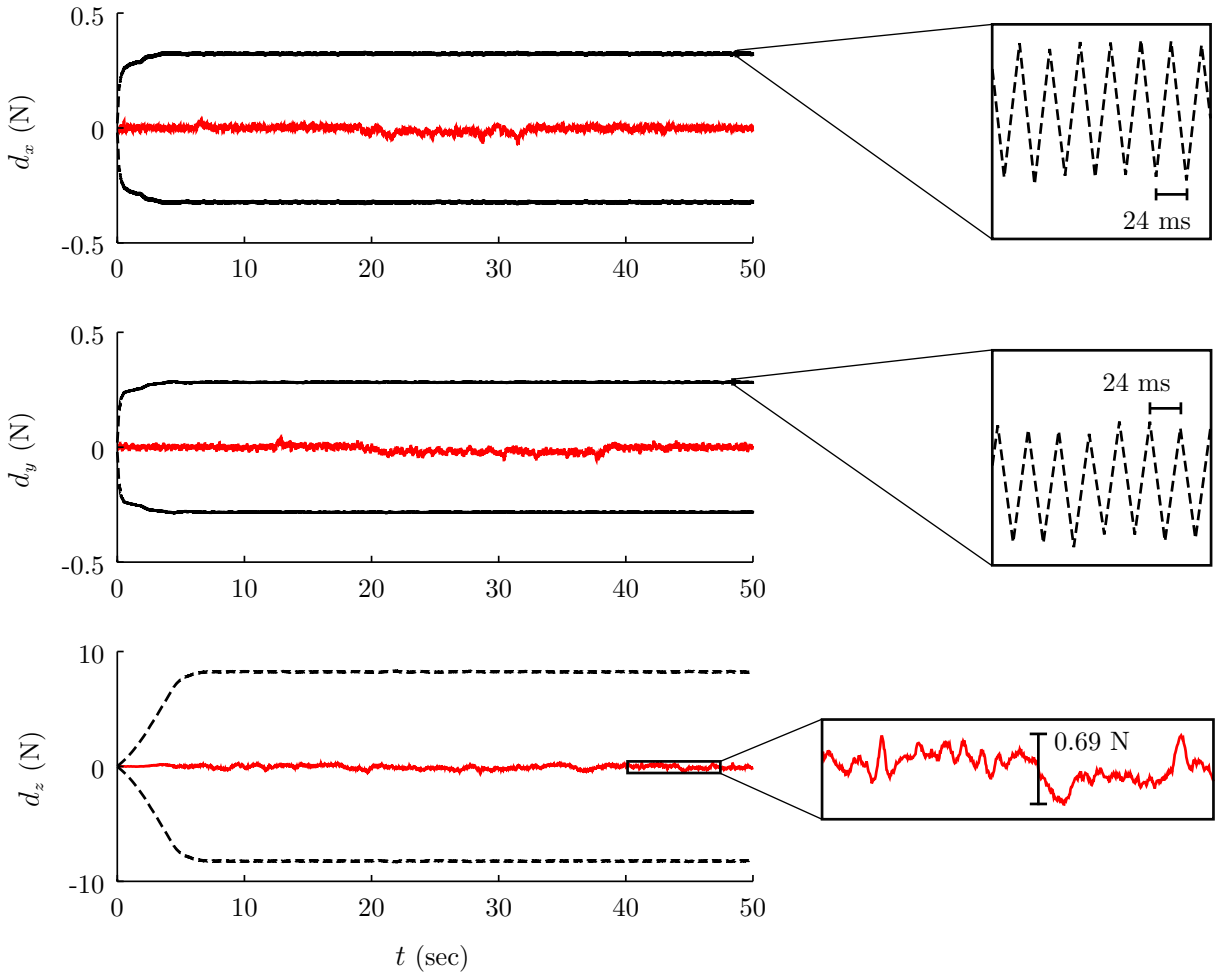

Figure 5.45: Estimation error of the disturbances with the ZSE, for the second trajectory with the mixed $\mathcal{H}_2/\mathcal{H}_\infty$ controller. Solid lines denote estimation error, while dashed lines denote confidence limits.

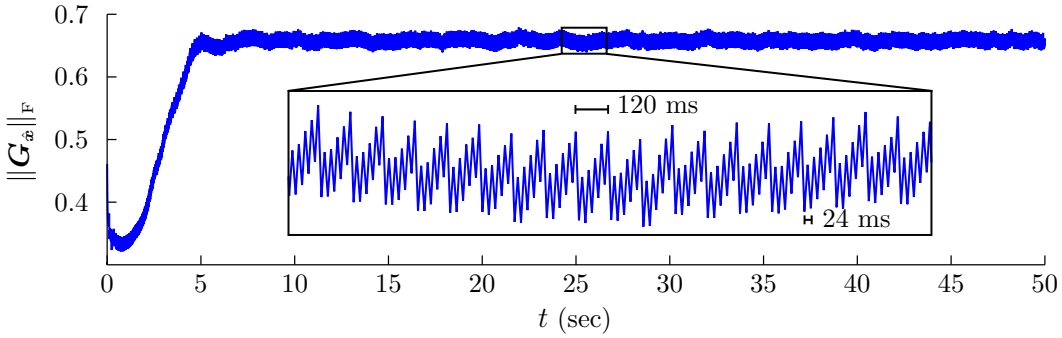

Figure 5.46: Frobenius norm of the estimated zonotope's generator matrix, for the second trajectory with the mixed $\mathcal{H}_2/\mathcal{H}_\infty$ controller.

5.5 Comparison between scenarios

This section compares the performance indexes associated with each scenario, to analyze performance loss when the ideal scenario is not considered, and also between the LKF and ZSE scenarios.

Table 5.11 compares the performance indexes for the first desired trajectory. Note that the ISE indexes are higher in general for the LKF and ZSE scenarios, when compared to the FSI scenario, for both controllers. Since the feedback connection was performed using estimated states, it is expected that the trajectory tracking is less accurate for the LKF and ZSE scenarios. The only exception was the trajectory tracking of ψ for the mixed $\mathcal{H}_2/\mathcal{H}_\infty$ controller and LKF scenario. This result can be explained by the fact that the mixed $\mathcal{H}_2/\mathcal{H}_\infty$ controller was designed for improved transient response, and since the system is being affected by measurement noise, is it always in transient state. The IADU indexes corroborate this statement, being much higher for the LKF and ZSE scenarios, in comparison with the FSI scenario.

On the other hand, the ISE and IADU indexes were higher in general for the ZSE scenario, in comparison with the LKF scenario, due to effects from the different sampling times, harsher and non-Gaussian noise, and most measurements being associated with coordinates from the tilt-rotor UAV instead of the load. The exception is the ISE index associated with ψ, showing that the trajectory tracking of ψ was more accurate in the ZSE scenario. A possible explanation is that, in the ZSE scenario the time derivative of ψ is indirectly associated with the measured angular velocity $\boldsymbol{\omega}_{\mathcal{IB}}^{\mathcal{B}}$ (see equation (4.20)). On the other hand, in the LKF scenario, this variable is not associated with any measurement.

Table 5.11: Performance indexes for the first trajectory, comparison between scenarios.

Index	LKF/FSI		ZSE/FSI		ZSE/LKF	
	DLQR	$\mathcal{H}_2/\mathcal{H}_\infty$	DLQR	$\mathcal{H}_2/\mathcal{H}_\infty$	DLQR	$\mathcal{H}_2/\mathcal{H}_\infty$
ISE(x)	1.0337	1.1177	2.6391	1.6963	2.5531	1.5177
ISE(y)	1.0765	1.1868	2.6058	1.5433	2.4206	1.3004
ISE(z)	1.1519	0.9870	3.2453	3.4442	2.8173	3.4896
ISE(ψ)	37.2310	17.9070	33.3660	12.3710	0.8962	0.6908
IADU(f_{R})	29.1920	34.6840	42.3383	51.4337	1.4503	1.4829
IADU(f_{L})	26.6966	30.7034	40.4850	42.0933	1.5165	1.3710
IADU($\tau_{\alpha_{\mathrm{R}}}$)	27.6900	26.2289	36.8831	30.8479	1.3320	1.1761
IADU($\tau_{\alpha_{\mathrm{L}}}$)	27.6998	27.0126	37.0994	32.4242	1.3393	1.2003

Table 5.12 compares the performance indexes for the second desired trajectory. Note that the ISE indexes are again higher in general for the LKF and ZSE scenarios, when compared to the FSI scenario. The only exception is the trajectory tracking of x for the mixed $\mathcal{H}_2/\mathcal{H}_\infty$ controller and LKF scenario. The same argument based on improved transient response can be stated here, being corroborated by the IADU indexes, which are again higher for the LKF and ZSE scenarios, in comparison with the FSI scenario.

As in the first trajectory, the ISE and IADU indexes were higher in general for the ZSE scenario, in comparison with the LKF scenario, with exception of the ISE index associated with ψ. The same arguments based on its time derivative and available measurements can be stated for this case.

Table 5.12: Performance indexes for the second trajectory, comparison between scenarios.

Index	LKF/FSI		ZSE/FSI		ZSE/LKF	
	DLQR	$\mathcal{H}_2/\mathcal{H}_\infty$	DLQR	$\mathcal{H}_2/\mathcal{H}_\infty$	DLQR	$\mathcal{H}_2/\mathcal{H}_\infty$
ISE(x)	1.0491	0.9967	1.5610	1.4145	1.4879	1.4192
ISE(y)	1.0811	1.2034	1.4365	1.4802	1.3287	1.2300
ISE(z)	13.3129	9.9177	107.5567	91.9036	8.0791	9.2666
ISE(ψ)	3.4788	8.5654	2.4039	1.6962	0.6910	0.1980
IADU(f_R)	11.1600	13.4385	16.8062	19.0146	1.5059	1.4149
IADU(f_L)	11.1196	14.2518	16.7471	19.2631	1.5061	1.3516
IADU(τ_{α_R})	24.0979	20.9894	31.5476	24.6056	1.3091	1.1723
IADU(τ_{α_L})	25.1602	22.6114	33.3527	27.0485	1.3256	1.1962

5.6 Final remarks

This chapter evaluated the proposed control and state estimation strategies, designed in the previous chapters, by means of simulations in MATLAB/Simulink® environment. Two reference trajectories were specified for path tracking of the suspended load, and three scenarios were addressed: (i) the full state information scenario, in which all states were available for feedback connection, at every time instant; (ii) the linearized Kalman filter scenario, in which only a half of the state vector was available, corrupted with zero-mean Gaussian noise; and (iii) the zonotopic state estimator scenario, in which measurements were provided by a GPS, a barometer, an IMU, a camera, and sensors embedded at the UAV's servomotors, corrupted with unknown but bounded noise and with different sampling times. Moreover, the system was subject to external forces, applied to the suspended load's center of mass.

For the FSI scenario, the feedback connection was performed with the system states. The proposed control strategies were successful in performing path tracking of the suspended load for the two reference trajectories, while rejecting the external disturbances applied to the suspended load and stabilizing the remaining degrees of freedom and the tilt-rotor UAV as well. The behavior of the closed-loop system was similar for both controllers, yielding close performance indexes.

For the LKF scenario, the feedback connection was performed using the states provided by the linearized Kalman filter, with proper adaptations using equilibrium values, since the estimator was designed based on linearized state-space equations. The path tracking was performed successfully for the two reference trajectories, showing the good performance

of the proposed control structure, designed controllers and the linearized Kalman filter. However, due to the nonlinearities of the system, the estimation error left the confidence regions of the filter at some time instants, and also become biased. Despite these problems, the linearized Kalman filter proved capable of estimating the system states in the carried out simulations.

For the ZSE scenario the feedback connection was performed using the center of the estimated zonotope, provided by the zonotopic state estimator, also with proper adaptations using equilibrium values. The path tracking was performed with success also for this more realistic scenario, for the two reference trajectories, showing the good performance of the proposed control structure and the zonotopic state estimator.

6 Conclusions

This thesis dealt with the problem of path tracking of a suspended load using a tilt-rotor UAV. A modeling approach was presented, and control and state estimation strategies were proposed for the accomplishment of the task.

The kinematics of the system were formulated from the load's perspective, in which the load's position and orientation were chosen as degrees of freedom of the mechanical system. The aircraft's position and orientation were regarded only relatively to the suspended load. The dynamic equations of the system were then obtained through the Euler-Lagrange formulation, taking into account the dynamic coupling between the aircraft and the load, the existence of viscous friction at the suspension point, and also the possibility of external disturbances affecting the load, yielding a nonlinear state-space representation of the system, affine in the inputs, with the load's position and orientation as states.

Discrete-time, robust linear state-feedback control strategies were proposed for path tracking of the suspended load with stabilization of the tilt-rotor UAV. The nonlinear state-space equations of the system were linearized around a generic trajectory, augmented with integral actions over the error of the regulated states for constant disturbances rejection, and discretized for the controller sampling time. Based on the linear discrete-time system, two strategies were proposed:

- A discrete-time linear quadratic regulator, in which the state-feedback gains were computed by solving a discrete-time algebraic Riccati equation, minimizing an infinite-horizon quadratic cost functional associated to the energy of the tracking error and control signals;

- A discrete-time mixed $\mathcal{H}_2/\mathcal{H}_\infty$ controller with pole placement constraints, in which the state-feedback gains were computed through LMI approach, minimizing the $\mathcal{H}_2$ norm of the system for a specified upper-bound of the $\mathcal{H}_\infty$ norm, while guaranteeing time response specifications by means of pole placement in LMI regions;

State estimators were also designed to provide information on the system states for feedback connection. The linearized state-space equations were evaluated at an equilibrium point, yielding a time-invariant system, and augmented with the external disturbances affecting the system. Two different strategies were proposed based on this model:

- A linearized Kalman filter, for a scenario in which only a half of the state vector is measured, corrupted with zero-mean Gaussian noise. The presented algorithm is classical, derived through propagation of means and covariances, and the Kalman gain computed through a closed solution that minimizes the estimation error variance at each time step. The unmodelled dynamics due to linearization were regarded as process noise.

- A zonotopic state estimator, for a scenario in which available information is composed of the UAV's position and orientation, its angular velocity and the load's position with respect to it. This information was provided by a GPS equipment, an IMU, a camera, and embedded sensors at the servomotors, each one with its own sampling time, and corrupted with unknown but bounded noise. The algorithm was derived by extending the technique presented in Alamo et al. (2005), based on zonotopes and strips, for multi-output systems and multiple sampling times. Despite being formulated for nonlinear systems, due to computational effort the linear discrete-time, time-invariant model was used for the prediction step. In order to prevent interval dependency, the measurement equations were also linearized around an equilibrium point for the update step. Due to linearization, the zonotopes had to be adjusted so to contain all the associated unmodelled dynamics.

The proposed strategies were evaluated through simulations in MATLAB/Simulink® environment. Two reference trajectories were specified: a ring in the three-dimensional Euclidean space, proposed to evaluate the performance of the designed strategies in a scenario without aggressive maneuvers; and a path composed of several interconnected stretches, proposed to evaluate the performance of the designed strategies in a diversified scenario that includes vertical take-off in a spiral path, straight line following with rapid changing in direction, and vertical landing. The system was subjected to external forces applied to the suspended load. Three scenarios were addressed:

- Full state information, to evaluate the performance of the proposed controllers for the ideal conditions based on which they were designed, in which the feedback connection

was performed with the system states. The design parameters of the state-feedback controllers were presented, along with the associated pole placements. The closed-loop system demonstrated similar behaviors using the DLQR and the mixed $\mathcal{H}_2/\mathcal{H}_\infty$ controller, which showed very close performance indexes, as expected from the pole placement results. Both controllers rejected the external disturbances, and were capable of performing path tracking of the suspended load in both trajectories. The load orientation and the UAV's orientation with respect to the load were both stabilized, from which it could be concluded that the tilt-rotor UAV remained stable as well.

- Linearized Kalman filter scenario, in which the feedback connection was performed with the estimation provided by the LKF, with proper adaptations. The design parameters of the filter and the control structure were presented, and additive noise was assumed for the load position measurement. Due to its disturbance compensation capabilities, the mixed $\mathcal{H}_2/\mathcal{H}_\infty$ controller demonstrated to be more aggressive than the DLQR for this scenario. The path tracking was performed successfully for both trajectories. The linearized Kalman filter was capable of reducing the variance of the estimation error substantially, while estimating the non-measured states.

- Zonotopic state estimator scenario, in which the feedback connection was performed with the center of the estimated zonotope, with proper adaptations. The design parameters of the zonotopic state estimator and the control structure were presented. Datasheet noise bounds were assumed for all sensors, and higher sampling times were assumed for the GPS and the camera. For simulation purposes, uniform noise was assumed for the camera and the servos, while Gaussian noise was assumed for the remaining sensors. The path tracking was performed successfully for both trajectories, and again the mixed $\mathcal{H}_2/\mathcal{H}_\infty$ controller showed to be more aggressive than the DLQR. The zonotopic state estimator was capable of reconstructing the system states from the available measurements. Furthermore, the higher sampling times of the GPS and the camera leaded to 'toothed' patterns in the confidence limits, since the update step was performed for these sensors only when their measurements were available.

Finally, the main contributions of this thesis are summarized as follows:

- Development of equations of motion for the tilt-rotor UAV with suspended load from the load's perspective;

- Design of robust, discrete-time linear state-feedback control strategies for path tracking of the suspended load with stabilization of the tilt-rotor UAV, featuring constant disturbances rejection;

- Design of state estimation strategies for scenarios in which not all the system states are available for feedback connection, measurements are corrupted with noise and sensors have different sampling times;
- Extension of the discrete-time, state-feedback $\mathcal{H}_2$ and $\mathcal{H}_\infty$ control design methodologies proposed in de Oliveira et al. (2002) for the mixed case with pole placement constraints;
- Extension of the zonotopic state estimation algorithm proposed in Alamo et al. (2005) for multi-output systems and multiple sampling times.

6.1 Future works

This section suggests possible future works in this line of research.

- **Validation of the proposed techniques in the Gazebo platform.** A simulation platform based on Gazebo is currently being developed in the ProVANT project. Validation of the proposed strategies in this platform would allow further testing their robustness.
- **Validation of the proposed techniques in experimental setup.** During the elaboration of this thesis, the ProVANT UAV 2.0 was almost ready for performing experimental flights. An important step in this research would be the implementation of the proposed control and estimation strategies in the real system.
- **Inclusion of parametric uncertainties.** The proposed techniques do not take into account parametric uncertainties in the system. The DLQR can be formulated using an LMI approach, allowing the inclusion of parametric uncertainties (see, e.g., Donadel (2015)). Moreover, the discrete-time mixed $\mathcal{H}_2/\mathcal{H}_\infty$ control formulation presented in this thesis and allows direct inclusion of parametric uncertainties.
- **Design of the linear control and state estimation strategies for the time-varying system.** In order to design the control strategies, the linearized time-varying state-space equations were approximated by time-invariant ones, valid around the equilibrium point. The design of time-varying control strategies would be of interest since this approximation would be not needed. Moreover, the state-estimation strategies were also designed based on a time-invariant model valid around the equilibrium point. The presented LKF algorithm is appliable to time-varying systems, and to the knowledge of the author, the ZSE can also be applied to time-varying systems.

- **Design of model predictive control strategies for obstacle avoidance.** Since the load's position is represented by states in the model, state-feedback model predictive control strategies with state constraints would be able to perform path tracking of the suspended load with obstacle avoidance.

- **Design of adaptive control strategies for dealing with unknown load's mass and wire's length.** In real applications, the mass of the suspended load and the length of the wire may not be accurately known. Moreover, the need to redesign the controllers for each different load to be transported would not be practical. Adaptive control strategies can overcome this problem by estimating those parameters on-line.

- **Design of nonlinear control and state estimation strategies**. The proposed control and state estimation strategies are either linear or were designed based on linearized state-space equations, so they are expected to work only at the vicinity of the desired trajectory. The design of nonlinear control and state estimation strategies, such as the Unscented Kalman Filter, would enlarge this domain of attraction, allowing the system to operate far from its equilibrium point, such as in aggressive maneuvers and path tracking at higher accelerations.

- **Design of control strategies for cooperative load transportation**. The formation control strategy presented in this thesis can be easily extended for cooperative load transportation, by switching the inner-loop controllers based on the tilt-rotor UAV dynamics to control strategies based on the load's perspective model, such as the ones proposed in Chapter 3.

Bibliography

Adorno, B., Fraisse, P., & Druon, S. (2010). Dual position control strategies using the cooperative dual task-space framework. In *Proc. of the IEEE/RSJ IROS* (pp. 3955–3960).

Adorno, B. V. (2011). *Two-arm Manipulation: From Manipulators to Enhanced Human-Robot Collaboration*. PhD thesis, LIRMM / Université Montpellier.

Alamo, T., Bravo, J., & Camacho, E. (2005). Guaranteed state estimation by zonotopes. *Automatica*, 41(6), 1035–1043.

Alfaro, R. A. A. (2016). Predictive control strategies for unmanned aerial vehicles in cargo transportation tasks. Master's thesis, Federal University of Santa Catarina.

Almeida, M. M. (2014). Control strategies of a tilt-rotor UAV for load transportation. Master's thesis, Federal University of Minas Gerais.

Almeida, M. M., Donadel, R., Raffo, G. V., & Becker, L. B. (2014). Full Control of a Tiltrotor UAV for Load Transportation. In *Proc. of the XX Congresso Brasileiro de Automática* (pp. 2097–2104).

Almeida, M. M. & Raffo, G. V. (2015a). Nonlinear balance control of an inverted pendulum on a tilt-rotor UAV. In *1st IFAC Workshop on Advanced Control and Navigation for Autonomous Aerospace Vehicles* (pp. 168–173).

Almeida, M. M. & Raffo, G. V. (2015b). Nonlinear control of a tiltrotor UAV for load transportation. In *11th IFAC Symposium on Robot Control* (pp. 234–239).

Andrade, R., Raffo, G. V., & Rico, J. E. N. (2016). Model predictive control of a tilt-rotor UAV for load transportation. In *European Control Conference* (pp. 2165–2170).

Bernard, M. & Kondak, K. (2009). Generic slung load transportation system using small size helicopters. In *IEEE International Conference on Robotics and Automation* (pp. 3258–3264).

Bernard, M., Kondak, K., Maza, I., & Ollero, A. (2011). Autonomous transportation and deployment with aerial robots for search and rescue missions. *Journal of Field Robotics*, 28(6), 914–931.

Bisgaard, M. (2008). *Modeling, Estimation and Control of Helicopter Slung Load System*. PhD thesis, Aalborg University.

Bisgaard, M., Bendtsen, J. D., & Cour-Harbo, A. l. (2009a). Modelling of generic slung load system. *Journal of Guidance, Control, and Dynamics*, 32(2), 573–585.

Bisgaard, M., Bendtsen, J. D., & la Cour-Harbo, A. (2006). Modelling of a generic slung load system. In *AIAA Modeling and Simulation Technologies Conference and Exhibit*.

Bisgaard, M., Cour-Harbo, A. l., & Bendtsen, J. D. (2010). Adaptive control system for autonomous helicopter slung load operations. *Control Engineering Practice*, 18(7), 800–811.

Bisgaard, M., la Cour-Harbo, A., & Bendtsen, J. D. (2009b). Swing damping for helicopter slung load systems using delayed feedback. In *AIAA Guidance, Navigation, and Control Conference*.

Bisgaard, M., la Cour-Harbo, A., Johnson, E. N., & Bendtsen, J. D. (2007a). Full state estimation for helicopter slung load system. In *AIAA Guidance, Navigation and Control Conference and Exhibit*.

Bisgaard, M., la Cour-Harbo, A., Johnson, E. N., & Bendtsen, J. D. (2007b). Vision aided state estimator for helicopter slung load system. In *17th IFAC Symposium on Automatic Control in Aerospace* (pp. 425–430).

Bodanese, J. (2014). Infraestrutura de comunicação sem fio para um veículo aéreo não tripulado de curto alcance. Master's thesis, Federal University of Santa Catarina.

Boyd, S., Ghaoui, L. E., Feron, E., & Balakrishnan, V. (1994). *Linear Matrix Inequalities in System and Control Theory*. Society for Industrial and Applied Mathematics.

Burden, R. L. & Faires, J. D. (2010). *Numerical Analysis*. Brooks Cole, 9th edition.

Candy, J. V. (2009). *Bayesian Signal Processing: Classical, Modern and Particle Filtering Methods*. John Wiley & Sons, Inc.

Cardoso, D. N., Raffo, G. V., & Esteban, S. (2016a). Modeling and control of a tilt-rotor UAV with improved forward flight. In *Proc. of XXI Congresso Brasileiro de Automática* (pp. 1–6).

Cardoso, D. N., Raffo, G. V., & Esteban, S. (2016b). A robust adaptive mixing control for improved forward flight of a tilt-rotor UAV. In *Proc. of IEEE 19th International Conference on Intelligent Transportation Systems*.

Castillo, P., Lozano, R., & Dzul, A. (2005). Stabilization of a mini rotorcraft with four rotors. *IEEE control systems magazine*, 25(6), 45–55.

Chen, C.-T. (1999). *Linear System Theory and Design*. Oxford University Press, 3rd edition.

Chen, Y. Q. & Wang, Z. (2005). Formation control: a review and a new consideration. In *Proc. of the IEEE/RSJ IROS* (pp. 3181–3186).

Chilali, M. & Gahinet, P. (1996). $\mathcal{H}_\infty$ design with pole placement constraints: an lmi approach. *IEEE Transactions on Automatic Control*, 41(3), 358–367.

Combastel, C. (2003). A state bounding observer based on zonotopes. In *2003 European Control Conference* (pp. 2589–2594).

Dai, S., Lee, T., & Bernstein, D. S. (2014). Adaptive control of a quadrotor UAV transporting a cable-suspended load with unknown mass. In *53rd IEEE Conference on Decision and Control* (pp. 6155–6160).

de Crousaz, C., Farshidian, F., & Buchli, J. (2014). Agressive optimal control for agile flight with a slung load. In *IEEE/RSJ International Conference on Intelligent Robots and Systems Workshop on Machine Learning in Planning and Control of Robot Motion*.

de Oliveira, M. C., Geromel, J. C., & Bernussou, J. (2002). Extended $\mathcal{H}_2$ and $\mathcal{H}_\infty$ norm characterizations and controller parametrizations for discrete-time systems. *International Journal of Control*, 75(9), 666–679.

de Souza, C. E. & Xie, L. (1992). On the discrete-time bounded real lemma with application in the characterization of static state feedback $\mathcal{H}_\infty$ controllers. *System & Control Letters*, 18(1), 61–71.

Donadel, R. (2015). Modeling and control of a tiltrotor unmanned aerial vehicle for path tracking. Master's thesis, Federal University of Santa Catarina.

Donadel, R., de Almeida Neto, M. M., Raffo, G. V., & Becker, L. B. (2014). Path tracking control of a small scale tiltrotor unmanned aerial vehicle. In *Proc. of the XX Congresso Brasileiro de Automática* (pp. 1450–1457).

Dorato, P. & Levis, A. H. (1971). Optimal linear regulators: The discrete-time case. *IEEE Transactions on Automatic Control*, 16(6), 613–620.

Dullerud, G. E. & Paganini, F. (2005). *A Course in Robust Control Theory: A Convex Approach (Texts in Applied Mathematics)*. Springer.

Faust, A., Palunko, I., Cruz, P., Fierro, R., & Tapia, L. (2013). Learning swing-free trajectories for UAVs with a suspended load. In *IEEE International Conference on Robotics and Automation* (pp. 4887–4894).

Goldstein, H., Poole, C., & Safko, J. (2001). *Classical Mechanics*. Addison-Wesley, 3rd edition.

Gonçalves, F. S. (2014). Projeto da arquitetura de software embarcado de um veículo aéreo não tripulado. Master's thesis, Federal University of Santa Catarina.

Goodarzi, F. A., Lee, D., & Lee, T. (2014). Geometric stabilization of a quadrotor UAV with a payload connected by a flexible cable. In *American Control Conference* (pp. 4925–4930).

Jain, R. P. K. (2015). Transportation of a cable suspended load using unmanned aerial vehicles. Master's thesis, Delft University of Technology.

Jaulin, L., Kieffer, M., Didrit, O., & Éric Walter (2001). *Applied Interval Analysis*. Springer.

Jazar, R. N. (2010). *Theory of applied robotics: kinematics, dynamics, and control*. Springer Science & Business Media.

Johnson, M. A. & Grimble, M. J. (1987). Recent trends in linear optimal quadratic multivariable control system design. In *IEE Proceedings D - Control Theory and Applications*, volume 134 (pp. 53–71).

Kalman, R. E. (1960). A new approach to linear filtering and prediction problems. *AMSE Journal of basic Engineering*, 82(1), 35–45.

Kane, T. R. & Levinson, D. A. (1985). *Dynamics: Theory and Applications*. Mcgraw-Hill College.

Kühn, W. (1998). Rigorously computed orbits of dynamical systems without the wrapping effect. *Computing*, 61(1), 47–67.

la Cour-Harbo, A. & Bisgaard, M. (2009). State-control trajectory generation for helicopter slung load system using optimal control. In *AIAA Guidance, Navigation, and Control Conference*.

Lathi, B. P. (2005). *Linear Systems and Signals*. Oxford University Press, 2nd edition.

Le, V. T. H., Stoica, C., Alamo, T., Camacho, E. F., & Dumur, D. (2013a). *Zonotopes: From Guaranteed State-estimation to Control*. ISTE Ltd. and John Wiley & Sons.

Le, V. T. H., Stoica, C., Alamo, T., Camacho, E. F., & Dumur, D. (2013b). Zonotopic guaranteed state estimation for uncertain systems. *Automatica*, 49(11), 3418–3424.

Lee, S.-G., Dang, V.-H., Moon, S., & Kim, B. (2013a). Partial feedback linearization control of a three-dimensional overhead crane. *International Journal of Control, Automation and Systems*, 11(4), 718–727.

Lee, T. (2014). Geometric control of multiple quadrotor UAVs transporting a cable-suspended rigid body. In *53rd IEEE Conference on Decision and Control* (pp. 6155–6160).

Lee, T., Leok, M., & McClamroch, N. H. (2011). Control of complex maneuvers of a quadrotor UAV using geometric methods on SE(3). *Asian Journal of Control*.

Lee, T., Sreenath, K., & Kumar, V. (2013b). Geometric control of cooperating multiple quadrotor UAVs with a suspended payload. In *52nd IEEE Conference on Decision and Control* (pp. 5510–5515).

Löfberg, J. (2004). Yalmip: A toolbox for modeling and optimization in matlab. In *2004 IEEE International Symposium on Computer Aided Control Systems Design* (pp. 284–289).

Machado, P. H. & Raffo, G. V. (2015). A quad-rotor platform for load transportation using visual feedback. In *Proc of the XII Simpósio Brasileiro de Automação Inteligente* (pp. 1895–1900).

Maza, I., Kondak, K., Bernard, M., & Ollero, A. (2009). Multi-UAV cooperation and control for load transportation and deployment. *Journal of Intelligent and Robotic Systems*, 57(1), 417–449.

Moore, R. E. (1966). *Interval Analysis*. Prentice-Hall Englewood Cliffs.

Moore, R. E., Kearfott, R. B., & Cloud, M. J. (2009). *Introduction to Interval Analysis*. Philadelphia, PA, USA: SIAM.

Murray, R. M., Li, Z., & Sastry, S. S. (1994). *A Mathematical Introduction to Robotic Manipulation*. CRC Press.

Omar, H. M. (2009). New fuzzy-based anti-swing controller for helicopter slung-load system near hover. In *IEEE International Symposium on Computational Intelligence in Robotics and Automation*.

Palunko, I., Cruz, P., & Fierro, R. (2012). Agile load transportation: safe and efficient load manipulation with aerial robots. *IEEE Robotics & Automation Magazine*, 19(3), 69–79.

Palunko, I., Faust, A., Cruz, P., Tapia, L., & Fierro, R. (2013). A reinforcement learning approach towards autonomous suspended load manipulation using aerial robots. In *IEEE International Conference on Robotics and Automation* (pp. 4881–4886).

Pereira, P. O. & Dimarogonas, D. V. (2016). Lyapunov-based generic controller design for thrust-propeller underactuated systems. In *European Control Conference* (pp. 594–599).

Pereira, P. O., Herzog, M., & Dimarogonas, D. V. (2016). Slung load transportation with a single aerial vehicle and disturbance rejection. In *24th Mediterranean Conference on Control and Automation* (pp. 671–676).

Peres, P. L. D. & Geromel, J. C. (1993). $\mathcal{H}_2$ control for discrete-time systems optimality and robustness. *Automatica*, 29(1), 225–228.

Phillips, C. L. & Nagle, H. T. (1995). *Digital Control System Analysis and Design*. Prentice Hall, 3rd edition.

Raffo, G. V. & Almeida, M. M. (2016). Nonlinear robust control of a quadrotor UAV for load transportation with swing improvement. In *American Control Conference* (pp. 3156–3162).

Raffo, G. V., Ortega, M. G., & Rubio, F. R. (2011). Nonlinear $\mathcal{H}_\infty$ controller for the quad-rotor helicopter with input coupling. In *Proc. of the 18th World Congress of the IFAC*, volume 18 (pp. 13834–13839).

Raffo, G. V., Ortega, M. G., & Rubio, F. R. (2015). Robust nonlinear control for path tracking of a quad-rotor helicopter. *Asian Journal of Control*, 17(1), 142–156.

Rego, B. S., Adorno, B. V., & Raffo, G. V. (2016). Formation backstepping control based on the cooperative dual task-space framework: a case study on unmanned aerial vehicles. In *Proc. of the 2016 XIII Latin American Robotics Symposium and IV Brazilian Robotics Symposium* (pp. 163–168).

Rego, B. S. & Raffo, G. V. (2016a). Path tracking control based on guaranteed state estimation for a tilt-rotor UAV. In *Proc. of the XXI Congresso Brasileiro de Automática* (pp. 1–6).

Rego, B. S. & Raffo, G. V. (2016b). Suspended load path tracking by a tilt-rotor UAV. In *Proc. of the 1st IFAC Conference on Cyber-Physical & Human-Systems*. To be published.

Rego, B. S. & Raffo, G. V. (2016c). Suspended load path tracking control based on zonotopic state estimation using a tilt-rotor UAV. In *Proc. of the IEEE 19th International Conference on Intelligent Transportation Systems* (pp. 1445–1451).

Rigatos, G. G. & Raffo, G. V. (2015). Input-output linearizing control of the underactuated hovercraft using the derivative-free nonlinear Kalman filter. *Unmanned Systems*, 3(2), 127–142.

Santos, F. (2015). Avaliação do uso de agentes no desenvolvimento de aplicações com veículos aéreos não-tripulados. Master's thesis, Federal University of Santa Catarina.

Santos, M. A. & Raffo, G. V. (2016a). Adaptive control of a tilt-rotor UAV in load transportation tasks - a lmi based approach. In *Proc. of the XXI Congresso Brasileiro de Automática* (pp. 1–6).

Santos, M. A. & Raffo, G. V. (2016b). Path tracking model predictive control of a tilt-rotor UAV carrying a suspended load. In *Proc. of the IEEE 19th International Conference on Intelligent Transportation Systems*. To be published.

Seborg, D. E., Edgar, T. F., & Mellichamp, D. A. (2003). *Process Dynamics and Control*. John Wiley & Sons, Inc, 2nd edition.

Selig, J. M. (2005). *Geometric Fundamentals of Robotics*. Springer, 2nd edition.

Shabana, A. A. (2010). *Computational Dynamics*. John Wiley and Sons, 3rd edition.

Shabana, A. A. (2013). *Dynamics of Multibody Systems*. Cambridge, 4th edition.

Siciliano, B., Sciavicco, L., Villani, L., & Oriolo, G. (2009). *Robotics: modelling, planning and control*. Springer Science & Business Media.

Simon, D. (2006). *Optimal State Estimation: Kalman, H_∞ and Nonlinear Approaches*. John Wiley & Sons, Inc.

Slotine, J.-J. E. (1991). *Applied Nonlinear Control*. Prentice-Hall International.

Spong, M. W., Hutchinson, S., & Vidyasagar, M. (2006). *Robot Modeling and Control*. John Wiley & Sons, Inc.

Sreenath, K., Lee, T., & Kumar, V. (2013a). Geometric control and differential flatness of a quadrotor UAV with a cable-suspended load. In *52nd IEEE Conference on Decision and Control* (pp. 2269–2274).

Sreenath, K., Michael, N., & Kumar, V. (2013b). Trajectory generation and control of a quadrotor with a cable-suspended load - a differentially-flat hybrid system. In *IEEE International Conference on Robotics and Automation* (pp. 4873–4880).

Starr, G., Wood, J., & Lumia, R. (2005). Rapid transport of suspended payloads. In *IEEE International Conference on Robotics and Automation* (pp. 1394–1399).

Tang, S. & Kumar, V. (2015). Mixed integer quadratic program trajectory generation for a quadrotor with a cable-suspended payload. In *IEEE International Conference on Robotics and Automation* (pp. 2216–2222).

Toh, K.-C., Todd, M. J., & Tütüncü, R. H. (1999). Sdpt3 – a matlab software package for semidefinite programming, version 1.3. *Optimization methods and software*, 11(1-4), 545–581.

Trofino, A., Coutinho, D. F., Barbosa, K. A., Dezuo, T. M., & Schariau, C. C. (2015). *Controle Robusto*. Technical report.

Vicino, A. & Zappa, G. (1996). Sequential approximation of feasible parameter sets for identification with set membership uncertainty. *IEEE Transactions on Automatic Control*, 41(6), 774–785.

Wang, F., Liu, P., Zhao, S., Chen, B. M., Phang, S. K., Lai, S., Lee, T. H., & Cai, C. (2014). Guidance, navigation and control of an unmanned helicopter for automatic cargo transportation. In *33rd Chinese Control Conference* (pp. 1013–1020).

Wu, C., Qi, J., Song, D., Qi, X., Liu, T., & Han, J. (2015). Development of an unmanned helicopter automatic barrels transportation system. In *IEEE International Conference on Robotics and Automation* (pp. 4686–4691).

A

Path tracking control based on ZSE for the tilt-rotor UAV

This appendix presents the results published in Rego & Raffo (2016a). The purpose of the work was to familiarize the author with the zonotopic state estimation technique by addressing a simpler problem, in order to solve the problem of path tracking control of the suspended load in a latter stage.

This appendix addresses only the problem of path tracking control of a tilt-rotor UAV. The considered scenario is similar to the one described in Sections 4.3 and 5.4, i.e., the system must follow a desired trajectory while being affected by external disturbances, with incomplete state information, unknown but bounded measurement noise and sensors with different sampling times. A zonotopic state estimator is designed to provide information about the entire state vector from the available measurements. Thereafter, a discrete-time linear quadratic regulator is designed for the path tracking task, based on discrete-time linearized error dynamics with integral actions. The control loop is closed by choosing the centers of the zonotopes as estimated states.

This appendix is organized as follows: Section A.1 presents the dynamic modeling of the tilt-rotor UAV; Section A.2 designs a zonotopic state estimator for the tilt-rotor UAV; Section A.3 obtains the discrete-time linearized error dynamics and describes the control design; Section A.4 presents simulation results; and Section A.5 concludes the appendix.

A.1 System modeling

This section describes in a brief way the dynamic model of the tilt-rotor UAV, obtained through the Euler-Lagrange formulation. The detailed modeling can be found in Donadel (2015). The aircraft under study is the ProVANT UAV 2.0, illustrated in Figure A.1.

As mentioned in Chapter 2, the aircraft is regarded as a mechanical system composed of three rigid bodies. The inertial frame, the aircraft's geometric center frame, and the frame attached to the i-th rigid body's center of mass, $i \in \{1, 2, 3\}$, are denoted by $\mathcal{I}$, $\mathcal{B}$ and $\mathcal{C}_i$, respectively. Again, it is assumed that the rotor groups' centers of mass are located at their respective tilting axes. The aircraft position with respect to $\mathcal{I}$ is denoted by $\boldsymbol{\xi} \triangleq [x\ y\ z]^T$, and its orientation is described by Euler angles $\boldsymbol{\eta} \triangleq [\phi\ \theta\ \psi]^T$ using the roll-pitch-yaw convention. Vectors $\boldsymbol{d}^{\mathcal{B}}_{\mathcal{C}_i}$ denote displacements from $\mathcal{B}$ to $\mathcal{C}_i$, and $\boldsymbol{R}^{\mathcal{B}}_{\mathcal{C}_i}$ are the same defined in Section 2.2, for $i \in \{1, 2, 3\}$.

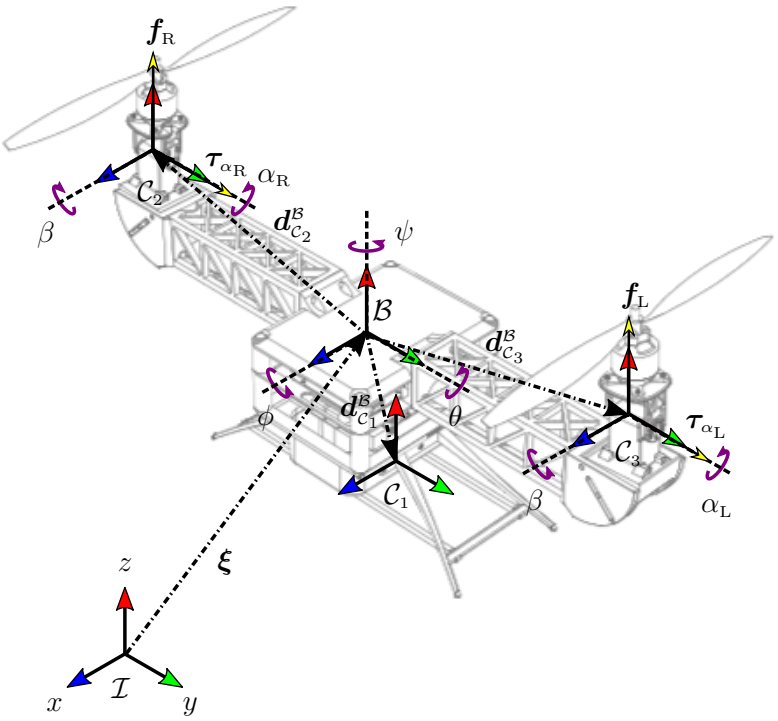

Figure A.1: Tilt-rotor UAV and kinematics.

Choosing $\boldsymbol{q} \triangleq [\boldsymbol{\xi}^T\ \boldsymbol{\eta}^T\ \alpha_R\ \alpha_L]^T \in \mathbb{R}^8$ as generalized coordinates, the tilt-rotor UAV's equations of motion are written in the canonical form

$$\boldsymbol{M}(\boldsymbol{q})\ddot{\boldsymbol{q}} + \boldsymbol{C}(\boldsymbol{q}, \dot{\boldsymbol{q}})\dot{\boldsymbol{q}} + \boldsymbol{g}(\boldsymbol{q}) = \boldsymbol{L}(\boldsymbol{q})\boldsymbol{u} + \boldsymbol{d}, \tag{A.1}$$

where $\boldsymbol{M}(\boldsymbol{q}) \in \mathbb{R}^{8\times8}$, $\boldsymbol{C}(\boldsymbol{q}, \dot{\boldsymbol{q}}) \in \mathbb{R}^{8\times8}$, $\boldsymbol{g}(\boldsymbol{q}) \in \mathbb{R}^8$ and $\boldsymbol{L}(\boldsymbol{q}) \in \mathbb{R}^{8\times4}$ are presented in Donadel (2015), $\boldsymbol{u} \triangleq [f_{\mathrm{R}}\ f_{\mathrm{L}}\ \tau_{\alpha_{\mathrm{R}}}\ \tau_{\alpha_{\mathrm{L}}}]^T \in \mathbb{R}^4$ and $\boldsymbol{d} \in \mathbb{R}^8$ is a vector of external disturbances. Defining $\boldsymbol{x} \triangleq [\boldsymbol{q}^T\ \dot{\boldsymbol{q}}^T]^T$, the dynamic equation (A.1) is written in the nonlinear state-space

representation

$$\dot{\boldsymbol{x}} = \boldsymbol{\varphi}(\boldsymbol{x}, \boldsymbol{u}, \boldsymbol{d}) = \begin{bmatrix} \dot{\boldsymbol{q}} \\ \boldsymbol{M}^{-1}(\boldsymbol{q})\left[-\boldsymbol{C}(\boldsymbol{q}, \dot{\boldsymbol{q}})\dot{\boldsymbol{q}} - \boldsymbol{g}(\boldsymbol{q}) + \boldsymbol{L}(\boldsymbol{q})\boldsymbol{u} + \boldsymbol{d}\right] \end{bmatrix}. \tag{A.2}$$

For control strategy purposes, system (A.2) is linearized through first order expansion in Taylor series around a generic time-varying trajectory, in a disturbance-free scenario, yielding to (3.4), where $\boldsymbol{A}_{\mathrm{c}}(t)$, $\boldsymbol{B}_{\mathrm{c}}(t)$ and $\boldsymbol{F}_{\mathrm{c}}(t)$ have appropriate dimensions.

A.2 Zonotopic state estimator design

This section presents the design of a zonotopic state estimator to provide information on all states of the tilt-rotor UAV. It is assumed that available measurements are corrupted with unknown but bounded noise and provided by sensors with different sampling times. This section uses definitions, theorems, and algorithms presented in Section 4.3. Moreover, the sensors available are the same from Section 4.3, with exception of the camera. Considering additive noise, the measurement vector is given by

$$\boldsymbol{y}_k \triangleq \begin{bmatrix} \boldsymbol{q} \\ \dot{\boldsymbol{\eta}} \\ \dot{\alpha}_{\mathrm{R}} \\ \dot{\alpha}_{\mathrm{L}} \end{bmatrix} + \boldsymbol{v}_k = \underbrace{\begin{bmatrix} \mathbb{I}_{8\times8} & \boldsymbol{0}_{8\times3} & \boldsymbol{0}_{8\times3} & \boldsymbol{0}_{8\times1} & \boldsymbol{0}_{8\times1} \\ \boldsymbol{0}_{3\times8} & \boldsymbol{0}_{3\times3} & \mathbb{I}_{3\times3} & \boldsymbol{0}_{3\times1} & \boldsymbol{0}_{3\times1} \\ \boldsymbol{0}_{1\times8} & \boldsymbol{0}_{1\times3} & \boldsymbol{0}_{1\times3} & 1 & 0 \\ \boldsymbol{0}_{1\times8} & \boldsymbol{0}_{1\times3} & \boldsymbol{0}_{1\times3} & 0 & 1 \end{bmatrix}}_{\boldsymbol{H}_{\mathrm{d}}} \boldsymbol{x}_k + \boldsymbol{v}_k. \tag{A.3}$$

Similar to the case of the tilt-rotor UAV with suspended load, due to computational complexity, the linearized system (4.13) is used in the prediction step instead of (A.2), with appropriate changes in dimensions. Rewriting (A.3) as a function of $\Delta\boldsymbol{x}$ yields $\boldsymbol{y}_k = \boldsymbol{H}_{\mathrm{d}}\Delta\boldsymbol{x}_k + \bar{\boldsymbol{v}}_k$, where $\bar{\boldsymbol{v}}_k \triangleq \boldsymbol{H}_{\mathrm{d}}\boldsymbol{x}^{\mathrm{eq}} + \boldsymbol{v}_k$.

Considering that the system is affected only by forces applied to the UAV's geometric center, define $\boldsymbol{d} = [\bar{\boldsymbol{d}}\ \boldsymbol{0}_{1\times5}]^T$, $\bar{\boldsymbol{d}} \in \mathbb{R}^3$, and $\tilde{\boldsymbol{d}}_{k-1} \triangleq \bar{\boldsymbol{d}}_k - \bar{\boldsymbol{d}}_{k-1}$. In order to estimate the external disturbances along with the system states, the augmented state vector $\boldsymbol{\nu} \triangleq [\Delta\boldsymbol{x}^T \quad \bar{\boldsymbol{d}}^T]^T$ is introduced, yielding (4.24) and (4.26), where

$$\boldsymbol{A}_{\boldsymbol{\nu}} = \begin{bmatrix} \boldsymbol{A}_{\mathrm{d}} & \bar{\boldsymbol{F}}_{\mathrm{d}} \\ \boldsymbol{0}_{3\times16} & \mathbb{I}_{3\times3} \end{bmatrix} \in \mathbb{R}^{19\times19}, \quad \boldsymbol{B}_{\boldsymbol{\nu}} = \begin{bmatrix} \boldsymbol{B}_{\mathrm{d}} \\ \boldsymbol{0}_{3\times4} \end{bmatrix} \in \mathbb{R}^{19\times4},$$
$$\boldsymbol{H}_{\boldsymbol{\nu}} = \begin{bmatrix} \boldsymbol{H}_{\mathrm{d}} & \boldsymbol{0}_{13\times3} \end{bmatrix} \in \mathbb{R}^{13\times19}, \quad \bar{\boldsymbol{w}} \triangleq \begin{bmatrix} \boldsymbol{w}^T & \tilde{\boldsymbol{d}}^T \end{bmatrix}^T,$$

in which $\bar{\boldsymbol{F}}_{\mathrm{d}}$ corresponds to the first three columns of $\boldsymbol{F}_{\mathrm{d}}$.

Assume that $\bar{\boldsymbol{w}}$ and $\bar{\boldsymbol{v}}$ belong to zonotopes $\bar{\mathbb{W}} = \boldsymbol{c}_{\bar{w}} \oplus \boldsymbol{G}_{\bar{w}}\mathbb{B}^{r_{\bar{w}}}$ and $\bar{\mathbb{V}} = \boldsymbol{c}_{\bar{v}} \oplus \boldsymbol{G}_{\bar{v}}\mathbb{B}^{r_{\bar{v}}}$, and let $\boldsymbol{\nu}_{k-1} \in \hat{\mathbb{X}}_{k-1} = \boldsymbol{c}_{\hat{x}_{k-1}} \oplus \boldsymbol{G}_{\hat{x}_{k-1}}\mathbb{B}^{r_{\hat{x}_{k-1}}}$. Moreover, denote $\mathbb{I}_k$ as the set of available

measurements at time instant k. Then, similarly to the procedure presented in Section 4.3, the state estimation Algorithm 4.4 is obtained, with appropriate change of dimensions in the variables.

A.3 Control design

A discrete-time linear quadratic regulator is proposed to solve the path tracking problem of the tilt-rotor UAV, with constant disturbances rejection. The derivation of the discrete-time linearized error dynamics, augmented with integral actions, as well as the design of the controller, are performed in the same lines of Sections 3.2 and 3.3, just adapted for the tilt-rotor UAV dynamic equations.

A.4 Simulation results

The model parameters of the tilt-rotor UAV, which are the same from Table 5.1, resulted in the following equilibrium used for linearization

$$\begin{aligned} \boldsymbol{q}^{\text{eq}} &= [\mathbf{0}_{3\times 1} \quad -0.00015712 \quad -0.02887388 \quad 0 \quad 0.02899790 \quad 0.02853108]^T, \\ \dot{\boldsymbol{q}}^{\text{eq}} &= \mathbf{0}_{8\times 1}, \quad \boldsymbol{u}^{\text{eq}} = [9.74110841 \quad 9.77602843 \quad 0 \quad 0]^T. \end{aligned} \tag{A.4}$$

The controllability matrix for pair $(\boldsymbol{A}_{\boldsymbol{\chi}}, \boldsymbol{B}_{\boldsymbol{\chi}})$ was verified to be full rank, thus the associated system is controllable. Moreover, the observability matrix for pair $(\boldsymbol{A}_{\boldsymbol{\nu}}, \boldsymbol{H}_{\boldsymbol{\nu}})$ were verified to be full rank, thus the associated system is observable, however only when all measurements are available.

The sensors parameters are shown in Table A.1. For simulation purposes, the noise from the servos' sensors was assumed to have zero-mean uniform distribution, and noise from the other sensors was assumed to have zero-mean Gaussian distribution. For the latter, "noise bound" means three times the standard deviation.

Table A.1: Sensors parameters

Sensor	$\mathbb{I}$	Noise bounds	Sampling time
GPS	$1, 2$	$\pm 0.15\,\text{m}$	$120\,\text{ms}$
Barometer	3	$\pm 0.51\,\text{m}$	$12\,\text{ms}$
IMU	$4, 5, 6$	$\pm 5.15{\cdot}10^{-3}\,\text{rad}$	$12\,\text{ms}$
	$9, 10, 11$	$\pm 5.15{\cdot}10^{-3}\,\text{rad/s}$	
Servos	$7, 8$	$\pm 5.67{\cdot}10^{-3}\,\text{rad}$	$12\,\text{ms}$
	$12, 13$	$\pm 0.50772\,\text{rad/s}$	

Discretizations were performed for sampling time 12 ms. For the zonotopic state estimator, it was assumed that $\bar{\mathbb{X}}_0 = [(\boldsymbol{\xi}_0^{\text{tr}})^T \ \mathbf{0}_{1\times 16}]^T \oplus \boldsymbol{G}_{\bar{x}_0}\mathbb{B}^{19}$, $\bar{\mathbb{W}} = \mathbf{0}_{19\times 1} \oplus \boldsymbol{G}_{\bar{w}}\mathbb{B}^{19}$ and

$\bar{\mathbb{V}} = \boldsymbol{H}_{\mathrm{d}}\boldsymbol{x}^{\mathrm{eq}} \oplus \boldsymbol{G}_{\bar{v}}\mathbb{B}^{13}$, where

$$
\begin{aligned}
\boldsymbol{G}_{\bar{x}_0} =& \mathrm{diag}(0.5{\cdot}\mathbf{1}_{3\times1}, 0.2{\cdot}|\phi^{\mathrm{eq}}|, 0.2{\cdot}|\theta^{\mathrm{eq}}|, \pi/180, 0.2{\cdot}|\alpha_{\mathrm{R}}^{\mathrm{eq}}|, 0.2{\cdot}|\alpha_{\mathrm{L}}^{\mathrm{eq}}|, 0.02{\cdot}\mathbf{1}_{11\times1}),\\
\boldsymbol{G}_{\bar{w}} =& \mathrm{diag}(10^{-4}{\cdot}\mathbf{1}_{16\times1}, 0.1, 0.1, 0.2),\\
\boldsymbol{G}_{\bar{v}} =& \mathrm{diag}(0.15{\cdot}\mathbf{1}_{2\times1}, 0.51, 5.15{\cdot}10^{-3}{\cdot}\mathbf{1}_{3\times1}, 5.67{\cdot}10^{-3}{\cdot}\mathbf{1}_{2\times1}, 5.15{\cdot}10^{-3}{\cdot}\mathbf{1}_{3\times1}, 0.50772{\cdot}\mathbf{1}_{2\times1}),
\end{aligned}
$$

in which $\boldsymbol{G}_{\bar{w}}$ was adjusted by trial and error. The Bryson's method was used again as starting point for choosing the weighting matrices, which are given by

$$
\begin{aligned}
\boldsymbol{\Omega}_{\boldsymbol{x}} = \mathrm{diag}\Bigg(&\frac{20}{2^2}, \frac{20}{2^2}, \frac{20}{2^2}, \frac{10}{(\pi/2)^2}, \frac{10}{(\pi/2)^2}, \frac{15}{\pi^2}, \frac{0.01}{(\pi/2)^2}, \frac{0.01}{(\pi/2)^2}, \frac{1}{2^2}, \frac{1}{2^2}, \frac{1}{2^2}, \frac{5}{(3\pi)^2}, \frac{5}{(3\pi)^2},\\
&\frac{1}{(\pi/4)^2}, \frac{0.01}{(3\pi)^2}, \frac{0.01}{(3\pi)^2}, 30, 30, 30, 1\Bigg),\\
\boldsymbol{\Omega}_{\boldsymbol{u}} = \mathrm{diag}\Bigg(&\frac{750}{(30 - f_{\mathrm{L}}^{\mathrm{eq}})^2}, \frac{750}{(30 - f_{\mathrm{L}}^{\mathrm{eq}})^2}, \frac{5000}{2^2}, \frac{5000}{2^2}\Bigg),
\end{aligned}
\tag{A.5}
$$

where $f_{\mathrm{R}}^{\mathrm{eq}}$ and $f_{\mathrm{L}}^{\mathrm{eq}}$ are values from equilibrium $\boldsymbol{u}^{\mathrm{eq}}$. The control loop was closed using the first 16 elements of $\boldsymbol{c}_{\hat{x}_k}$, as $\delta\boldsymbol{x} = (\boldsymbol{c}_{\hat{x}_k}(1, 2, \ldots, 16) + \boldsymbol{x}^{\mathrm{eq}}) - \boldsymbol{x}^{\mathrm{tr}}$. Moreover, the order of $\hat{\mathbb{X}}_k$ was limited to fifty times its dimension.

The trajectory to be performed is defined by the following equations: $x^{\mathrm{tr}}(t) = 4\cos(\pi t/40)$; $y^{\mathrm{tr}}(t) = 4\sin(\pi t/40)$; $z^{\mathrm{tr}}(t) = 17 - 16\cos(\pi t/40)$; and $\psi^{\mathrm{tr}} = 0$. The initial states are $\boldsymbol{x}_0 = [3.9 \quad 0.1 \quad 0.9 \quad \phi^{\mathrm{eq}} \quad \theta^{\mathrm{eq}} \quad 0 \quad \alpha_{\mathrm{R}}^{\mathrm{eq}} \quad \alpha_{\mathrm{L}}^{\mathrm{eq}} \quad \mathbf{0}_{1\times8}]^T$.

Figure A.2 shows the desired trajectory and the performed trajectory. Figure A.3 shows the applied external disturbances, and Figure A.4 shows the error of the regulated states. Note that, despite noise, external disturbances and multiple sampling times, the path tracking is performed with almost null steady-state error, presenting good performance of the designed DLQR controller and the guaranteed state estimator. The time evolution of the remaining generalized coordinates is illustrated in Figure A.5. These variables remain stable throughout the trajectory tracking. Figure A.6 shows the computed control signals.

Estimation error and confidence limits for x, y, $\dot{x}$ and $\dot{y}$, are shown in Figure A.7. Note the pattern that arises in the behavior of the limits, which is a consequence of the GPS's higher sampling time. Figure A.8 shows the estimation error and confidence limits for the remaining states.

A.5 Conclusions

This appendix presented a path tracking control strategy based on zonotopic state estimation for a tilt-rotor UAV. The aircraft's equations of motion were presented. Assuming that available information is provided by noisy measurements with different sampling times, a zonotopic state estimator was designed, providing information about the entire state vector at the controller sampling time. Based on the discrete-time linearized error

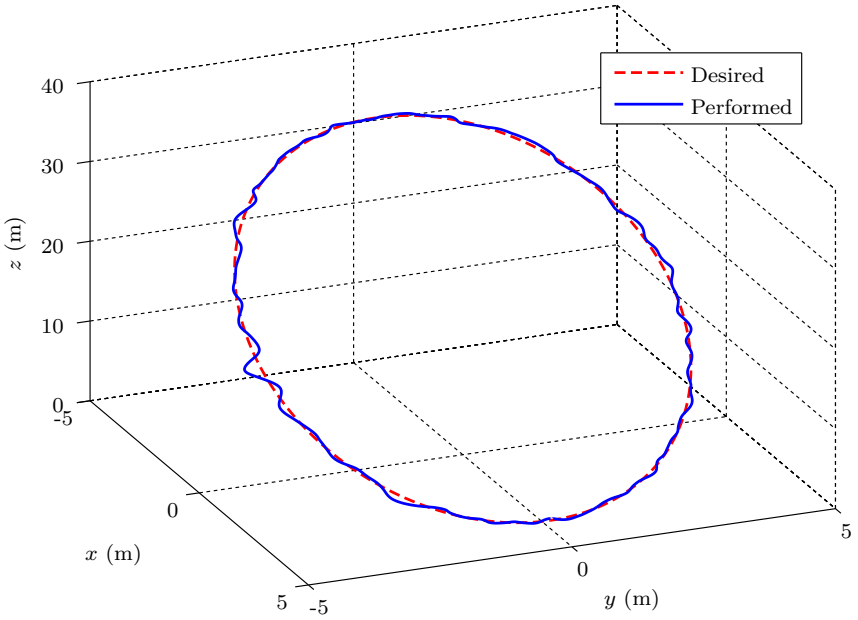

Figure A.2: Desired and performed trajectories.

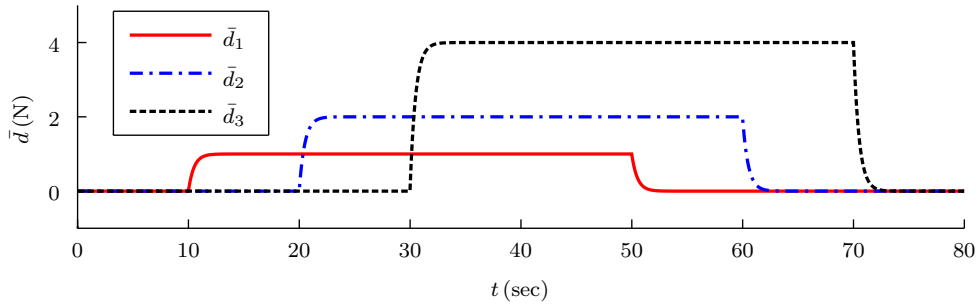

Figure A.3: Applied external disturbances.

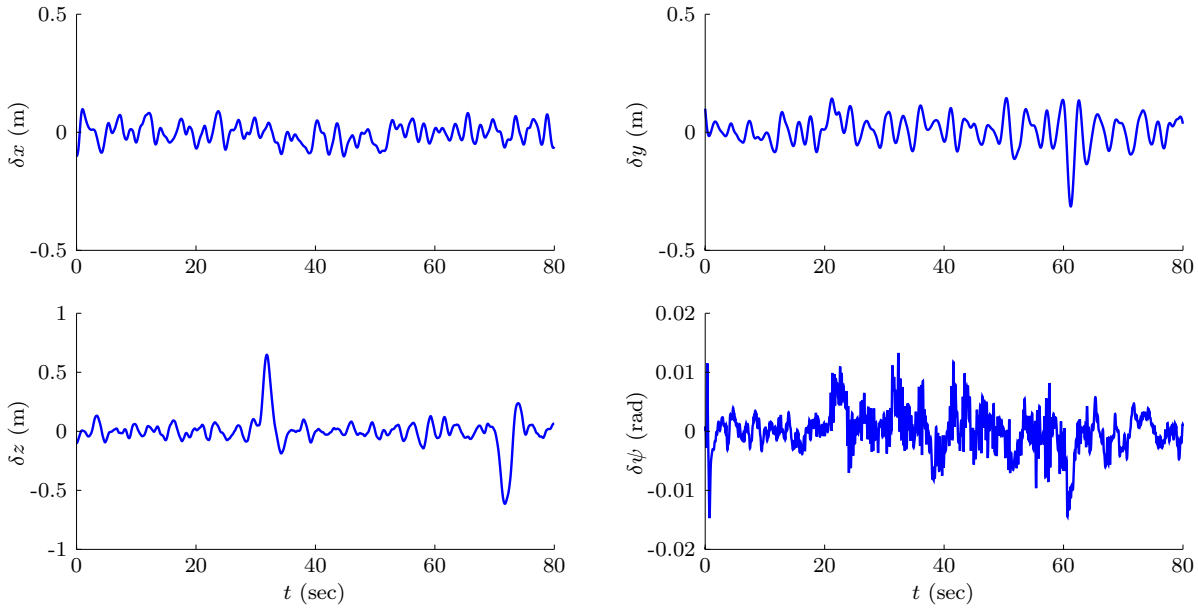

Figure A.4: Error over the regulated states.

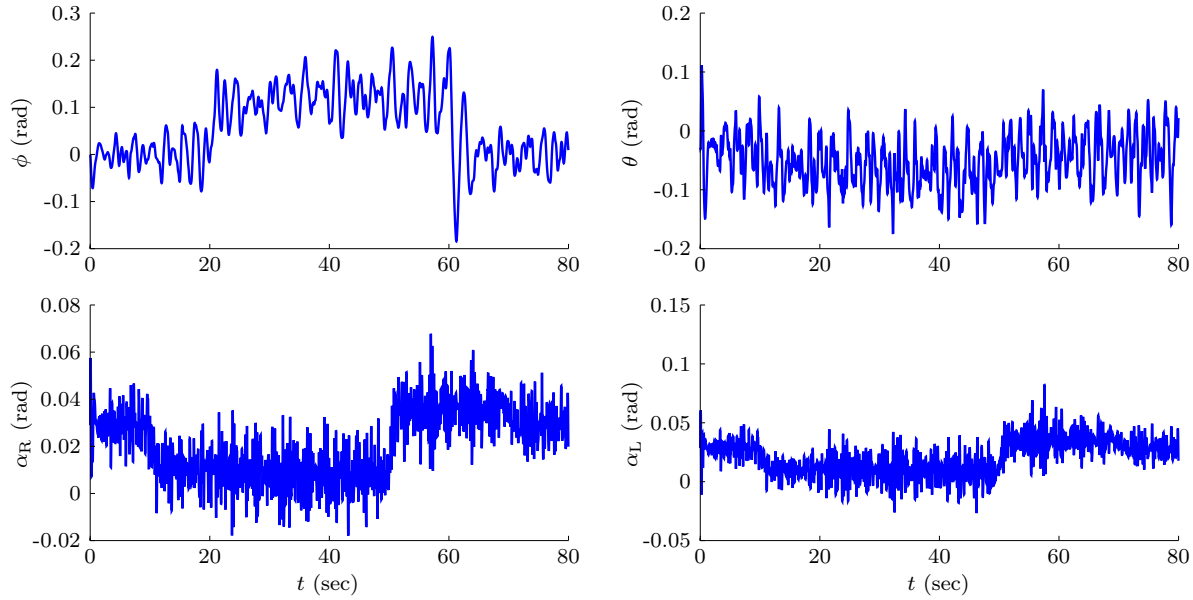

Figure A.5: Time evolution of the remaining generalized coordinates.

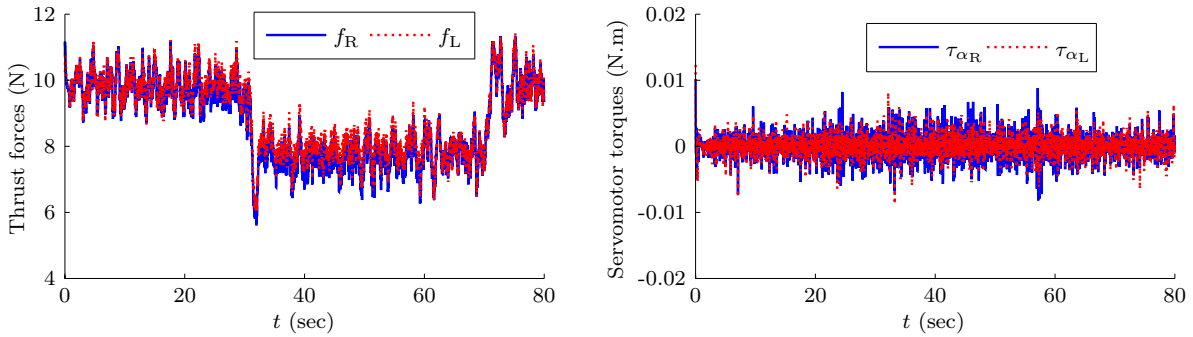

Figure A.6: Control signals.

dynamics with integral actions, a DLQR controller was designed for path tracking with constant disturbances rejection capability. Simulation results corroborated the validity of the control strategy, and also showed the good performance of the state estimator.

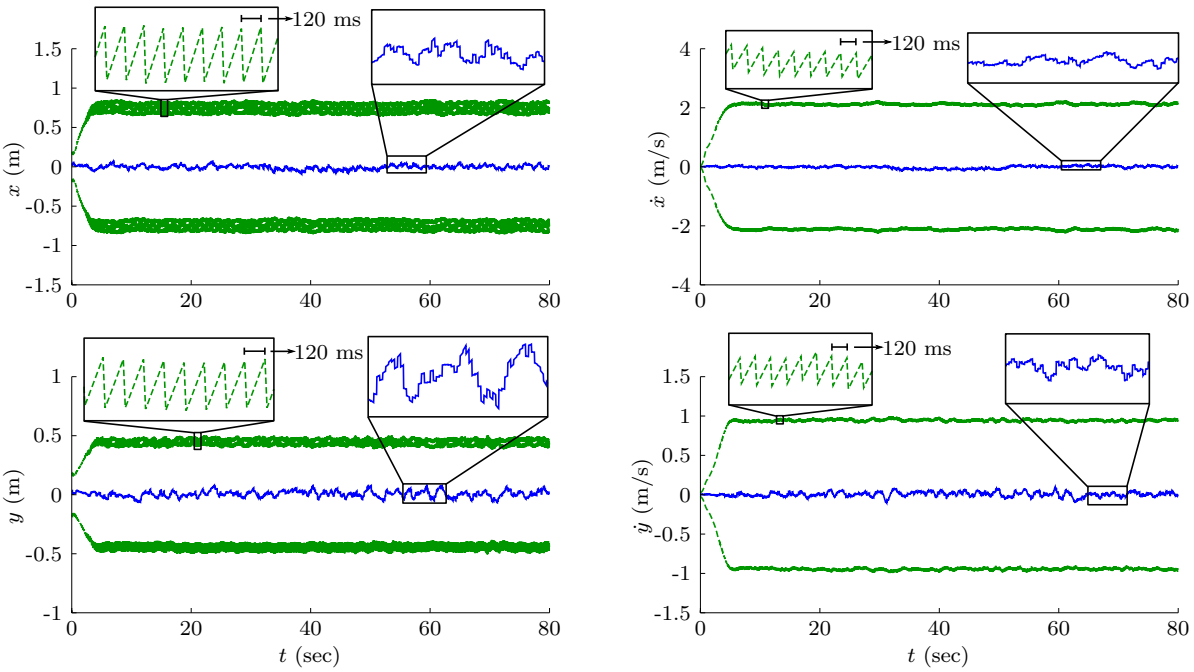

Figure A.7: Estimation error of x, y, $\dot{x}$ and $\dot{y}$. Outer lines are confidence limits.

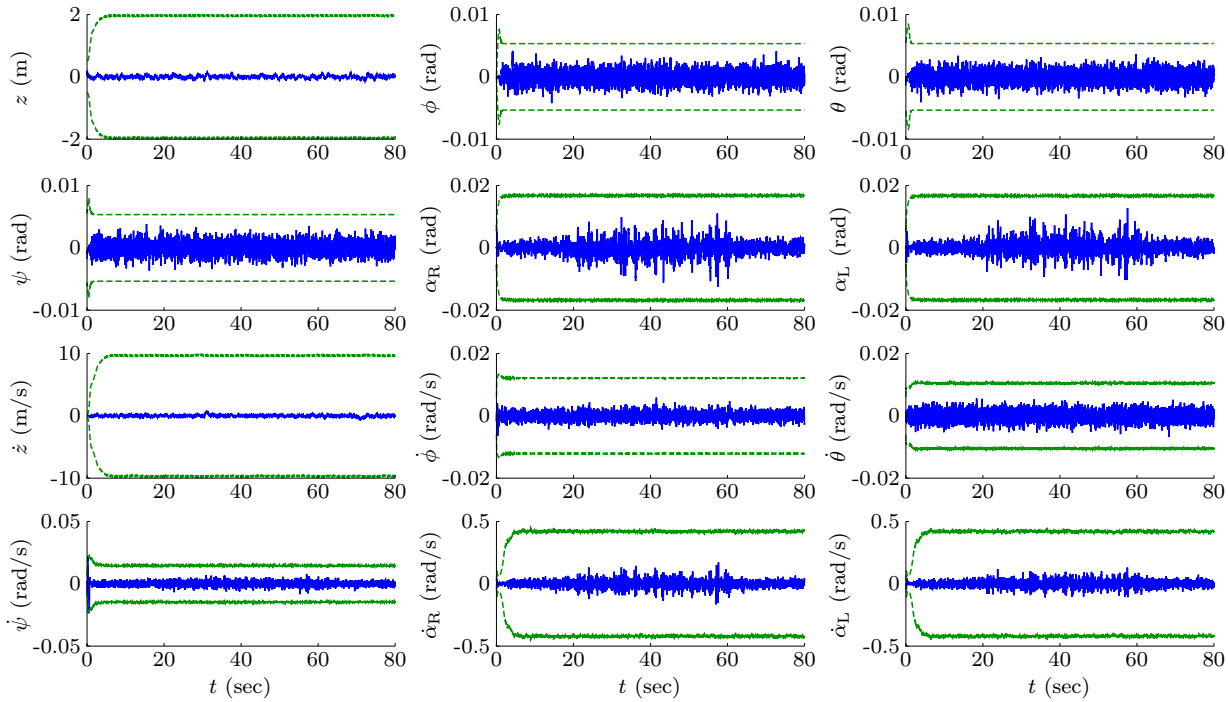

Figure A.8: Estimation error of the remaining states. Outer lines are confidence limits. Variables without specified units are given in rad/s.

B

Formation control of tilt-rotor UAVs

This appendix presents the results published in Rego et al. (2016), in which the problem of formation control of tilt-rotor UAVs was considered. The purpose of the work was to familiarize the author with the tilt-rotor UAV.

A control problem that arises in the field of robot cooperation is the formation control, in which the robot team must perform a specified task while a desired formation is maintained. There exist several approaches in the literature that deal with this problem (Chen & Wang, 2005), and a particular one is the leader-follower.

The present appendix formulates the leader-follower control problem by means of the cooperative dual task-space, which was introduced by Adorno et al. (2010). This approach benefits from the unit dual quaternion representation, which encapsulates position and orientation together in a single algebraic structure and does not have representational singularities. The addressed formation scheme is composed of three agents: one leader, which performs tracking of a desired trajectory, and two followers that keep a desired time variant formation while following the leader. A backstepping control strategy with integral action (Raffo et al., 2015) is designed based on the formation kinematics. As a case study, tilt-rotor UAVs are chosen as agents. A linear state-feedback controller based on the UAV's linearized dynamic equations is designed to perform individual reference tracking, while in an hierarchical structure the formation backstepping controller computes the desired trajectory.

This appendix is organized as follows: Section B.1 presents the formation kinematic model formulated using the cooperative dual task-space; Section B.2 presents the dynamic

equations of the tilt-rotor UAV; Section B.3 presents the design of the formation backstepping controller, the linear state-feedback controller, and also a formation controller based on the task-space inverse dynamics technique (for comparison); Section B.4 presents simulation results and, finally, Section B.5 concludes the work.

B.1 Formation modeling

This section presents the formation kinematic model, which is developed using unit dual quaternions.

B.1.1 Mathematical preliminaries

Consider the quaternionic units $\hat{\imath}$, $\hat{\jmath}$ and $\hat{k}$, such that $\hat{\imath}^2 = \hat{\jmath}^2 = \hat{k}^2 = \hat{\imath}\hat{\jmath}\hat{k} = -1$. A quaternion $h \in \mathbb{H}$ is defined as $h \triangleq \mathrm{Re}(h) + \mathrm{Im}(h)$, where $\mathrm{Re}(h) \triangleq h_1$ and $\mathrm{Im}(h) \triangleq h_2\hat{\imath} + h_3\hat{\jmath} + h_4\hat{k}$, with h_1, h_2, h_3, $h_4 \in \mathbb{R}$. The conjugate of h is given by $h^* \triangleq \mathrm{Re}(h) - \mathrm{Im}(h)$.

Furthermore, let ε be the nilpotent Clifford unit, such that $\varepsilon \neq 0$ and $\varepsilon^2 = 0$ (Selig, 2005). A dual quaternion $\underline{h} \in \mathcal{H}$ is defined as $\underline{h} \triangleq \mathrm{P}(\underline{h}) + \varepsilon\mathrm{D}(\underline{h})$, where $\mathrm{P}(\underline{h}) \triangleq h_p$ and $\mathrm{D}(\underline{h}) \triangleq h_d$, with h_p, $h_d \in \mathbb{H}$. The real and imaginary parts of $\underline{h}$ are $\mathrm{Re}(\underline{h}) \triangleq \mathrm{Re}(\mathrm{P}(\underline{h})) + \varepsilon\mathrm{Re}(\mathrm{D}(\underline{h}))$ and $\mathrm{Im}(\underline{h}) \triangleq \mathrm{Im}(\mathrm{P}(\underline{h})) + \varepsilon\mathrm{Im}(\mathrm{D}(\underline{h}))$, respectively. The conjugate of $\underline{h}$ is given by $\underline{h}^* \triangleq \mathrm{Re}(\underline{h}) - \mathrm{Im}(\underline{h})$.

The $\mathbf{vec}_4$ operator is defined for quaternions as $\mathbf{vec}_4(h) \triangleq [h_1\ h_2\ h_3\ h_4]^T$. An analogous operator is defined for dual quaternions as $\mathbf{vec}_8(\underline{h}) \triangleq [\mathbf{vec}_4(\mathrm{P}(\underline{h}))^T\ \mathbf{vec}_4(\mathrm{D}(\underline{h}))^T]^T$. The Hamilton operators $\overset{+}{\mathbf{H}}_4$ and $\overset{-}{\mathbf{H}}_4$ are matrices that satisfy, for h_a, $h_b \in \mathbb{H}$ (Adorno, 2011),

$$\mathbf{vec}_4(h_a h_b) = \overset{+}{\mathbf{H}}_4(h_a)\mathbf{vec}_4(h_b) = \overset{-}{\mathbf{H}}_4(h_b)\mathbf{vec}_4(h_a).$$

For dual quaternions, the Hamilton operators $\overset{+}{\mathbf{H}}_8$ and $\overset{-}{\mathbf{H}}_8$ are defined analogously (switching $\mathbf{vec}_4$ to $\mathbf{vec}_8$).

A rigid transformation from an arbitrary frame $\mathcal{S}$ to another arbitrary frame $\mathcal{T}$, composed of translation followed by rotation around a specific axis, is represented by the unit dual quaternion $\underline{x}^{\mathcal{S}}_{\mathcal{T}} = r^{\mathcal{S}}_{\mathcal{T}} + \varepsilon(1/2)p^{\mathcal{S}}_{\mathcal{S}\mathcal{T}}r^{\mathcal{S}}_{\mathcal{T}}$, where $p^{\mathcal{S}}_{\mathcal{S}\mathcal{T}} \triangleq x^{\mathcal{S}}_{\mathcal{S}\mathcal{T}}\hat{\imath} + y^{\mathcal{S}}_{\mathcal{S}\mathcal{T}}\hat{\jmath} + z^{\mathcal{S}}_{\mathcal{S}\mathcal{T}}\hat{k}$ corresponds to the translation quaternion from the origin of $\mathcal{S}$ to the origin of $\mathcal{T}$, expressed in $\mathcal{S}$, and $r^{\mathcal{S}}_{\mathcal{T}} \triangleq \cos(\alpha/2) + n\sin(\alpha/2)$ corresponds to the rotation quaternion associated with the orientation between $\mathcal{S}$ and $\mathcal{T}$, described by a rotation of angle α around axis $n \triangleq n_x\hat{\imath} + n_y\hat{\jmath} + n_z\hat{k}$.

B.1.2 Formation model using the cooperative dual task-space

The formation scheme addressed in this paper, shown in Fig. B.1 along with all the reference frames and transformations that are discussed in this section, consists of three agents. Agent σ tracks a reference trajectory and acts as a leader. Agent τ performs an

arbitrary movement with respect to agent ζ. Furthermore, frame a, located at a fraction of the relative transformation $\underline{x}_r$, keeps a desired pose (position and orientation) with respect to agent σ.

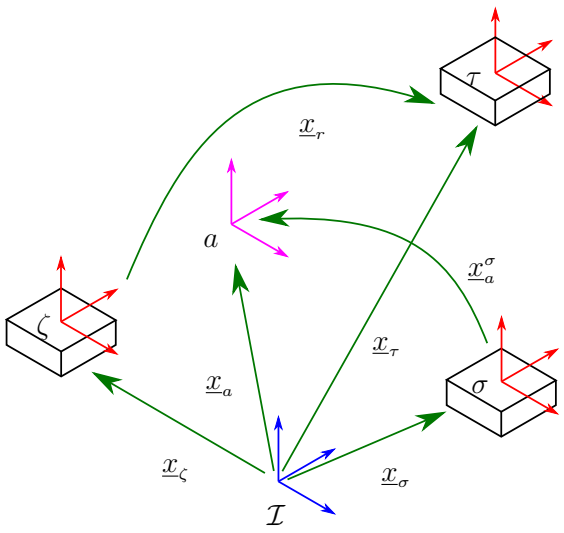

Figure B.1: Formation scheme, reference frames and transformations.

The rigid transformation from inertial frame, $\mathcal{I}$, to a frame rigidly attached to agent i, denoted by $\underline{x}_i$, is a function of the configuration variables of the latter, $\boldsymbol{\rho}_i \in \mathbb{R}^{n_i}$, with $i = \{\sigma, \zeta, \tau\}$. The associated differential kinematic mapping is given by

$$\mathbf{vec}_8(\dot{\underline{x}}_i) = \boldsymbol{J}_i \dot{\boldsymbol{\rho}}_i, \tag{B.1}$$

where $\boldsymbol{J}_i \triangleq \boldsymbol{J}_i(\boldsymbol{\rho}_i) \in \mathbb{R}^{8\times n_i}$ is the analytical Jacobian (Adorno, 2011).

Transformations $\underline{x}_r$ and $\underline{x}_a$ called the relative and absolute dual positions, respectively, are defined by (Adorno et al., 2010)

$$\underline{x}_r \triangleq \underline{x}_\zeta^* \underline{x}_\tau, \tag{B.2}$$

$$\underline{x}_a \triangleq \underline{x}_\zeta \underline{x}_{r/\varphi}, \tag{B.3}$$

where φ is a constant such that $\underline{x}_{r/\varphi}$ is a φ-th part of transformation $\underline{x}_r$ (Adorno et al., 2010).

Performing the time derivative of (B.2) and applying the $\mathbf{vec}_8$ operator to both sides of the resulting equation, leads to the differential kinematic mapping associated with $\underline{x}_r$,

$$\mathbf{vec}_8(\dot{\underline{x}}_r) = \boldsymbol{J}_r \dot{\boldsymbol{\rho}}_c, \tag{B.4}$$

where $\boldsymbol{J}_r \triangleq \boldsymbol{J}_r(\boldsymbol{\rho}_c) \in \mathbb{R}^{8\times(n_\zeta+n_\tau)}$ and $\boldsymbol{J}_r = [\bar{\mathbf{H}}_8(\underline{x}_\tau)\boldsymbol{E}_8\boldsymbol{J}_\zeta \quad \overset{+}{\mathbf{H}}_8(\underline{x}_\zeta^*)\boldsymbol{J}_\tau]$, with $\boldsymbol{\rho}_c \triangleq \begin{bmatrix}\boldsymbol{\rho}_\zeta^T & \boldsymbol{\rho}_\tau^T\end{bmatrix}^T$ and $\boldsymbol{E}_8 \triangleq \mathrm{diag}([1, -1, -1, -1, 1, -1, -1, -1])$.

The differential kinematic mapping $\mathbf{vec}_8(\dot{\underline{x}}_{r/\varphi}) = \boldsymbol{J}_{r/\varphi}\dot{\boldsymbol{\rho}}_c$ can be obtained, where $\boldsymbol{J}_{r/\varphi} \triangleq \boldsymbol{J}_{r/\varphi}(\boldsymbol{\rho}_c) \in \mathbb{R}^{8\times(n_\zeta+n_\tau)}$,

$$\boldsymbol{J}_{r/\varphi} = \frac{1}{\varphi}\begin{bmatrix}\boldsymbol{J}_{11} & \boldsymbol{0}_{4\times4}\\ \boldsymbol{J}_{21} & \boldsymbol{J}_{22}\end{bmatrix}\boldsymbol{J}_r,$$

with $\boldsymbol{J}_{11}, \boldsymbol{J}_{21}, \boldsymbol{J}_{22} \in \mathbb{R}^{4\times4}$,

$$\begin{aligned}
\boldsymbol{J}_{11} =& \bar{\mathbf{H}}_4(\mathrm{P}(\underline{x}_r^*)\mathrm{P}(\underline{x}_{r/\varphi})),\\
\boldsymbol{J}_{21} =& \bar{\mathbf{H}}_4(\mathrm{P}(\underline{x}_{r/\varphi}))\dot{\mathbf{H}}_4(\mathrm{D}(\underline{x}_r))\boldsymbol{E}_4 + \dot{\mathbf{H}}_4(\mathrm{D}(\underline{x}_{r/\varphi})\mathrm{P}(\underline{x}_{r/\varphi}^*)) + \bar{\mathbf{H}}_4(\mathrm{D}(\underline{x}_r^*)\mathrm{P}(\underline{x}_{r/\varphi})),\\
\boldsymbol{J}_{22} =& \bar{\mathbf{H}}_4(\mathrm{P}(\underline{x}_{r/\varphi}))\bar{\mathbf{H}}_4(\mathrm{P}(\underline{x}_r^*)),
\end{aligned}$$

$\boldsymbol{E}_4 \triangleq \mathrm{diag}([1,-1,-1,-1])$.

Performing the time derivative of (B.3), and applying the $\mathbf{vec}_8$ operator to both sides of the resulting equation, yields

$$\begin{aligned}
\mathbf{vec}_8(\dot{\underline{x}}_a) =& \bar{\mathbf{H}}_8(\underline{x}_{r/\varphi})\mathbf{vec}_8(\dot{\underline{x}}_\zeta) + \dot{\mathbf{H}}_8(\underline{x}_\zeta)\mathbf{vec}_8(\dot{\underline{x}}_{r/\varphi})\\
=& \bar{\mathbf{H}}_8(\underline{x}_{r/\varphi})\boldsymbol{J}_\zeta\dot{\boldsymbol{\rho}}_\zeta + \dot{\mathbf{H}}_8(\underline{x}_\zeta)\boldsymbol{J}_{r/\varphi}\dot{\boldsymbol{\rho}}_c.
\end{aligned} \tag{B.5}$$

Defining $\boldsymbol{J}_K \triangleq [\bar{\mathbf{H}}_8(\underline{x}_{r/\varphi})\boldsymbol{J}_\zeta \quad \boldsymbol{0}_{8\times n_\tau}] \in \mathbb{R}^{8\times(n_\zeta+n_\tau)}$, from (B.5) the differential kinematic mapping $\mathbf{vec}_8(\dot{\underline{x}}_a) = \boldsymbol{J}_a\dot{\boldsymbol{\rho}}_c$ associated with $\underline{x}_a$ is obtained, where $\boldsymbol{J}_a \triangleq \boldsymbol{J}_a(\boldsymbol{\rho}_c) = (\boldsymbol{J}_K + \dot{\mathbf{H}}_8(\underline{x}_\zeta)\boldsymbol{J}_{r/\varphi}) \in \mathbb{R}^{8\times(n_\zeta+n_\tau)}$.

Transformation $\underline{x}_a^\sigma$ is given by

$$\underline{x}_a^\sigma = \underline{x}_\sigma^*\underline{x}_a. \tag{B.6}$$

Performing the time derivative of (B.6), and applying the $\mathbf{vec}_8$ operator to both sides of the resulting equation, leads to the differential kinematic mapping associated with $\underline{x}_a^\sigma$,

$$\mathbf{vec}_8(\dot{\underline{x}}_a^\sigma) = \boldsymbol{J}_{\sigma a}\dot{\boldsymbol{\rho}}_S, \tag{B.7}$$

where $\boldsymbol{J}_{\sigma a} \triangleq \boldsymbol{J}_{\sigma a}(\boldsymbol{\rho}_S) \in \mathbb{R}^{8\times(n_\sigma+n_\zeta+n_\tau)}$,

$$\boldsymbol{J}_{\sigma a} = [\bar{\mathbf{H}}_8(\underline{x}_a)\boldsymbol{E}_8\boldsymbol{J}_\sigma \quad \dot{\mathbf{H}}_8(\underline{x}_\sigma^*)\boldsymbol{J}_a], \tag{B.8}$$

and $\boldsymbol{\rho}_S \triangleq \begin{bmatrix}\boldsymbol{\rho}_\sigma^T & \boldsymbol{\rho}_\zeta^T & \boldsymbol{\rho}_\tau^T\end{bmatrix}^T$.

Given the previously stated formation control problem, the appropriate differential kinematic model is obtained combining (B.1) for $i = \sigma$, (B.4) and (B.7), as

$$\dot{\boldsymbol{x}}_S = \boldsymbol{J}_S\dot{\boldsymbol{\rho}}_S, \tag{B.9}$$

where $\dot{\boldsymbol{x}}_S \triangleq [\mathbf{vec}_8(\underline{\dot{x}}_\sigma)^T \quad \mathbf{vec}_8(\underline{\dot{x}}_r)^T \quad \mathbf{vec}_8(\underline{\dot{x}}_a^\sigma)^T]^T$ and $\boldsymbol{J}_S \triangleq \boldsymbol{J}_S(\boldsymbol{\rho}_S) \in \mathbb{R}^{24\times(n_\sigma+n_\zeta+n_\tau)}$,

$$\boldsymbol{J}_S = \left[\begin{array}{c|c|c} \boldsymbol{J}_\sigma & \mathbf{0}_{8\times n_\zeta} & \mathbf{0}_{8\times n_\tau} \\ \hline \mathbf{0}_{8\times n_\sigma} & \multicolumn{2}{c}{\boldsymbol{J}_r} \\ \hline \multicolumn{3}{c}{\boldsymbol{J}_{\sigma a}} \end{array}\right].$$

Moreover, performing the time derivative of (B.9), yields to

$$\ddot{\boldsymbol{x}}_S = \dot{\boldsymbol{J}}_S\dot{\boldsymbol{\rho}}_S + \boldsymbol{J}_S\ddot{\boldsymbol{\rho}}_S, \tag{B.10}$$

which is the formation's second order differential kinematic model.

B.2 Tilt-rotor UAV modeling

This section presents the linearized dynamic equations of the tilt-rotor UAV used to design the linear state-feedback $\mathcal{D}$-stable $\mathcal{H}_\infty$ controller. The UAV's differential kinematic mapping used in the formation control is also described.

B.2.1 Uncertain linearized dynamic equations

The studied tilt-rotor UAV is the ProVANT UAV 2.0. Its dynamic equations are the same presented in Section A.1, which are linearized around the individual reference trajectory, under zero disturbance scenario, and augmented with integral actions, in order to design the linear state-feedback $\mathcal{D}$-stable $\mathcal{H}_\infty$ controller, yielding

$$\dot{\boldsymbol{\chi}} = \underbrace{\left[\begin{array}{cccccc|c|c} \multicolumn{6}{c|}{\boldsymbol{A}_{\mathrm{c}}} & & \mathbf{0}_{16\times 4} \\ \hline 1 & 0 & 0 & 0 & 0 & 0 & \multirow{4}{*}{$\mathbf{0}_{4\times 10}$} & \multirow{4}{*}{$\mathbf{0}_{4\times 4}$} \\ 0 & 1 & 0 & 0 & 0 & 0 & & \\ 0 & 0 & 1 & 0 & 0 & 0 & & \\ 0 & 0 & 0 & 0 & 0 & 1 & & \end{array}\right]}_{\boldsymbol{A}_{\boldsymbol{\chi}}} \boldsymbol{\chi} + \underbrace{\begin{bmatrix} \boldsymbol{B}_{\mathrm{c}} \\ \mathbf{0}_{4\times 4} \end{bmatrix}}_{\boldsymbol{B}_{\boldsymbol{\chi}}} \delta\boldsymbol{u} + \underbrace{\begin{bmatrix} \boldsymbol{F}_{\mathrm{c}} \\ \mathbf{0}_{4\times 3} \end{bmatrix}}_{\boldsymbol{F}_{\boldsymbol{\chi}}} \boldsymbol{d}. \tag{B.11}$$

Taking into account the existence of uncertain parameters, system (B.11) is rewritten using convex polytope representation, as follows:

$$\dot{\boldsymbol{\chi}} = \boldsymbol{A}_{\boldsymbol{\chi}}(\boldsymbol{\alpha})\boldsymbol{\chi} + \boldsymbol{B}_{\boldsymbol{\chi}}(\boldsymbol{\alpha})\delta\boldsymbol{u} + \boldsymbol{F}_{\boldsymbol{\chi}}(\boldsymbol{\alpha})\boldsymbol{d}, \tag{B.12}$$

where $\boldsymbol{\alpha} \in \mathbb{R}^n$ with $n = 2^p$ and p being the number of uncertain parameters in (B.12), $\boldsymbol{A}_{\boldsymbol{\chi}}(\boldsymbol{\alpha}) = \sum_{i=1}^n \alpha_i \boldsymbol{A}_{\boldsymbol{\chi}_i}$, $\boldsymbol{B}_{\boldsymbol{\chi}}(\boldsymbol{\alpha}) = \sum_{i=1}^n \alpha_i \boldsymbol{B}_{\boldsymbol{\chi}_i}$, and $\boldsymbol{F}_{\boldsymbol{\chi}}(\boldsymbol{\alpha}) = \sum_{i=1}^n \alpha_i \boldsymbol{F}_{\boldsymbol{\chi}_i}$, with $0 \leq \alpha_i \leq 1$ and $\sum_{i=1}^n \alpha_i = 1$. This appendix consider uncertainties in the fixed mechanical angle β, assumed to vary from 0 to $\pi/18$ radians, then $p = 1$ and $n = 2$.

B.2.2 Differential kinematic mapping of the tilt-rotor UAV

The approach described in Section B.1 requires that the differential kinematic mapping (B.1) is available for every agent. Thus, the differential kinematic mapping of the tilt-rotor UAV must be obtained.

For formation purposes[1], it is assumed that the kinematic model of the UAV comprises only its position, x, y, and z, and yaw angle, ψ. Then, the transformation associated with the tilt-rotor UAV i, with $i = \{\sigma, \zeta, \tau\}$, is given by $\underline{x}_i = r_i + \varepsilon(1/2)p_i r_i$, where $p_i = x_i\hat{\imath} + y_i\hat{\jmath} + z_i\hat{k}$, and $r_i = \cos(\psi_i/2) + \hat{k}\sin(\psi_i/2)$. Differentiating $\underline{x}_i$ with respect to time and applying the $\mathbf{vec}_8$ operator, equation (B.1) is obtained with $\boldsymbol{\rho}_i = \begin{bmatrix} x_i & y_i & z_i & \psi_i \end{bmatrix}^T$.

B.3 Control design

This section presents the overall control strategy. A backstepping controller based on the formation kinematic model, which is formulated using the cooperative dual-task space framework, is designed. Also, a controller based on task-space inverse dynamics is presented for comparison purposes. Furthermore, a linear state-feedback $\mathcal{D}$-stable $\mathcal{H}_\infty$ controller, based on the dynamic equations of the tilt-rotor UAV, is designed for individual reference tracking. Finally, a hierarchical structure is built.

B.3.1 Formation controller based on backstepping approach

Combining (B.9) and (B.10), and defining $\boldsymbol{x}_A \triangleq \boldsymbol{x}_S$ and $\boldsymbol{x}_B \triangleq \dot{\boldsymbol{x}}_S$, the formation kinematic model can be written in the state-space form

$$\begin{cases} \dot{\boldsymbol{x}}_A = \boldsymbol{x}_B \\ \dot{\boldsymbol{x}}_B = \dot{\boldsymbol{J}}_S \boldsymbol{J}_S^+ \boldsymbol{x}_B + \boldsymbol{J}_S \ddot{\boldsymbol{\rho}}_S, \end{cases}$$

where $\boldsymbol{J}_S^+$ denotes the pseudo-inverse of $\boldsymbol{J}_S$.

The following change of variables is applied (Raffo et al., 2015):

$$\begin{cases} \boldsymbol{e}_A = \boldsymbol{x}_A - \boldsymbol{x}_d \\ \boldsymbol{e}_B = \boldsymbol{x}_B - \Phi \\ \boldsymbol{e}_C = \int_0^T \boldsymbol{e}_B(t)dt, \end{cases}$$

where $\boldsymbol{x}_d$ is a vector which contains all reference signals information for $\underline{x}_\sigma$, $\underline{x}_r$ and $\underline{x}_a^\sigma$, and Φ is a virtual control law to be determined. The first step of the backstepping approach is

[1] And also to take into account the underactuated nature of the tilt-rotor UAV.

based on the subsystem

$$\begin{cases} \dot{\boldsymbol{e}}_A = \boldsymbol{x}_B - \dot{\boldsymbol{x}}_d \\ \boldsymbol{e}_B = \boldsymbol{x}_B - \Phi. \end{cases} \tag{B.13}$$

The Lyapunov function candidate $V_1(\boldsymbol{e}_A) = (1/2)\boldsymbol{e}_A^T\boldsymbol{e}_A$ is proposed for stability analysis of (B.13), and its time derivative is $\dot{V}_1 = \boldsymbol{e}_A^T[\boldsymbol{e}_B + \Phi - \dot{\boldsymbol{x}}_d]$. Choosing $\Phi = -\boldsymbol{K}_A\boldsymbol{e}_A + \dot{\boldsymbol{x}}_d$, with $\boldsymbol{K}_A \in \mathbb{R}^{24\times 24}$ a positive definite matrix, results in $\dot{V}_1 = -\boldsymbol{e}_A^T\boldsymbol{K}_A\boldsymbol{e}_A + \boldsymbol{e}_A^T\boldsymbol{e}_B$, which is negative definite when $\boldsymbol{e}_B = \boldsymbol{0}_{24\times 1}$. The error $\boldsymbol{e}_B$ is stabilized at the origin in the next step of the backstepping approach, being its dynamics the fast one.

For the second step, the following system is considered:

$$\begin{cases} \dot{\boldsymbol{e}}_C = \boldsymbol{e}_B \\ \dot{\boldsymbol{e}}_B = \dot{\boldsymbol{x}}_B - \dot{\Phi}. \end{cases} \tag{B.14}$$

The Lyapunov function candidate

$$V_2(\boldsymbol{e}_A, \boldsymbol{e}_B, \boldsymbol{e}_C) = V_1(\boldsymbol{e}_A) + \frac{1}{2}\boldsymbol{e}_C^T\boldsymbol{K}_C\boldsymbol{e}_C + \frac{1}{2}\boldsymbol{e}_B^T\boldsymbol{e}_B$$

is proposed for (B.14), with $\boldsymbol{K}_C \in \mathbb{R}^{24\times 24}$ a positive definite matrix, and its time derivative is

$$\dot{V}_2 = -\boldsymbol{e}_A^T\boldsymbol{K}_A\boldsymbol{e}_A + \boldsymbol{e}_A^T\boldsymbol{e}_B + \boldsymbol{e}_C^T\boldsymbol{K}_C\boldsymbol{e}_B + \boldsymbol{e}_B^T\left[\dot{\boldsymbol{J}}_S\boldsymbol{J}_S^+\boldsymbol{e}_B + \dot{\boldsymbol{J}}_S\boldsymbol{J}_S^+\Phi + \boldsymbol{J}_S\ddot{\boldsymbol{\rho}}_S - \dot{\Phi}\right].$$

Therefore, choosing the control law

$$\ddot{\boldsymbol{\rho}}_S = \boldsymbol{J}_S^+\left[-\boldsymbol{K}_B\boldsymbol{e}_B + \dot{\Phi} - \dot{\boldsymbol{J}}_S\boldsymbol{J}_S^+[\boldsymbol{e}_B + \Phi] - \boldsymbol{K}_C\boldsymbol{e}_C - \boldsymbol{e}_A\right], \tag{B.15}$$

with $\boldsymbol{K}_B \in \mathbb{R}^{24\times 24}$ a positive definite matrix, yields $\dot{V}_2 = -\boldsymbol{e}_A^T\boldsymbol{K}_A\boldsymbol{e}_A - \boldsymbol{e}_B^T\boldsymbol{K}_B\boldsymbol{e}_B$, which guarantees that the equilibrium $(\boldsymbol{e}_A, \boldsymbol{e}_B, \boldsymbol{e}_C) = 0$ of the closed-loop is UGAS (uniform global asymptotic stable).

B.3.2 Formation controller based on task-space inverse dynamics technique

Considering (B.10), by the task-space inverse dynamics (TSID) technique, the control law is given by (Spong et al., 2006)

$$\ddot{\boldsymbol{\rho}}_S = \boldsymbol{J}_S^+\left[\ddot{\boldsymbol{x}}_d - \dot{\boldsymbol{J}}_S\dot{\boldsymbol{\rho}}_S - \boldsymbol{K}_1\dot{\boldsymbol{e}}_A - \boldsymbol{K}_2\boldsymbol{e}_A\right], \tag{B.16}$$

with $\boldsymbol{K}_1, \boldsymbol{K}_2 \in \mathbb{R}^{24\times 24}$, $\boldsymbol{K}_1, \boldsymbol{K}_2 > 0$.

Taking the second order time derivative of $\boldsymbol{e}_A$ from (B.13), we have

$$\ddot{\boldsymbol{e}}_A = \ddot{\boldsymbol{x}}_S - \ddot{\boldsymbol{x}}_d = \dot{\boldsymbol{J}}_S\dot{\boldsymbol{\rho}}_S + \boldsymbol{J}_S\ddot{\boldsymbol{\rho}}_S - \ddot{\boldsymbol{x}}_d. \tag{B.17}$$

Substituting (B.16) in (B.17) yields to $\ddot{\boldsymbol{e}}_A = -\boldsymbol{K}_1\dot{\boldsymbol{e}}_A - \boldsymbol{K}_2\boldsymbol{e}_A$, which implies asymptotic stability.

B.3.3 Tilt-rotor UAV controller design

The chosen state-feedback control law is given by $\delta\boldsymbol{u} = -\boldsymbol{K}\boldsymbol{\chi}$, where $\boldsymbol{K} \in \mathbb{R}^{4\times 20}$ is computed through the linear $\mathcal{H}_\infty$ control problem formulated via linear matrix inequalities (LMIs). The optimization problem also considers a $\mathcal{D}$-stability region.

Consider the uncertain system (B.12) along with the cost variable $\boldsymbol{z} \in \mathbb{R}^{n_z}$ defined by

$$\boldsymbol{z} = \boldsymbol{H}_z\boldsymbol{\chi} + \boldsymbol{D}_{zu}\delta\boldsymbol{u} + \boldsymbol{D}_{zd}\boldsymbol{d},$$

where $\boldsymbol{H}_z$, $\boldsymbol{D}_{zu}$ and $\boldsymbol{D}_{zd}$ are weighting matrices. Then, the $\mathcal{H}_\infty$ norm of the system is defined by

$$\|\boldsymbol{\Psi}_{dz}(s)\|_\infty = \sup_{\boldsymbol{d}\neq 0} \frac{\|\boldsymbol{z}(t)\|_2}{\|\boldsymbol{d}(t)\|_2} < \gamma.$$

The control law $\delta\boldsymbol{u} = -\boldsymbol{K}\boldsymbol{\chi}$ that minimizes the attenuation level γ for the worst case of disturbances is obtained through the following LMI (Dullerud & Paganini, 2005):

$$\begin{bmatrix} \boldsymbol{A}(\boldsymbol{\alpha})\boldsymbol{Q} + \boldsymbol{Q}\boldsymbol{A}(\boldsymbol{\alpha})^T + \boldsymbol{B}(\boldsymbol{\alpha})\boldsymbol{Y} + \boldsymbol{Y}^T\boldsymbol{B}(\boldsymbol{\alpha})^T & \boldsymbol{F}(\boldsymbol{\alpha}) & \boldsymbol{Q}\boldsymbol{H}_{\boldsymbol{z}}^T + \boldsymbol{Y}^T\boldsymbol{D}_{\boldsymbol{zu}}^T \\ * & -\gamma\mathbb{I}_{8\times 8} & \boldsymbol{D}_{\boldsymbol{zd}}^T \\ * & * & -\gamma\mathbb{I}_{n_z\times n_z} \end{bmatrix} < 0, \tag{B.18}$$

with $\boldsymbol{K}$ computed by $\boldsymbol{K} = -\boldsymbol{Y}\boldsymbol{Q}^{-1}$. Terms denoted by $*$ are deduced by symmetry.

The eigenvalues of the closed-loop system belong to a $\mathcal{D}$ sub-region of the complex plane if there exists $\boldsymbol{Q} > 0$ such that (Chilali & Gahinet, 1996):

Region 1: For $\mathrm{Re}(s) < -\lambda$:

$$\boldsymbol{A}(\boldsymbol{\alpha})\boldsymbol{Q} + \boldsymbol{Q}\boldsymbol{A}(\boldsymbol{\alpha})^T + \boldsymbol{Y}^T\boldsymbol{B}(\boldsymbol{\alpha})^T + \boldsymbol{B}(\boldsymbol{\alpha})\boldsymbol{Y} + 2\lambda\boldsymbol{Q} < 0; \tag{B.19}$$

Region 2: For a disc centered in $(c, 0)$ with radius r:

$$\begin{bmatrix} -r\boldsymbol{Q} & -c\boldsymbol{Q} + \boldsymbol{A}(\alpha)\boldsymbol{Q} + \boldsymbol{B}_u(\alpha)\boldsymbol{Y} \\ * & -r\boldsymbol{Q} \end{bmatrix} < 0; \tag{B.20}$$

Region 3: For a conic region defined by $|\mathrm{Im}(s)| < \tan(\mu)\,|\mathrm{Re}(s)|$:

$$\begin{bmatrix} \sin(\mu)\,(\boldsymbol{U}+\boldsymbol{U}^T) & \cos(\mu)\,(\boldsymbol{U}-\boldsymbol{U}^T) \\ * & \sin(\mu)\,(\boldsymbol{U}+\boldsymbol{U}^T) \end{bmatrix}, \tag{B.21}$$

where $\boldsymbol{U} \triangleq \boldsymbol{A}(\boldsymbol{\alpha})\boldsymbol{Q} + \boldsymbol{B}(\boldsymbol{\alpha})\boldsymbol{Y}$. To design the $\mathcal{H}_\infty$ controller taking into account $\mathcal{D}$-stability based on these three regions, LMIs (B.18)–(B.21) are considered.

Furthermore, the feed-forward term $\boldsymbol{u}^{\mathrm{tr}} = \boldsymbol{L}(\boldsymbol{q}^{\mathrm{tr}})^{+}\left[\boldsymbol{M}(\boldsymbol{q}^{\mathrm{tr}})\ddot{\boldsymbol{q}}^{\mathrm{tr}} + \boldsymbol{C}(\boldsymbol{q}^{\mathrm{tr}},\dot{\boldsymbol{q}}^{\mathrm{tr}})\dot{\boldsymbol{q}}^{\mathrm{tr}} + \boldsymbol{g}(\boldsymbol{q}^{\mathrm{tr}})\right]$ is added to the state-feedback control law, where $\boldsymbol{q}^{\mathrm{tr}}$, $\dot{\boldsymbol{q}}^{\mathrm{tr}}$ and $\ddot{\boldsymbol{q}}^{\mathrm{tr}}$ are the reference signals provided by the formation controller, and $\boldsymbol{L}(\boldsymbol{q}^{\mathrm{tr}})^{+}$ denotes the left pseudo-inverse of $\boldsymbol{L}(\boldsymbol{q}^{\mathrm{tr}})$, such that $\boldsymbol{L}(\boldsymbol{q}^{\mathrm{tr}})^{+}\boldsymbol{L}(\boldsymbol{q}^{\mathrm{tr}}) = \mathbb{I}$. Then, the complete control law is given by $\boldsymbol{u} = \delta\boldsymbol{u} + \boldsymbol{u}^{\mathrm{tr}} = -\boldsymbol{K}\boldsymbol{\chi} + \boldsymbol{L}(\boldsymbol{q}^{\mathrm{tr}})^{+}\left[\boldsymbol{M}(\boldsymbol{q}^{\mathrm{tr}})\ddot{\boldsymbol{q}}^{\mathrm{tr}} + \boldsymbol{C}(\boldsymbol{q}^{\mathrm{tr}},\dot{\boldsymbol{q}}^{\mathrm{tr}})\dot{\boldsymbol{q}}^{\mathrm{tr}} + \boldsymbol{g}(\boldsymbol{q}^{\mathrm{tr}})\right]$.

B.3.4 Control structure

To perform the proposed task, a hierarchical structure is built with the formation controller and one linear state-feedback $\mathcal{D}$-stable $\mathcal{H}_\infty$ controller per tilt-rotor UAV. Either (B.15) or (B.16) provides individual acceleration references to the UAVs. To generate velocity and position references to the linear controllers, these accelerations are integrated once and twice, respectively.

B.4 Results

The physical parameters of the tilt-rotor UAV are the same from Table 5.1. The equilibrium used for linearization of (A.2) is given by (A.4). The controllability matrix for pair $(\boldsymbol{A}_{\boldsymbol{\chi}}, \boldsymbol{B}_{\boldsymbol{\chi}})$ was verified to be full rank for the given model parameters, thus system (B.12) is controllable for the nominal parameter β.

The weighting matrices used for the $\mathcal{H}_\infty$ controller are given by

$$\boldsymbol{H}_{\boldsymbol{z}} = \mathrm{diag}\left(\frac{\sqrt{20}}{2}, \frac{\sqrt{20}}{2}, \frac{\sqrt{20}}{2}, \frac{\sqrt{10}}{\pi/2}, \frac{\sqrt{10}}{\pi/2}, \frac{\sqrt{15}}{\pi}, \frac{0.1}{\pi/2}, \frac{0.1}{\pi/2}, \frac{1}{2}, \frac{1}{2}, \frac{1}{2}, \frac{\sqrt{5}}{3\pi}, \frac{\sqrt{5}}{3\pi}, \frac{1}{\pi/4}, \frac{0.1}{3\pi}, \frac{0.1}{3\pi}, \sqrt{30}, \sqrt{30}, \sqrt{30}, 1\right),$$

$$\boldsymbol{D}_{\boldsymbol{zu}} = \begin{bmatrix} \frac{\sqrt{750}}{30 - f_{\mathrm{R}}^{\mathrm{eq}}} & 0 & 0 & 0 \\ 0 & \frac{\sqrt{750}}{30 - f_{\mathrm{R}}^{\mathrm{eq}}} & 0 & 0 \\ 0 & 0 & \frac{\sqrt{5000}}{2} & 0 \\ \mathbf{0}_{2\times1} & \mathbf{0}_{2\times1} & \mathbf{0}_{2\times1} & \mathbf{0}_{2\times1} \\ 0 & 0 & 0 & \frac{\sqrt{5000}}{2} \\ \mathbf{0}_{14\times1} & \mathbf{0}_{14\times1} & \mathbf{0}_{14\times1} & \mathbf{0}_{14\times1} \end{bmatrix}, \quad \boldsymbol{D}_{\boldsymbol{zd}} = \begin{bmatrix} \mathbf{0}_{8\times3} & \mathbf{0}_{8\times3} & \mathbf{0}_{8\times2} \\ \mathbb{I}_{3\times3} & \mathbf{0}_{3\times3} & \mathbf{0}_{3\times2} \\ \mathbf{0}_{3\times3} & \mathbb{I}_{3\times3} & \mathbf{0}_{3\times2} \\ \mathbf{0}_{2\times3} & \mathbf{0}_{2\times3} & \mathbf{0}_{2\times2} \\ \mathbb{I}_{3\times3} & \mathbf{0}_{3\times3} & \mathbf{0}_{3\times2} \\ \mathbf{0}_{1\times3} & \boldsymbol{v} & \mathbf{0}_{1\times2} \end{bmatrix},$$

where $\boldsymbol{v} \triangleq [0\ 0\ 1]$. Matrices $\boldsymbol{H_z}$ and $\boldsymbol{D_{zu}}$ were adjusted such that $\boldsymbol{H_z^T H_z} = \boldsymbol{\Omega_\chi}$ and $\boldsymbol{D_{zu}^T D_{zu}} = \boldsymbol{\Omega_u}$, where $\boldsymbol{\Omega_\chi}$ and $\boldsymbol{\Omega_u}$ are given in (A.5), while $\boldsymbol{D_{zd}}$ was adjusted by trial and error. Table B.1 shows the gain matrices used in both formation controllers and the $\mathcal{D}$-stability parameters. For these matrices and the presented $\mathcal{D}$-stability parameters, the attenuation level γ comes to be 113.4739. The gain matrices of the formation controllers were adjusted by trial and error, whilst the $\mathcal{D}$-stability parameters were adjusted according to time-response properties associated with each region (Chilali & Gahinet, 1996).

Table B.1: Gain matrices of the formation controllers and $\mathcal{D}$-stability parameters

Backstepping		TSID		$\mathcal{D}$-stability	
$\boldsymbol{K}_A$	$1.2 \cdot \mathbb{I}_{24\times24}$	$\boldsymbol{K}_1$	$1.3 \cdot \mathbb{I}_{24\times24}$	λ	2.2
$\boldsymbol{K}_B$	$0.1 \cdot \mathbb{I}_{24\times24}$	$\boldsymbol{K}_2$	$1.12 \cdot \mathbb{I}_{24\times24}$	c	0
$\boldsymbol{K}_C$	$0.1 \cdot \mathbb{I}_{24\times24}$			r	100
				μ	$\pi/10$

The reference signals for the formation in all simulations are given by $\underline{x}_{\sigma d} = 1 + \varepsilon(1/2)[(2t)\hat{\imath} + (\cos(0.2t) - 1)\hat{k}]$, $\underline{x}_{rd} = 1 + \varepsilon(1/2)[3\cos(0.3t)\hat{\jmath} + 3\sin(0.3t)\hat{k}]$ and $\underline{x}_{ad}^{\sigma} = 1 + \varepsilon(1/2)(-\hat{\imath})$, which are concatenated into $\boldsymbol{x}_d$ after applying the $\mathbf{vec}_8$ operator. The formation's parameter φ was chosen as 3.

The first simulation was performed considering a disturbance free scenario. The Euclidean norm of the error vector is shown in Fig. B.2. Note that its time evolution is almost the same for the backstepping controller and the TSID controller, both achieving null steady-state error. Since the Euclidean norm cannot assume negative values, at some point between three and five seconds it increases due to overshoot.

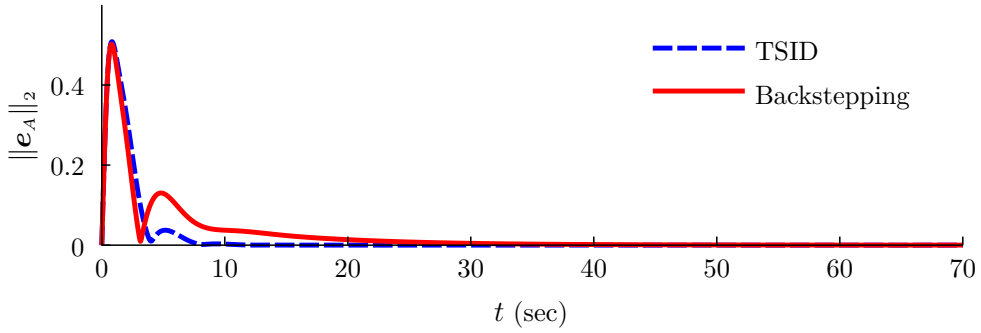

Figure B.2: Euclidean norm of the error vector in the disturbance-free scenario.

The second simulation considered constant disturbances added to the acceleration signals generated by the formation controller. As illustrated in Fig. B.3, unlike the TSID controller, which not achieved null steady-state error, the backstepping controller was capable of rejecting the disturbances. To demonstrate the sustained disturbances rejection feature of the $\mathcal{D}$-stable $\mathcal{H}_\infty$ controller, external forces are also applied to the UAVs. The disturbance profiles are shown in Fig. B.4. Finally, Fig. B.5 illustrates the trajectories

performed by the tilt-rotor UAVs for the scenario with disturbances using the backstepping controller.

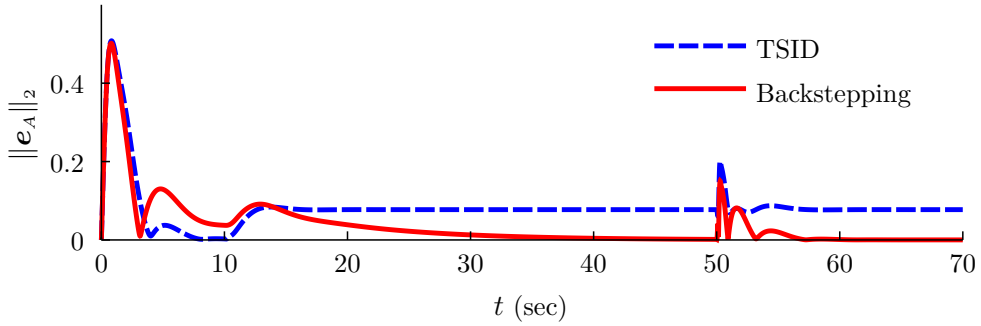

Figure B.3: Euclidean norm of the error vector in the scenario with external disturbances.

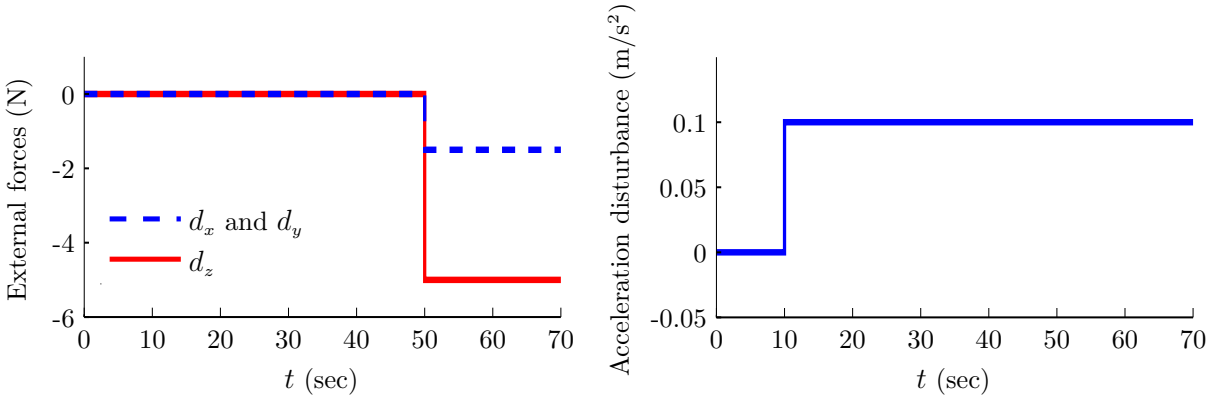

Figure B.4: Applied disturbances: external forces (*left*) and acceleration disturbance (*right*). The former ones are applied to the geometric center of each tilt-rotor UAV, whilst the latter is added to the reference signals $\ddot{x}_i^{\text{tr}}$, $\ddot{y}_i^{\text{tr}}$ and $\ddot{z}_i^{\text{tr}}$ provided by the formation controller, with $i \in \{\sigma, \zeta, \tau\}$.

B.5 Conclusions and future work

A control strategy for the leader-follower formation problem was presented in this appendix. The formation model was formulated using the cooperative dual task-space, and a backstepping controller based on this approach was proposed. Another control strategy, based on the TSID technique, was designed for comparison purposes. A group of tilt-rotor UAVs was taken as case study, and a linear state-feedback $\mathcal{D}$-stable H_∞ controller was designed for each individual reference tracking based on the UAV's linearized dynamic equations. Then, the backstepping controller and one linear state-feedback controller per UAV were arranged in a hierarchical structure. Simulation results performed in the MATLAB/Simulink environment for the backstepping controller and the TSID controller were presented and compared. In a disturbance-free scenario, the UAVs' behavior was

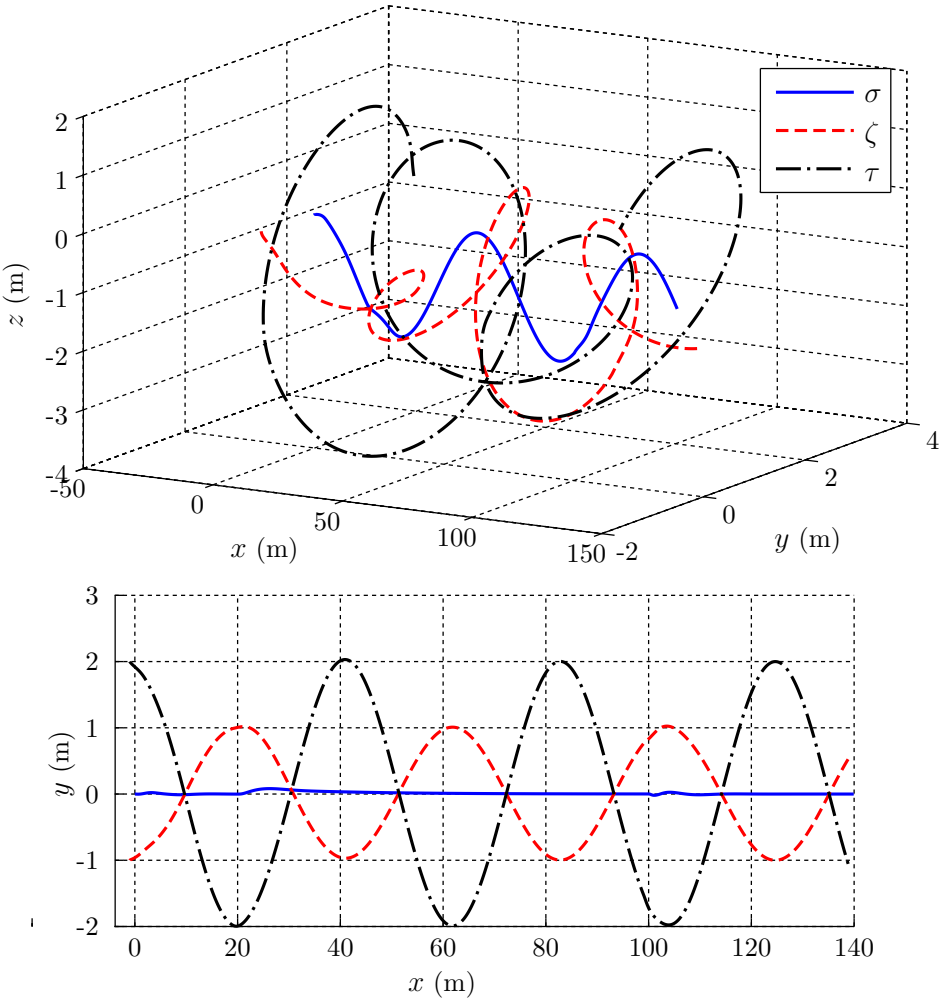

Figure B.5: Trajectories performed by the tilt-rotor UAVs: 3D view (*top*) and top view (*bottom*).

almost the same for both controllers. However, when constant disturbances were added to the acceleration signals generated by the formation controller, the backstepping controller rejected them, while the TSID controller did not. Also, constant external forces were added, so the sustained disturbances rejection feature of the $\mathcal{D}$-stable $\mathcal{H}_\infty$ controller could be shown.

The presented formation control strategy is based on a centralized approach. When the formation is scaled up (which is possible by defining multiple relative and absolute positions), $\boldsymbol{J}_S$ increases in eight rows and n_i columns per agent, and also becomes ill-conditioned. Therefore, the computational effort necessary to compute $\boldsymbol{J}_S^+$ grows polynomially (Burden & Faires, 2010). Considering this fact, future works may deal with decentralized formation control strategies.

C Miscellaneous proofs

In Chapter 3, it was claimed that the inverse of the positive definite matrix $\boldsymbol{P}_2$, defined for derivation of the discrete-time $\mathcal{H}_2$ control, satisfies the inequalities (3.2) and (3.3) for the closed-loop system (3.21). A proof is presented in this appendix.

Firstly, since $\boldsymbol{P}_2 > 0$, we have that $\boldsymbol{P}_2^{-1} > 0$, hence the inequality (3.2) is satisfied. For clarity, the inequality (3.24) is repeated here,

$$(\boldsymbol{A}_\chi - \boldsymbol{B}_\chi \boldsymbol{K})\boldsymbol{P}_2(\boldsymbol{A}_\chi - \boldsymbol{B}_\chi \boldsymbol{K})^T - \boldsymbol{P}_2 + \boldsymbol{F}_\chi \boldsymbol{F}_\chi^T < 0.$$

Since $\boldsymbol{F}_\chi \boldsymbol{F}_\chi^T$ is positive semi-definite[1], we have that

$$(\boldsymbol{A}_\chi - \boldsymbol{B}_\chi \boldsymbol{K})\boldsymbol{P}_2(\boldsymbol{A}_\chi - \boldsymbol{B}_\chi \boldsymbol{K})^T - \boldsymbol{P}_2 < 0,$$

which is equivalent to

$$(\boldsymbol{A}_\chi - \boldsymbol{B}_\chi \boldsymbol{K})\boldsymbol{P}_2\boldsymbol{P}_2^{-1}\boldsymbol{P}_2(\boldsymbol{A}_\chi - \boldsymbol{B}_\chi \boldsymbol{K})^T - \boldsymbol{P}_2 < 0.$$

By applying the Schur complement, yields

$$\begin{bmatrix} \boldsymbol{P}_2 & (\boldsymbol{A}_\chi - \boldsymbol{B}_\chi \boldsymbol{K})\boldsymbol{P}_2 \\ \boldsymbol{P}_2(\boldsymbol{A}_\chi - \boldsymbol{B}_\chi \boldsymbol{K})^T & \boldsymbol{P}_2 \end{bmatrix} < 0.$$

[1] $\boldsymbol{x}^T \boldsymbol{F}_\chi \boldsymbol{F}_\chi^T \boldsymbol{x} = \|\boldsymbol{F}_\chi^T \boldsymbol{x}\|_2^2 \geq 0, \ \forall \boldsymbol{x} \in \mathbb{R}^{24}$

Then, through the congruence transformation

$$\begin{bmatrix} \mathbf{0} & \boldsymbol{P}_2^{-1} \\ \boldsymbol{P}_2^{-1} & \mathbf{0} \end{bmatrix} \begin{bmatrix} \boldsymbol{P}_2 & (\boldsymbol{A}_{\boldsymbol{\chi}} - \boldsymbol{B}_{\boldsymbol{\chi}}\boldsymbol{K})\boldsymbol{P}_2 \\ \boldsymbol{P}_2(\boldsymbol{A}_{\boldsymbol{\chi}} - \boldsymbol{B}_{\boldsymbol{\chi}}\boldsymbol{K})^T & \boldsymbol{P}_2 \end{bmatrix} \begin{bmatrix} \mathbf{0} & \boldsymbol{P}_2^{-1} \\ \boldsymbol{P}_2^{-1} & \mathbf{0} \end{bmatrix} < 0,$$

leads to

$$\begin{bmatrix} \boldsymbol{P}_2^{-1} & (\boldsymbol{A}_{\boldsymbol{\chi}} - \boldsymbol{B}_{\boldsymbol{\chi}}\boldsymbol{K})^T\boldsymbol{P}_2^{-1} \\ \boldsymbol{P}_2^{-1}(\boldsymbol{A}_{\boldsymbol{\chi}} - \boldsymbol{B}_{\boldsymbol{\chi}}\boldsymbol{K}) & \boldsymbol{P}_2^{-1} \end{bmatrix} < 0.$$

Finally, by applying the Schur complement yields

$$(\boldsymbol{A}_{\boldsymbol{\chi}} - \boldsymbol{B}_{\boldsymbol{\chi}}\boldsymbol{K})^T\boldsymbol{P}_2^{-1}(\boldsymbol{A}_{\boldsymbol{\chi}} - \boldsymbol{B}_{\boldsymbol{\chi}}\boldsymbol{K}) - \boldsymbol{P}_2^{-1} < 0,$$

which is the inequality (3.3) for the closed-loop system (3.21).